



HAL
open science

Development of numerical modelling chains to account for the effects of wind small scales space-time variability in the simulation of power production with wind turbines

Ángel García Gago

► **To cite this version:**

Ángel García Gago. Development of numerical modelling chains to account for the effects of wind small scales space-time variability in the simulation of power production with wind turbines. Environmental Engineering. École des Ponts ParisTech, 2023. English. NNT : 2023ENPC0041 . tel-04579420

HAL Id: tel-04579420

<https://pastel.hal.science/tel-04579420>

Submitted on 17 May 2024

HAL is a multi-disciplinary open access archive for the deposit and dissemination of scientific research documents, whether they are published or not. The documents may come from teaching and research institutions in France or abroad, or from public or private research centers.

L'archive ouverte pluridisciplinaire **HAL**, est destinée au dépôt et à la diffusion de documents scientifiques de niveau recherche, publiés ou non, émanant des établissements d'enseignement et de recherche français ou étrangers, des laboratoires publics ou privés.



École des Ponts
ParisTech

THÈSE DE DOCTORAT
de l'École des Ponts ParisTech

Development of numerical modelling chains to account for the effects of wind small scales space-time variability in the simulation of power production with wind turbines

Développement de chaînes de modélisation numérique pour prendre en compte les effets de la variabilité à petites échelles du vent dans la simulation de la production électrique avec des éoliennes.

École doctorale N° 531, Sciences, Ingénierie et Environnement (SIE)

Spécialité : Sciences et Techniques de l'Environnement

Thèse préparée au sein des laboratoires HM&Co

Thèse soutenue le 06 December 2023, par
Ángel García Gago

Composition du jury :

Martin, OBLIGADO
Professor, Centrale Lille Institut

*Président du jury
Rapporteur*

Rudy, CALIF
Professeur, Université des Antilles

Rapporteur

Sandrine, AUBRUN
Professeure des universités, Ecole Centrale de Nantes

Examineur

Paul, VEERS
Senior Research Fellow, National Renewable Energy Laboratory

Examineur

Maxime, THIÉBAUT
Chercheur, France Energies Marines

Examineur

Ioulia, TCHIGUIRINSKAIA
Directrice de recherche, École des Ponts ParisTech

Examinatrice

Daniel, SCHERTZER
Professeur, École des Ponts ParisTech

Examineur

Auguste, Gires
Professeur associé, École des Ponts ParisTech

Directeur de thèse

Development of numerical modelling chains to account for the effects of wind small scales space-time variability in the simulation of power production with wind turbines

Ángel García Gago

Acknowledgements

The author is very grateful to the École des Ponts ParisTech and Hidrology Meteorology & Complexity lab for hosting his PhD and to the ANR JCJC RW-Turb project (ANR-19-CE05-0022-01) for funding it.

During the research that has led to this manuscript, I have met many amazing people from different backgrounds who have helped me grow not only as a researcher but also as a person and have been a great help in getting me to the end. The main credit goes to my thesis supervisor, Auguste Gires, who is the main person responsible for making this document possible. I would also like to thank him for the moments that are not directly related to research that have made my day-to-day life much easier, as well as for the merit of appreciating science in other very different forms such as food. I would also like to thank Daniel Schertzer and Ioulia Tchiguirinskaia, whose advice greatly advanced my results.

I greatly appreciate the rest of the jury members, Prof. Rudy Calif, Prof. Martin Obligado, Prof. Sandrine Aubrun, Paul Veers and Dr. Maxime Thiebaut for going through the manuscript and their valuable comments during their report and the thesis Defence.

Outside the scientific area there are also many people I would like to acknowledge, first of all my colleagues in the lab who welcomed me when I arrived, Alejandra, Guillaume, Hai, Pierre, Sitian, Xin or Yangzi, also the people in the lab like Albertine or Pierre Antoine for making my stay easier. I want to make special mention to Arun and Adarsh for all the good times over coffee or beer, and to Jerry for being the person with whom I have shared the most time and helped me the most. Many thanks also to my family because I know how difficult it has been for them to have me away. Many thanks to Diego, because France has not been so bad sharing a flat with him, to my friends Fran, Noelia, Peque, Mario and Diego who have shown that friends are that family that you choose.

And last but not least to Vero, who in the end is the one who has suffered the most from this thesis, the long hours putting up with each and every detail of the document, all her advice, all the bad moments it has entailed, and yet here she is still by my side. Thank you very much indeed.

Abstract

Atmospheric fields, and notably wind fields are known to exhibit extreme variability across wide ranges of space-time scales. This makes them complex to analyse, model and even to observe. Standard Gaussian tools are not able to deal with such variability and underestimate extreme fluctuations. However, the ongoing increase of wind power production in energy transition scenarios highlights the need to better characterize and simulate these fields.

Multifractals are an appropriate candidate for this required framework. Indeed, they rely on the physically based concept of scale invariance retrieved from the governing Navier-Stokes equations. In this framework, fields are generated through a multiplicative cascade process, where activity is iteratively transferred from large scales down to dissipation scales, which is of few millimeters in the case of wind. In the specific framework of Universal Multifractals (UM) only three parameters with clear physical interpretations are needed to fully characterize the fields' variability. UM have been extensively used to characterize and simulate a wide range of geophysical fields such as wind, rainfall or river flow.

In a first step of this PhD, realistic wind fields are simulated. First, UM analysis were implemented on high-resolution 3D anemometer data collected during the RW-Turb measurement campaign that took place over 2.5 years on the operational wind farm of Pays d'Othe. A good scaling behaviour between 4 s and 17 min was observed and trends of retrieved UM parameters were identified depending on average wind. Rapid changes are found up to roughly 4 m/s before reaching a plateau. Then wind fields are simulated relying on existing methods for continuous cascades. These tools are designed to facilitate the simulation of both scalar and vector geophysical fields, expanding beyond the constraints of one-dimensional scenarios. They offer the flexibility to extend their application to spatial, temporal, or spatio-temporal fields, providing a versatile approach to modeling complex vector fields. Four distinct wind simulation methods are implemented on the range of scales identified in the analysis. The first one entails the reconstruction of wind fields from point measurements using scaling laws, although it does involve certain oversimplifications. The next two methods, are both based on Fractionally Integrated Flux. One directly simulates wind fields, while the second is tailored to model wind fluctuations and reconstruct wind from there. Tools to simulate scalars (horizontal wind) or vectors for time series, maps or in a 3D space plus time framework were developed. Finally, fields were also generated using the commercial software Turbsim, developed by the US National Renewable Energy Laboratory (NREL). It relies on Gaussian statistics which are known to exhibit limitations in capturing the true nature of wind fields. Simulations were analysed in 1D and 2D to confirm validity. It appears that observed wind properties are best reproduced by direct FIF simulations.

Finally, the wind fields simulated are used to investigate the effects of small-scale wind variability on the wind turbine torque computation by imputing the simulated vector fields into three

modelling chains with increasing complexity. The first one only considers the temporal variability, averaging the wind field and considering it at hub height. The second one is based on the angular moment definition and allows to consider both spatial and temporal variability by computing the torque at each blade point and integrating it along the radius for each time step. Finally, the third one uses the commonly used in research and industry software OpenFAST developed by the NREL. Overall similar features are observed for three types of simulated time series. UM analysis implemented on ensemble of simulations enabled to highlight a better ability of the integral method to account for the small scale wind fluctuations.

keywords: turbulence, multifractals, wind modelling, wind energy, atmospheric variability

Résumé

Les champs atmosphériques, dont le vent, présentent une variabilité extrême sur une large gamme d'échelles spatio-temporelles. Cela les rend complexes à analyser, modéliser et même observer. Les outils gaussiens standard ne permettent pas de prendre en compte cette variabilité et sous-estiment les fluctuations extrêmes. L'augmentation continue de la production éolienne dans les scénarios de transition énergétique souligne la nécessité de mieux caractériser et simuler ces champs.

Les Multifractales Universels (UM) sont un candidat approprié pour ce cadre requis. En effet, elles reposent sur le concept physique d'invariance d'échelle, hérité des équations de Navier-Stokes, et sont parcimonieuses avec seulement trois paramètres physiquement interprétables pour caractériser pleinement la variabilité des champs. Dans ce cadre, les champs sont générés par un processus de cascade multiplicative, où l'activité est transférée itérativement des grandes échelles jusqu'aux échelles de dissipation (quelques mm pour le vent). Les UM ont été largement mis en oeuvre sur large spectre de champs géophysiques.

D'abord, des champs de vent réalistes ont été simulés. Une analyse UM a été mise en oeuvre sur des données d'anémomètres 3D à haute résolution collectées lors de la campagne de mesure du projet RW-Turb qui a eu lieu pendant 2,5 ans sur le parc éolien des Pays d'Othe. On a observé un bon comportement invariant d'échelles entre 4 secondes et 17 minutes et identifié des tendances sur paramètres UM en fonction de la vitesse moyenne du vent. Des changements rapides sont notés jusqu'à environ 4 m/s avant d'atteindre un plateau. Ensuite, des champs de vent sont simulés en utilisant des méthodes existantes pour les cascades continues. Ces outils sont conçus pour faciliter la simulation de champs géophysiques scalaires et vectoriels. Ils offrent la flexibilité d'étendre leur application à des champs 1D, 2D et 2D+1, fournissant ainsi une approche polyvalente pour la modélisation de champs vectoriels complexes. Quatre méthodes de simulation du vent sont mises en oeuvre sur la plage d'échelles identifiées dans l'analyse. La première, simpliste, implique la reconstruction des champs de vent à partir de mesures ponctuelles et de lois d'échelles. Deux autres sont basées sur les Flux Intégrés Fractionnairement (FIF). L'une simule directement les champs de vent, tandis que la seconde est adaptée pour modéliser les fluctuations du vent et le reconstruire à partir de là. Des outils ont été développés pour simuler des scalaires (vent horizontal) ou des vecteurs pour des séries temporelles, des cartes ou dans un espace 3D avec le temps. Enfin, des champs ont également été générés en utilisant le logiciel commercial Turbsim, développé par le NREL (Etats-Unis). Il repose sur des statistiques gaussiennes, dont les limites sont connues pour le vent. Les simulations ont été analysées en 1D et 2D pour confirmer leur validité. Les propriétés du vent observées sont mieux reproduites par des simulations FIF directes.

Enfin, les champs de vent simulés sont utilisés pour étudier les effets de la variabilité du vent à petites échelles sur le couple de l'éolienne en les intégrant dans trois chaînes de modélisation à la

complexité croissante. La première ne prend en compte que la variabilité temporelle, en moyennant le vent et en le considérant à la hauteur de la nacelle. La deuxième intègre la contribution de chaque portion de pale pour calculer à chaque pas de temps le couple global et ainsi prendre en compte à la fois la variabilité spatiale et temporelle. La troisième utilise le logiciel largement utilisé dans la recherche et l'industrie, OpenFAST (NREL). Dans l'ensemble, des caractéristiques similaires sont observées pour les trois types de séries temporelles simulées. L'analyse UM mise en œuvre sur un ensemble de simulations montre une meilleure capacité de la méthode intégrale à tenir compte des fluctuations du vent à petite échelle.

Mots clés: turbulence, multifractals, modélisation du vent, énergie éolienne, variabilité atmosphérique.

Contents

Acknowledgements	2
Abstract	3
Abbreviations	18
List of symbols	19
Introduction	22
1 Universal Multifractals	29
1.1 Introduction	29
1.2 Theoretical framework	33
1.2.1 Towards fractal geometry	33
1.2.2 Fractal Dimension	34
1.2.3 Towards multifractality	36
1.2.4 Multifractal Properties	37
1.2.5 Universality	39
1.2.6 Phase transitions	41
1.2.6.1 Divergence of moments	41
1.2.6.2 Sampling limitation	42
1.3 Simulation	43
1.3.1 Simulating tools	43
1.3.1.1 Introduction to cascade phenomenology	43
1.3.1.1.1 Self-similar cascades	46
1.3.1.1.2 Self-affine cascades	47
1.3.1.1.3 General Scale Invariance (GSI)	47
1.3.1.2 Lévy sub-generator	48
1.3.2 Discrete Cascades	50
1.3.2.1 β -model	50

1.3.2.2	UM discrete cascades	53
1.3.3	Continuous cascades	55
1.3.3.1	Unidimensional case	55
1.3.3.2	Extension to multidimensional case	58
1.3.3.2.1	General case	58
1.3.3.2.2	Space-time cascades	58
1.3.3.3	Extension to non-conservative fields	59
1.3.4	Vector fields	61
1.3.4.1	Theoretical background	61
1.3.4.2	Clifford Algebra	61
1.3.4.3	Multifractal Operators	63
1.4	Analysis	65
1.4.1	Trace moments techniques	65
1.4.2	Spectral analysis	68
1.4.3	Validation of the simulations	69
1.4.3.1	Illustration of the analysis techniques for simulations over vari- ous dimensions	69
1.4.3.2	Sensitivity analysis of the input parameters	72
1.4.3.3	Effect of H	73
1.4.3.4	Vector fields	76
1.5	Summary	80
2	Wind simulation	83
2.1	Introduction	83
2.2	Data & analysis	85
2.2.1	Description of the data	85
2.2.2	Data preparation	87
2.2.3	Comparison with previous studies	91
2.3	Turbsim	93
2.3.1	Runtime options	94
2.3.2	Turbine/Model Specifications	95
2.3.3	Meteorological Boundary Conditions	96
2.3.3.1	General overview	96
2.3.3.2	Spectral models	97
2.3.3.3	Wind profiles	100
2.3.4	Non-IEC Meteorological Boundary Conditions	101
2.3.5	Spatial Coherence Parameters	102
2.3.6	Coherent Turbulence Scaling Parameters	103
2.3.7	Examples of use	104

2.4	Simplistic approach	106
2.4.1	Theoretical background	106
2.4.2	Example of simulations	111
2.4.3	Limitations	112
2.5	The Fractionally Integrated Flux (FIF)	115
2.5.1	FIF on direct fields	115
2.5.2	Reconstruction of Fluctuations (RoF)	116
2.6	Comparison between the methods	121
2.6.1	Temporal analysis of each pixel	122
2.6.2	Spatial analysis	123
2.7	Summary	132
3	Modelling chains	135
3.1	Introduction	135
3.2	Modelling chains	137
3.2.1	Theoretical background	137
3.2.1.1	Conservation of mass	137
3.2.1.2	Momentum theory	138
3.2.1.3	Power coefficient	139
3.2.1.4	Angular momentum theory	141
3.2.1.5	Vector behaviour	144
3.2.2	Traditional approach	144
3.2.2.1	Theoretical description	144
3.2.2.2	Tower shadow correction	146
3.2.2.3	Practical implementation	146
3.2.3	Integral approach	147
3.2.3.1	Theoretical description	149
3.2.3.1.1	Blade element theory	149
3.2.3.1.2	Torque computation	150
3.2.3.2	Practical implementation	151
3.2.4	OpenFAST	151
3.2.4.1	Overview of theoretical description	153
3.2.4.1.1	Wake modelling	153
3.2.4.1.2	Blade aerodynamics	156
3.2.4.1.3	Tower shadow correction	158
3.2.4.2	Practical implementation	159
3.2.5	Summary	160
3.3	Validation of modelling chains	161
3.3.1	Properties of the simulations	161

3.3.2	First tests with uniform fields	161
3.3.3	Test of input parameters	164
3.3.4	Test with non-uniform fields	165
3.4	Results & discussion	166
3.4.1	Results using 10 samples	167
3.4.2	Results using 100 samples	169
3.5	Summary	176
Conclusions and perspectives		177
References		181
Appendix		202
A	Drive codes	203
A.1	Turbsim input File	203
A.2	OpenFAST Drive Code	209
A.3	AeroDyn Drive Code	213
B	Simulations with Turbsim and Simplistic Approach	219
B.1	Turbsim	219
B.2	Simplistic Approach	219
C	UM analysis Torque	229
C.1	10 samples	229
C.2	100 samples	229
D	Scripts	237
D.1	UM scripts	237
D.2	Wind simulation scripts	239
D.3	Torque computation scripts	240
E	Publications	243

List of Figures

1.1	Examples of fractal objects	34
1.2	Example of 2D field to illustrate the computation of the D_F	35
1.3	Explanation of fractal dimension computation for cantor set	36
1.4	Rainfall data from Dedougou for a period of 45 years	36
1.5	Example of the effect of different thresholds in the computation of the D_F	38
1.6	Illustration of the concept of singularity using variability in rainfall intensities across various scales	39
1.7	Illustration of scaling function, $K(q)$ and codimension function $c(\gamma)$	40
1.8	PDF of wind data (RW-Turb measurement campaign) and comparison with Gaus- sian distribution	42
1.9	Illustration of the energy spectra for wind turbulence	46
1.10	Examples of GSI with different values of the parameters c, d, e, f	48
1.11	Illustration of a discrete cascade process in 1D and 2D	51
1.12	Illustration of a β -model with different values of c_β	52
1.13	Illustration of a UM discrete cascades for input parameters $\alpha = 1.5$ and $C_1 = 0.1$ in 1D and 2D	54
1.14	Illustration of a 2D+t UM discrete cascades for input parameters $\alpha = 1.5$ and $C_1 =$ 0.1 and 5 cascade steps	54
1.15	Illustration of the UM continuous cascade process in 1D	57
1.16	Illustration of the 2D UM continuous cascade fields	58
1.17	Illustration of the 2D+t UM continuous cascade field with input parameters $\alpha = 1.5$ and $C_1 = 0.1$ over and area of 256x256, and 256 time steps.	60
1.18	Illustration of the 2D UM non-conservative continuous cascade fields	62
1.19	Example of a snapshots of a 2D+1 and 3D+1 multifractal vector fields	65
1.20	Illustration of a Trace moment technique using a simulated ensemble	66
1.21	Illustration of a Double Trace moment technique using a simulated ensemble	67
1.22	Illustration of a spectral analysis from 1 sample and 100 samples	69
1.23	Illustration of the analysis techniques for 1D	70
1.24	Illustration of the analysis techniques for 2D	70

1.25	Illustration of the analysis techniques for 2D+time in the spatial dimension	71
1.26	Illustration of the analysis techniques for 2D+time in the temporal dimension	71
1.27	Sensitivity analysis on the UM parameters retrieved on the ensemble simulation	71
1.28	Sensitivity analysis of the UM parameters (α and C_1) retrieved on the analysis of 512x512 ensemble field for several inputted α	72
1.29	Sensitivity analysis of the UM parameters (α and C_1) retrieved on the analysis of 512x512 ensemble field for several inputted C_1	73
1.30	Illustration of the effect of positive H on the UM techniques	74
1.31	Illustration of the effect of negative H on the UM techniques	74
1.32	Effect of different values of H in the behaviour of the TM and the parameters retrieved	75
1.33	Illustration of the correction in TM graphs	76
1.34	Validation of the simulations of Vector fields for the first component	77
1.35	Validation of the simulations of Vector fields for the second component	77
1.36	Validation of the simulations of Vector fields for the resultant component	77
1.37	Sensitivity analysis on the UM parameters retrieved on the vector simulation	78
1.38	Validation of the simulations of Vector fields for the first component	78
1.39	Validation of the simulations of Vector fields for the second component	78
1.40	Validation of the simulations of Vector fields for the third component	79
1.41	Validation of the simulations of Vector fields for the resultant component	79
1.42	Sensitivity analysis on the UM parameters retrieved on the vector simulation	79
2.1	Illustration of the location and map of the surroundings of the meteorological mast used on RW-Turb measurement campaign	85
2.2	Scheme of the distribution of the devices in the meteorological masts (from Gires et al., 2022a)	86
2.3	Example of x component wind speed retrieved from the 3D anemometers in the period December 2020 and May 2022	87
2.4	Example of TM analysis for 8 m/s with one scaling regime and with three scaling regimes	88
2.5	Evolution of the UM parameters with the average wind speeds retrieved for the analysis of the wind fields	89
2.6	Evolution of the UM parameters with the average wind speeds retrieved for the analysis of the fluctuations of the wind	90
2.7	Evolution of the UM parameters with the average wind speeds retrieved for the analysis of the wind. Direct field and corrected field	91
2.8	Evolution of the UM parameters with the average wind speeds retrieved for the analysis of the fluctuations of the wind. Direct field and corrected field	92
2.9	UM analysis of the ensemble used for the Fig. 2.5 but corrected to obtain $H = 0$	93
2.10	Example of wind profiles computed in TurbSim	102

2.11	Illustration of coherent structures	104
2.12	Example of Wind field simulated with Turbsim	105
2.13	Analysis of one of the points of the Fig. 2.14 situated at $x=-24\text{m}$ and $z=123.31\text{m}$.	107
2.14	Spatial distribution of UM parameters retrieved on the analysis of the Turbsim wind fields	108
2.15	Illustration of analysis of the differences between the two anemometers	110
2.16	Temporal evolution of c_ε	111
2.17	Spatial distribution of wind field on the 3 consecutive time steps simulated using simplistic approach	112
2.18	Wind time series ensemble at 3 different distances from anemometer data	113
2.19	Percentiles 10, 50 and 90 of 2.19a Wind time series and of 2.19b Wind increments at different distances from anemometer data	114
2.20	Spatial distribution of the UM parameters retrieved on the analysis of wind fields simulated the simplistic approach	114
2.21	Scheme of the process followed to simulate wind fields using FIF approaches . . .	115
2.22	Example of five 17-minutes wind fields simulated using FIF approach for target average wind speed 9.5 ms^{-1}	116
2.23	Evolution of the UM parameters with the wind speeds in the simulation using the FIF approach	117
2.24	Example of each step of the process used for the simulation of the wind field using the RoF approach	118
2.25	Evolution of the UM parameters with the wind speeds in the simulation of the fluctuations of the wind fields	119
2.26	Evolution of the UM parameters with the wind speeds in the simulation using the RoF approach	120
2.27	Comparison between the average velocity retrieved in the ensemble of the simulated wind fields and velocity used to initialize the simulation.	121
2.28	Example of extension of wind fields	122
2.29	Spatial distribution of r^2 using different methods of wind simulation	124
2.30	Spatial distribution of α using different methods of wind simulation	125
2.31	Spatial distribution of C_1 using different methods of wind simulation	126
2.32	Spatial distribution of H using different methods of wind simulation	127
2.33	UM analysis in the spatial dimension of a ensemble of 100 samples simulated with Simplistic approach	128
2.34	UM analysis in the spatial dimension of a ensemble of 100 samples simulated with FIF using the properties of fields with average velocity 11 ms^{-1} as input	129
2.35	UM analysis in the spatial dimension of a ensemble of 100 samples simulated with RoF approach using the properties of fields with average velocity 11 ms^{-1} as input	130

2.36	UM analysis in the spatial dimension of a ensemble of 100 samples simulated with Turbsim using the event of 20/12/2020 as input	131
3.1	Scheme of the control volume used in the wind turbine	137
3.2	Wind turbine power coefficient vs. tip speed ratio at various pitch angles	141
3.3	Illustration of how the tangential velocity grows across the blade thickness (Adapted from Burton et al., 2011).	142
3.4	Scheme of the vector wind speed	145
3.5	Geometry of the wind turbine used for the tower shadow correction	147
3.6	Scheme of traditional approach	148
3.7	Illustration of velocities and forces presented in airfoil	149
3.8	Scheme of Integral approach	152
3.9	Available modules on OpenFAST	154
3.10	Effect of tower shadow modelled by AeroDyn	158
3.11	Example of torque time series computed with different methods	162
3.12	Example of normalized torque time series computed with the different angles of the turbine	163
3.13	3.13a Example of torque time series computed with a uniform vector field with increasing wind speed	164
3.14	Example of torque time series computed with a uniform vector fields	165
3.15	Example of normalized torque time series computed with different methods using as input wind fields simulated using the FIF approach and input parameters $\alpha = 1.5$ and $C_1 = 0.1$, and target velocity of 11 ms^{-1}	166
3.16	Illustration of the correction in torque data	168
3.17	Analysis of the horizontal wind field of the center of the grid (10 samples)	169
3.18	Analysis of the horizontal wind field averaged over the grid (10 samples)	170
3.19	Analysis of the torque time series computed using Traditional Approach (10 samples)	170
3.20	Analysis of the torque time series computed using Integral Approach (10 samples)	170
3.21	Analysis of the torque time series computed using OpenFAST (10 samples)	171
3.22	Effect of C_1 on the computation of UM parameters	171
3.23	Analysis of the horizontal wind field of the center of the grid (100 samples)	173
3.24	Analysis of the horizontal wind field averaged over the grid (100 samples)	173
3.25	Analysis of the torque time series computed using Traditional Approach (100 samples)	174
3.26	Analysis of the torque time series computed using Integral Approach (100 samples)	174
B.1.1	Spatial distribution of α for different input days simulated with Turbsim	220
B.1.2	Spatial distribution of C_1 for different input days simulated with Turbsim	221
B.1.3	Spatial distribution of H for different input days simulated with Turbsim	222
B.1.4	Spatial distribution of r^2 for different input days simulated with Turbsim	223

B.2.5 Spatial distribution of α for different input days simulated with Simplistic approach	224
B.2.6 Spatial distribution of C_1 for different input days simulated with Simplistic approach	225
B.2.7 Spatial distribution of H for different input days simulated with Simplistic approach	226
B.2.8 Spatial distribution of r^2 for different input days simulated with Simplistic approach	227
C.1.1 Analysis of the horizontal wind field of the center of the grid (10 samples) $\alpha = 1.8$, $C_1 = 0.05$	230
C.1.2 Analysis of the horizontal wind field of the center of the grid (10 samples) $\alpha = 1.1$, $C_1 = 0.1$	231
C.1.3 Analysis of the horizontal wind field of the center of the grid (10 samples) $\alpha = 1.5$, $C_1 = 0.3$	232
C.2.4 Analysis of the horizontal wind field of the center of the grid (100 samples) $\alpha = 1.8$, $C_1 = 0.05$	233
C.2.5 Analysis of the horizontal wind field of the center of the grid (100 samples) $\alpha = 1.1$, $C_1 = 0.1$	234
C.2.6 Analysis of the horizontal wind field of the center of the grid (100 samples) $\alpha = 1.5$, $C_1 = 0.3$	235

List of Tables

2.1	List of TurbSim ScaleIEC Values	95
2.2	List of TurbSim spectral models	96
2.3	List of TurbSim Wind profiles	97
2.4	List of TurbSim type of coherence events	103
2.5	Summary of the UM parameters obtained in the analysis of the spatial dimension of the different methods	129
3.1	Summary of the properties of the different torque computation methods	160
3.2	Correlation between OpenFAST and traditional approach with different Lags . . .	164
3.3	Summary of the parameters retrieved in the analysis of the time series simulated with input parameters $\alpha = 1.55, C_1 = 0.05$ (10 samples)	171
3.4	Summary of the parameters retrieved in the analysis of the time series simulated with input parameters $\alpha = 1.8, C_1 = 0.05$ (10 samples)	172
3.5	Summary of the parameters retrieved in the analysis of the time series simulated with input parameters $\alpha = 1.1, C_1 = 0.1$ (10 samples)	172
3.6	Summary of the parameters retrieved in the analysis of the time series simulated with input parameters $\alpha = 1.5, C_1 = 0.3$ (10 samples)	172
3.7	Summary of the parameters retrieved in the analysis of the time series simulated with input parameters $\alpha = 1.5, C_1 = 0.05$ (100 samples)	174
3.8	Summary of the parameters retrieved in the analysis of the time series simulated with input parameters $\alpha = 1.8, C_1 = 0.05$ (100 samples)	175
3.9	Summary of the parameters retrieved in the analysis of the time series simulated with input parameters $\alpha = 1.1, C_1 = 0.1$ (100 samples)	175
3.10	Summary of the parameters retrieved in the analysis of the time series simulated with input parameters $\alpha = 1.5, C_1 = 0.3$ (100 samples)	175

List of acronyms and abbreviations

IEC	International Electrotechnical Commission
UM	Universal Multifractals
NREL	National Renewable Energy Laboratory
ANR	Agence Nationale de la Recherche
Pr	Probability
RW-Turb	Rainfall Wind Turbine or Turbulence
PDF	Probability distribution function
BO	Bolgiano-Obukhov
KO	Kolmogorov-Obukhov
GSI	General Scale Invariance
TM	Trace Moment
DTM	Double Trace Moment
TurbSim	Turbulent Simulator
TI	Turbulent Intensity
(i)FFTs	(inverse) Fast Fourier Transform
FIF	Fractionally Integrated Flux
$Cl_{p,q}$	Clifford Algebra with signature p, q
TSR	Tip Speed Ratio
RE	Reynolds number
BEM	Blade Element Momentum Theory

List of recurring variables and symbols

L	Outer scale (m)
l	Observation scale (m)
λ	Scale ratio or resolution
D	Topological dimension
D_F	Fractal dimension
c_F	Fractal codimension
R	Rain rate (mm h^{-1})
γ	Singularity
$\varepsilon_\lambda, \phi_\lambda, \varphi_\lambda$	Process/structure/field under consideration at resolution λ
$\langle \rangle$	Ensemble averaging
\approx	Statistical equivalence
$c(\gamma)$	Codimension function
$K(q)$	Scaling moment function
q	Statistical moment order
α	Multifractality index
C_1	Mean intermittency parameter
q_s, q_D	Critical orders corresponding to sampling limitation and divergence of moments
γ_s, γ_D	Critical singularities corresponding to sampling limitation and divergence of moments
D_s	Sampling dimension
τ	Time scales (s)
\underline{u}	velocity field (ms^{-1})
p	Pressure (Pa)

ρ	Air density (kg m^{-3})
f	forcing
ν	Kinematic viscosity (m^2s^{-1})
H	Degree of Non conservation
$H_t, H_h, H_v,$	Anisotropic exponents space-time, horizontal, and vertical
τ_l	life time of the eddy
$E(k)$	Power spectrum
k	Wave number
β	Spectral exponent
T_λ	change of scale operator
$\stackrel{d}{=}$	Equal in distribution
G	Generator
c, d, e, f	paramters of the GSI
γ_α	Lévy sub-generator
c_β	order of singularity of the $\beta - model$
$\mu\varepsilon$	Random increment used in discrete cascades
$L(\alpha)$	Extremal Lévy-stable random variable of index α
Γ_Λ	Generator of the continuous cascade
$G(x)$	Green function
\mathcal{F}	Fourier transform
D_{el}	Elliptical dimension
$ $	Euclidean norm
\bar{x}	Spatial dimension
a	Dimensional exponent

$\zeta(q)$	Structure function
r^2	Quality of scaling
A_∞, A_d, A_w	Area turbine at upstream (inf), disc (d), and wake (w)
U_∞, U_d, U_w	Wind velocity at upstream (inf), disc (d), and wake (w)
a_b, a'_b	axial flow induction factor and tangential induction factor
P	Wind power (kW)
F, L, D	Aerodynamic force, Lift and Drag (N)
C_P, C_L, C_D	Power, Lift and Drag coefficients
β_b	pitch angle of the blade($^\circ$)
R_b, r_b	radius of the blade, and local radius of the blade (m)
Ω, ω	Angular velocity, and angular velocity imparted to the flow stream (rad/s)
Q	Torque(kNm)
c_b	Chord of the blade m)
W	Relative velocity (ms^{-1})
Δx	the vector pair separation (m)
$\Delta x, \Delta z$	the vector pair separation in horizontal and vertical (m)
Δv	the induced velocity component shear (ms^{-1})
u, v, w	3D components of wind velocity (ms^{-1})

Introduction

In recent years, the adoption and advancement of renewable energies such as solar energy, wind energy, biomass energy, and geothermal energy have emerged as basic strategy for nations worldwide in addressing the energy crisis and environmental pollution. Among the variety of renewable energies, wind energy has firmly established itself as a major option (IEA, 2021)

Its widespread use around the world can be attributed to the fact that wind is an inexhaustible resource with a very low environmental price tag, reducing CO₂ emissions with minimal water consumption. Numerous studies reveal that the total onshore wind resource exceeds 1 trillion kW, with estimated potential electricity generation from wind amounting to approximately 840 PW-h (Denny and O'Malley, 2006, McElroy et al., 2009, Council, 2019).

In fact, in the last 25 years, the world's installed wind power capacity, both onshore and offshore, has increased from 7.5 GW in 1997 to 743 GW in 2020 (IEA, 2021, Council, 2021), with plans for 50% of the EU's energy demand to be covered by wind power in 2050 (EWEA, 2012). Specifically, France ranks 4th in Europe in terms of installed onshore capacity with 17 GW, accounting for approximately 7.2% of its total energy consumption (Journal de l'éolien, 2021, Electricite de France, 2021). In addition, it has scheduled around 3.5GW of offshore projects by the end of 2026 (France Energie Eolienne, 2022, Kinani et al., 2023).

Despite the rapid development of wind energy, its integration and consumption is not as straightforward due to the intermittent nature of wind in both space and time, i.e. wind energy cannot be generated when and where it is needed (Rao et al., 2013 Yang et al., 2014, Anvari et al., 2016 ,Ren et al., 2017) whereas energy sources such as thermal, nuclear or hydroelectric power plants can. This extreme variability in space and time yields to a real impact in different aspects of the energy system (Ren et al., 2017) such as system reserves, system reliability, CO₂ emissions and the costs.

System reserves play a crucial role in balancing power generation and load demand in electricity systems (Bai et al. 2007, Gutiérrez-Martín et al. 2013). However, the intermittent nature of wind power introduces additional uncertainty that operators must deal with. Often, variations in wind generation and load demand are opposite, especially during peak hours (Bai et al. 2007, Gutiérrez-

Martín et al. 2013). This requires more reserves to cover sudden increases in load demand and decreases in wind generation (Wan and Parsons 1993, Swider and Weber, 2007).

Several studies have investigated the impact of intermittency on reserve capacities. For example, the Canadian Wind Energy Association examined reserve requirements under different scenarios of intermittent wind power penetration (Energy and Truewind, 2006), i.e. percentage of the energy cover by wind energy. It was observed that as wind penetration increases, load-following requirements become more significant. In addition, the increase in load-following reserve requirements can exceed the capacity of existing generators when the rated wind power is high. Similar results have been observed by other studies (Lee and Yamayee 1981, Gross et al. 2006, Brouwer et al. 2014) demonstrating a linear relationship between the level of intermittent wind power penetration and the additional load-following and back-up requirements.

The reliability of the energy system is composed of two fundamental aspects: system adequacy and system security. Adequacy is assessed in terms of the system's ability to cover load demand during peak load hours, and is expressed as a percentage of peak load demanded. In Europe, this percentage is around 15-23% while in the United States is around 15% (Cauley et al. 2011, Brouwer et al. 2014).

Renewable energy sources that exhibit variable power generation can effectively meet peak electricity demand if their output fluctuations align positively with demand (Yuan et al., 2011). However, it is noteworthy that intermittent wind power often demonstrates a negative correlation with demand and this at various scales. For example, in Ontario, peak load demand occurs in summer meanwhile the wind capacity is higher in winter (Albadi and El-Saadany 2007). Similar behaviour is observed in daily scales, e.g. in Spain (Gutiérrez-Martín et al. 2013), wind generation peaks around midnight, while the highest electricity demand transpires between 1:00 PM and 10:00 PM. This variability translates into a negative impact on the adequacy of the system in the face of the irruption of wind energy.

System security is commonly assessed using risk analysis methods. For example, in George et al. (2011) the risk associated with wind power intermittency in California is quantified using the *R* risk index, which combines the probability of energy shortfalls and the economic impact of such shortfalls. In Wangdee (2014), the system security is analysed using three states: healthy state, marginal state and risk state. In both approaches, it was observed that system security deteriorates with large-scale integration of wind power due to its high spatio-temporal variability.

The variability of wind power has an impact on the actual reduction of CO_2 emissions in electricity systems. Although theoretically it is expected that replacing a conventional power plant unit with a wind power plant unit will equate to an equivalent reduction in CO_2 emissions; in practice the actual reduction is less (Gross et al. 2006). The intermittent nature of wind power requires conventional power plants to be flexible in order to maintain system balance, which implies frequent

changes in power output and plant start-up and shut-down. This negatively affects the efficiency of the plants, as they are often designed to operate at a constant level of output (Cheng 2005, Albadi and El-Saadany 2010, Gutiérrez-Martín et al. 2013, Brouwer et al. 2014). The resulting reduction in system efficiency leads to an increase in fuel consumption and thus in CO_2 emissions.

However, few studies have explicitly assessed the efficiency reduction in thermal power plants due to this factor. In Gross et al. (2006) it is estimated that the efficiency reduction can vary between 0% and 10%. This is in line with the results obtained by Brouwer et al. (2014) and Liik et al. (2003) where a 4% reduction in electricity efficiency, and an 8-10% increase in emissions from thermal power plants were observed respectively. A similar impact has also been documented in Spanish industry (Gutiérrez-Martín et al. 2013).

The impact on the above factors translates into an impact on the economic costs in the wind energy industry due to the high variability of the wind resource. In fact, it is estimated that the total balancing costs are between 0.5 /MW h and 6 /MW h (Bach, 2004, Dale et al., 2004, Fabbri et al., 2005, Swider and Weber, 2007, Notton et al., 2018).

Wind fields are known to be extremely variable across spatio-temporal scales, so the problems arising from wind intermittency are not restricted to the large-scale problems mentioned in the previous paragraphs, but small-scale turbulence is another factor that is still not fully accounted for in terms of its impact on wind power generation (Brand et al. 2011, Van Kuik et al. 2016, Veers et al., 2019). In recent years, several authors have investigated how turbulence produces a decrease in the power generated by wind turbines (Lubitz 2014, Evans et al. 2018, Bashirzadeh Tabrizi et al. 2019, among others). Other authors have studied how turbulence plays a crucial role in the wake effect within wind farms (Vermeer et al. 2003, Maeda et al. 2017, Kadum et al., 2019 Neunaber 2019, van der Deijl et al., 2022). Extreme wind conditions such as extreme mean wind speeds, wind speed gusts (i.e. rapid change wind speed), or wind direction gusts (i.e. rapid change wind direction) can lead to a decrease in the wind energy production (Riziotis and Voutsinas 2000, and Kanev and van Engelen, 2010), however, in some situations they involve an increase in power production (Onol and Yesilyurt, 2017). These extreme events are translated into greater mechanical stresses on turbine components causing fatigue, automatic shutdowns or even damage to some turbine components (Bierbooms and Cheng 2002, Kanev and van Engelen 2010, Lubitz, 2014). Gaussian tools commonly used in the industry underestimate those extremes (Calif et al., 2013; Fitton et al., 2014) resulting in a decrease in the life expectancy of turbines (Riziotis and Voutsinas 2000, Zhou et al. 2018). This highlights the need of non-Gaussian framework.

Other authors such as Mücke et al., 2011 confirm the non-Gaussian nature of the wind field statistics and its translation to the power production in the form of torque fluctuations. This behaviour was further analysed in Schottler et al., 2017 through the analysis of two various wind flows with similar standard characteristics (mean, turbulence intensity) but difference in the the

distribution of their velocity increments (one Gaussian and one highly intermittent). They demonstrated that the intermittency of the wind flow is not mitigated in the power produced by the wind turbine.

Despite the importance of understanding the effect of turbulence on the performance of wind generators, international standards only consider turbulence in terms of structural aspects and not in terms of performance. For example, the IEC 61400-2 (IEC, 2015) standard used for design sets a limited range of turbulence intensities. Whereas IEC 61400 (IEC, 1999), used to determine the performance of wind turbines in their environment, does not include any turbulence-related requirements in relation to the performance of wind power generation.

Indeed, the problem areas of the wind industry highlighted in the state-of-the-art wind resource assessment report, deliverable D7 (Rodrigo, 2010) are in line with the challenges facing the turbulence field (Marusic et al., 2010), which include: (i) The existence of universal principal models. (ii) The validity of approximations to Reynolds stresses and whether they represent micro-scale wind conditions and extremes. (iii) The effect of non-neutral stability effects and complex topographic features.

To address these challenges, a potential solution could be the implementation of statistical modeling of turbulence (Fitton, 2013, Van Kuik et al., 2016). However, despite the potential benefits, there is a lack of such approaches in the wind industry. Instead, the industry tends to rely on the outcomes of numerical simulations from the numerical weather prediction (NWP) community. The majority of commercial nesting site models are often modified versions of NWP models (as described by Holmes, 2011), with a truncation of time and space scales in simulations, employing "turbulence intensity" (TI) parameterizations (Wallbank, 2008). However, these parameterizations of small-scale velocity fluctuations do not correspond to the scales required for modeling wind turbines, as evident in studies like Schertzer et al. (2012). We can find an example of this type of methodology in Gottschall and Peinke (2008) where the estimation of the power curves of wind turbine was divided in a deterministic part and in a stochastic one improving the accuracy in the calculus of the power curves.

Traditional numerical approaches attempt to deal with these challenges by transforming partial differential equations (PDEs) into ordinary differential equations (ODEs) to simplify the solving process. However, this transformation implicitly imposes assumptions of regularity and homogeneity through parameterization methods, leading to a reduction in variability. This discrepancy questions the relevance of the resulting numerical codes because their range of numerically solved scales differs from that of the observations.

For the reasons mentioned above there is a need for a theoretical framework that is able to deal with the high variability of the wind fields. Multifractal tools, specifically the Universal Multifractals, UM, (Schertzer and Lovejoy, 1987a) offer a scale-independent approach and provide a

mathematically robust and physically based description of the wind velocity field. These unique features enable understanding and modeling of spatio-temporal fields extremely variable across a wide range of scales, accounting for extreme events or gusts.

This thesis is done in the framework of the ANR JCJC Rainfall Wind Turbine or Turbulence (RW-Turb) project (grant no. ANR-19-CE05-0022). This project aims to quantify the effect of precipitation on wind turbulence and wind turbine efficiency by combining data analysis set and numerical simulations. More precisely, RW-Turb is structured around three main tasks: a dedicated high-resolution measurement campaign (Gires et al., 2022b) on an operational wind farm, data analysis and characterisation of the observed fields which are meteorological ones and power production (Jose 2023), and finally numerical simulations. This thesis covers the numerical simulations through the development of different modelling chains which use as input spatio-temporal scalar and vector wind fields to compute of torque time series.

With the aforementioned we can define the objectives of the thesis as:

- How to simulate, from existing theoretical framework, and validate, spatio-temporal wind fields, both scalar and vector, reproducing multifractal features retrieved from analysis of 3D wind anemometer time series ?
- What is the effect of the spatio-temporal variability of wind fields on wind power production through the development and implementation of various modelling chains to simulate torque time series?

The thesis is structured into three chapters. The first chapter provides an overview of the Universal Multifractal framework, focusing on its theoretical development. It starts by reminding the significance of fractal geometry and subsequently delves into multifractals. The chapter further explores the use of multiplicative cascades for simulating geophysical fields, starting with the basic β – *model* that simulates only the occurrence and progressing towards discrete cascades and continuous cascades for various dimensions. Finally, the chapter incorporates the use of fields simulated obtained with the help of these diverse techniques to illustrate multifractal analysis methods.

The second chapter of the thesis is dedicated to the simulation of wind fields characterized by realistic spatio-temporal variability. To achieve this, 3D sonic anemometer data obtained from a high-resolution campaign are utilized. These data serves as the basis for extracting wind multifractal properties and conducting a comparative analysis of different simulation methods. The chapter begins with a review of Turbsim, a widely used software in the industry that employs Gaussian statistics for wind field simulation. However, since Gaussian statistics do not accurately fully capture the true characteristics of wind fields, three alternative methods based on non-Gaussian statistics have been developed. The first method, although simplistic, involves reconstructing wind fields from point measurements using well-established scaling laws. However, this method entails

several simplifications which are discussed. To address these limitations, two other methods based on well established Fractionally Integrated Flux (Schertzer and Lovejoy, 1997) have been implemented, yielding promising results. The first method focuses on directly simulating wind fields, while the second method specifically targets wind fluctuations. Both approaches can be extended to encompass vector wind fields by combining stable Lévy processes and Clifford algebra. Subsequently, a comparative analysis of all the aforementioned methods is conducted, assessing their performance and distinctive features. This comprehensive evaluation aims to facilitate the generation of more realistic wind field simulations, effectively capturing the non-Gaussian variability observed in real-world scenarios. Such advancements are crucial for enhancing our understanding and prediction of wind power generation.

In the final chapter of the thesis, the impact of small scale spatio-temporal variability in wind fields on wind energy production is analyzed through computation of simulated torque time series. To accomplish this, three distinct modeling chains with increasing complexity have been developed. The first modelling chain only accounts for the temporal variability of the wind field, using the average wind speed and considering it at the turbine hub height. The second approach is based on the concept of angular momentum, enabling the consideration of both spatial and temporal variability. It calculates the torque at each point along the turbine blade and then integrates these values radially at each time step. The third approach utilizes the realistic software OpenFAST, developed by the National Renewable Energy Laboratory (NREL) in the United States. This modeling chain integrates multiple modules, enabling non-linear aero-hydro-servo-elastic simulations in the time domain. This comprehensive approach enables considering a wider range of processes involved in wind turbine power production. To ensure the reliability and accuracy of the modeling chains, a validation process has been conducted, demonstrating their good performance in the computation of the torque. Finally, a series of tests has been conducted using simulated vector wind, with a sensitivity analysis on the various parameters to better grasp their influence on wind energy production. These tests aim to gain insights into the interplay between different factors and their effects on overall energy production.

Overall, the thesis presents a comprehensive study of wind field simulation, the impact of spatio-temporal variability on wind energy production, and the development of accurate modeling techniques for better understanding and prediction of wind for power generation.

Chapter 1

Universal Multifractals

1.1 Introduction

Geophysical fields, like rain and wind, exhibit extreme variability across scales in both space and time. These fluctuations are particularly challenging to analyze, simulate, or measure due to their complexity. For instance, during a storm event, you can observe large fluctuations in rainfall, with heavy rain alternating with periods of no rainfall in a short time span. These fluctuations also manifest in the spatial distribution of rainfall, with some areas receiving much more rain than others.

Universal Multifractals (UM, Schertzer and Lovejoy, 1987a, Schertzer and Lovejoy, 1997) is a powerful tool that allows to characterise and simulate this extreme variability of geophysical fields across scales with the help of only three parameters with physical interpretation. It is reviewed in details in following sections.

- The mean intermittency codimension C_1 , which measures how concentrated is the average field.
- The multifractality index α , which measures how fast the intermittency evolves when going away from the average field.
- The degree of non-conservation H

while the 4th, the power a of a conservative flux, is absorbed by the empirical estimation of the mean singularity over a non-conservative field.

This framework is widely use in the literature for the analysis of the atmospheric fields such as rainfall. For example in the study conducted by De Lima and Grasman(1999) rainfall data from

Vale Formoso, Portugal were analyzed using both recording and non-recording rain gauges. The analysis included 15-minute and daily resolution data. The obtained UM parameters, specifically $C_1 = 0.51$ and $\alpha = 0.49$, were found to be similar to those commonly reported in the scientific literature (e.g., Tessier et al., 1996; Hubert et al., 1993; Ladoy et al., 1991; de Lima, 1998) for long-term rainfall series.

Comparing the results with other studies, it was observed that the probability of extreme events in Vale Formoso was higher than what would be predicted by more traditional models, such as the Gumbel distribution (Ladoy et al., 1991). This finding suggests that the multifractal analysis also reveals a climatological dependence in the structural characteristics of the rainfall, as highlighted in previous studies by de Lima (1998) and Svensson et al. (1996).

Furthermore, the 15-minute resolution analysis in De Lima and Grasman (1999) demonstrated a favorable scaling behavior across a range of scales from 15 minutes up to approximately 11 days. This implies that high rainfall intensities might be underestimated due to undersampling at larger scales, resulting from the finite size of the sample. Conversely, lower intensities could be overestimated. In contrast, the analysis of the daily time series in the same study revealed the existence of two scaling regimes, with a scale break occurring at approximately one week (8 days).

These UM parameters are consistent with the findings of De Lima and De Lima (2009), where the spatial variation of rainfall in the Madeira archipelago was analyzed. This study examined 10-minute and daily rainfall data recorded at various meteorological stations across the archipelago for a period of 3.8 months. They reported lower values of α for the drier southern sector of Madeira Island and Porto Santo Island. Additionally, the lowest values of C_1 were observed in central Madeira Island, indicating a lower level of intermittency and sparsity in the rain process. It is worth noting that a non-conservativeness parameter close to 0 was also reported in the literature Royer et al. (2008).

Both analyzed rainfall series exhibited comparable fractal dimensions across scales, ranging from 1 day to 16 days for daily resolution, which is consistent with previous studies (e.g. Tessier et al., 1996; Royer et al., 2008). For the 10-minute data, the scaling behavior was observed from 10 minutes up to approximately 3.6 days, with good scaling observed up to roughly two weeks. The scaling range was found to be similar across all locations where rainfall data was recorded. However, the fractal dimension exhibited different patterns in the northern and central parts of the island, with a higher fraction of events (greater fractal dimension) in the northern region compared to the southern region. This difference can be attributed to the influence of orography on rainfall distribution.

The UM analysis is affected by the impact of zero value intervals in the rainfall time series. de Montera et al. (2009), investigated this impact using rainfall data collected from various regions. The data were obtained using a dual-beam spectropluviometer (DBS). An event-based analysis was

carried out, excluding zero values and considering the total time. The analysis aimed to assess the effect of intermittency on the UM parameters. This study reported different parameter estimates in their event analysis, namely $H \approx 0.53$, $\alpha \approx 1.7$, and $C_1 \approx 0.13$. These values differ from the estimates discussed earlier in this study. However, when the entire series was analyzed, different values were observed, specifically $H \approx 0$, $\alpha \approx 0.5 - 0.7$, and $C_1 \approx 0.4 - 0.6$. These findings align with those reported by other authors who used low-resolution data. This suggests that the presence of intermittency leads to changes in the UM parameters.

Furthermore, the study explored the scaling behavior during event analysis and revealed a scaling regime up to 1/64 Hz, obtained after applying spectral flattening. When analyzing time series longer than 1 minute, scaling was observed up to approximately 1 hour, with noticeable variations at larger and smaller scales. These results are consistent with the influence of rain-no-rain intermittency on the scaling properties of the rainfall data.

However, this type of analysis is not restricted to the analysis of the rainfall time series, since it is possible to analyse scaling behaviour not only in the temporal dimension but also in the spatial dimension. Gires et al. (2015) investigated the raindrop distribution structure in space and time using rainfall data collected with a 2D video disdrometer (2DVD) during four heavy rainfall events in Ardèche (France). For the analysis, a 11x11x36cm column is reconstructed, and pseudo synthetic fields with homogeneously distributed drops are also generated for comparison. Reconstructed snapshot fields showed a scaling regime in the range between 36 and 1m. For smaller scales, the spectra becomes flat. These behaviours were confirmed through Trace Moments (TM) analysis, although the scaling regime break is observed close to 0.5 m. For smaller scales, drops could be homogeneously distributed. In synthetic fields, TM analysis retrieves no scaling in all scales and flat spectra are observed. These results could mean that the Poisson hypothesis of a homogeneous drop distribution, commonly used to model rainfall, is incorrect during the heaviest rainfall period. In the 1 ms rain-rate reconstructed time series for the 24/10/2012 event, it is possible to observe two scaling regimes with a scaling transition in TM curves, the first one with good scaling in the smallest scales from 32s up to 1 ms with a monofractal behaviour, a transition regime from few minutes (2-8 in this event) to 32 seconds with a rather bad scaling, and a last one from 140 min to few minutes with a good scaling. However, these results could not be confirmed with spectral analysis in which a good scaling is not reflected. For this reason, results from TM analysis should not be overestimated. Similar results are obtained in other studies (Schertzer and Lovejoy, 2011, and Salles et al., 1998).

Other authors use these tools to characterize other properties of rainfall e.g. Valencia et al. (2010) studied how the rainfall pattern changes in the Ebro River Basin using UM analysis is conducted. The study focused on estimating the UM parameters, including C_1 , α , and the maximum singularity (γ_s). Rainfall data were collected from 14 stations along the river from 1957 to 2002, divided into two subperiods (1957-1980 and 1981-2002).

1. Universal Multifractal

The retrieved UM parameters were found to be similar to those observed in previous analyses conducted by Labat et al. (2002), Tessier et al. (1996), and García-Marín et al. (2008). When comparing the two sub-periods, it was observed that α exhibited a more homogeneous spatial distribution in the second sub-period, with smaller differences between the highest and lowest values. However, consistently, α remained greater than 1. On the other hand, C_1 did not show significant differences across the stations, except for a small increment in the higher values. The probability of rainfall occurrence was found to be higher closer to the coast, which aligns with the findings reported by Gonzalez-Hidalgo et al. (2009) and López and Frances (2010).

Additionally, an analysis of the evolution of UM parameters was conducted using a moving time window with year breaks. Three distinct patterns were identified. The most frequent pattern was a steady series on the parameters. The second trend, observed in the station with the lowest values on the parameter exhibited a decreasing trend until 1989, followed by an increase thereafter. The third trend is observed in other four stations, where changes in α and C_1 occurred simultaneously, with an increase in α and a decrease in C_1 . These results are consistent with the findings reported by Royer et al. (2008). These trends became more prominent after 1990.

UM analysis is also used to characterize wind fields, obtaining results slightly different; for example, Fitton et al. (2011) studied the relationship between small and large scales in the boundary layer using wind data recorded at a wind farm in Corsica, France. The data were obtained from three 10 Hz sonic anemometers positioned at different heights. The study focused on analyzing the scaling behavior of the three components of the wind.

It is observed that the three wind components exhibited similar scaling behavior, characterized by three scaling regimes and two scaling breaks. At higher frequencies, the scaling behavior partially followed the $-5/3$ Kolmogorov locally isotropic turbulence law (Kolmogorov, 1941). Over the medium frequencies, the scaling behavior resembled the -1 exponent of wall-bounded theory. However, at higher frequencies, it was challenging to distinguish between the scaling laws of Bolgiano-Obukhov (BO) (Bolgiano Jr, 1959 and Obukhov, 1959) and Lumley-Shur (Lumley, 1964 and Shur, 1964) due to the sensitivity of the analysis to the data size. Nonetheless, BO scaling was confirmed in spectral analysis when an intermittency correction was applied.

By examining the integrated energy spectra, it is revealed a change in scaling between the vertical and horizontal directions. This finding aligns with the semi-theoretical results obtained for the surface layer. The results indicated that the variance flux of buoyancy force (ϕ) played a role similar to that of the energy flux (ε) but along the vertical direction in three-dimensional turbulence. This allowed for the definition of anisotropic scaling at all significant scales, rather than two isotropic regimes separated by a scaling break.

Other example can be found in Fitton et al. (2014), where the impact of wind speed on torque fluctuations is analyzed. The analysis involved two wind datasets from different locations: the

Corsica dataset and the Growian wind data, which was obtained using an array of cup anemometers with a sampling frequency of 2.5 Hz.

The study revealed that the torque fluctuations exhibited a higher value of α , indicating a strong non-linearity in the scaling moment function. Interestingly, the results showed that the torque fluctuations and velocity fluctuations had similar values of α . However, the non-conservativeness parameter, H , doubled in magnitude. Consequently, the critical exponent for torque fluctuations was halved, leading to larger fluctuations in the empirical statistics for orders greater than 3 as the sample size increased. This suggests that standard statistical methods underestimate extreme events in torque fluctuations.

The quantification of fluctuations varies depending on the turbulent process (e.g., KO, BO, macro weather) associated with each scaling exponent. This implies that, depending on the specific turbulent process, high-velocity and torque fluctuations may be smoothed according to a factor λ^H .

In this chapter, we introduce the Universal Multifractals framework, commencing with a foundation in fractal geometry. We define the fractal dimension and elucidate the motivation for transitioning to multifractality. We delve into the key properties of this multifractal framework. Furthermore, we provide an overview of various simulation methods, including multiplicative cascades encompassing both discrete and continuous forms. We also extend the simulation to vector fields. Lastly, we illustrate the analysis techniques through the validation of these simulation methods.

1.2 Theoretical framework

1.2.1 Towards fractal geometry

In nature, some objects such as cauliflowers or clouds are too complex to be represented with classical Euclidean geometry, because when observed at smaller and smaller scales, more and more details become visible. However, these objects have similar characteristics at all scales, which makes it possible to characterise them using a tailored framework called fractal geometry (Mandelbrot, 1977; Mandelbrot, 1983). In fact, we can define a fractal object as a geometric set of points that exhibits this scale invariant behaviour.

Let us start by discussing two famous fractal objects for pedagogical purposes, the Cantor set and Von Koch snowflake. A Cantor set is built by taking a segment and removing the middle part iteratively, i.e. removing the middle part of each new segment generated (it is shown in Fig. 1.1b). Von Koch snowflake is created by splitting each side of an equilateral triangle into three equal segments and using the middle one to create a new triangle in an iterative process (illustrated in Fig. 1.1a). In this example, it is possible to observe that as the number of iterations increases, the shape becomes more and more tortuous. It can be showed that the perimeter becomes infinite while

the area remains bounded with an infinite number of steps.

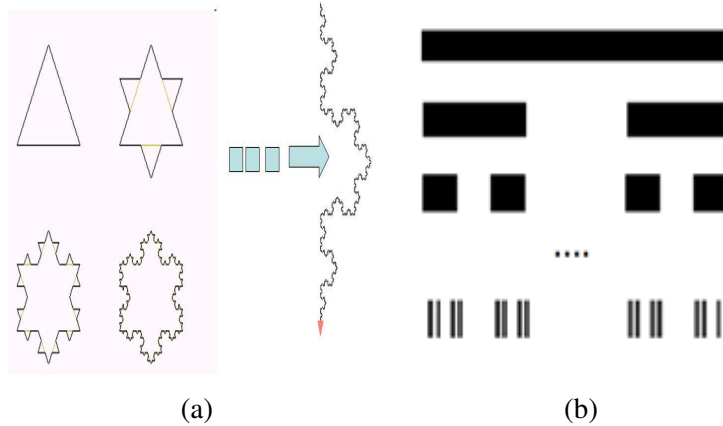


Figure 1.1: Examples of fractal objects. (a) the Von Koch snowflake and (b) the Cantor set (adapted from Gires, 2012).

1.2.2 Fractal Dimension

The concept of the fractal dimension (D_F) was introduced to characterize complex geometric shapes (Mandelbrot, 1977; Mandelbrot, 1983). In order to describe it, we will first focus on the traditional concept of Euclidean dimension. For this, we can define the number of non-overlapping structures (segments in 1D, squares in 2D, cubes in 3D, and so on) of size l required to cover a space of size L as :

$$N(l) = \left(\frac{L}{l}\right)^D \quad (1.1)$$

Where D is the dimension of the embedding space (1D for time series, 2D for maps ... etc).

D_F is an extension of this concept where analogously as the previous case, the number of structures of size l needed to cover a fractal set A of size L can be expressed as:

$$N_A(l) \approx \left(\frac{L}{l}\right)^{D_F} \quad (1.2)$$

This expression can be written using the resolution which is defined as the ratio between the outer scale and observation scale ($\lambda = L/l$) as:

$$N_{\lambda,A}(l) \approx \lambda^{D_F} \quad (1.3)$$

D_F measures how much space is covered by a fractal object, and, generally, it is not an integer (see review of Schertzer et al., 2002 for more details). An example of computation of D_F can be

observed in Fig. 1.2a, where the studied field is created using the β -model, which will be presented later. For computing D_F of the set, N_λ is calculated using Eq. 1.3, and it is plotted vs. the resolution in a log-log plot. If it is a fractal set, the plot will be a straight line whose slope is D_F . Fig. 1.2b illustrates an example of this, showing excellent scaling (i.e., well-aligned points) and a coefficient of determination (r^2) of 0.99, resulting in $D_F = 1.83$.

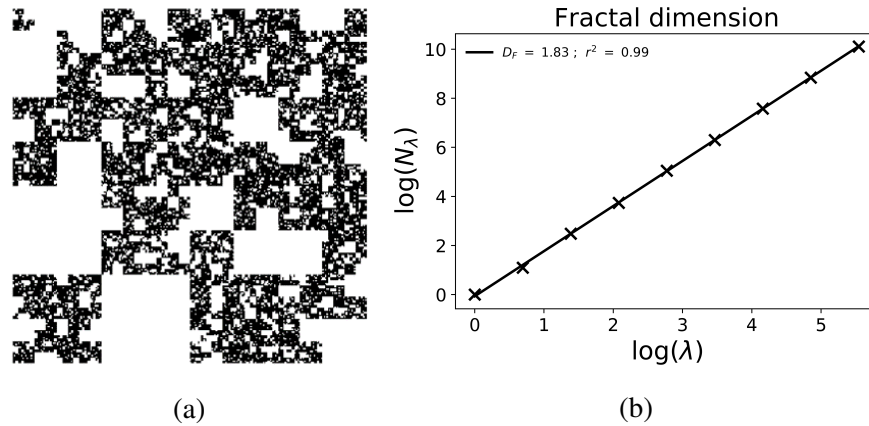


Figure 1.2: (a) Field created using the β model with $c=0.17$ (see section 1.3.2.1) and (b) the computation of its fractal dimension (1.2b)

The fractal dimension can be interpreted in a probabilistic way as the probability that a certain structure intersects a fractal set in the embedded space of dimension D . This probability is defined by the ratio between the number of structures needed to cover the fractal set A and the total number of structures needed to cover the whole space of dimension D :

$$Pr = \frac{N_{\lambda,A}}{N_\lambda} = \frac{\lambda^{D_F}}{\lambda^D} = \lambda^{-c_F} \quad (1.4)$$

Where c_F is the fractal codimension defined by $c_F = D - D_F$.

Cantor set defined in Fig. 1.1b is widely used to illustrate this concept of fractal dimension (see review Schertzer et al., 2002). Fig. 1.3 shows the computation of its fractal dimension obtaining a fractal dimension $D_F = \log(2)/\log(3) \approx 0.63$. Other typical illustration is the analysis of rainfall events (points) of one year (row) during 45 years in Dedougou present in Fig. 1.4, made by Hubert et al. (1989). There, it is possible to observe that rainfall events show a fractal behaviour with $D_F \sim 0.8$. It is consistent with taking into account the wet season as seven months, which is commonly observed, $0.8 \approx \log(7)/\log(12)$.

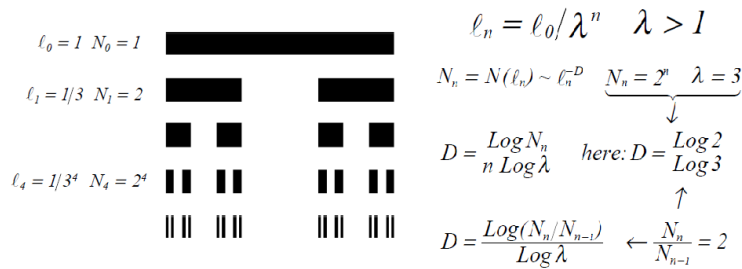


Figure 1.3: Explanation of fractal dimension computation for cantor set (from Schertzer et al., 2002)

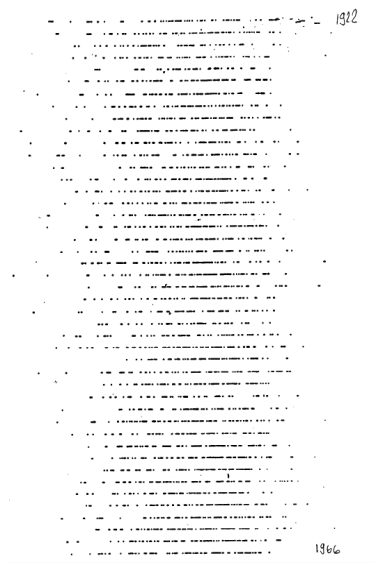


Figure 1.4: Rainfall data from Dedougou for a period of 45 years. Each line is a different year, each point a rainy day (From Hubert et al., 1989)

1.2.3 Towards multifractality

Although it is usually more useful to analyse fields with intensity values at each of their points rather than those geometrical sets which are only binary, it is interesting to analyse whether the occurrence of those fields depends on the threshold by which the intensity is made negligible (Schertzer et al., 2002).

To illustrate the impact of the chosen threshold, we analyze a rainfall event recorded by a disdrometer located in Champs-sur-Marne (France) on 23/05/2016 (Gires et al., 2018). In Fig. 1.5a, the rainfall event is depicted in black, while two different thresholds are illustrated: 3mm/h in blue and 7mm/h in orange.

In the second row of the Fig. 1.5, we calculate the rainfall occurrence using three different scenarios: no threshold, $3\text{mm}/h$ threshold, and $7\text{mm}/h$ threshold, from left to right respectively. Finally, the last row presents the computed fractal dimension, denoted D_F . It is observed that as the threshold increases, the computed fractal dimension, D_F , decreases. It is important to note that the quality of the scaling is decreasing with the thresholds (i.e. the points are going away of the regression line).

Fig. 1.5 shows that a single fractal dimension cannot fully characterize a scaling field, since each threshold presents a different D_F . For that reason, we need an infinite number of fractal dimensions to characterize the field, one per threshold. This approach is known as multifractal (Benzi et al., 1984; Parisi et al., 1985).

1.2.4 Multifractal Properties

The use of intensity as a threshold is not appropriate since it has a scale-dependent value. In order to illustrate that, we can use Nîmes rainfall time series as it is done in Ladoy et al. (1993). In Fig. 1.6a the rainfall time series are plotted with decreasing time resolution. It can be observed that the maximum intensity decreases with decreasing resolution from 35 to 0.1 mm/h in this case, although the intensity peaks keep grouped in the same points .

Therefore, a scale-invariant threshold is needed. We can use the concept of singularity (γ) which characterize the field intensity at each scale through a power law λ^γ . To illustrate this concept, we can use again Nîmes rainfall time series but using now the singularity time series displayed in Fig. 1.6b. It is observed that as the time resolution decreases, the vertical scale range remains similar, i.e between 0 and 0.7 confirming its scale invariant nature.

With the help of the singularity we can generalized Eq. 1.4 obtaining the codimension function ($c(\gamma)$) which can be understood as a representation of the infinite number of fractal (co-)dimensions (i.e. one per scale-invariant thresholds) required to characterize a multifractal field. It is defined by the probability of the studied field (ε_λ , energy flux) of exceeding a scale-invariant threshold λ^γ (Schertzer and Lovejoy, 1987b):

$$Pr(\varepsilon_\lambda \geq \lambda^\gamma) \approx \lambda^{-c(\gamma)} \quad (1.5)$$

If we consider the part of the field which exceed the threshold, we can give also a geometric interpretation to $c(\gamma)$ as its fractal codimension. This codimension function is equivalent to the scaling of the moments of order q (Parisi et al., 1985, Schertzer and Lovejoy, 1987a):

$$\langle \varepsilon_\lambda^q \rangle \approx \lambda^{K(q)} \quad (1.6)$$

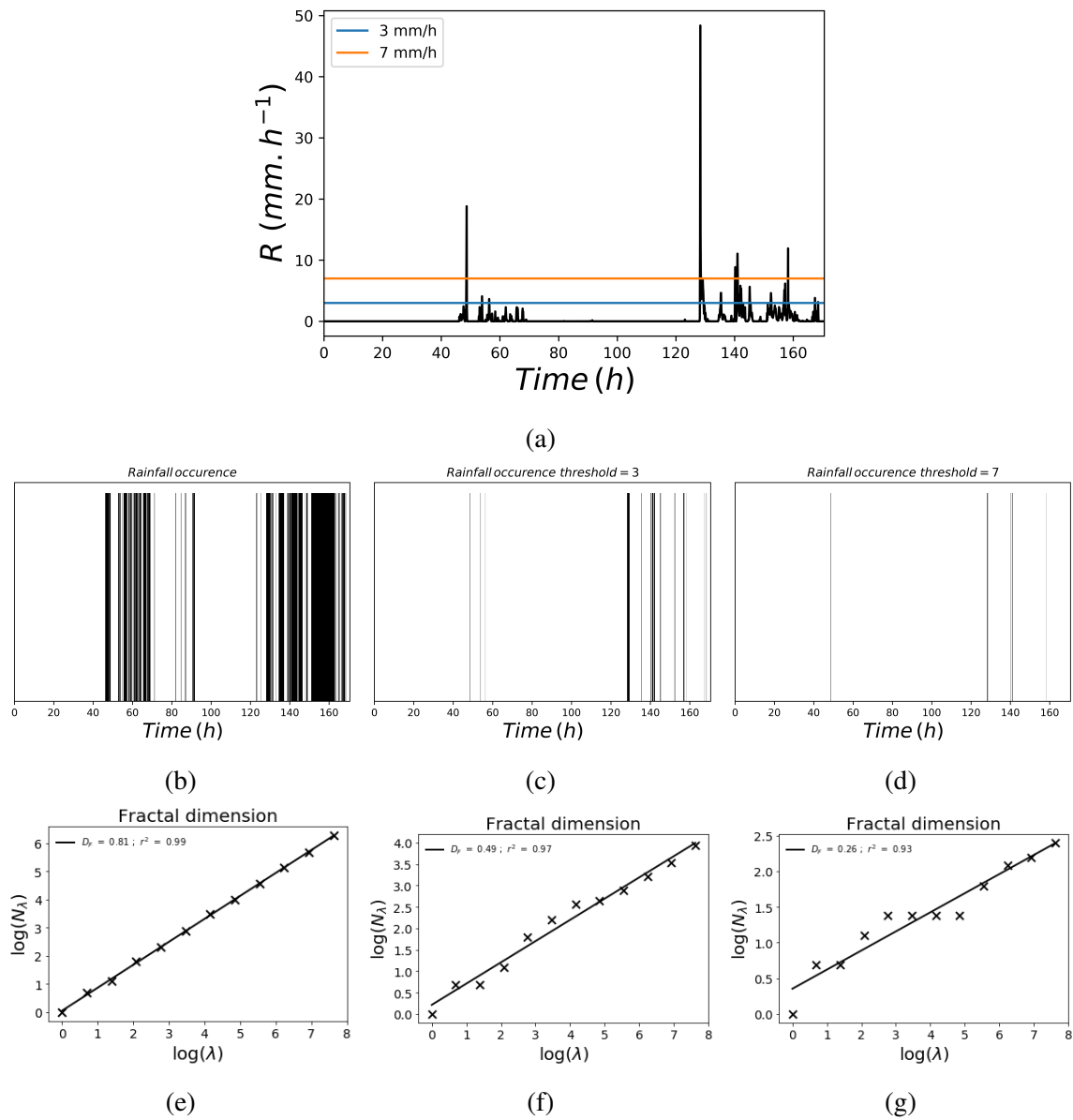


Figure 1.5: (a) Example of rainfall data recorded on 23/05/2026 in Champs-sur-Marne (France) with 3 mm/h threshold (blue) and 7 mm/h threshold (orange), (b) rain occurrence of the data, (c) and (d) rain occurrence with the thresholds (3 and 7 mm/h respectively); and (e),(f) and (g) computation of the fractal dimension of the previous fields.

which defines the moment scaling function $K(q)$.

We can relate both scaling functions using the Legendre transform (Parisi et al., 1985):

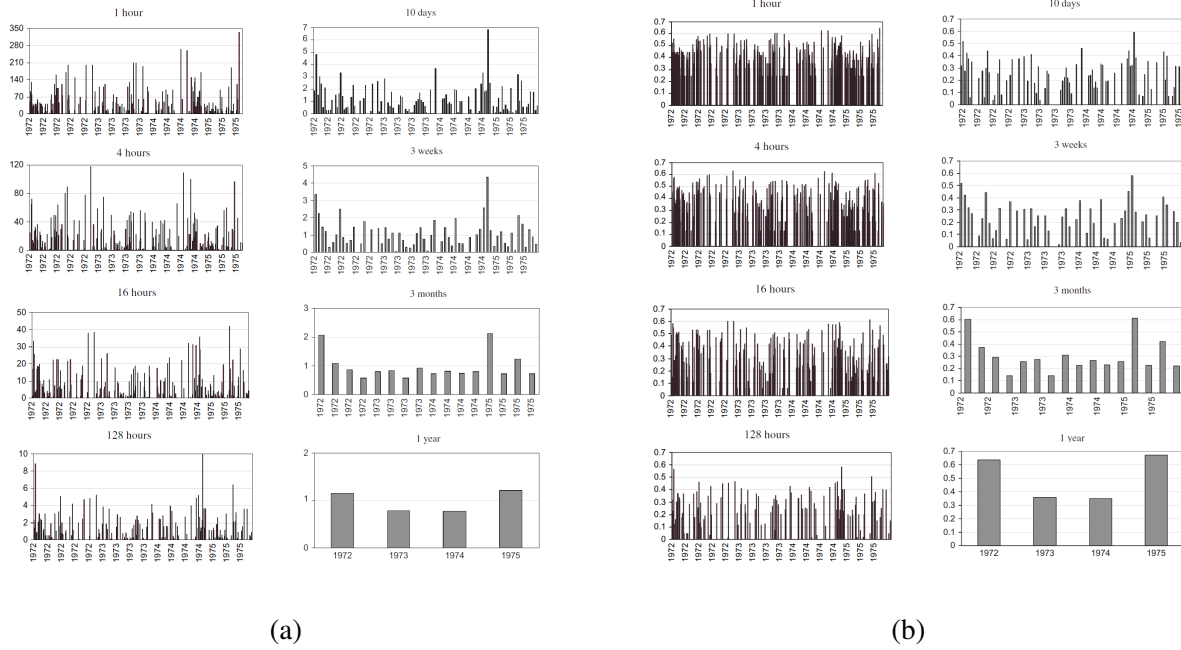


Figure 1.6: (a) Observed rainfall rain rate (R with 0.1 mm/h resolution) at Nîmes (1972–1975) with duration ranging from 1 hour to 1 year. (b) The corresponding singularities computed as $\gamma = \log \lambda(R_\lambda)$, where R_λ is the normalized rain rate (from Ladoy et al., 1993)

$$K(q) = \max_{\gamma} (q\gamma - c(\gamma)) = q\gamma_q - c(\gamma_q) \quad (1.7)$$

$$c(\gamma) = \max_q (q\gamma - K(q)) = q_\gamma\gamma - K(q_\gamma) \quad (1.8)$$

Where γ_q is calculated with $c'(\gamma_q) = q$, and q_γ is calculated with $K'(q_\gamma) = \gamma$

With this relation it is possible to obtain a singularity γ_q for each statistical moment order q . The reverse process is also true, i.e. it is possible to assign a moment order q_γ value to each singularity γ (see Schertzer et al., 2002 for a fully detailed justification)

1.2.5 Universality

With the help of generalization of the central limit theorem, it is possible to reduce to 2 the parameters needed to define the scaling functions (Schertzer and Lovejoy, 1987a; Schertzer and Lovejoy, 1997) since in the UM framework, the full description of the functions is done through the local description around the mean field ($q = 1$ and the corresponding singularity γ_1 denoted as C_1). It yields for scaling moment function and codimension function:

$$c(\gamma) = \begin{cases} C_1 \left(\frac{\gamma}{C_1 \alpha'} + \frac{1}{\alpha} \right)^\alpha & \alpha \neq 1 \\ C_1 \exp \left(\frac{\gamma}{C_1} - 1 \right) & \alpha = 1 \end{cases} \quad (1.9)$$

$$K(q) = \begin{cases} \frac{C_1}{\alpha-1} (q^\alpha - q) & \alpha \neq 1 \\ C_1 q \ln q & \alpha = 1 \end{cases} \quad (1.10)$$

where $\frac{1}{\alpha} + \frac{1}{\alpha'} = 1$, and C_1 and α have the following physical interpretation:

- C_1 is the mean intermittency codimension; quantifies how concentrated is the average field. It is the codimension of the singularity of the mean field for a conservative field. $C_1 = 0$ for uniform fields.
- α is the multifractality index; it measures how fast the intermittency evolves when going away from the average field. $\alpha = 0$ represents a monofractal case (β -model) where all the singularities possesses the same fractal dimension, and $\alpha = 2$ represents the upper limit and it corresponds to a lognormal case.

Grater values of α and C_1 corresponds to stronger extremes.

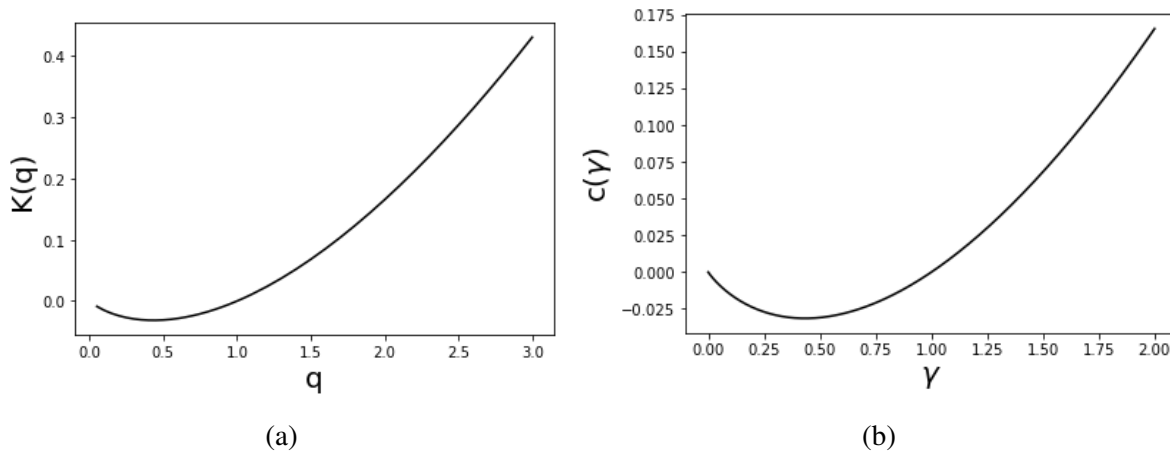


Figure 1.7: (a) Illustration of scaling function, $K(q)$ and (b) codimension function $c(\gamma)$, for 15/12/2020 wind data (RW-Turb measurement campaign, see section 2.2).

An illustration of $K(q)$ and $c(\gamma)$ can be found in Fig. 1.7. It corresponds to a plot with the UM parameters retrieved for the analysis of 15/12/2020 wind data using trace moment functions which are reviewed in the following sections.

Using theoretical properties of the $K(q)$ curve α and C_1 may be calculated with the first and second derivative, i.e.:

$$C_1 = K'(1) \quad \text{and} \quad \alpha C_1 = K''(1) \quad (1.11)$$

1.2.6 Phase transitions

1.2.6.1 Divergence of moments

Although in general, fluxes tend to converge as $\lambda \rightarrow \infty$, there exists a critical moment denoted as q_D where strong fluctuations are no longer dampened, and the flux may even diverge (Schertzer et al., 2002). As a consequence, it is theoretically expected to observe a fall-off in the probability distribution (Schertzer and Lovejoy, 1987a; Schertzer and Lovejoy, 1991) which follows a power-law with an exponent q_D defined by:

$$Pr(\varepsilon_\lambda \geq x) \approx x^{-q_D} \quad (1.12)$$

It is illustrated in Fig. 1.8.

In Fig. 1.8b probability distribution function of normalised (with the variance σ) horizontal velocity increments $(\Delta u(\tau))/\sigma = u(t + \tau) - u(\tau)$ for different time-scales using data from 2 high resolution 3D sonic anemometers located on a meteorological mast in a wind farm situated approximately 110 km south-east of Paris (more details of the measurement campaign in the section 2.2). PDFs "diverge" more from Gaussian distribution (computed with mean and variance of the data) with increasing resolution due greater presence of extremes.

Due to the divergence of moments, high-order moments (i.e. moments $q > q_D$) result in an infinite value for the moment scaling function ($K(q)$). And although it is empirically feasible to calculate $K(q)$, it should be noted that for $q > q_D$, this computation lacks robustness and stability. Additionally, due to the divergence of moments, discontinuities emerge in the first derivative of $K(q)$. This is why this phenomenon is known as the first-order multifractal phase transition (Schertzer and Lovejoy, 1987a).

Using Legendre transform, we can compute singularity γ_D where the condimension function $c(\gamma)$ is not reliable since it becomes linear for singularities greater than it.

The effect of the first-order transition is reported in the literature, e.g. De Lima and Grasman (1999) found divergence of moments from q larger than $q_D \sim 3.1$ for 15-min resolution and larger than $q_D \sim 3.7$ in daily resolution rainfall data, or Fitton (2013) observed $4 \leq q_D \leq 5$ for wind data measured at 50 m in two different datasets (Growian and Corsica) and a decreasing q_D with the increase of the anisotropy related to the appearance of wilder extremes.

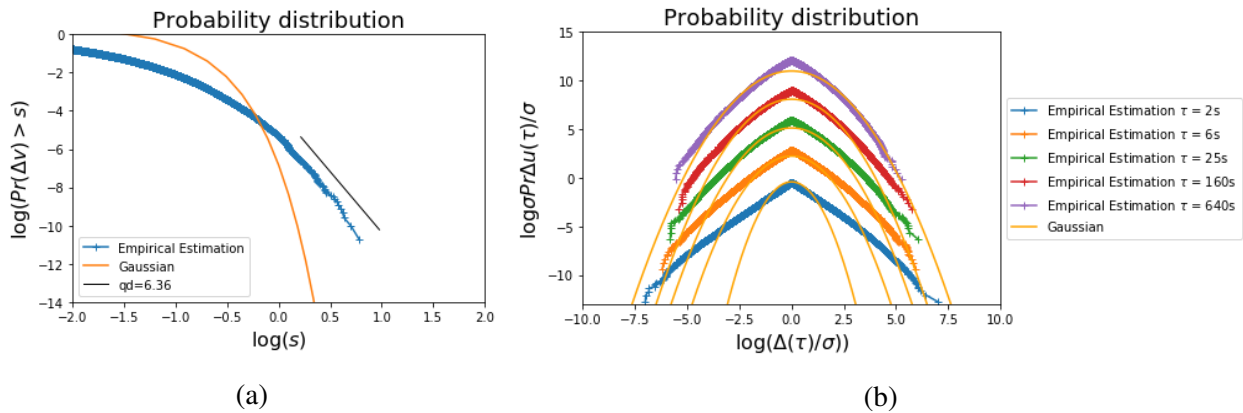


Figure 1.8: (a) Probability distribution function (PDF) of wind data (RW-Turb measurement campaign) and comparison between Gaussian distribution and the probability distribution of the wind data, q_D is shifted for clarity. (b) PDF for different time-scales $\tau = 2, 6, 25, 160$ and $640s$ respectively, sifted vertical for clarity.

1.2.6.2 Sampling limitation

The size of the sample limits the amount of information that can be extracted by analyzing a statistical process. In the UM framework this means that the computation of scaling functions is not possible for singularities and statistical moments of order greater than certain maximum values (Schertzer and Lovejoy, 1989, Lavallée et al., 1991). We can understand this through the codimension function for which the maximum value is given by (with N_s the number of samples):

$$\Pr(\epsilon_\lambda \geq \lambda^{\gamma_s}) N_s \lambda^D \approx 1 \quad (1.13)$$

which yields to compute the maximum singularity γ_s as:

$$c(\gamma_s) = D + D_s \quad (1.14)$$

Where D_s is the sampling dimension ($D_s = 0$ for sample size equal to 1) defined by (Schertzer and Lovejoy, 1989, Lavallée et al., 1991):

$$N_s = \lambda^{D_s} \quad (1.15)$$

For $\gamma > \gamma_s$, the codimension function $c(\gamma)$ becomes infinite. Through the Legendre transform Eq. 1.8, it is possible to obtain q_s . Analogously to divergence of moments, the computation of $K(q)$ becomes linear for $q > q_s$. Finite sample size also translates into discontinuities in the second

derivative of $K(q)$, yields to calling it second order-phase multifractal transition (Schertzer et al., 2002).

As an illustration, computation of this maximum observable singularity γ_s was carried out on climate change scenarios. Royer et al. (2008) performed UM analysis on rainfall time series in different regions of France simulated by climate model CNRM-CM3 of Météo-France. They found opposite trends in both UM parameters α (decreasing) and C_1 (increasing), so γ_s was calculated, obtaining an increase during the XXI century. It means an increase in rainfall extremes.

Computation of this maximum order singularity was also analyzed by Valencia et al. (2010) studying rainfall patterns in Ebro River basins, where similar results were found obtaining also a increase of γ_s , and consequently an increase of the probability of possible extreme precipitation events.

1.3 Simulation

In this section, we describe the various simulation techniques utilized throughout the thesis. The initial part (Section 1.3.1) provides an overview of the tools essential for these simulation methods. Among these tools, we introduce the concept of cascade phenomenology, and delve into the Lévy subgenerator.

Subsequently, we review the theoretical foundations of discrete cascades (Section 1.3.2), commencing with the β -model and progressing towards the UM discrete cascades. This methodology is replicated for continuous cascades (Section 1.3.3), where we begin with the theoretical aspects of the simplest unidimensional case and subsequently expand our exploration to encompass higher dimensions and the extension to non-conservative fields.

The section culminates with an examination of the simulation of vector fields, reviewing the Clifford algebra and the description of the Multifractal operators.

Using these existing theoretical tools we adapted and developed Python scripts for the different simulation methods (reviewed in Appendix D.1 with a dedicated project in gitlab). Full validation of the simulation scripts is carried out in Section 1.4.3, especially for the vector fields which is not done in the past.

1.3.1 Simulating tools

1.3.1.1 Introduction to cascade phenomenology

Geophysical fields exhibit extreme variability in both space and time over a wide range of scales. These fields are governed by a complex set of nonlinear partial differential equations, such

as the Navier-Stokes equations:

$$\frac{\partial \underline{u}}{\partial t} + \underline{u} \nabla \underline{u} = \frac{\nabla p}{\rho} + \nu \nabla^2 \underline{u} + \underline{f} = 0 \quad (1.16)$$

Where \underline{u} is the velocity field, p is the pressure, ρ is the density, t is the time, \underline{f} is the forcing term (representing the boundary conditions), and ν is the kinematic viscosity.

Through the following transformations:

$$\begin{aligned} x &\rightarrow \frac{x}{\lambda} \\ t &\rightarrow \frac{t}{\lambda^{1-H_t}} \\ u &\rightarrow \frac{u}{\lambda^H} \\ \nu &\rightarrow \frac{\nu}{\lambda^{1+H}} \\ \underline{f} &\rightarrow \frac{\underline{f}}{\lambda^{2H-1}} \end{aligned} \quad (1.17)$$

we can define a scale invariant properties associated to relation between two scales λ . Where H_t corresponds to the anisotropy exponent between space and time, and H corresponds to the degree of non-conservation. This scale invariant properties are suppose to be common to other sets of partial differential equations which govern other atmospheric fields (Schertzer and Lovejoy, 1985a, Lovejoy and Schertzer, 1990, Tessier et al., 1993, Marsan, 1998 or Biauou, 2004)

In general, geophysical fields are generated via a multiplicative cascade process, as they have demonstrated the ability to replicate these characteristics at all scales (Yaglom, 1966).

Historically, the concept of the multiplicative cascades was introduced to study turbulence as described by Richardson (1922) in his famous poem:

*Big whorls have little whorls,
Which feed on their velocity ;
And little whorls have lesser whorls,
And so on to viscosity*

This cascade phenomenology provides a physical explanation for the framework discussed earlier, which allows for the simulation of geophysical fields. In this approach the energy is distributed from the largest to the smallest scales splitting the eddies into smaller ones in the form of a multiplicative cascade. This cascade process is iteratively repeated until the eddies become so small that

the energy is dissipated due to viscosity (Marsan, 1998).

we can define the life time of the eddy as:

$$\tau_l \sim l/\Delta u_l \quad (1.18)$$

Where Δu_l represents the variation in the velocity of an eddy of size l .

Since the kinetic energy of the eddy must be transferred during its lifetime, the energy flux across scales, can be defined as:

$$\varepsilon_l \approx \Delta u_l^3/l \quad (1.19)$$

And re-writing in the form:

$$\Delta u_l \approx \varepsilon_l^{1/3} l^{1/3} \quad (1.20)$$

We can determine $H = H_l = 1/3$.

Because of this scale invariance, the power spectra ($E(k)$) of wind turbulence is a power law related with regards to the wavenumber (k) (Mandelbrot, 1983;Schertzer and Lovejoy, 1985a):

$$E(k) \approx k^\beta \quad (1.21)$$

Where β is the spectral slope and it is illustrated in Fig. 1.9.

Kolmogorov (Kolmogorov, 1941) originally posited that the energy flux ε exhibits statistical isotropy in both space and time at the small scales leading to obtain scaling exponent β of $5/3$ for the energy spectrum. Nevertheless, practical observations reveal significant deviations from this exponent due to intermittency. Subsequently, Bolgiano (Bolgiano Jr, 1959) and Obukhov (Obukhov, 1959) introduce the buoyancy force variance flux in order to consider the effect of the vertical direction in the large scales yielding a Bolgiano-Obukhov (BO) scaling exponent of $-11/5$. Later, Kolmogorov (Kolmogorov, 1962 and Oboukhov, 1962) proposed that energy flux follows a log-normal distribution in order to accommodate intermittency and introduce variability into the energy flux. Other models have been proposed to incorporate intermittency, which will be examined in subsequent sections, including the β -model (Frisch et al., 1978) and, ultimately, the Universal Multifractals (Schertzer and Lovejoy, 1987a).

To simulate these multiplicative cascades, two types of generators are essential. The first one generates a random variable that adheres to a specified distribution, referred to as the sub-generator

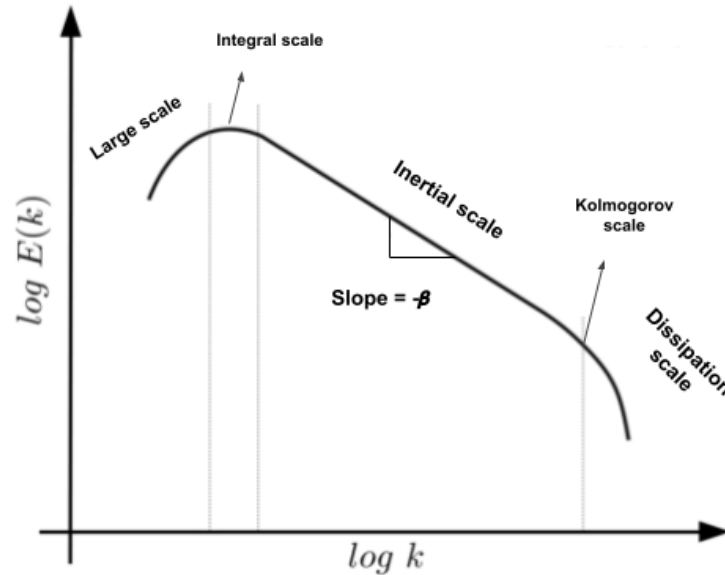


Figure 1.9: Illustration of the energy spectra for wind turbulence (adapted from Fitton, 2013)

(as discussed in Section 1.3.1.2). Meanwhile, the second one serves as the generator for the physical structures within the cascade.

Indeed, we can categorize cascades based on the type of generator used for the physical structures. This categorization encompasses Self-similar cascades, Self-affine cascades, and, in a broader sense, General Scale Invariance (GSI).

1.3.1.1.1 Self-similar cascades

Self-similar cascades represent the most fundamental type of cascades (Yaglom, 1966, Schertzer and Lovejoy, 1985a). These cascades involve a uniform (isotropic) expansion in all directions. To illustrate this concept, let's consider the example of 2-dimensional self-similar cascades, we can express the scale transformation in matrix form:

$$T_\lambda = \begin{bmatrix} \lambda^{-1} & 0 \\ 0 & \lambda^{-1} \end{bmatrix} \quad (1.22)$$

This may be denoted as:

$$T_\lambda = \lambda^{-G} \quad (1.23)$$

with:

$$G = \begin{pmatrix} 1 & 0 \\ 0 & 1 \end{pmatrix} \quad (1.24)$$

It can be generalised with G as the identity matrix, which has dimensions $n \times n$, where n means the invariant axis count. (Schertzer and Lovejoy, 1985a, Schertzer and Lovejoy, 1987a).

1.3.1.1.2 Self-affine cascades

Self-affine cascades (Mandelbrot, 1986) represent a basic means of introducing some degree of anisotropy. Returning to the example from the preceding section, we can quantify the anisotropy between the two directions using the generator (Schertzer and Lovejoy, 1985a, Marsan, 1998, Biaou, 2004, and Macor, 2007):

$$G = \begin{pmatrix} 1 & 0 \\ 0 & 1 - H_y \end{pmatrix} \quad (1.25)$$

Where H_y is the anisotropy exponent between the two axes.

This translates to an expansion or contraction with distinct values in each direction (λ^{-1} and λ^{1-H_y} in this instance).

1.3.1.1.3 General Scale Invariance (GSI)

General Scale Invariance (GSI) (Schertzer and Lovejoy, 1985b, Schertzer and Lovejoy, 1987a, Schertzer and Lovejoy, 1997) represents an extension of self-affine cascades that includes non-orthogonal axes, considering elements outside the diagonal in the generator matrix G . In the case of 2D fields, it becomes possible to generalize G with the assistance of pseudo-quaternions, such as Pauli matrices (Okubo, 1978, Schertzer and Tchiguirinskaia, 2015). We can employ the vector basis as follows:

$$G = dI + eI + gJ + cK \quad (1.26)$$

Where $1, I, J, K$ are the following matrix:

$$1 = \begin{bmatrix} 1 & 0 \\ 0 & 1 \end{bmatrix}, \quad I = \begin{bmatrix} 0 & 1 \\ -1 & 0 \end{bmatrix}, \quad J = \begin{bmatrix} 0 & 1 \\ 1 & 0 \end{bmatrix}, \quad K = \begin{bmatrix} -1 & 0 \\ 0 & 1 \end{bmatrix} \quad (1.27)$$

These matrix follow anti-commutation relations

$$IJ=-JI=-K; \quad JK=-KJ=I; \quad KI=-IK=-J; \quad (1.28)$$

and

$$1=-I^2 = J^2 = K^2 = -IJK \quad (1.29)$$

In this context, I represents the orthogonal rotation with respect to the origin, J and K give information about the stratification (Schertzer and Tchiguirinskaia, 2020).

Then, using Eqs. 1.26 and 1.27 leads to write G as:

$$G = \begin{pmatrix} d-c & f+e \\ f-e & d+c \end{pmatrix} \quad (1.30)$$

Where d determines isotropic expansion/contraction, c and f determine the stratification, and e determines the rotation.

Fig. 1.10 shows an illustration of the GSI for four different scenarios, Fig. 1.10a isotropy, Fig. 1.10b pure stratification, Fig. 1.10c dominant stratification and Fig. 1.10d dominant rotation.

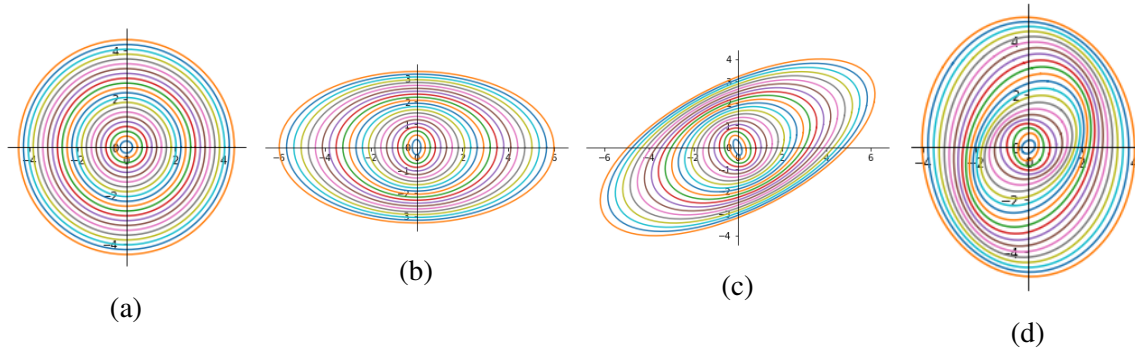


Figure 1.10: Contours of 2D balls B_λ for scale ratio $\lambda \in [1/4, 5]$ in steps of 0.2 using a pseudo-quaternion generator with: (a) $d = 1, c = f = e = 0$; (b) $d = 1, c = 0.2, f = e = 0$; (c) $d = 1, c = f = 0.2, e = 0.1$; and (d) $d = 1, c = f = 0.2, e = 0.7$.

1.3.1.2 Lévy sub-generator

The sub-generator follows a process with a Lévy distribution. It is a generalization of the Gaussian distribution where if we consider a set of n independent random variables X_i with statistical

moment defined up to α , then their normalized sum converges to (Schertzer and Lovejoy, 1987a):

$$L \stackrel{d}{=} \lim_{n \rightarrow \infty} \frac{(\sum_{i=1}^{\infty} X_i)}{b_n} - a_n \quad (1.31)$$

With

$$b_n = n^{1/\alpha} \quad (1.32)$$

and,

$$a_n = n \langle X_i \rangle - \langle X_i \rangle \quad (1.33)$$

Where $\alpha \in [0, 2]$ is the order of divergence and it is known as Lévy index.

These variables represent stable fixed points of hyperbolic variables with a power-law tail in their probability distribution (Schertzer and Lovejoy, 1987b) defined by :

$$Pr(|X_i| \geq s) \approx s^{-\alpha} \quad s \gg 1 \quad (1.34)$$

These Lévy distribution exhibit the following feature:

$$\langle \exp(qL(\alpha)) \rangle = \exp(q^\alpha) \quad (1.35)$$

To construct the Lévy distribution, we begin with white noise and introduce the parameter α . We employ the method proposed in Chambers et al. (1976), where the highly stable variable γ_α with index α is calculated as follows:

$$\begin{aligned} \gamma_\alpha &= \frac{\sin(\alpha(\phi - \phi_0))}{\cos(\phi)^{1/\alpha}} \left(\frac{\cos(\phi - \alpha(\phi - \phi_0))}{W} \right)^{(1-\alpha)/\alpha} \quad \text{if } \alpha \neq 1 \\ \gamma_\alpha &= \frac{2}{\pi} \left(\left(\frac{\pi}{2} - \phi \right) \tan \phi + \ln \left(\frac{\pi W \cos \phi}{\pi - 2\phi} \right) \right) \quad \text{if } \alpha = 1 \end{aligned} \quad (1.36)$$

Where

$$\phi_0 = \frac{\pi}{2} \left(\frac{1 - |1 - \alpha|}{\alpha} \right) \quad (1.37)$$

ϕ is an uniform random variable which varies from $(-\pi/2, \pi/2)$ and W is an standard exponential variable independent of ϕ .

1.3.2 Discrete Cascades

In the scenario of discrete multiplicative cascades, the process consists of splitting each structure into a smaller ones by dividing the number of structures by a scale factor of λ_1 (resolution). To transfer the activity from the larger to the smaller scales, the intensity is multiplied by a random increment of a given probability distribution $\mu\varepsilon$ (Schertzer and Lovejoy, 1987a, Lovejoy and Schertzer, 1990, Marsan, 1998). This process is is illustrated in Fig. 1.11 .

Therefore, to construct a discrete cascade, it is essentially necessary to determine the scale ratio required to divide the structures (usually is used 2^D but the only necessary condition is that this ratio must be grater than 1) and define which probability distribution use for the multiplicative increment. These two properties remain constant across all scales.

Consequently, after n steps, the resolution becomes $\lambda_1^n = \lambda_n$, and the intensity of the field B is equal to the product of all the increments and the initial value B_0 (Schertzer and Lovejoy, 1987a):

$$B_{n,i} = B_0 \prod_{i=s}^n \mu\varepsilon_i \quad (1.38)$$

1.3.2.1 β -model

The β -model represents the most basic cascade model (Novikov and Stiuart, 1964, Mandelbrot, 1974, Frisch et al., 1978), where there are only two possible states, the structures are either active or inactive. Consequently, multiplicative increments can be either 0 for the inactive (death structures) or $\lambda^{c\beta}$ for active ones (live structures), with a probability of occurrence of:

$$Pr(\mu\varepsilon = \lambda_1^{c\beta}) = \lambda_1^{-c\beta} \text{ (Alive)} \quad (1.39)$$

$$Pr(\mu\varepsilon = 0) = 1 - \lambda_1^{-c\beta} \text{ (Death)} \quad (1.40)$$

To be sure that the activity is conserved at each step, the energy flux density ε has to be increased by the factor of $1/\beta$, where $\beta = \lambda_1^{-c\beta}$. This factor represents how the number of active eddies decreases at each step of the cascade. Therefore, after n steps, there are only two possible outcomes: the density either diminishes to zero or diverges with a singularity order of $c\beta$ (see review Schertzer et al., 2002 for more details).

Fig. 1.12 shows two examples of fields created using this model. Greater values of $c\beta$ mean more empty fields as is shown in 1.12c and 1.12d.

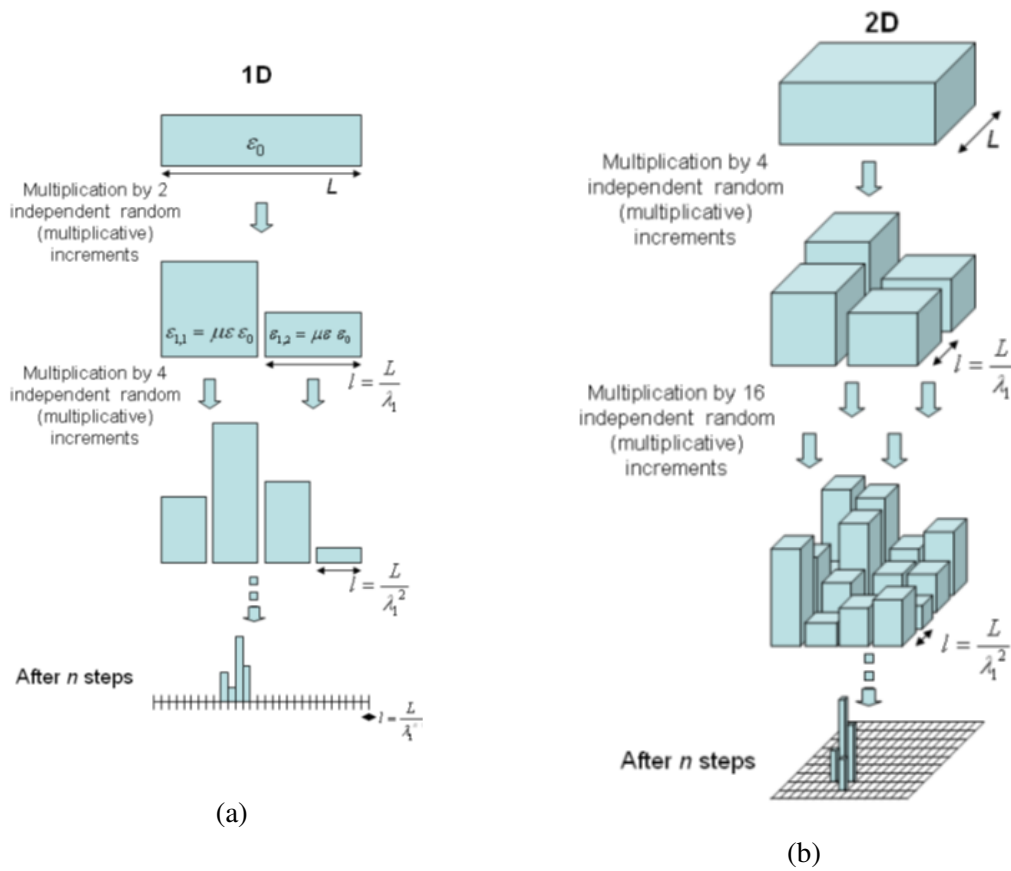


Figure 1.11: Illustration of a discrete cascade process (a) in 1D and (b) 2D. (From Gires, 2012)

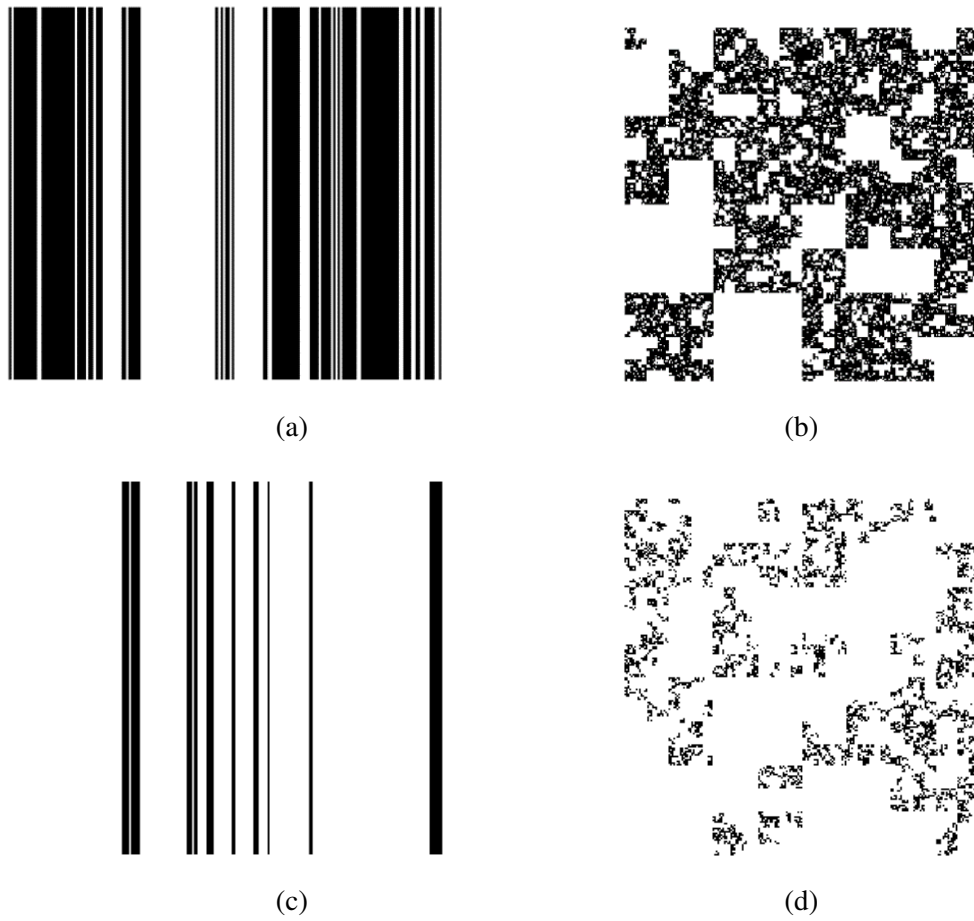


Figure 1.12: Illustration of a β -model with $c_\beta = 0.17$ for (a) 1D and (b) 2D; and with $c_\beta = 0.5$ for (c) 1D and (d) 2D

β -model is widely used in the literature, e.g. Frisch et al. (1978) studied effect of intermittency; Gupta and Waymire (1993), Over and Gupta (1994) and Schmitt et al. (1998), among others, use it to model rainfall occurrence; or Gires et al. (2021) for the treatment of missing data on the imperviousness of urban areas.

1.3.2.2 UM discrete cascades

For the UM cascades (Schertzer and Lovejoy, 1987a), the structures are divided following the process illustrated in Fig. 1.11 using a scale ratio equal to 2^D , while the random increment, $\mu\varepsilon$, is computed following:

$$\mu\varepsilon = \exp \left[\left(\frac{C_1 \ln(\lambda_0)}{|\alpha - 1|} \right)^{\frac{1}{\alpha}} L(\alpha) \right] / \lambda_0^{\frac{C_1}{\alpha-1}} \quad (1.41)$$

Where $L(\alpha)$ is a Lévy-stable random variable of index α which has been re-normalization by the constant $(C_1/|\alpha - 1|)^{1/\alpha}$ to retrieve the proper C_1 . Proof that UM properties are retrieved is obtained through:

$$\langle \varepsilon_\lambda^q \rangle = \left(\prod_{i=1}^n \langle \exp \left[\left(\frac{C_1 \ln(\lambda_0)}{|\alpha - 1|} \right)^{\frac{1}{\alpha}} q L(\alpha) \right] \rangle \right) / \lambda_0^{q \frac{C_1}{\alpha-1}} \quad (1.42)$$

Using Eq. 1.43, we obtain:

$$\langle \varepsilon_\lambda^q \rangle = \left(\prod_{i=1}^n \exp \left[\left(\frac{C_1 \ln(\lambda_0)}{|\alpha - 1|} \right)^{\frac{1}{\alpha}} q^\alpha \right] \right) / \lambda_0^{q \frac{C_1}{\alpha-1}} = \lambda^{\frac{C_1}{\alpha-1}(q^\alpha - q)} \quad (1.43)$$

Fig. 1.13 shows an illustration of the process for 1D and 2D. It displays a simulated field with input parameters $\alpha = 1.5$, and $C_1 = 0.1$; and 8 cascade steps.

For the simulation of the space-time fields, it is necessary to take into account the anisotropy between space and time. As it is mentioned in previous sections, it is possible to define the anisotropy scaling exponent H_t from Eq. 1.19 as $H_t = 1/3$. This allows us to define the resolution in the time dimension as $\lambda_t = \lambda_x^{1-H_t} = \lambda_x^{2/3}$.

To achieve that, we use $\lambda_x = 3$ which leads to $\lambda_t = 3^{2/3} = 2.08 \approx 2$. Hence at each step, the structures are divided in 3 in space and 2 in time leading to 18 sub-structures (Biaou, 2004). For example, Fig. 1.14 shows a simulated field using 5 cascade steps ($3^5 \times 3^5 \times 2^5 = 243 \times 243 \times 32$) and input parameters $\alpha = 1.5$ and $C_1 = 0.1$.

1. Universal Multifractal

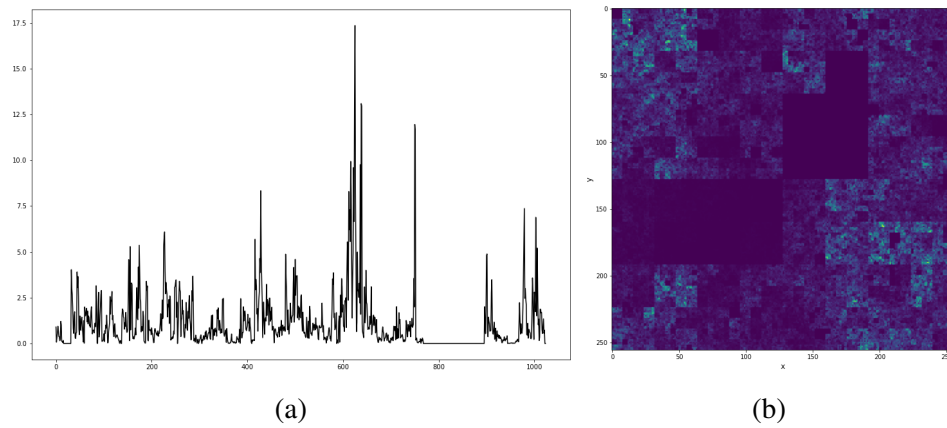


Figure 1.13: Illustration of a UM discrete cascades for input parameters $\alpha = 1.5$ and $C_1 = 0.1$ in (a) 1D and (b) 2D.

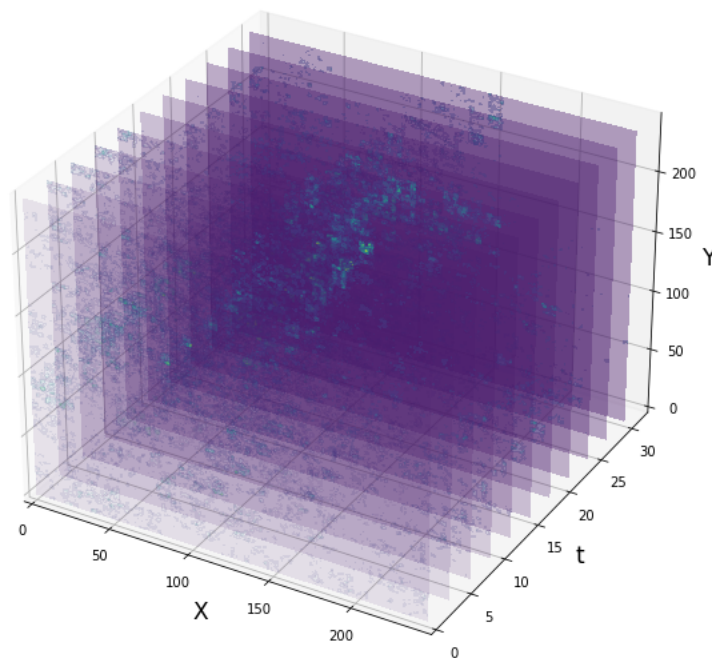


Figure 1.14: Illustration of a 2D+t UM discrete cascades for input parameters $\alpha = 1.5$ and $C_1 = 0.1$ and 5 cascade steps

1.3.3 Continuous cascades

The cascades described in the previous sections have many limitations due to their discrete nature. This translates into the operator which can be only applied to certain scales introducing artificial geometric structures (squares, cubes, ... etc.) that are not realistic (see an example Fig. 1.13). To improve the simulations, it is necessary to perform a densification of the cascade process by considering a continuous construction keeping constant the maximum scale ratio Λ (Schertzer and Lovejoy, 1987a, Schertzer and Lovejoy, 1991, Schertzer and Lovejoy, 1997, Macor, 2007). We can define, then, the generator of the cascade Γ_Λ as follows:

$$\varepsilon_{\Gamma_\Lambda} = \exp(\Gamma_\Lambda) \quad (1.44)$$

Since the field ε_Λ keeps a scale invariance properties it means a $\log(\Lambda)$ divergence in the second characteristic function of the generator (Macor, 2007), similar as is stated in Eq. 1.6:

$$\langle \varepsilon_{\Gamma_\Lambda}^q \rangle \approx \Lambda^{K_{\Gamma_\Lambda}(q)} \quad (1.45)$$

where the divergence is defined as:

$$K_{\Gamma_\Lambda}(q) = K(q)\log(\Lambda) \quad (1.46)$$

1.3.3.1 Unidimensional case

To construct the generator for continuous cascades, we start with Lévy white noise characterized by a Lévy index α . This Lévy noise is then fractionally integrated using the Green function ($G(x)$) of a fractional Laplace operator, resulting in a generator with a resolution within logarithmic divergence (Lovejoy and Schertzer, 2010a, Lovejoy and Schertzer, 2010b). Mathematically, this can be expressed as:

$$\Gamma_\lambda(x) = \int_{D_\lambda} G(x-x')d\gamma_\alpha(x') \quad (1.47)$$

with

$$\int_{D_\lambda} G^\alpha(x)dx = \log(\lambda) \quad (1.48)$$

In this context, D_λ represents the domain, $d\gamma_\alpha$ is the Lévy noise, and the Green function is determined typically as follows:

$$G(x) = |x|^{-1/\alpha} \quad (1.49)$$

with $|x| \in D_\lambda$

This fractional integration is carried out using the theorem of convolution (Bracewell and Bracewell, 1986). It postulates that the convolution of 2 functions, $f(x)$ and $g(x)$, denoted as $f * g$ is defined by:

$$f * g \equiv \int_{-\infty}^{\infty} f(x')g(x-x')dx' = \int_{-\infty}^{\infty} g(x')f(x-x')dx \quad (1.50)$$

This theorem also states that the Fourier transform of the convolution of 2 functions is equivalent to the product of the Fourier transform of each function:

$$\mathcal{F}(f * g) = \mathcal{F}(f)\mathcal{F}(g) \quad (1.51)$$

Where Fourier transform is represented by \mathcal{F}

Finally, the UM conservative field ε_λ is obtained by taking the exponential of the generator Γ_λ and making the renormalization to ensure the conservation ($\langle \varepsilon_\lambda \rangle = 1$).

Then, we can summarize the process of UM continuous cascades in 4 steps (which are illustrated in Fig. 1.15):

1. Generate the sub-generator as extremely asymmetric Lévy white noise with index α (Fig. 1.15a and Eqs. 1.36 and 1.37)
2. Obtain the generator using a fractional integration of the sub-generator (Fig. 1.15b and Eq. 1.50)
3. Calculate the conservative field through the exponential of the generator (Fig. 1.15c and Eq. 1.44)
4. Renormalize the field with parameters α and C_1 to ensure the conservation (Fig. 1.15d)

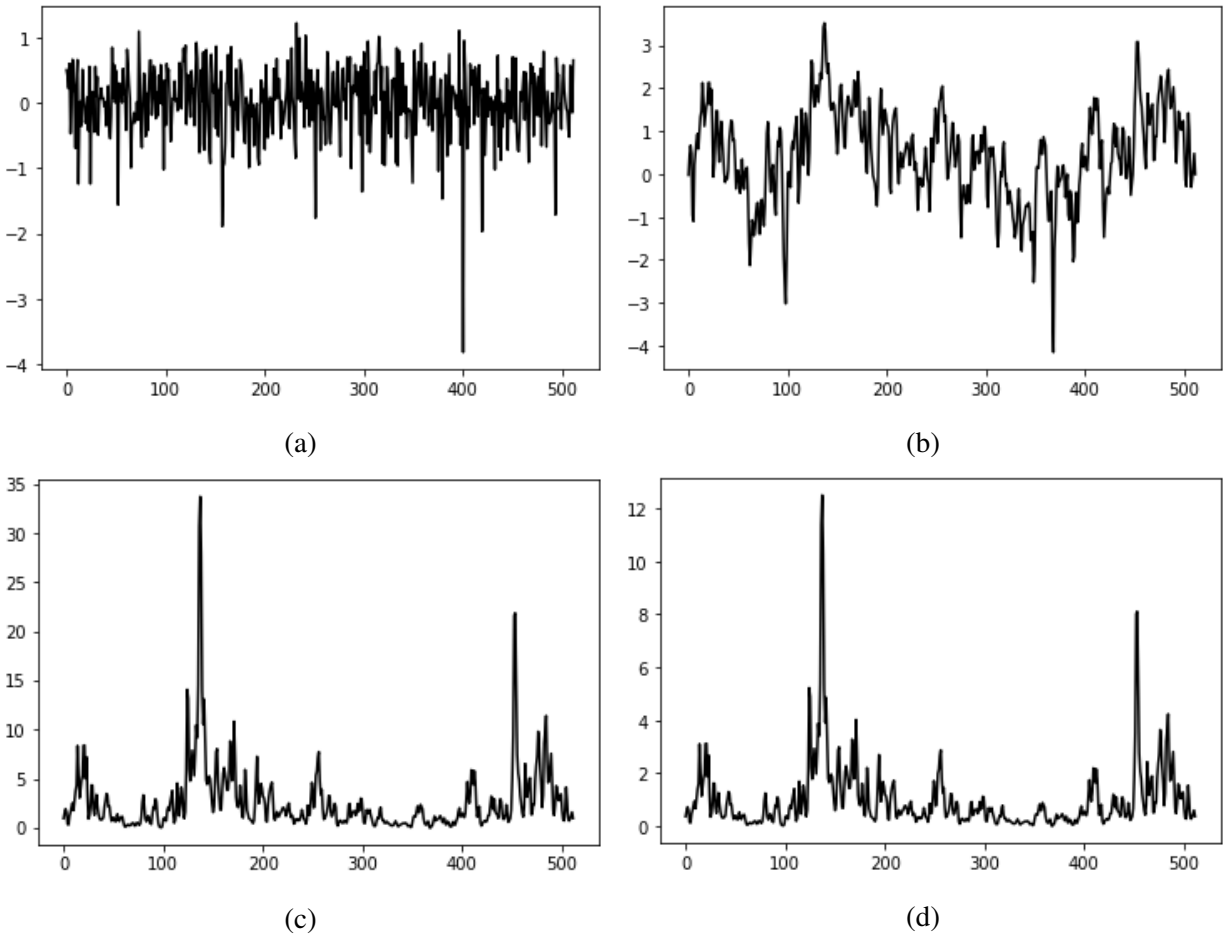


Figure 1.15: Illustration of the UM continuous cascade process in 1D with parameters $\alpha = 1.8$ and $C_1 = 0.1$ and length = 512, (a) sub-generator, (b) generator, (c) field, and (d) renormalized field

1.3.3.2 Extension to multidimensional case

1.3.3.2.1 General case

This method can be expanded to accommodate multidimensional scenarios with the assistance of the elliptical dimension denoted as D_{el} (Schertzer and Lovejoy, 1987a). We redefine the Green's function (as given in Eq. 1.58) in a more comprehensive form (Marsan, 1998) as.

$$G(\bar{x}) \approx \|\bar{x}\|^{-D_{el}/\alpha} \quad (1.52)$$

In this context, \bar{x} denotes the spatial dimension, and $\|\bullet\|$ represents the Euclidean norm. For instance, in the case of two spatial dimensions (x and y), $\|\bar{x}\| = \sqrt{x^2 + y^2}$. Fig. 1.16 illustrates the field, showcasing a simulated field with input parameters $\alpha = 1.5$, $C_1 = 0.1$, and $H = 0$, comprising 256x256 points.

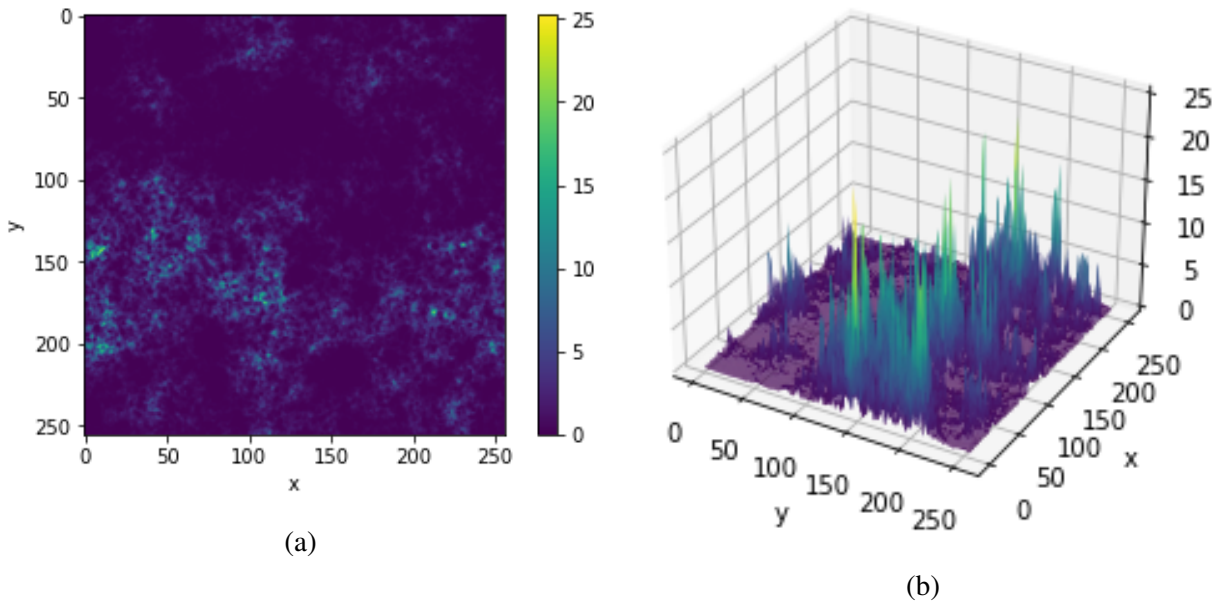


Figure 1.16: Illustration of the 2D UM continuous cascade fields in with parameters $\alpha = 1.5$ and $C_1 = 0.1$ over and area of 256x256, 1.16a) for 2D image and 1.16b) for 3D image for visualize the intermittency of the flux

1.3.3.2.2 Space-time cascades

Space-time cascades must adhere to two essential properties. The first property is an anisotropic relationship between space and time. The second property is causality, which implies the sub-

generator only propagates into the future, aided by a retarded Green's function (see detailed examples of use in Biaou, 2004, Macor, 2007).

The space-time cascade domain is $D + 1$ (where D denotes the spatial dimensions). Then for this the process consists in an isotropic expansion in space (λ^{-1}) and an anisotropic expansion related to $1 - H_t$ in time (Schertzer and Lovejoy, 1997). We can illustrate the process for a 2D+1 case with the following generator:

$$G = \begin{pmatrix} 1 & 0 & 0 \\ 0 & 1 & 0 \\ 0 & 0 & 1 - H_t \end{pmatrix} \quad (1.53)$$

So $D_{el} = 2 + (1 - H_t)$.

To introduce the causality on the generator $\Gamma_\lambda(\bar{x}, t)$, the sub-generator $\gamma_\alpha(\bar{x}, t)$ is fractionally integrated with the help of the retarded Green function (Biaou, 2004, Macor, 2007) as:

$$G(\bar{x}', t') = \begin{cases} \|\bar{x}, t\|^{-D_{el}/\alpha} & t \geq 0 \\ 0 & t < 0 \end{cases} \quad (1.54)$$

Then the generator is obtained as:

$$\Gamma_\lambda(\bar{x}, t) = \iint_{\|\bar{x}', t'\| \in D_\lambda} G(\bar{x}', t') \gamma_\alpha(\bar{x} - \bar{x}', t - t') d\bar{x}' dt' \quad (1.55)$$

An example of simulation with this process is displayed in Fig. 1.17, which displays a simulated field with input parameters $\alpha = 1.5$, $C_1 = 0.1$, and $H = 0$; and 256x256 points and 256 time steps.

1.3.3.3 Extension to non-conservative fields

In the previous sections, the simulating process of the continuous cascades has been described for the conservative case, however there are many physical processes in which the activity is not conserved between scales such as the velocity (Oboukhov, 1962). To obtain a non-conservative field it is necessary to perform a fractional integration over the conservative flow (Schertzer and Lovejoy, 1987a; Schertzer and Lovejoy, 1997):

$$\varphi_\lambda \simeq \lambda^{-H} \varepsilon_\lambda^a \quad (1.56)$$

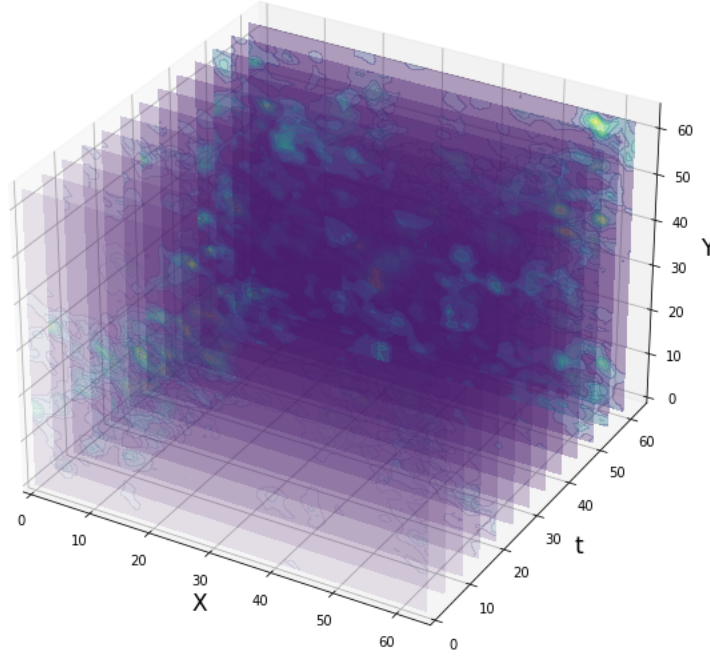


Figure 1.17: Illustration of the 2D+t UM continuous cascade field with input parameters $\alpha = 1.5$ and $C_1 = 0.1$ over an area of 256x256, and 256 time steps.

where φ_λ is the non-conservative field at resolution λ , H measures the degree of non conservation ($H = 0$ when the field is conservative), and could be either positive or negative. ε_λ is the underlying conservative field, and a is the dimensional exponent which implies a change in the singularities (Marsan, 1998):

To obtain the non-conservative field φ we can operate in a similar form as the previous case where the fractional integration is done through :

$$\varphi_\lambda(\bar{x}) = \int_{\|\bar{x}'\| \in D_\lambda} G(\bar{x}) \varepsilon_\lambda^a(\bar{x} - \bar{x}') d\bar{x}' \quad (1.57)$$

with,

$$G(x) = \|\bar{x}\|^{-D_{el}+H} \quad (1.58)$$

This process can be extended to the space-time cascades following the same methodology explained in the previous sections. An example of this process is illustrated in Fig. 1.18, which displays a simulated field with input parameters $\alpha = 1.5$, $C_1 = 0.1$, and $H = 0.3$; and 256×256 points. The expected features are visible when H is greater than 0, there is a visual effect which translates in a smoothing of the surface.

1.3.4 Vector fields

1.3.4.1 Theoretical background

In the previous sections, we delved into the concept of cascades, which, in theory, can be applied also to vectors and not only to scalars, since they only need a structure with addition and multiplication (Schertzer and Tchiguirinskaia, 2020). However, conventional vector spaces are constructed solely using scalar multiplication and do not incorporate vector multiplication operations. This limitation implies that there are no natural multiplicative cascades for vectors. To address this, we need a more extensive algebraic framework that includes (multiplicative) operations of vectors by vectors. The condition of conservation necessitates that the algebra employed has to be a unitary algebra (Schertzer and Tchiguirinskaia, 2015).

One example of such an algebra can be the set of linear operators. We can define a vector cascade by utilizing vector operators that act on an homogeneous vector field, following a similar approach to that outlined in Schertzer and Lovejoy (1995) for the case of a 2D discrete complex cascade. However, discrete operators share limitations akin to those of discrete cascades and introduce their own set of challenges.

To address these issues, one strategy is to employ a similar process to the one employed in the continuous cascade section, involving exponential operators. By incorporating exponential operators and exploring the utilization of vector operators, it is possible to overcome the limitations associated with discrete cascades and advance the concept of cascades for vector fields. This approach offers the potential for a more comprehensive and realistic representation of multifractal properties in vector fields (Schertzer and Tchiguirinskaia, 2015, Schertzer and Tchiguirinskaia, 2020).

1.3.4.2 Clifford Algebra

Clifford algebra is a good candidate to use as generator algebra for the simulation of vectors fields (Schertzer and Lovejoy, 1995, Schertzer and Tchiguirinskaia, 2015, Schertzer and Tchiguirinskaia, 2020). This algebra makes it possible to characterise a field with the help of entities of different dimensions, such as vectors, matrices, quaternions, and other entities of higher dimensions. It expands upon the principles of vector algebra by introducing the concept of the geometric product, which unifies the inner product (dot product) and the outer product (wedge product) of

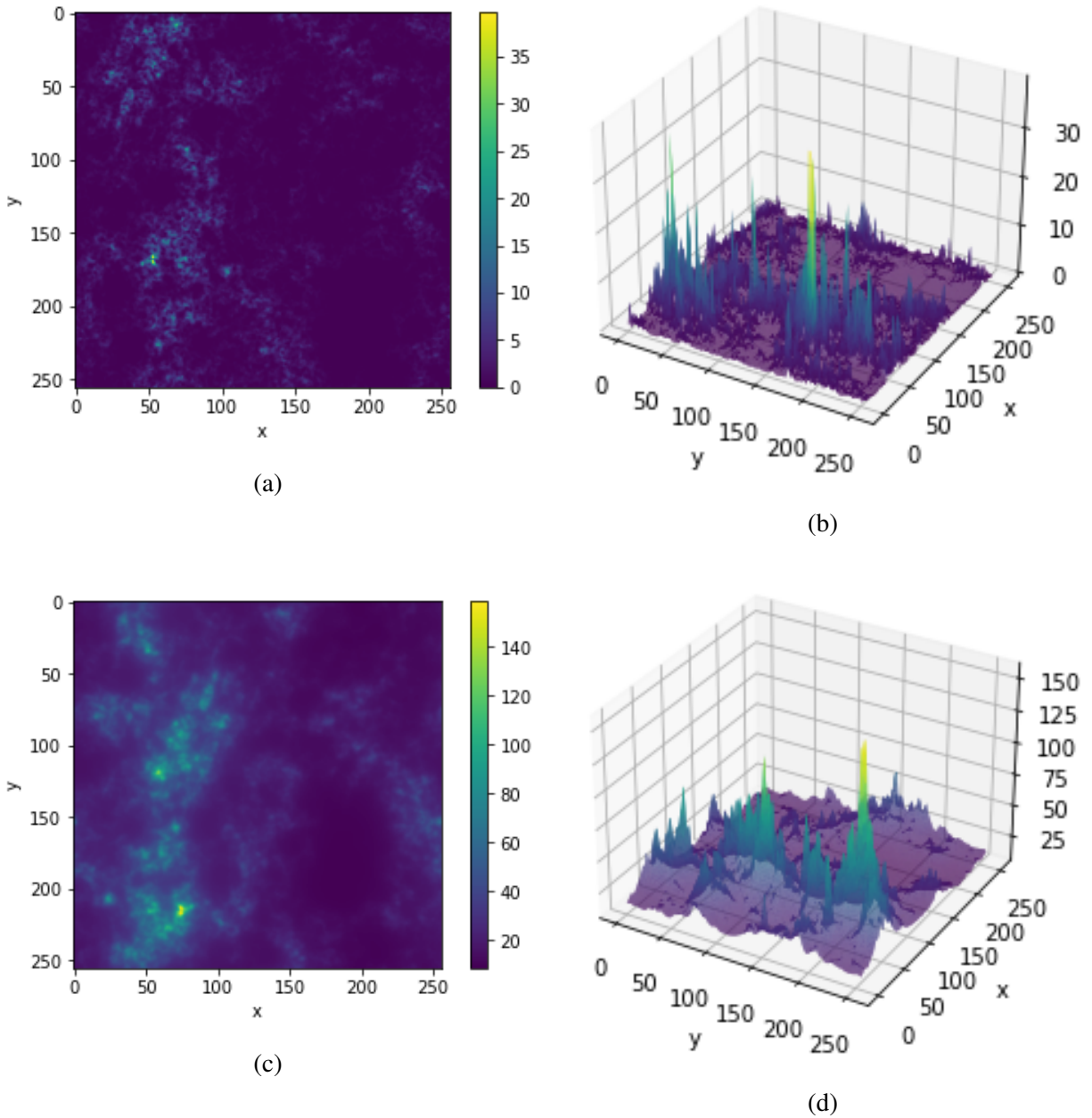


Figure 1.18: Illustration of the 2D UM non-conservative continuous cascade fields with inputted parameters $\alpha = 1.5$, $C_1 = 0.1$, and $H = 0.3$ over an area of 256x256 pixels. (a) and (b) show the conservative field while (c) and (c) the non-conservative

vectors (Lounesto, 2001).

Within the realm of Clifford algebra, the geometric product of two vectors produces a multivector, which can possess components at various levels. These multivectors not only encapsulate the magnitude and direction of vectors but also incorporate information about their orientation and geometric attributes in higher dimensions (Clifford, 1871, Clifford, 2007).

Clifford algebra, is defined in a vector space x using a non-degenerate quadratic form Q . The quadratic form $Q(x)$ is given by:

$$Q(x) = x_1^2 + x_2^2 + \dots + x_p^2 - x_{p+1}^2 - \dots - x_n^2 \quad (1.59)$$

Where x represents the vector space, within the canonical symmetric matrix with dimensions $n \times n$, satisfying the condition $p + q = n$, being p and q the positive and negative eigenvalues, respectively. This algebra is characterized by the signature $Cl_{p,q}$ of Q determined by the pair (p, q) . In this Algebra is possible to define a vector as a summation of basis vectors which squared to either +1 or -1 (Renaud, 2020).

Using the properties of this algebra we can define some examples that share an isomorphism with some traditional sets (Schertzer and Tchiguirinskaia, 2015). For example the simplest case $Cl_{0,0}(R)$ is isomorphic to \mathbb{R} , where there are only scalars. $Cl_{0,1}(R)$ is isomorphic to the complex numbers \mathbb{C} where the basis $(1, e_1)$ counts with a single vector e_1 which squares to -1, ($a + be_1 \longleftrightarrow a + bi$). $Cl_{2,0}(R) = Cl_{1,1}(R)$ correspond to pseudo-quaternions case (section 1.3.1.1.3). $Cl_{0,2}(R)$ is isomorphic to quaternions \mathbb{H} with a basis formed by $1, I_2, J_2, K_2$ where $I_2, J_2,$ and K_2 square to -1 , and act as rotations (Schertzer and Tchiguirinskaia, 2018). The case of the quaternion can be extended to higher values of n , however, for $n > 3$ some properties are no longer supported (Schertzer and Tchiguirinskaia, 2015).

1.3.4.3 Multifractal Operators

In this section, we will provide a summary of the mathematical developments in the work by Schertzer and Tchiguirinskaia (2020) that are essential for the simulation of multifractal vector processes. They states that it is possible to construct a stochastic generator algebra by mapping the generators of a specified probability space into the desired type of algebra, in this case the Clifford algebra. We can illustrate the process with a simpler case, the Gaussian vectors using one of their main properties such as all their components are, by definition, Gaussian variables. This can also be interpreted in the opposite way: a vector in which all its components are Gaussian is therefore a Gaussian vector. (Schertzer and Tchiguirinskaia, 2015, Schertzer and Tchiguirinskaia, 2020).

Using the scalar product definition of Clifford algebra we can define the components (defined

by the subscript i) of the stochastic generator as:

$$\Gamma_i = \langle \Gamma, e_i \rangle = \Gamma_{e_i} \quad (1.60)$$

Where e_i is a unitary vector of the basis which squares to ± 1

Eq. 1.60 enables us to determine the statistics of the generator along any direction of the basis in a similar manner as in the scalar case, as long as all of these vectors are part of the same Clifford algebra. For that, it is employed a process similar to a polar decomposition (Schertzer and Tchiguirinskaia, 2020). It yields to write Eq. 1.11 as:

$$K_{e_i}(q) = C_1(e_i)(q^2 - q) \quad (1.61)$$

for a Gaussian vector, where the main intermittency codimension $C_1(e_i)$ is generalized for any e_i direction of the basis. And analogously to the case of continuous cascades (Eq. 1.44), this leads to obtain the field through the exponential of the generator:

$$\varepsilon_\lambda = \exp(\Gamma_\lambda) = \lambda^{C_1(e_i)(q^2 - q)} \quad (1.62)$$

Since Lévy variables generalize Gaussian ones (Section 1.3.1.2), we can think the Lévy vector also as a generalization of the Gaussian vector where the properties of stability and attractivity of these variables are kept for all their components (Schertzer and Tchiguirinskaia, 2020). It generalizes Eq. 1.61 as:

$$K_{e_i}(q) = \frac{C_1(e_i)}{\alpha - 1} (q^\alpha - q) \quad (1.63)$$

And consequently,

$$\exp(\Gamma_\lambda) = \lambda^{\frac{C_1(e_i)}{\alpha - 1} (q^\alpha - q)} \quad (1.64)$$

This expression can be even more generalized considering the stability index (α) as a matrix instead of a scalar. However, this process is only straightforward when the matrix α is diagonalizable obtaining a stability index for each eigenspace of α :

$$K_{\gamma_i}(q) = \frac{C_1(e_i)}{\alpha_i - 1} (q^{\alpha_i} - q) \quad (1.65)$$

and,

$$\exp(\Gamma_\lambda) = \lambda^{\frac{C_1(e_i)}{\alpha_i-1}(q^{\alpha_i}-q)} \quad (1.66)$$

Fig. 1.19a illustrates the process for scalar parameters $\alpha = 1.5$ and $C_1 = 0.1$ obtaining a complex cascade valued in the $CI(0,1)$ for a $16 \times 16 \times 512$ conservative flux, and Fig. 1.19b illustrates the process for scalar parameters $\alpha = 1.5$ and $C_1 = 0.1$ obtaining a quaternion cascade valued in the $CI(0,2)$ for a $16 \times 16 \times 16 \times 512$ conservative flux.

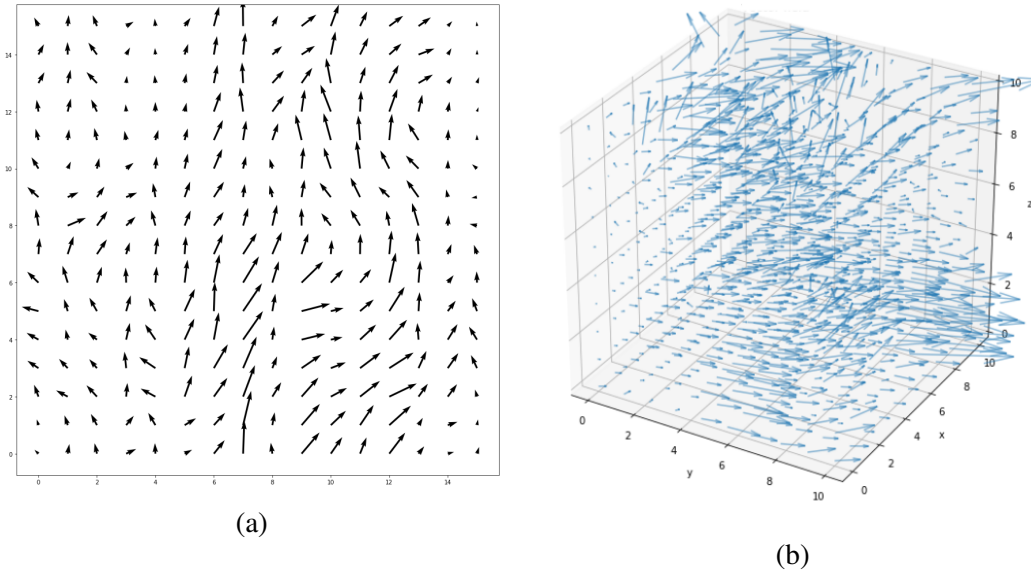


Figure 1.19: (a) Example 2D+1 multifractal vector field obtained by a complex cascade, i.e., with values of $CI(0,1)$ and (b) Example of a 3D+1 multifractal vector field obtained by a quaternion cascade, i.e., with values of $CI(0,2)$

1.4 Analysis

Multifractal analysis of a field consists in first assessing the quality of the scaling and second estimating the scaling functions $K(q)$, and $c(\gamma)$, as well as the UM parameters α and C_1 which characterize the field. In this section, we review the Trace moment techniques to estimate these features and also review the spectral analysis.

1.4.1 Trace moments techniques

To calculate UM parameters (C_1 and α) Trace moments techniques (Schertzer and Lovejoy, 1987a) are used.

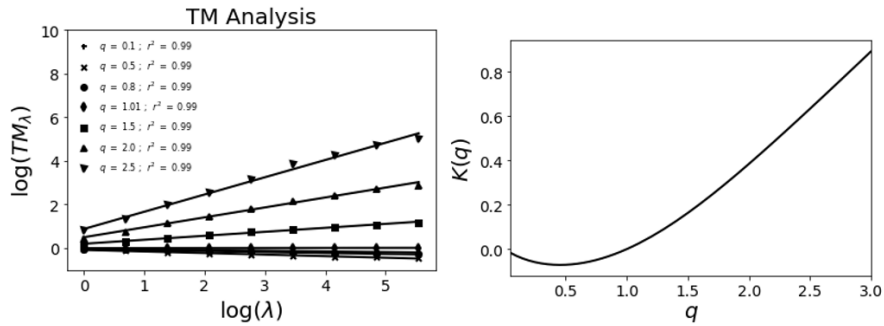


Figure 1.20: Illustration of a Trace moment technique using a simulated ensemble with input parameters $\alpha = 1.65$ and $C_1 = 0.25$, and 100 samples in 1D with size 256

Trace moment (TM) is based on Eq. 1.6. For that the field is upscaled and evaluated for different statistical moments of order in an iterative process, i.e. at each step:

1. The field (from the field at maximum resolution at step 1) is averaged by the scale ratio λ_1
2. The averaged field is evaluated for different statistical moments of order q

This process is plotted against the resolution in a $\log - \log$ plot. If the field is multifractal, then the empirical points of the plot are aligned along straight line whose slope is $K(q)$. It received its name because the trace of moments of the fluxes is equivalent to the empirical statistical moments (Schertzer et al., 2002).

Based in the fact that C_1 and α are theoretically the first and the second derivatives respectively (Section 1.2.5), a discrete approximation can be used to compute them is:

$$C_1 = K'(1) \approx \frac{K(1.05) - K(0.95)}{0.1} \quad (1.67)$$

$$\alpha = \frac{K''(1)}{K'(1)} \approx \frac{0.1}{0.05^2} \frac{K(1.05) + K(0.95)}{K(1.05) - K(0.95)} \quad (1.68)$$

This technique is illustrated in Fig. 1.20, which uses a 1D simulation created with Eq. 1.41 and input parameters $\alpha = 1.7$ and $C_1 = 0.25$ and 256 points. In the left part, each statistical moment q vs λ is plotted for a different values of q , then the slopes of these curves are plotted vs. q , obtaining the figure on the right. We consider the quality of the scaling based on how well the points fit a linear regression, considering a good scaling to be values of the linear regression coefficient as close to 1 as possible. We also consider other methods of curve fitting such as Ordinary least squares (OLS) or Weighted least squares (WLS) but selected the former as we did not see significant differences

in the result but it increases the computational cost.

The Double Trace moment technique calculates UM parameters directly if the field is conservative and exhibits UM behaviour (Lavallée et al., 1993). For this purpose, the field is renormalized to the η -power :

$$\varepsilon_\lambda^{(\eta)} = \frac{\varepsilon_\lambda^\eta}{\langle \varepsilon_\lambda^\eta \rangle} \quad (1.69)$$

And then a TM analysis is performed, which yields:

$$\langle \varepsilon_\lambda^{(\eta)q} \rangle = \frac{\langle \varepsilon^{\eta q} \rangle}{\langle \varepsilon_\lambda^\eta \rangle^q} \approx \frac{\lambda^{K(\eta q)}}{\lambda^{qK(\eta)}} = \lambda^{K(q,\eta)} \quad (1.70)$$

$$K(q, \eta) = K(\eta q) - qK(\eta) \quad (1.71)$$

In the Universal Multifractal framework we have,

$$K(q, \eta) = \eta^\alpha K(q) \quad (1.72)$$

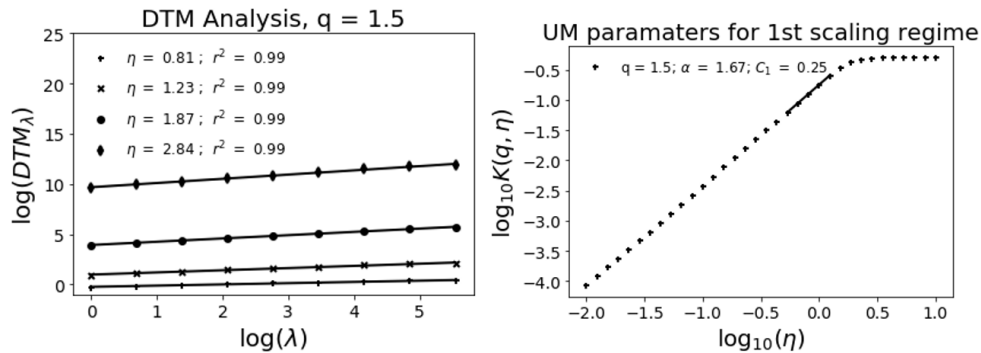


Figure 1.21: Illustration of a Double Trace moment technique using a simulated ensemble with input parameters $\alpha = 1.65$ and $C_1 = 0.25$, and 100 samples

For each η and q , TM technique is applied to the up-scaled field raised to the power η to calculate $K(q, \eta)$, then for a given q (usually $q = 1.5$), $K(q, \eta)$ vs. η is plotted in $\log - \log$ plot and the slope of the linear part of the graph is α . C_1 derived from the intercept b with the equation:

$$C_1 = 10^b \frac{(\alpha - 1)}{(q^\alpha - q)} \quad (1.73)$$

as Eq. 1.72 reflects (the 10^b comes from the fact that \log_{10} are used in Fig. 1.21).

This technique is illustrated in Fig. 1.21 (using the same simulation as in Fig. 1.20); the left figure illustrates DTM technique to the up-scaled field for several η . The right figure illustrates the curve fitting to compute the parameter α . With regards to the upper plateau visible for greatest η , the explanation lies in the multifractal phase transition associated with maximum observable singularities as $K(q)$ becomes linear for $q > q_s$:

$$K(q) = \gamma_s(q - q_s) + K(q_s) \quad (1.74)$$

With this linear form and Eq. 1.70, a constant value is obtained in $K(q, \eta)$.

There is also the possibility to observe a plateau for smallest η , for a similar multifractal phase transition, but associated with the effect of the zeros on the data. Such phenomenon is commonly observed for rainfall but it is not visible with wind data as studied in this document which do not contain numerous zeros.

1.4.2 Spectral analysis

Spectral analysis is a second-order statistical analysis to study the scaling behaviour of the field. It consists in plot Eq. 1.21 in a log-log plot. The statistical properties do not have to be satisfied by analysing a single sample but are satisfied over the average of several samples, i.e. as it is a statistical behaviour, it is valid on average over several samples. Hence, it is expected that quality of scaling will be worse when analysing a single sample. For that reason, degraded scaling is often observed when only one sample is analysed in multifractal fields. However, the results are much better when a larger number of samples are used. Fig. 1.22 is an example of this statistical behaviour. There, better results are shown in 100 samples simulation with r^2 close to 1. Both figures are created with field simulated using discrete cascades and the same set of parameters $\alpha = 1.5$ and $C_1 = 0.1$

It is possible estimate H parameter from the spectra using the formula stated in Tessier et al. (1993):

$$\beta = 1 + 2H - K(2) \quad (1.75)$$

It means that if the spectral slope β retrieved in the spectral analysis of a time series φ_λ is different to 1, it indicates that φ_λ is then a non-conservative field ($\langle \varphi_\lambda \rangle \neq 1$) and could be written as states in Eq. 1.75.

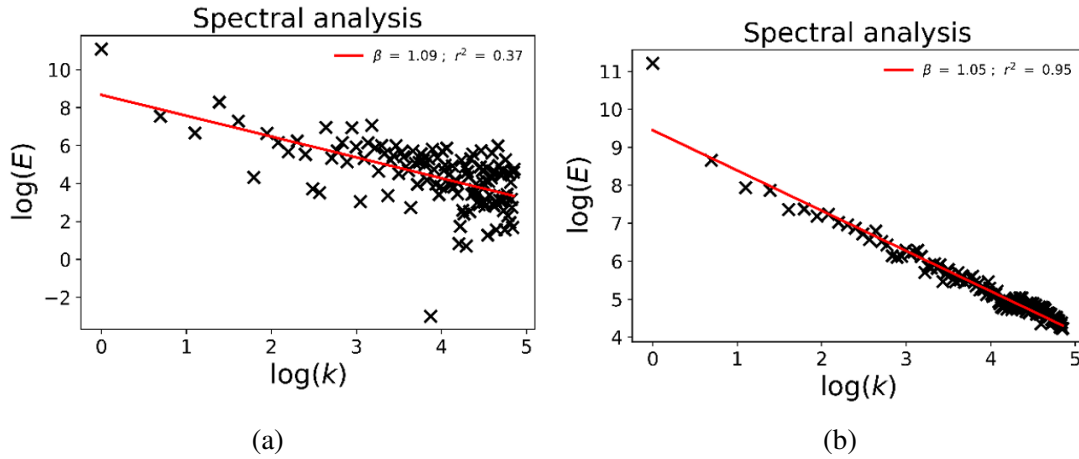


Figure 1.22: Illustration of a spectral analysis from (a) 1 sample and (b) 100 samples. The data is created using UM discrete cascades with the same set of parameters $\alpha = 1.5$ and $C_1 = 0.1$.

1.4.3 Validation of the simulations

In the following paragraphs, the fluxes simulated in the previous section are used to illustrate the analysis techniques reviewed. This process is also used to validate the results obtained in the simulation section. The section is organized as follows. First the sensitivity analysis of the simulation to the input set of UM parameters and dimension is reported. Then, the effect of the non-conservativeness parameter in the analysis techniques is discussed.

1.4.3.1 Illustration of the analysis techniques for simulations over various dimensions

To illustrate these techniques, simulation with different dimensions (1D (Fig. 1.23), 2D (Fig. 1.24), and 2D+time (2 spatial dimension and 1 temporal (Figs. 1.25 and 1.26)) are used. The analysis consists of the spectral analysis (panel(a)), the Trace moment analysis (panel (b)), and the Double Trace moments analysis (panels (c) and (d)). For the spatio-temporal simulations, we first performed a spatial analysis and then a temporal one.

We will consider that spectral analysis retrieved good results if it shows a straight line with a slope approximately to 1 ($\approx H = 0$). TM retrieved good results if the graph does not show any scaling break with a correlation coefficient of the linear regression as close as possible to 1. And for the DTM techniques if it obtains a good scaling, retrieving the same parameters as the inputted ones.

Figs. 1.23-1.26 show the ensemble analysis for input parameters $\alpha = 1.5$ and $C_1 = 0.1$ retrieving good results for the spectral analysis in all (a) panels. Good scaling is retrieved for both TM and DTM graphs where good correlation in the linear regression is shown, except for the case of

the temporal dimension of the 2D+t where rather good results are found $r^2 \approx 0.97$ (Figs. 1.26b and 1.26c). 1D and 2D simulations show good agreement between the inputs and the outputs. Meanwhile, a small difference appears in C_1 for the spatial dimension of the 2D+t and in α for the temporal one.

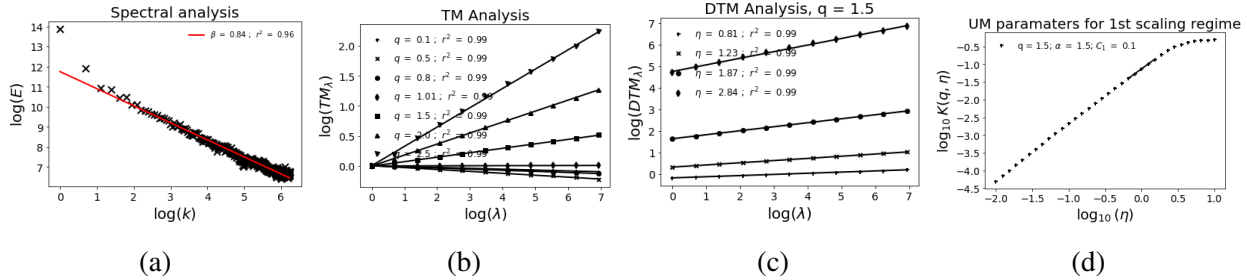


Figure 1.23: Illustration of the analysis techniques in 1D. (a) Spectral analysis (Eq. 1.21 in log-log), (b) TM (Eq. 1.6 in log-log), (c) and (d) DTM (Eqs. 1.70 and 1.72 in log-log respectively). The experiment consists of an ensemble of 100 samples with a length of 512. Input parameters are $\alpha = 1.5$ and $C_1 = 0.1$.

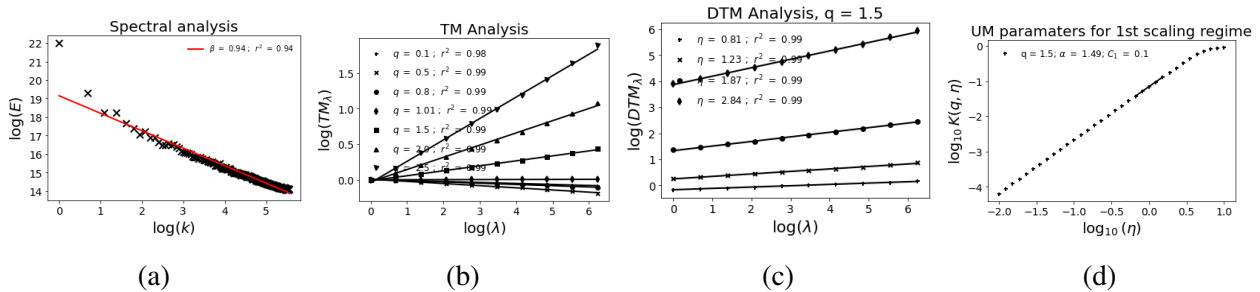


Figure 1.24: Illustration of the analysis techniques in 2D. (a) Spectral analysis (Eq. 1.21 in log-log), (b) TM (Eq. 1.6 in log-log), (c) and (d) DTM (Eqs. 1.70 and 1.72 in log-log respectively). The experiment consists of an ensemble of 100 samples with 512x512 spatial resolution. Input parameters are $\alpha = 1.5$ and $C_1 = 0.1$.

Fig. 1.27 shows a summary of the parameters retrieved on the analysis using boxplots, i.e. first each sample is analysed separately and then the whole ensemble is analysed. This is done to show the variability of the parameters retrieved using the same set of input parameters. It is important to note that the statistical properties do not have to be satisfied by analysing a single sample but are satisfied over the ensemble. All the cases show good agreement between the inputs and the outputs, with more deviation in 1D and spatial dimension than in the 2D+t case.

1. Universal Multifractal

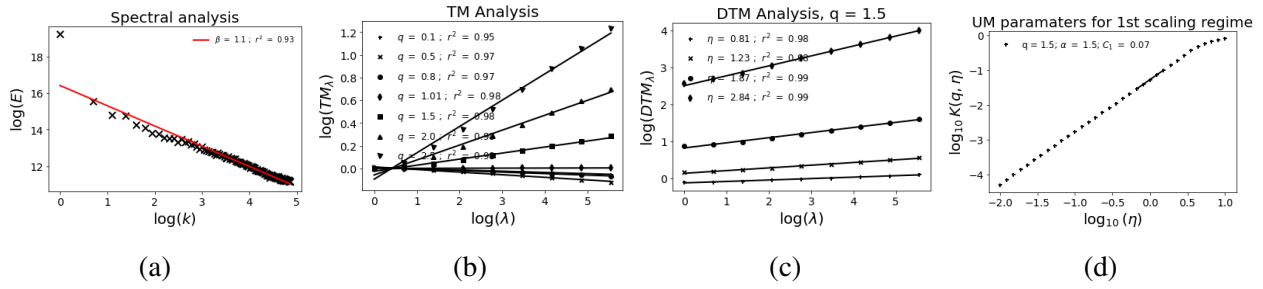


Figure 1.25: Illustration of the analysis techniques in 2D+time in the spatial dimension. (a) Spectral analysis (Eq. 1.21 in log-log), (b) TM (Eq. 1.6 in log-log), (c) and (d) DTM (Eqs. 1.70 and 1.72 in log-log respectively). The experiment consists of an ensemble of 100 samples with 512x512 spatial resolution and 512 time steps. Input parameters are $\alpha = 1.5$ and $C_1 = 0.1$.

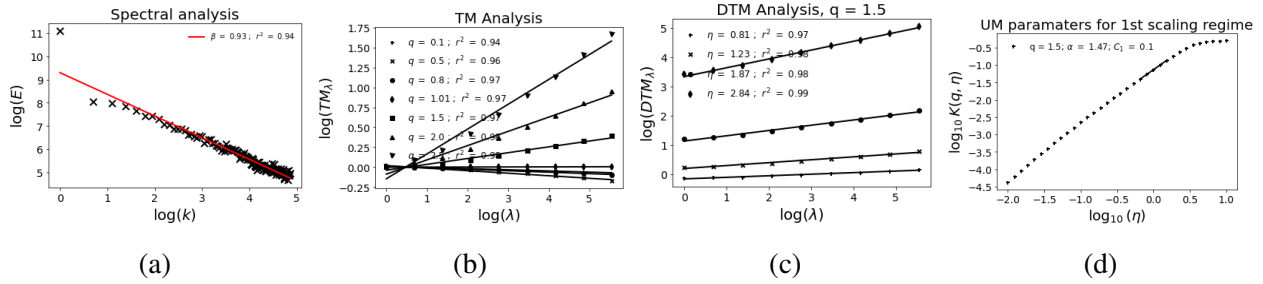


Figure 1.26: Illustration of the analysis techniques in 2D+time in the temporal dimension. (a) Spectral analysis (Eq. 1.21 in log-log), (b) TM (Eq. 1.6 in log-log), (c) and (d) DTM (Eqs. 1.70 and 1.72 in log-log respectively). The experiment consists of an ensemble of 100 samples with 512x512 spatial resolution and 512 time steps. Input parameters are $\alpha = 1.5$ and $C_1 = 0.1$.

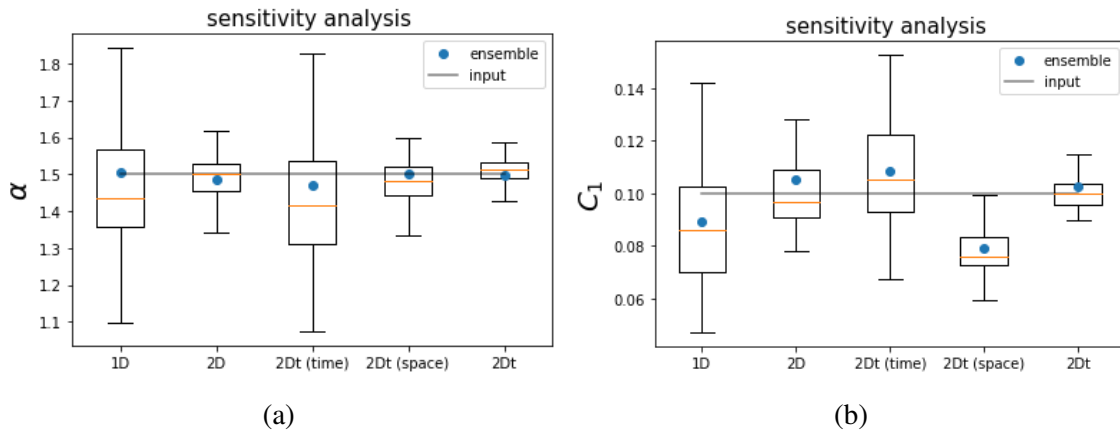


Figure 1.27: Boxplot analysis on the UM parameters retrieved on the ensemble simulation: (a) α and (b) C_1 . Input parameters $\alpha = 1.5$, $C_1 = 0.1$ and 100 samples.

1.4.3.2 Sensitivity analysis of the input parameters

Previous section validates the simulations for a given set of parameters, however, in order of fully validate them we need to carry out similar analysis with other sets of parameters. For this, we used the ensemble simulation of a 2D field of 512×512 points and 100 samples with different parameters for that. First, we realise the simulation fixing C_1 and increasing α (Fig. 1.28). Panels (a), (b), and (c) show the boxplot for α , C_1 , and r^2 respectively. Panels (d) and (e) show the absolute and relative errors for α and C_1 on ensemble analysis respectively.

For the first case, we found a good agreement between the α parameter inputted and the results for both α and C_1 , especially in the range $\alpha = 1.3 - 1.7$ where most of the atmospheric fields are included (Schertzer and Lovejoy, 1991). The error on the ensemble analysis varies from -0.06 to 0.08 in α , which is always less than $\pm 10\%$. For C_1 , the relative error is in the same range; meanwhile, the absolute error is one order of magnitude lower.

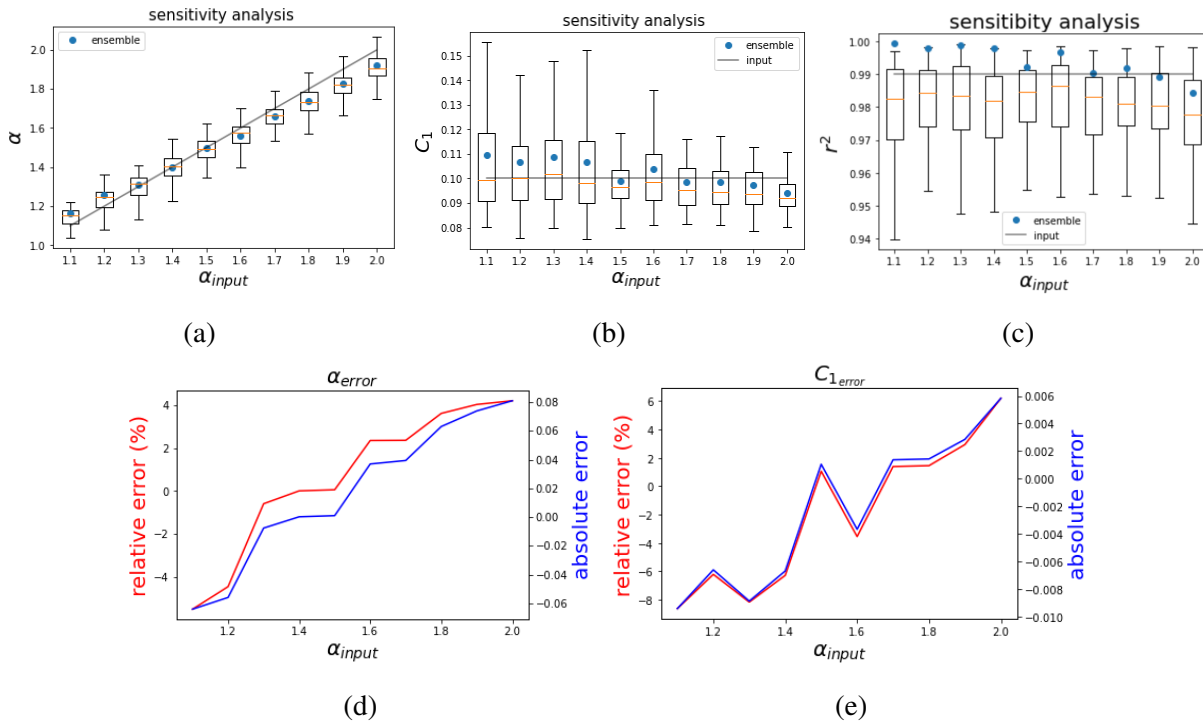


Figure 1.28: Sensitivity analysis of the UM parameters ((a) α and (b) C_1) retrieved on the analysis of 512×512 ensemble field for several inputted α , $C_1 = 0.1$ and 100 samples. The second row shows the absolute error and relative error (%) on both parameters on ensemble analysis.

We repeat the simulation fixing α and increasing C_1 (Fig. 1.29). When C_1 increases, however, the results are moving further and further from the inputs, especially in α . Although the results are worse than in the case of the sensitivity analysis in α the results are rather good with error $< 15\%$ for the range $C_1 = 0.05 - 0.3$ which corresponds to the one most often retrieved on atmospheric

fields (Schertzer and Lovejoy, 1991).

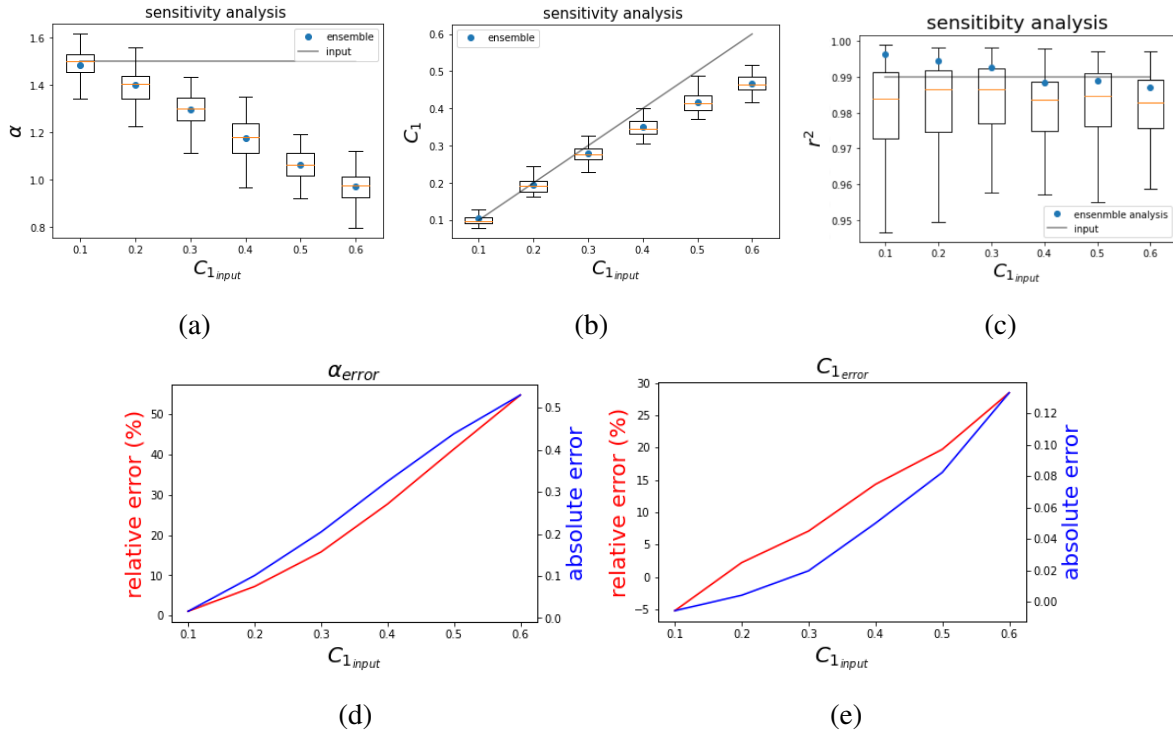


Figure 1.29: Sensitivity analysis of the UM parameters ((a) α and (b) C_1) retrieved on the analysis of 512x512 ensemble field for several inputted C_1 , $\alpha = 1.5$ and 100 samples. The second row shows the absolute error and relative error (%) on both parameters on ensemble analysis.

In both cases the analysis of the ensemble shows a good quality of the scaling with values close to $r^2 = 0.99$. When single samples are analysed this scaling is worse as we expect due to the statistical properties of the analysis.

1.4.3.3 Effect of H

When the field analysed is not conservative, some bias is introduced in the analysis. To illustrate this effect, we artificially impose different levels of non-conservativeness parameter H to the flux of Fig. 1.24 (i.e. ensemble of 100 samples with 512x512 spatial resolution and input parameters $\alpha = 1.5$ and $C_1 = 0.1$).

When the field shows a positive H (Fig. 1.30), as for wind fields, the slope of the spectral analysis increases (Fig. 1.30a), which is consistent with Eq. 1.75. The values obtained for β and H (1.61 and 0.51) are close to the theoretical one obtained using Eq. 1.75 (1.6 and 0.4).

It also appears a bias in both trace moment techniques, which is translated into a decrease in the correlation r^2 of the curve fitting (Figs. 1.30b and 1.30c) and, ultimately, to the computation of

the UM parameters (1.30d). In this case, the curves of the TM and DTM graphs become "concave", defining "concavity" as a decrease of the slope with $\log(\lambda)$.

When the field shows a negative H (Fig. 1.31), e.g. wind speed fluctuations, it is possible to find similar (but inverted) behaviour as the previous case. However, in this case, the spectral slope decrease (Fig. 1.31a) and the curve of the trace moment techniques become "convex".

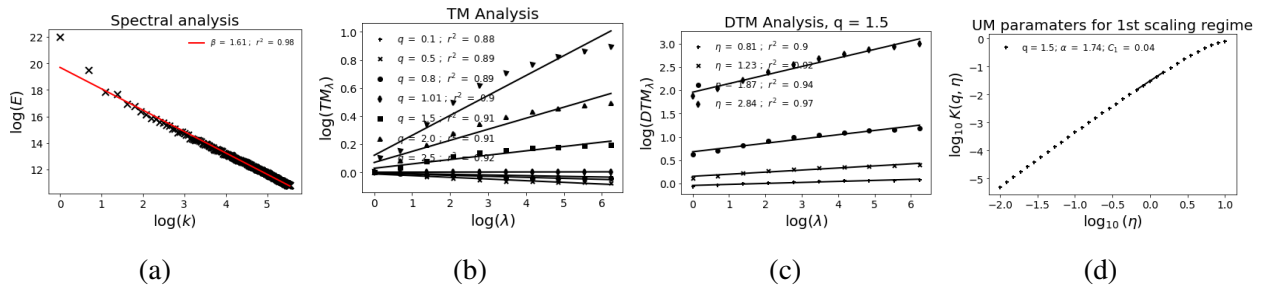


Figure 1.30: Illustration of the effect of positive H on the: (a) Spectral analysis (Eq. 1.21 in log-log), (b) TM (Eq. 1.6 in log-log), (c) and (d) DTM (Eqs. 1.70 and 1.72 in log-log respectively). The experiment consists of an ensemble of 100 samples with 512×512 spatial resolution with $\alpha = 1.5$, $C_1 = 0.1$ and $H = 0.3$.

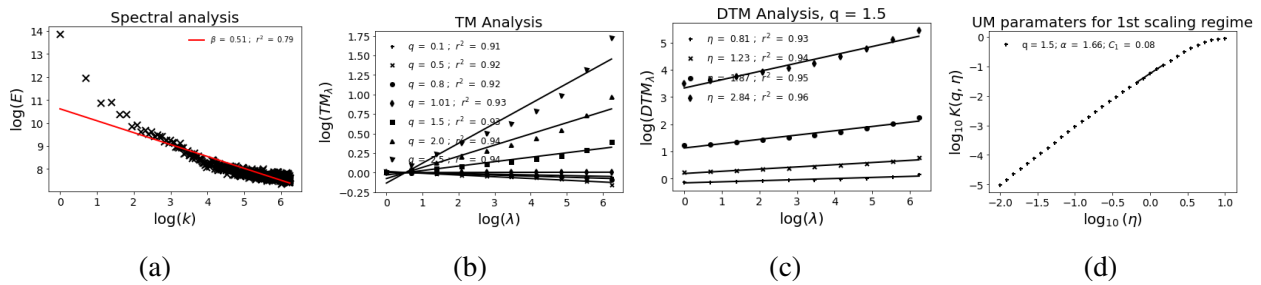


Figure 1.31: Illustration of the effect of positive H on the: (a) Spectral analysis (Eq. 1.21 in log-log), (b) TM (Eq. 1.6 in log-log), (c) and (d) DTM (Eqs. 1.70 and 1.72 in log-log respectively). The experiment consists of an ensemble of 100 samples with 512×512 spatial resolution with $\alpha = 1.5$, $C_1 = 0.1$ and $H = -0.3$.

We introduce a simplistic concavity indicator to measure the effect of the H on the TM and DTM graphs. For that, we divide the graph into two sub-graphs computing both slopes. Then, we make the difference between them. If the result is positive, we consider the graph "concave", and if it is negative, we consider it "convex". This indicator is plotted in Fig. 1.32a, and it shows that as the H of the field moves away from 0, the graph becomes more "concave" (for positive H) or more "convex" (for negative H). In the same figure, the coefficient of the linear regression (which is used as an indicator of the quality of the scaling) also decreases when the H moves away from 0. Fig. 1.32b shows the bias in the UM parameters retrieved when the value of H increases.

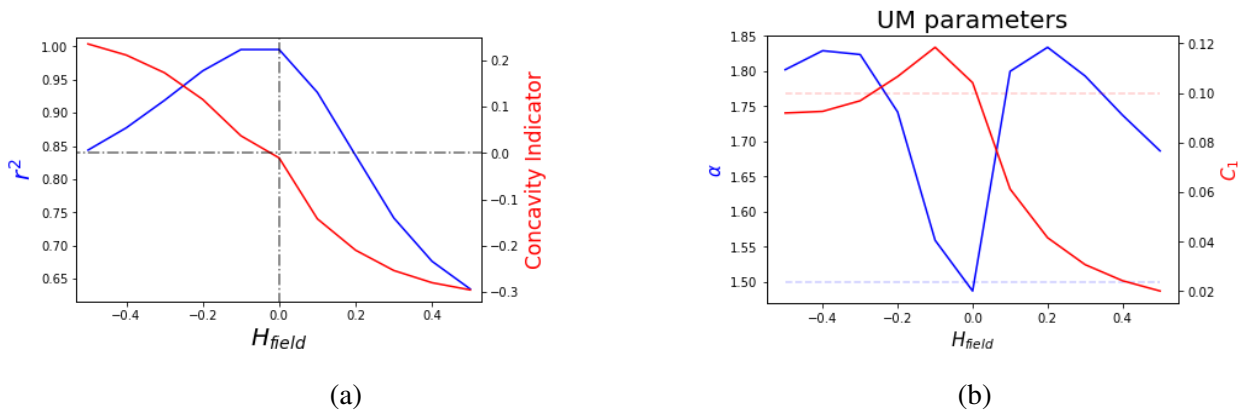


Figure 1.32: (a) The r^2 of Trace moment technique for $q = 1.5$ in blue, and a concavity indicator in red for different H values of the field. (b) α in blue and C_1 in red for simulated fields with different H values. Input parameters ($\alpha = 1.5$ and $C_1 = 0.1$) are dotted in blue and red respectively for clarity

In their study, Fitton (2013) also investigated the impact of the non-conservativeness parameter, H , in the field. To mitigate the potential bias caused by the effect of H , they recommended performing fractional integration. However, they found that using the H retrieved with Eq. 1.75 did not resolve the issue, as both the TM and DTM graphs exhibited either "concave" or "convex" behavior. Instead, they proposed using the H value that maximizes the linear part of these graphs, i.e. the value which maximizes the r^2 obtained in linear regression.

Relying on similar ideas, we developed an algorithm that performs iterative fractional integration to obtain the optimal value of the fractional integration order used in the analysis. The initial value for the iteration was set as the H value obtained from Eq. 1.75. The algorithm follows the following process:

1. Analyze the data (spectral analysis, TM and DTM) in order to obtain the quality of the scaling and the initial H of the field. We consider them as r_0^2 and H_0 respectively.
2. Perform the fractional integration/differentiation in the data using H_0 as the order of integration.
3. Analyze the new data obtaining H_1 and r_1^2 . If r_1^2 is greater than 0.99 then H_0 is set as optimal order of fractional integration/differentiation. If it is lower, there are 2 options:
 - (a) $r_1^2 > r_0^2$, H_1 is set as new order of fractional integration/differentiation and we repeat the process from step 2. Now the quality of scaling used for comparison is r_1^2 .
 - (b) $r_1^2 < r_0^2$, we keep r_0^2 and reduce the value of H_0 to introduce in step 2.

4. This process is repeated iteratively till $r_i^2 > 0.99$, setting H_i as the optimum order of fractional integration/differentiation. If the algorithm does not converge after a given number of iterations (we use 100) then the H_i which gives the greater r^2 is set optimum value.

One example of this method is illustrated in Fig. 1.33 where the coefficient of linear regression increases from $r^2 = 0.8$ before the correction (Fig. 1.33a) to $r^2 = 0.99$ after (Fig. 1.33b).

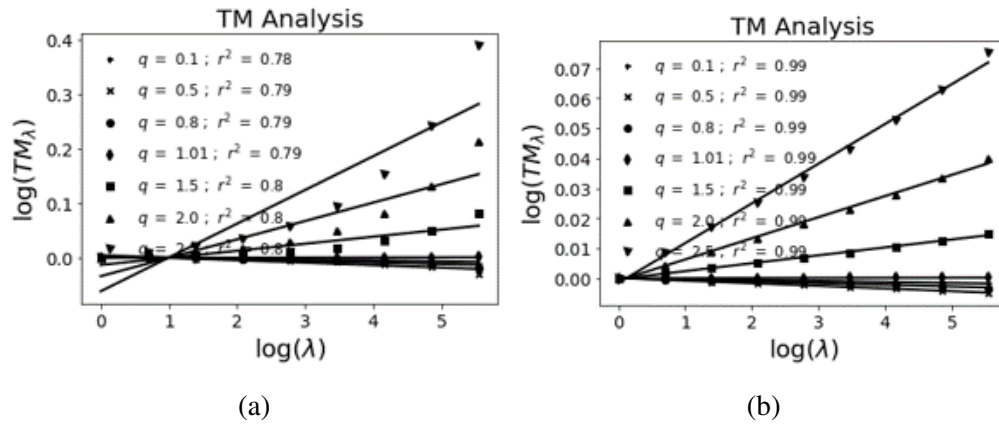


Figure 1.33: Illustration of the correction in the TM graphs (a) shows the graph before the correction and (b) after. The field used is the fluctuations of wind field event recorded in 20/12/2020.

1.4.3.4 Vector fields

For the validation of the simulation of vector fields we use 1D vector fields with two and three components. We use an ensemble of 100 samples 1024 points with input parameters $\alpha = 1.5$, $C_1 = 0.1$, and $H = 0$ in both cases. Figs. 1.34-1.36 shows the analysis for the two component case. The two components (Figs. 1.34 and 1.35) and the resultant (Fig. 1.36), i.e. the norm of the vector, show similar behaviour, with a good scaling (present in panels (b) and (c)) and similar values of the UM parameters to those inputted (panels (d)). Fig 1.37 shows a summary of the parameters retrieved on the analysis using boxplots, i.e. first each sample is analysed separately and then the whole ensemble is analysed. We found a good agreement between inputs and outputs with results slightly smaller in the second component.

Figs. 1.38-1.41 shows the analysis for the three component case. The three components (Figs. 1.34, 1.35, and 1.35) and the resultant (Fig. 1.36) confirm the behaviour observed in the two component analysis, with a good scaling (panels (b) and (c)) and similar values of the UM parameters to those inputted (panels (d)). Fig 1.37 shows again a summary of the parameters retrieved on the analysis using boxplots. We found a good agreement between inputs and outputs with bigger results in C_1 presented in the analysis of the components separately.

Once the behaviour of the vector field is verified obtaining similar results as in the scalar

1. Universal Multifractal

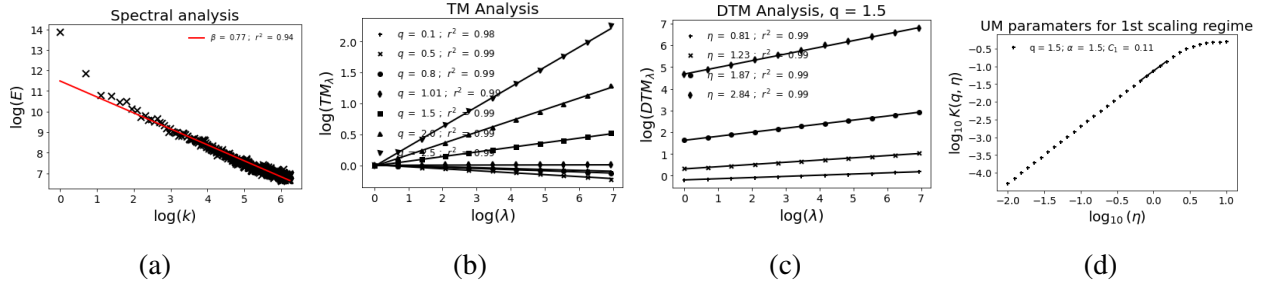


Figure 1.34: Validation of the simulations of Vector fields for the first component. (a) Spectral analysis (Eq. 1.21 in log-log), (b) TM (Eq. 1.6 in log-log), (c) and (d) DTM (Eqs. 1.70 and 1.72 in log-log respectively). The experiment consists of an ensemble of 100 samples with 1024 points and 2 components. Input parameters are $\alpha = 1.5$, $C_1 = 0.1$, and $H = 0$.

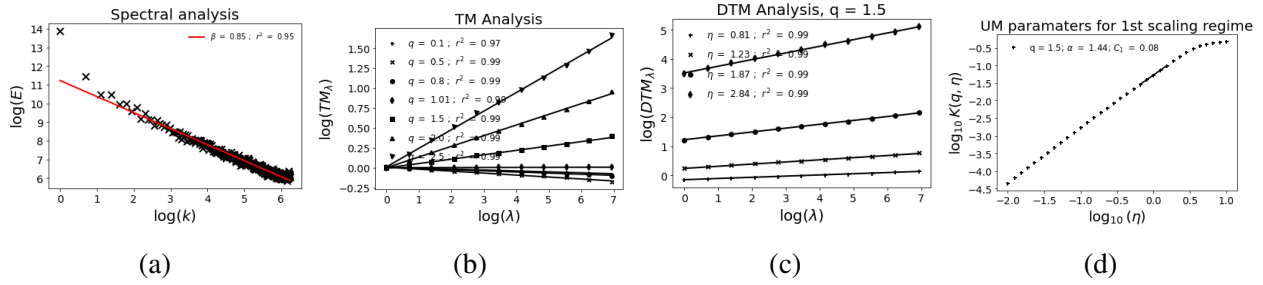


Figure 1.35: Validation of the simulations of Vector fields for the second component. (a) Spectral analysis (Eq. 1.21 in log-log), (b) TM (Eq. 1.6 in log-log), (c) and (d) DTM (Eqs. 1.70 and 1.72 in log-log respectively). The experiment consists of an ensemble of 100 samples with 1024 points and 2 components. Input parameters are $\alpha = 1.5$, $C_1 = 0.1$, and $H = 0$.

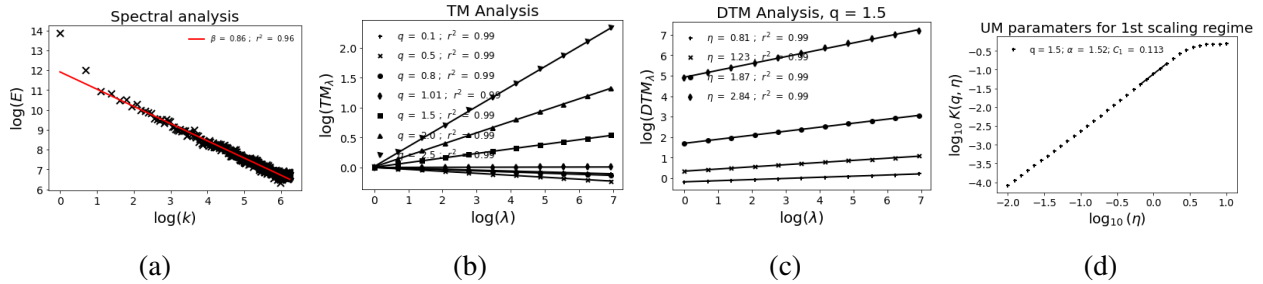


Figure 1.36: Validation of the simulations of Vector fields for the resultant component. (a) Spectral analysis (Eq. 1.21 in log-log), (b) TM (Eq. 1.6 in log-log), (c) and (d) DTM (Eqs. 1.70 and 1.72 in log-log respectively). The experiment consists of an ensemble of 100 samples with 1024 points and 2 components. Input parameters $\alpha = 1.5$, $C_1 = 0.1$, and $H = 0$.

1. Universal Multifractal

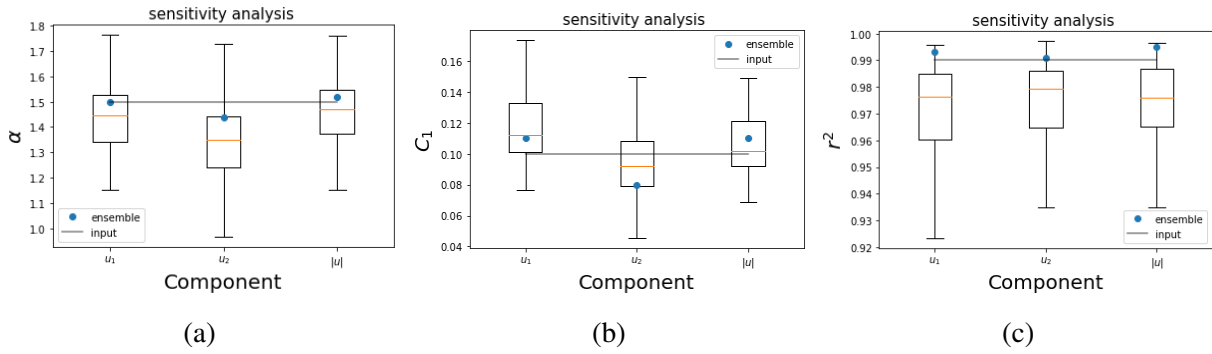


Figure 1.37: Sensitivity analysis on the UM parameters retrieved on the ensemble simulation: (a) using α , (b) C_1 and (c) r^2 . Input parameters are $\alpha = 1.5$, $C_1 = 0.1$, and $H = 0$ with 100 samples, and 2 components.

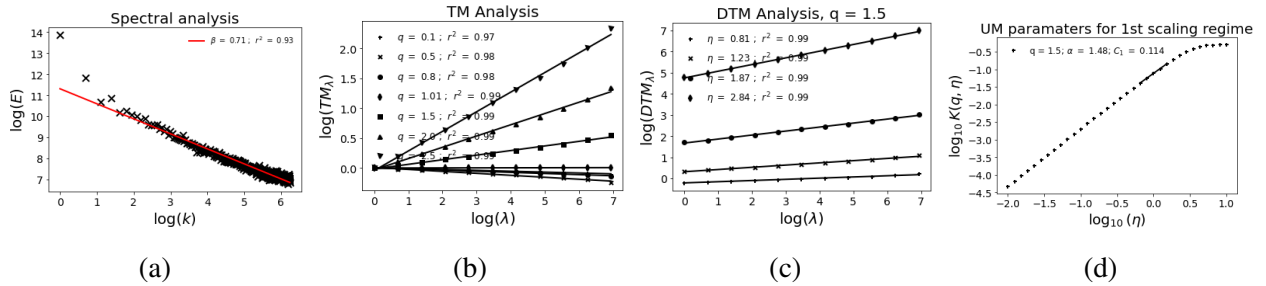


Figure 1.38: Validation of the simulations of Vector fields for the first component. (a) Spectral analysis (Eq. 1.21 in log-log), (b) TM (Eq. 1.6 in log-log), (c) and (d) DTM (Eqs. 1.70 and 1.72 in log-log respectively). The experiment consists of an ensemble of 100 samples with 1024 points and 3 components. Input parameters are $\alpha = 1.5$, $C_1 = 0.1$, and $H = 0$.

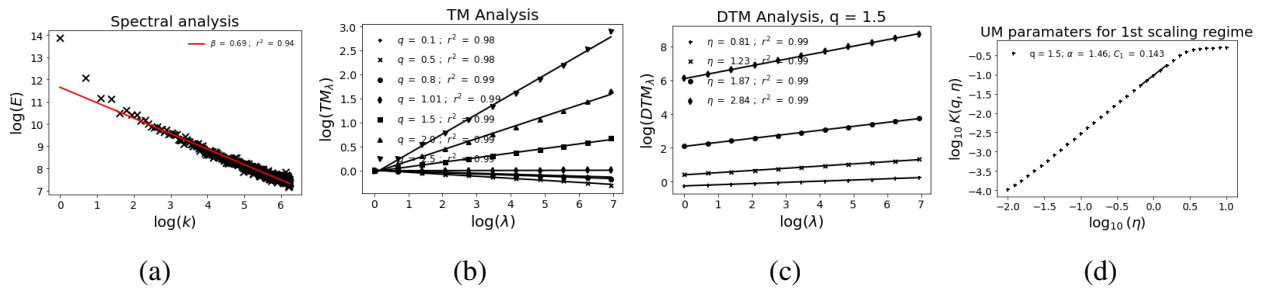


Figure 1.39: Validation of the simulations of Vector fields for the second component. (a) Spectral analysis (Eq. 1.21 in log-log), (b) TM (Eq. 1.6 in log-log), (c) and (d) DTM (Eqs. 1.70 and 1.72 in log-log respectively). The experiment consists of an ensemble of 100 samples with 1024 points and 3 components. Input parameters are $\alpha = 1.5$, $C_1 = 0.1$, and $H = 0$.

1. Universal Multifractal

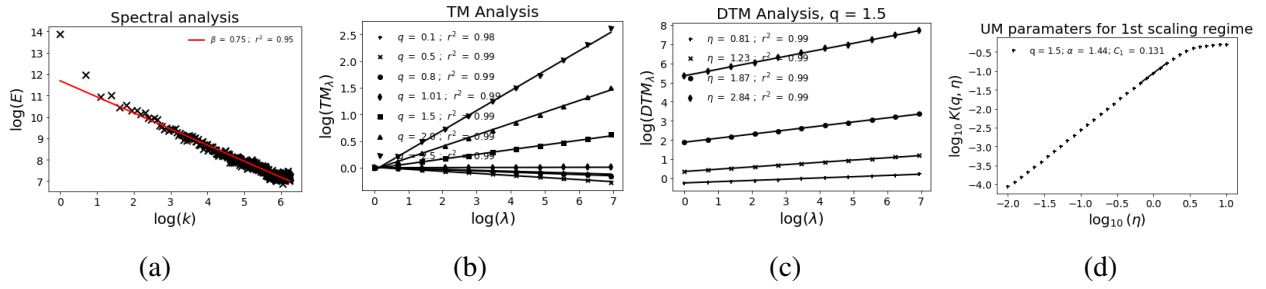


Figure 1.40: Validation of the simulations of Vector fields for the third component. (a) Spectral analysis (Eq. 1.21 in log-log), (b) TM (Eq. 1.6 in log-log), (c) and (d) DTM (Eqs. 1.70 and 1.72 in log-log respectively). The experiment consists of an ensemble of 100 samples with 1024 points and 3 components. Input parameters are $\alpha = 1.5$, $C_1 = 0.1$, and $H = 0$.

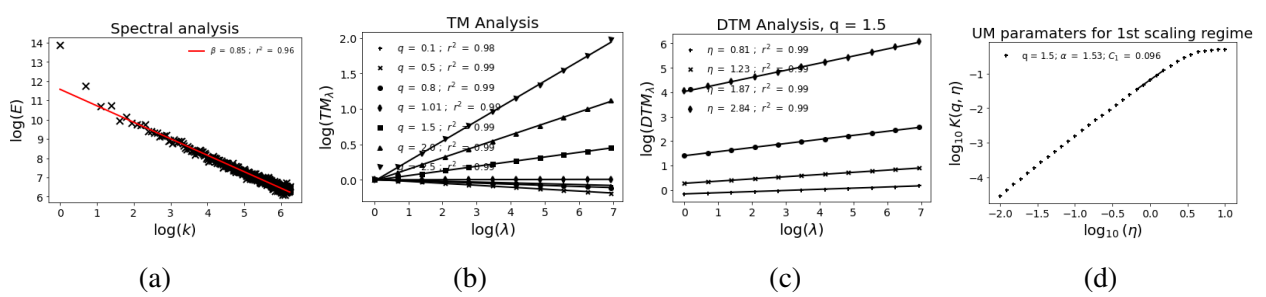


Figure 1.41: Validation of the simulations of Vector fields for the resultant component. (a) Spectral analysis (Eq. 1.21 in log-log), (b) TM (Eq. 1.6 in log-log), (c) and (d) DTM (Eqs. 1.70 and 1.72 in log-log respectively). The experiment consists of an ensemble of 100 samples with 1024 points and 3 components. Input parameters $\alpha = 1.5$, $C_1 = 0.1$, and $H = 0$.

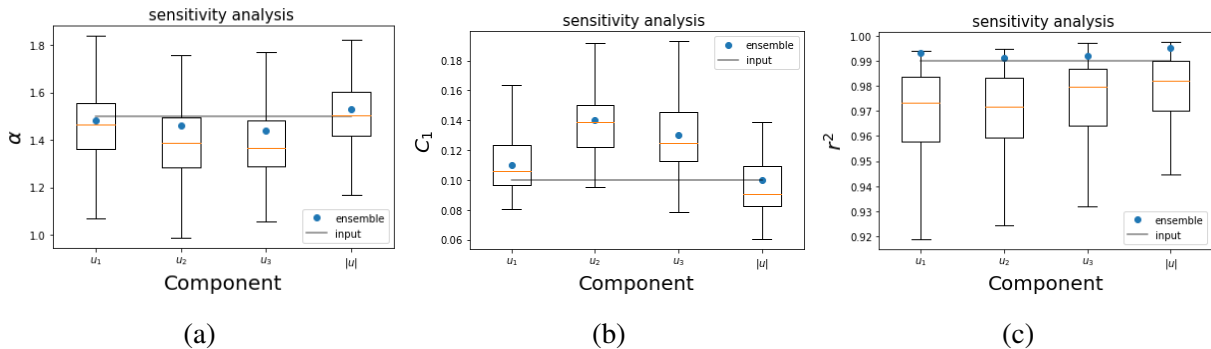


Figure 1.42: Sensitivity analysis on the UM parameters retrieved on the ensemble simulation: (a) using α , (b) C_1 and (c) r^2 . Input parameters $\alpha = 1.5$, $C_1 = 0.1$, and $H = 0$ with 100 samples, and 3 components.

case, the extension to more dimensions is straightforward extending the generator to the desired dimensions. Illustration of 2D+t and 3D+t vector fields can be found in Fig. 1.19. To fully address this validation a vector analysis technique is needed. However, this tool is not available at the moment and its development is outside the scope of the thesis.

1.5 Summary

The current chapter provides a comprehensive review of the Universal Multifractal (UM) framework, encompassing its theoretical foundations and various analysis and simulation techniques. These techniques, which are documented in the literature, have been used to develop a toolbox for simulation tools, mainly for continuous cascades, in 1D, 2D, and 2D+t scenarios (two spatial dimensions plus one temporal dimension). These tools were written in Python language.

In a first step, a detailed validation of the written tools was implemented. In order to achieve this, UM analysis was carried out on ensembles of simulated fields in various dimensions, including a sensitivity analysis using different sets of input parameters. As it could be expected for a theoretical framework already available in the literature, we found a good scaling and a notable agreement between input and output parameters, with the UM techniques demonstrating consistent responses across the tests. In addition to validation of developed scripts, which was a required step, this enabled to get familiar with the wide range of analysis tools available within the UM framework.

In a second step, we investigated the impact of the degree of non-conservation (H parameter) on the outputs of these analysis techniques. We found increasing spectral slope at higher values of H , which was theoretically expected and numerically confirmed. A worsening of the scaling in TM and DTM is found when $H \neq 0$. More precisely, a change in the curvature of the TM graph is observed, with convex graphs for positive H and concave for negative H . Hence, in order to retrieve unbiased results from TM and DTM analysis for non-conservative fields a correction is needed before applying these techniques. An algorithm has been developed to optimize the correction of analyzed fields based on the quality of scaling, relying on concepts presented by G. Fitton in his thesis (Fitton, 2013). Basically, the algorithm performs iterative fractional integration to obtain better scaling (regression coefficient $r^2 > 0.99$) in the analysis. The initial value for the iteration was set as the H retrieved from the analysis of the original field. The implementation of the correction algorithm enables to retrieve the inputted UM parameters also for simulations with $H \neq 0$.

Finally, existing theory has been applied to the development of a toolbox for simulating vector fields combining stable Levy processes and Clifford algebra. Python scripts were developed to simulate vector fields with 2 or 3 components. Similarly to the scalar case previously discussed, simulated fields, and more precisely each component and the norm, were analysed using UM tech-

1. Universal Multifractal

niques. We found good scaling with a good agreement between inputs and outputs, which enabled to validate the developed scripts. However, for a complete validation it would be necessary to develop tools tailored to these specific vector processes, i.e. analysis tools directly working on vectors and not isolated scalar components. This should be done in future investigations and will allow not only to validate these results but also to better understand this type of processes.

In summary, this chapter has established a robust toolbox for advancing the simulation of realistic geophysical fields, allowing for increased versatility and applicability across diverse research domains.

2. Wind Simulation

Chapter 2

Wind simulation

2.1 Introduction

Wind fields are known to be extremely variable in space and time over a wide range of scales and, although different measurement techniques exist, each has its own advantages and disadvantages. Eg. it is possible to know the wind data at isolated points, where high resolution sonic anemometers can be located, but this does not provide any spatial information. Other instruments such as LIDARs (e.g. Wang et al., 2015 or Shimada et al., 2020) or SODAR (e.g. Khan and Tariq, 2018 or Buzdugan and Stefan, 2020) give some spatial information but with low temporal resolution. The complexity of wind measurement makes obtaining wind speed at all points in a given area a major challenge and highlights the need to use simulations.

Computational fluid dynamics (CFD) models can grasp the turbulent properties of the wind fields but with a huge computational cost . However, parametrization of turbulence at small scales is still necessary, as viscosity only dissipates energy at the Kolmogorov scale of a few mm, making it impossible to simulate full turbulence over a wide range of scales in the near future. To reduce these costs synthetic turbulence models (e.g. Juneja et al., 1994 and Basu et al., 2004) are used for the computations and prediction of the structural loads. Many authors (Sahin and Sen, 2001 and Shamsad et al., 2005 among others) decide to only generate wind time series at hub height forgetting the idea of simulate 3D fields. But it is with the emergence of spectral models that the possibility to generate a 3D (or 4D if we take into account the time) full field became a reality. One example of these models can be found in Veers (1988) and in the software Turbsim which is reviewed in the following sections.

Classical approaches of synthetic turbulence usually assume Gaussian statistics for the turbulent wind fluctuations (Meneveau, 2019), however, there are many studies which suggest that these

fluctuations exhibit non-Gaussian statistics (Mücke et al., 2011, Hedevang et al., 2012, Wächter et al., 2012, Fitton, 2013 and Medina et al., 2015 to cite some examples). Generating 3D vector fields poses significant challenges, and there are only few examples reported in the literature. One example relies on the use of multiscale Lagrangian maps (Rosales and Meneveau, 2006 and Rosales and Meneveau, 2008), which can generate non-Gaussian 3D velocity fields by considering increments and gradients (Meneveau, 2019). However, these approaches are currently unable to reproduce temporal fluctuations and are limited to generating static velocity fields.

Another method is based on the use of an auxiliary turbulence simulation (i.e. driver) with a periodic computational domain. Some examples of turbulent wind simulation can be found in Spalart (1988) and Lund et al. (1998). However, although it is simpler to implement than synthetic turbulence, its computational cost is high and there is a problem of spurious periodicity arising from the periodicity of the current in the conductor simulation (Wu, 2017).

It is also possible to use machine learning as a tool for wind field simulation (Kutz, 2017, Ling et al., 2016, Gamahara and Hattori, 2017, Angriman et al., 2022), and although the use of deep learning in fluid dynamics is not a recent development, with studies using neural networks in the 90s for e.g. turbulent friction drag reduction (Choi et al., 1994, Lee et al., 1997) or flow field estimation (Milano and Koumoutsakos, 2002), it is in recent years through the boom in big data and artificial intelligence that it has gained popularity. Because even though these methods show lower efficiency than CFD methods, they give a rather good response with much shorter response times (Guo et al., 2016). Some examples can be found in Fukami et al. (2019b) in which a methodology for generating time-dependent turbulent inflow data with the aid of machine learning is proposed, or in Fukami et al. (2019a) in which machine learning is used to perform super-resolution reconstruction of flow field.

Many other authors also use weather forecast models such as Global Forecast System (GFS, developed by National Centers for Environmental Prediction (NCEP)) or Weather Research and Forecasting model (WRF, Skamarock et al., 2008) for the simulation wind fields (Carvalho et al., 2012, Jiménez et al., 2013 or Xu et al., 2021 just to mention some examples). However they cover range of scales in which we are not focusing for this work.

In this chapter, we investigate different processes to simulate 3D+time vector fields with non-Gaussian statistics over a grid covering an area corresponding to wind turbine swipe area (a square of 90m side) using Universal Multifractal framework (see Section 1.2). These ideas go from the oversimplified isotropic reconstruction from punctual measurement to more realistic wind fields with the help of UM vector fields using the framework introduced in Schertzer and Tchiguirinskaia (2015) and Schertzer and Tchiguirinskaia (2020).

The chapter is organized as follows. First a review of the measurement campaign and some data analysis (Section 2.2), followed by the review of available tools and and the various methods

for non-Gaussian wind field simulation. First method of wind simulation is Turbsim software developed by NREL, which simulate 3D turbulent wind fields using Gaussian statistics (Section 2.3). We use three non-Gaussian methods, the first is a simplistic approach which reconstructs the wind field over a given area based on well-established scaling laws (Section 2.4). The other two methods are based in the same principles (Fractional Integrated Flux) but differs in their objective since the first one is focused on the simulation of the direct fields (Section 2.5.1) and the second one is focus on the simulation of the fluctuations (Section 2.5.2). The chapter ends with an assessment of the different approaches (Section 2.6), helping in the selection of the most appropriate method for accurate and realistic wind field simulations.

2.2 Data & analysis

2.2.1 Description of the data

Data used is collected in the framework of high resolution measurement campaign part of the Rainfall Wind Turbine or Turbulence project (RW-Turb) which is supported by the French National Research Agency (ANR in French). It is presented in details in Gires et al. (2022a), and only the main elements are reported here. The campaign was carried out on a meteorological mast (operated by Boralex <https://www.boralex.com/our-projects-50and-sites/>) in a wind farm located in Pays d’Othe, France (roughly 110 km South-East of Paris). There are nine wind turbines operated by two different companies (Boralex <https://www.boralex.com/our-projects-and-sites/> and JP Énergie Environnement <https://pays-othe-89.parc-eolien-jpee.fr/>) in the wind farm. Location and situation of the wind farm and meteorological mast is illustrated in Figs. 2.1a and 2.1b respectively.

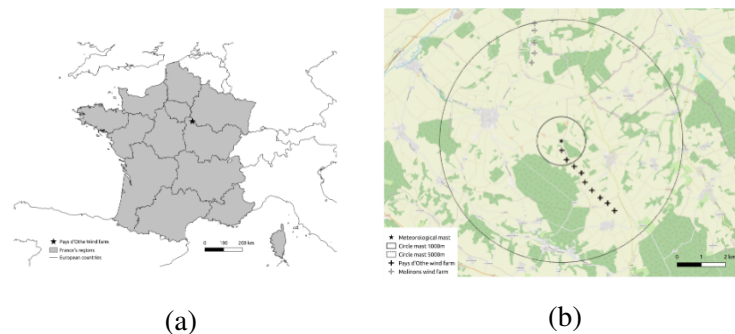


Figure 2.1: (a) Illustration of the location and (b) map of the surroundings of the meteorological mast used on RW-Turb high resolution measurement campaign (from Gires et al., 2022a)

Meteorological mast is equipped with three different types of devices repeated at roughly 45 and 78m height. Fig. 2.2 shows the location of the devices on the mast. First type is a high resolution 3D sonic anemometer manufactured by ThiesCLIMA (ThiesCLIMA, 2013a) with data

2. Wind Simulation

available at an original sampling frequency of 100 Hz but only can be used at 1 Hz) (see Gires et al., 2022a for more details). Mini meteorological station, also manufactured by ThiesCLIMA (ThiesCLIMA, 2013b), which consists of sonic 2D anemometer, a micro-electro-mechanical system for the pressure measurement, a mini Doppler radar to provide rainfall estimates and four photo sensors. The meteorological stations provides information about precipitation, air temperature, relative humidity, wind velocity and direction, and brightness with 1 Hz sampling rate. The last device is a OTT Parsivel² disdrometer (OTT Hydromet GmbH, 2014) which provides information on the size and velocity of the drops passing through its sampling area from which rain rate and drop size distribution can be estimated.

In this study, we only use the data obtained from the high-resolution 3D sonic anemometers. An analysis conducted in Gires et al., 2022a revealed a peak in the spectra at 30 Hz , which corresponds to the repetition rate of data measurements by the device. Additionally, the study finds that the Universal Multifractal (UM) obtained within the scale range of 30 Hz to 1 Hz suggests that for resolutions finer than 1 Hz the devices exhibit instrumental noise. Hence, to mitigate this noise, our analysis will be conducted using data with time steps of 1 s (or frequency of 1 Hz).

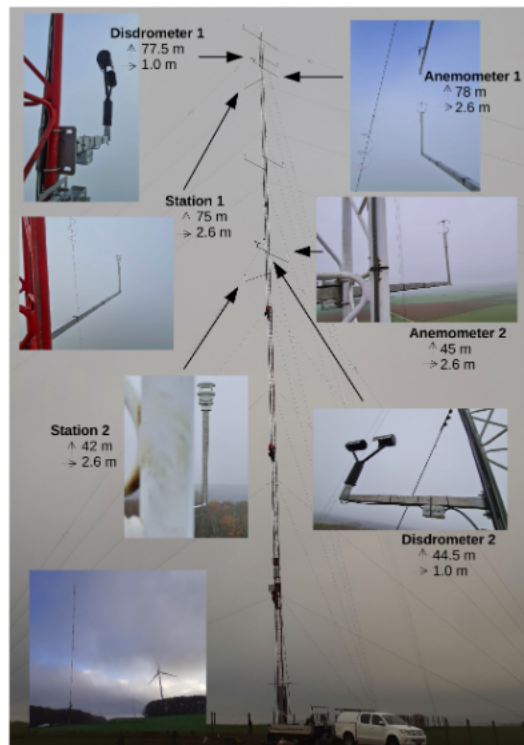


Figure 2.2: Scheme of the distribution of the devices in the meteorological masts (from Gires et al., 2022a)

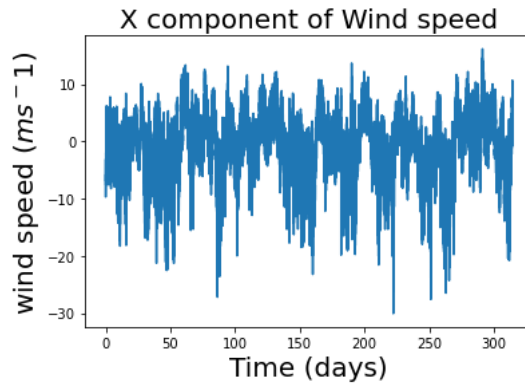


Figure 2.3: Example of x (towards East) component of the wind speed retrieved from the 3D anemometer (located at hub height, roughly 78m) in the period December 2020 and May 2021 with 1 s time steps.

2.2.2 Data preparation

All the data used in the subsequent sections is retrieved from the high-resolution 3D anemometers. We have employed data collected between December 2020 and May 2021 (see Fig. 2.3 for an illustration of the data). Since our objective is to simulate realistic wind fields, it is crucial to analyze their properties. The initial step involves determining the length of the data to be utilized. To accomplish this, we performed analyses on different data lengths to select which range was most suitable for the analysis. Finally, since we are interested in small-scale variability, we decided to use approximately 1 hour of data (4096 seconds, following what was done in Fitton (2013)) as a starting point. Upon conducting Trace Moment analysis (see Fig. 2.4), although we observe a good scaling on the the field (Fig. 2.4a), two different scaling breaks are accounted for to get more robust estimates (clearly visible in Fig. 2.4b). The first break occurs at 4 seconds, followed by another break close to 17 minutes. Consequently, we will focus on the interval between 4 seconds and 17 minutes for the following sections which is in agreement with the time scales over which the industrial practitioners usually average the wind data.

The next step involves characterizing the UM properties of the wind field. To accomplish this, we employ the tools outlined in the analysis section (Section 1.4). Furthermore, we have decided to analyze an ensemble of 100 samples comprising periods of 17 minutes (1024 seconds) each, grouped according to the average wind speed (starting in 0 ms^{-1} and using intervals of 0.5 ms^{-1}). It is important to note that all these analysis are done on the fields without any correction in order to characterise the behaviour of the fields and to be able to use them for later comparison.

By examining the parameters of the Fig. 2.5, we can observe two distinct trends associated with the wind speed. Specifically, α , r^2 , and H (computed using Eq. 1.75) exhibit an increase as the wind speeds escalate, up until approximately 4 ms^{-1} , beyond which these parameters remain relatively

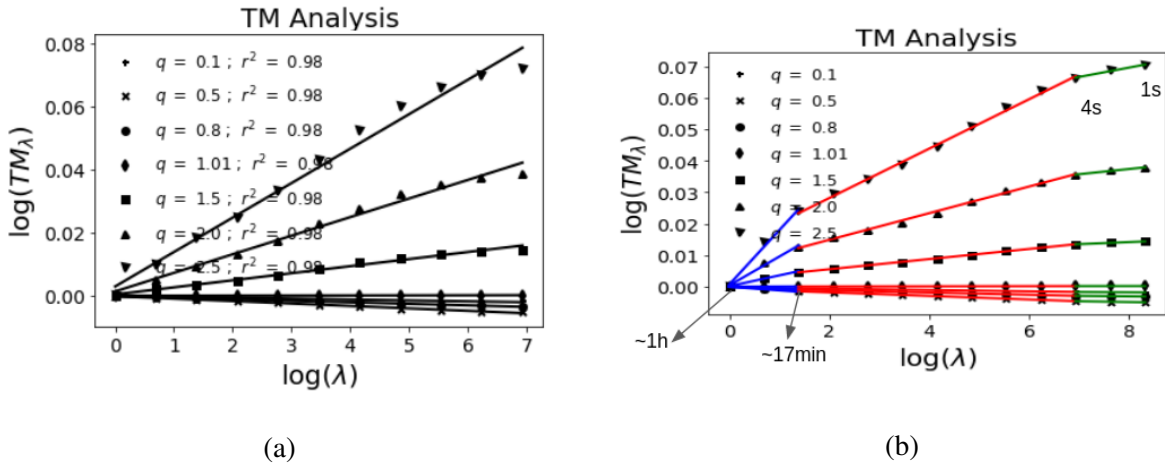


Figure 2.4: Example of TM analysis for 8 m/s. (a) shows the analysis with a single scaling regime and (b) with three scaling regimes 1s-4s, 4s-~17min, and ~17min-~1h.

stable. Conversely, we observe an inverse trend in the case of C_1 , where it decreases before reaching a constant value. These trends are visually depicted in Fig. 2.5. When examining the coefficient of linear regression of the trace moment (r^2 , used to quantify the quality of the scaling), we can observe that it is indicative of a not-good scaling for lower velocities ($<4 \text{ ms}^{-1}$) which means that the estimation of the parameters are not very reliable and should therefore be considered very cautiously. It suggests that the interval of 4 seconds to 17 minutes may not be suitable for this range of velocities due to a scaling that is not fully deployed, or to some instrumental limitations. However, considering the ultimate objective of utilizing this wind data for wind power applications, it is worth noting that velocities within this range are not utilized due to the turbine's cut-in speed (the minimum velocity at which the blades start rotating) as stated in Vestas Wind Systems A/S, 2023. Hence, this issue was not investigated further.

Similarly, we can characterize not only the direct wind field but also its fluctuations in a consistent manner. In this case, the trends observed in the previous analysis are no longer as apparent and the parameters are rather constant. However, in Figs. 2.6b-2.6d, it is possible to see a decrease trend in the lowest velocities. It is important to note that the estimates of UM parameters are not very reliable since the scaling exhibits poor performance, with r^2 values lower than 0.8. This finding is consistent with observations in the literature (e.g., Fitton, 2013) for negative values of H (refer to the Section 1.4.3.3 for further details).

In addition to serving as input parameters for the simulations, these results also play a crucial role in validating the wind simulation techniques reviewed in the next sections. By comparing the simulated wind fields with the characteristics observed in the analyzed data, we can assess the accuracy and reliability of the simulation methods. This validation process will help ensure that the simulated wind fields accurately capture the real-world behavior and can be utilized effectively in

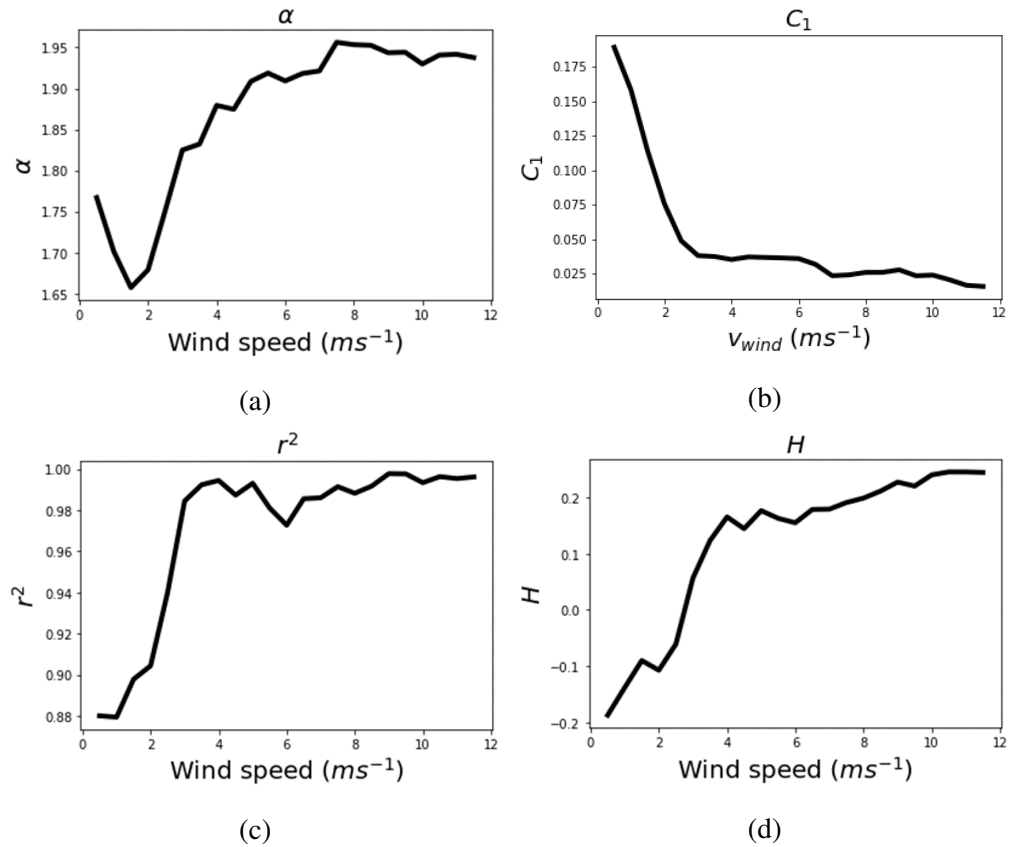


Figure 2.5: Evolution of the UM parameters with the average wind speeds retrieved for the analysis of the direct wind fields. Ensembles of 100 samples for each wind class are used. (a) shows the evolution of α , (b) shows the evolution of C_1 , (c) shows the evolution of r^2 , and (d) shows the evolution of H .

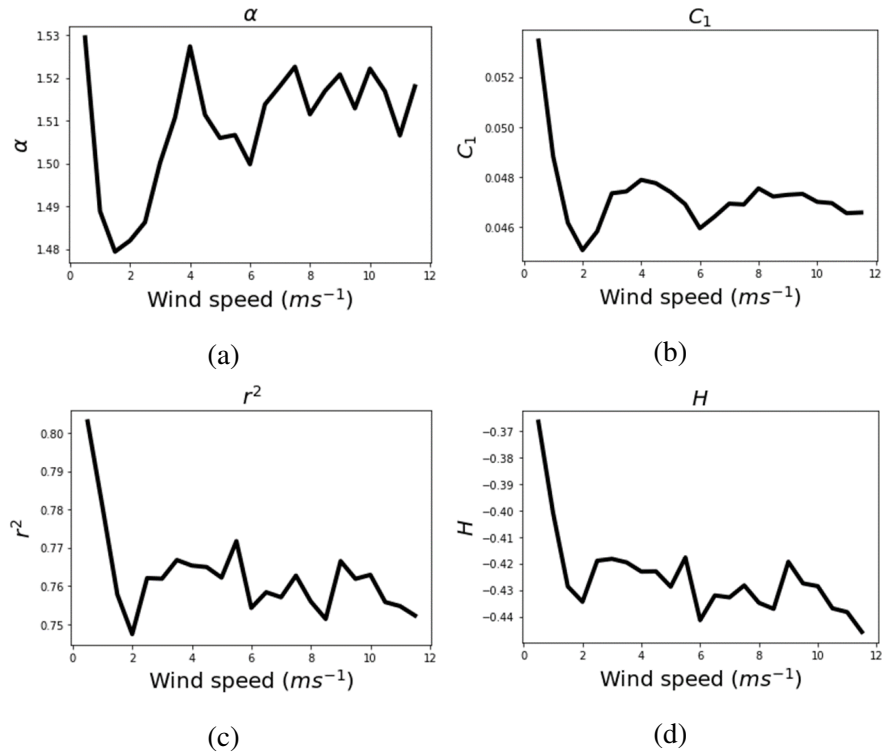


Figure 2.6: Evolution of the UM parameters with the average wind speeds retrieved for the analysis of the fluctuations of the wind. Ensembles of 100 samples for each wind class are used. (a) shows the evolution of α , (b) shows the evolution of C_1 , (c) shows the evolution of r^2 , and (d) shows the evolution of H . It is important to note that the estimation of the parameters is not very reliable since r^2 is very low.

various applications.

Following the methodology outlined in Section 1.4.3.3, a correction can be applied to achieve better scaling of the field by removing potential biases associated with H . The results are summarized in Fig. 2.7 for the wind data and in Fig. 2.8 for the fluctuations.

One notable observation is that the wind fields do not require any correction for wind speeds greater than 3.5 m/s , and the trends depicted in Fig. 2.5 are no longer apparent. That means the trends are, probably, only an effect of the negative H , which seems to be different for low winds.

However, in the case of the fluctuations, there is a significant difference after the correction. The values of α now exhibit a consistent value close to 2, suggesting a log-normal distribution (Schertzer and Lovejoy, 1987a).

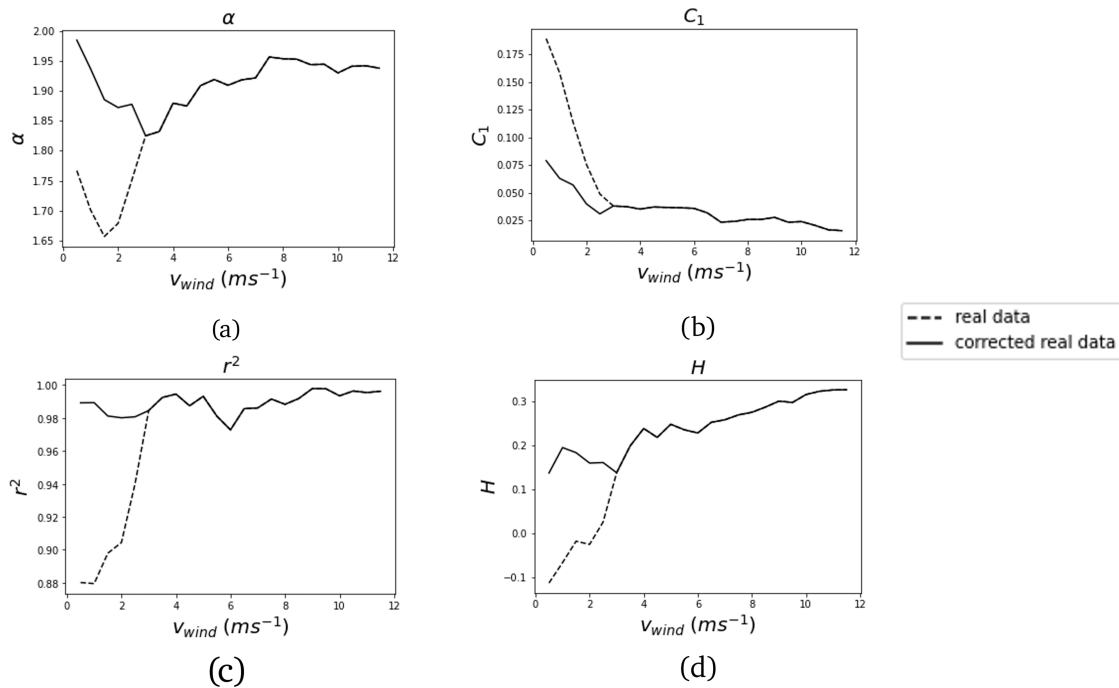


Figure 2.7: Evolution of the UM parameters with the average wind speeds retrieved for the analysis of the wind fields. Original field is plotted in dotted line and the corrected one in solid line. Ensembles of 100 samples for each wind class are used. (a) shows the evolution of α , (b) shows the evolution of C_1 , (c) shows the evolution of r^2 , and (d) shows the evolution of H .

2.2.3 Comparison with previous studies

The results obtained in the previous section differ from the traditional values reported in the literature (Schmitt et al., 1994, Lazarev et al., 1994 or Schmitt et al., 1998 among others), where

2. Wind Simulation

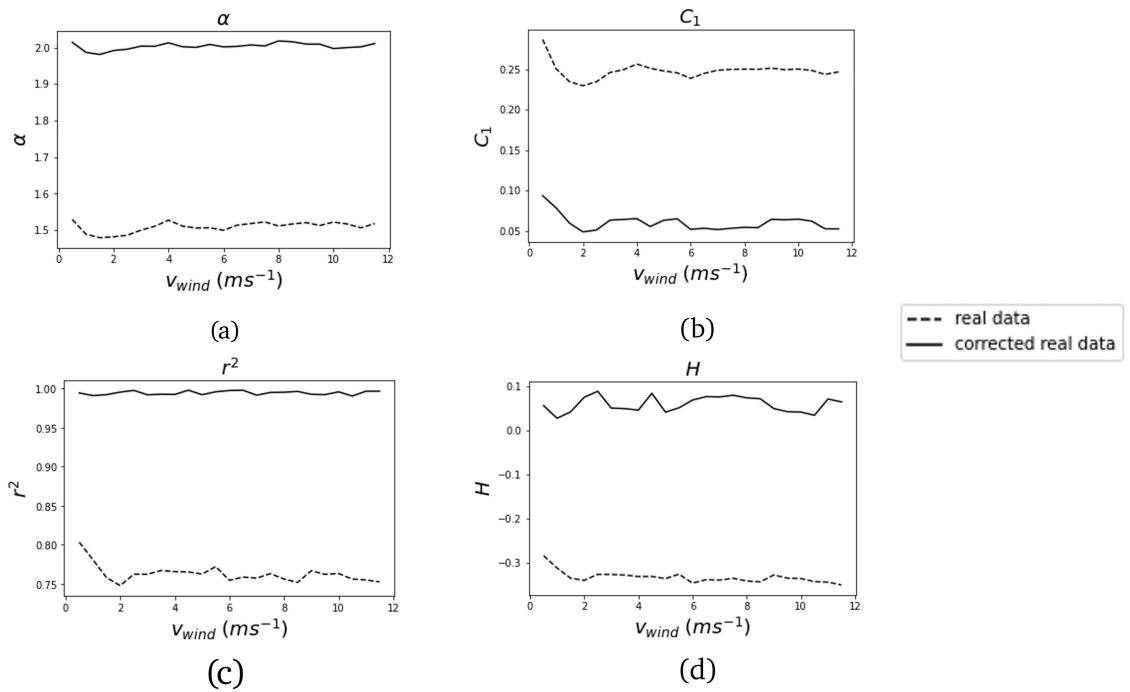


Figure 2.8: Evolution of the UM parameters with the average wind speeds for the fluctuations of the wind. Original field is plotted in dotted line and the corrected one in solid line. Ensembles of 100 samples for each wind class are used. (a) shows the evolution of α , (b) shows the evolution of C_1 , (c) shows the evolution of r^2 , and (d) shows the evolution of H .

the UM parameters for wind velocities are typically found to be $\alpha = 1.4 - 1.5$ and $C_1 = 0.05 - 0.2$ (Schmitt et al., 1994). However, it should be noted that the data analyzed in that study corresponds to much higher resolutions, ranging from hundreds of Hz to a few seconds. In that scale range, the field exhibits a theoretical $H = 1/3$ (derived from the Kolmogorov $-5/3$ power law Kolmogorov, 1941), and they obtain the parameters after fractional integration of the field to this order.

If we apply fractional integration to achieve $H = 0$ as is mentioned before, a scaling break occurs around 16 seconds, as depicted in Fig. 2.9b. When analyzing the field at smaller scales, the retrieved parameters ($\alpha = 1.43$ and $C_1 = 0.2$) are in agreement with the traditional results.

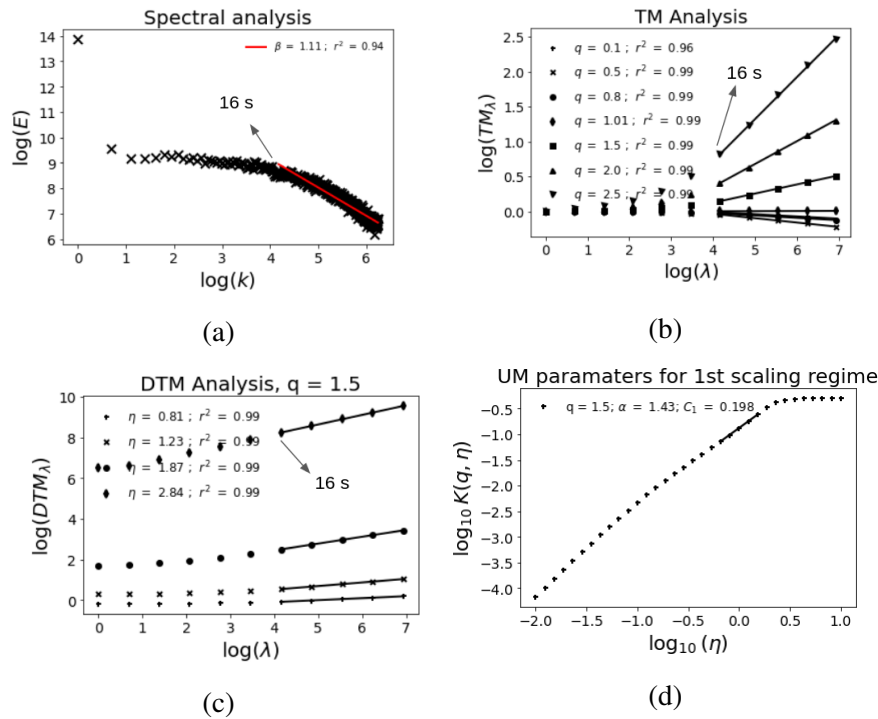


Figure 2.9: UM analysis of the ensemble used for the Fig. 2.5 but corrected to obtain $H = 0$. (a) Spectral analysis (Eq. 1.21 in log-log), (b) TM (Eq. 1.6 in log-log), (c) and (d) DTM (Eqs. 1.70 and 1.72 in log-log respectively).

Indeed, the results obtained in the previous section (Section 2.2.2) align more closely with recent studies. For example, in Fitton et al., 2011, a value of $\alpha = 1.78$ was reported for a similar range of scales.

2.3 Turbsim

One widely used software tool developed for simulation of turbulent wind fields is the Turbulent Simulator (TurbSim). TurbSim is a stochastic simulator that employs a statistical model

to generate simulated vector fields over a predefined grid of points. The software is based on the work of Veers (1988) Kelley (1992), with subsequent updates and enhancements to the code, spectral models (e.g., defined by the International Electrotechnical Commission), and the inclusion of coherent turbulent structures (e.g., the Lamar Low-Level Jet Project (LLLJP)).

Researchers across various studies have utilized TurbSim for simulating wind fields over specific areas. For instance, Ren et al., 2022 employed TurbSim to simulate wind fields over a 145x145 *m* area under different atmospheric conditions for load analysis in offshore wind turbines. Robertson et al., 2017 reconstructed full wind fields using measurement data at specific locations. Similarly, Jonkman, 2007 utilized simulated wind fields with varying mean velocities to analyze wind turbine control. The use of TurbSim for investigating wind turbine control is widespread, as demonstrated by studies such as Lackner and Rotea, 2011a, Jafarnejadsani et al., 2013, Lackner and Rotea, 2011b, and Si et al., 2014, among others. Furthermore, TurbSim is also employed to study the dynamics of wind turbines, with examples found in Jonkman, 2009b, Jonkman and Matha, 2011, and Ju, 2022, to name a few.

TurbSim uses a text input file to specify the parameters required for the simulation. These parameters are organized into different sections, providing flexibility and control over the simulation settings. For further details, please refer to the Appendix A.1 for an illustrative example of the input file structure. It is possible to find a full description of all the settings in Jonkman (2009a) and they are summarized in the following sections.

2.3.1 Runtime options

The "Runtime Options" section of the TurbSim input file serves to initialize the software and specify the desired outputs.

To initialize the pseudorandom number generator (pRNG), two seed parameters are required. The first seed is a random number within the range of -2147483648 to 2147483647. The second seed can be either a random number (between the same numbers) or one of two predefined options: "RanLux" or "RNSNLW". "RanLux" uses the SNLWIND algorithm (Veers, 1988) to generate random numbers, while "RNSNLW" utilizes Lüscher's level 3 "Luxury Pseudorandom Number" algorithm (Lüscher, 1994). It is recommended to use "RanLux" as the second seed. These random numbers are used to create random phases for the wind time series. By keeping the seeds constant, the same random phases can be reproduced in subsequent simulations.

Various outputs can be selected by setting the corresponding options to either "True" or "False" in the runtime options section of the input file. One of the main outputs is the time series data at hub heights (HH) in different formats, such as human-readable, AeroDyn, AeroDyn and Bladed, etc. Additionally, the direction of blade rotation can be specified as either clockwise (True) or not. This information is essential for the Inflow module of OpenFAST, a widely used wind turbine simulation

tool.

The last parameter in this section determines how the velocity output in the time domain is scaled when IEC spectral models (IEC, 1999) are chosen. When set to 0, the generated turbulent intensity (TI) is lower than the specified value, and the time series data are multiplied by a scaling factor to account for this discrepancy. When set to "1", each component has a different scaling factor, but the scaling factor remains constant across all points. On the other hand, when set to "2", there is independent scaling for each component, resulting in different scaling factors for each point. For a summary of these scaling options, refer to Table 2.1. Further details can be found in the appendix A.1.

Input Value	Description
0	No scaling
1	Scaling by components
2	Independent scaling

Table 2.1: List of TurbSim ScaleIEC Values, see text for more details (Jonkman, 2009a)

2.3.2 Turbine/Model Specifications

To accurately model the turbulent wind field using TurbSim, several specifications related to the wind turbine and simulation parameters need to be provided. These include the hub height, grid dimensions (width and height), and the number of points contained in the grid for both horizontal and vertical directions. Notably, TurbSim always includes a grid point at the hub height.

In the temporal dimension, the time step size is required to determine the maximum frequency for the computation of Fast Fourier Transforms (FFT) and inverse FFTs. It is recommended to set the time step size to 0.05 seconds.

Regarding the length of the simulation, it is essential to distinguish between three concepts:

- The length of analysis (AnalysisTime): This parameter determines the duration of the data analyzed by TurbSim. It is recommended to be at least 600 seconds and also influences the frequencies used for generating the output time series.
- The length of the usable time series (UsableTime): This parameter sets the length of the output data. However, it may differ slightly from the final output length due to that some software require more data. If all the AnalysisTime is used, the UsableTime parameter should be set as "ALL."
- The output time, this represents the actual length of the output time series. If UsableTime is a numerical value, TurbSim adds extra time equal to the width of the grid divided by the

average wind speed at the hub height. It is important to ensure that the AnalysisTime is greater than or equal to the OutputTime.

Additionally, TurbSim allows for simulating wind blowing at different angles, including uphill, downhill, left, or right, both vertically and horizontally.

2.3.3 Meteorological Boundary Conditions

2.3.3.1 General overview

In TurbSim, users have the flexibility to choose from a range of spectral models to simulate the meteorological boundary conditions. Table 2.2 provides a summary of the input tags and the corresponding types of spectral models that can be utilized. For more comprehensive information on these models, more details are available in section 2.3.3.2 and a full explanation can be found in Appendix G of Jonkman, 2009a .

Character Input Value	Description
IECKAI	IEC Kaimal
IECVKM	IEC von Karman
GP_LLJ	NREL Great Plains low-level jet
NWTCUP	NREL National Wind Technology Center
SMOOTH	Risø smooth terrain
WF_UPW	NREL wind farm: upwind
WF_07D	NREL wind farm: 7 rotor-diameters downwind
WF_14D	NREL wind farm: 14 rotor-diameters downwind
TIDAL	Tidal channel turbulence model (water)
API	API model for hurricane winds
USRINP	User defined using velocity spectra
TIMESR	User defined using time-series data
NONE	Steady winds (used only for testing)

Table 2.2: List of TurbSim spectral models (Jonkman, 2009a)

Certain spectral models in TurbSim require specific information, such as the IEC turbulence specification for the von Kármán and von Kármán coherent models, or the file path to user-defined time-series data or spectra.

The IEC turbulence intensity is determined based on the turbine type, with values of 1, 2, or 3 corresponding to standard cases (IEC, 1999), small turbines (IEC, 2015), and offshore wind turbines (IEC, 2019) respectively. The turbulence category according to the IEC standard (A, B, or C) can also be specified, with Category A representing the highest turbulence intensity. Alternatively,

turbulence intensity can be defined as a percentage. Furthermore, TurbSim provides the option to select the IEC turbulence model, including the Normal Turbulence Model (NTM), Extreme Turbulence Model (ETM), and Extreme Wind Speed Model (EWM) based on a 10-minute average wind speed and a recurrence period of 1 or 50 years. These models are documented in IEC, 1999.

TurbSim also supports the utilization of various wind profiles. Table 2.3 provides a summary of the input tags and the corresponding wind profile types. When the "default" argument is specified, GP_LLJ employs the JET wind profile, TIDAL uses H2L, API uses API, TIMESR uses TS when multiple points are provided, and PL otherwise. The remaining models employ the IEC wind profile. More details are given in section 2.3.3.3

Character Input Value	Description
PL	Power-law wind profile
LOG	Diabatic logarithm wind profile
H2L	Logarithmic velocity profile for MHK models
JET	Low-level jet wind profile
IEC	Power-law profile on the rotor disk; logarithmic profile elsewhere
API	API (Frøya) wind profile
USR	User-defined velocity profile
TS	Valid only with the "TIMESR" TurbModel
Default	Depend on turbulent spectral model

Table 2.3: List of TurbSim Wind profiles (Jonkman, 2009a)

As in the case of the spectral models, some wind profile models require additional arguments to be specified. For instance, the power law (PL) wind profile requires the power law exponent to be provided. The JET wind profile requires the height of the low-level jet, while the USR wind profile requires the name of the file containing the wind profile data.

Additional parameters in this section include the reference height, surface roughness, and reference wind speed. The reference height represents the height at which the reference wind speed is defined. The surface roughness is a parameter that characterizes the roughness of the underlying terrain and is used in determining the wind speed profile. The reference wind speed is the mean wind speed over the analysis time period. These default parameter values can be found in Jonkman (2009a).

2.3.3.2 Spectral models

In TurbSim, wind time series are generated using the modified Sandia method proposed by Veers (1988). This method simulates the correlated time series based on a spectral matrix S , which

captures the power spectral densities (PSDs) along the diagonal entries and the cross-spectral densities between points j and k along the off-diagonal entries.

The magnitude of the cross-spectrum is defined as follows:

$$|S_{j,k}| = Coh_{j,k}(f_m, \Delta r_{j,k}, U_{j,k}) \sqrt{S_{jj}(f_m)S_{kk}(f_m)} \quad (2.1)$$

In this equation, $Coh_{j,k}$ represents the coherence function, which is dependent on the frequency f_m , the distance between points j and k ($\Delta r_{j,k}$), and the mean wind speed at those points ($U_{j,k}$). Assuming the average phase between two points is zero, the imaginary part of the cross-spectrum is also zero. As a result, the spectral matrix can be defined solely in terms of the coherence function and the PSDs.

The spectral matrix can be expressed as the product of a transformation matrix H and its complex conjugate transpose Shinozuka and Jan (1972):

$$S(f_m) = H(f_m)H^{*T}(f_m) \quad (2.2)$$

Since the spectral matrix S is real, the transformation matrix H is constrained to be real as well, specifically $H = H^*$. When H is lower triangular, the computation can be simplified using a recursive equation, as described by Veers (1988):

$$\begin{aligned} H_{11} &= S_{11}^{1/2} \\ H_{12} &= S_{21}/H_{11} \\ H_{22} &= (S_{22} - H_{21}^2)^{1/2} \\ H_{31} &= S_{31}/H_{11} \\ &\vdots \\ H_{jk} &= (S_{jk} - \sum_{l=1}^{j-1} H_{jl}H_{kl})/H_{kk} \\ H_{jk} &= (S_{jk} - \sum_{k=1}^{j-1} H_{kl}^2)^{1/2} \end{aligned} \quad (2.3)$$

It means that the time series simulation is generated by linear combinations of independent white noise processes. The matrix H acts as a weighting factor matrix for the unitary white noise inputted. Each row gives the contribution of the inputs to a single point k , and each column gives the contribution of a single point j to all the outputs.

The independent white noise inputs are contained in a diagonal matrix X defined as:

$$X_{j,k}(f_m) = \begin{cases} e^{i\theta_{k,m}} & \text{if } j = k, \\ 0 & \text{if } j \neq k \end{cases} \quad (2.4)$$

Where θ_{km} is the phase angle. It is a uniformly random distributed variable in the range $(0, 2\pi)$ to ensure that the time series approach a Gaussian process. It depends on the point k and the frequency m .

Finally, the time series are obtained by the inverse Fourier transform of the complex Fourier coefficients given by the matrix equation:

$$V = H X 1 \quad (2.5)$$

Where 1 is $N \times 1$ vectors of ones (being N the number of output time series). Going to the summation notation of the Eq. 2.5 we can see that the purpose of this vector is only to make the operation along each column of H .

This equation can be expressed also as:

$$v_j(t_n) = \frac{1}{N_m} \sum_{m=1}^M V_j(f_m) e^{2\pi i f_m t_n} \quad (2.6)$$

where $v_j(t_n)$ is the output time series at time t_n , N_m is the total number of frequencies, and M is the number of frequencies to be included in the simulation, and $V_j(f_m)$ is the Fourier coefficient at frequency f_m for output time series j .

Turbosim posses different models to obtain the spectral matrix $S(f)$ described in the following paragraphs.

The International Electrotechnical Commission (IEC) models, as outlined in IEC 61400-1 (IEC, 1999), assume that turbulent velocity fluctuations follow a stationary random vector field with zero mean Gaussian statistics in its components. These models are applicable for neutral atmospheric stability conditions and include the Von Karman isotropic turbulence model as well as the Kaimal model for anisotropic turbulence.

The Risø smooth-terrain model (SMOOTH), developed by Højstrup (1982) and Olesen et al. (1984), provides different equations for neutral/stable and unstable flows defining the velocity spectra through the wind speed at local height. This differs from the IEC models that utilize hub-height conditions. The NREL spectral models enhance the SMOOTH model by incorporating additional

information, while the National Wind Technology (NWTCUP) Model computes the spectra by incorporating scaled versions of the SMOOTH spectra using data from the NWTC/LIST project. This project focuses on representing turbulent inflow downstream of a significant mountain, as discussed in Kelley et al., 2002.

The Great Plains model (GP_LLJ) supplements the SMOOTH spectra by incorporating peaks based on measurements from a 120 m tower equipped with a sonic detection and ranging (SODAR) instrument. This model characterizes the stable atmosphere and is detailed in Kelley et al. (2004).

The NREL Wind Farm, Upwind Model (WF_UPW) and Downwind Model (WF_14D) utilize 50 Hz wind speed measurements obtained from a 50 m tower located upwind of a large wind farm. These measurements are used to calculate corrections that enhance the SMOOTH spectra, as explained in Kelley (1992) with data from Kelly and Wright (1991). In the WF_14D model, the data is collected at a distance of approximately 14 rotor diameters from the wind turbine. While, the NREL Wind Farm, Downwind Model (WF_07D) employs the same approach as WF_14D, but the data is collected at a distance of 7 rotor diameters instead of 14, as reported in Thomson et al. (2012).

The tidal model is specifically designed for water turbulence. It supplements the SMOOTH spectral form with amplitude and shear information obtained from measurements taken in the tidally-mixed tidal boundary layer, as detailed in Thomson et al. (2012).

The API model incorporates the Frøya model spectral density (Det Norske Veritas, 2010). This model was originally created for neutral conditions in the water. The utilization of the Frøya spectrum may not be advisable in scenarios where stability effects exert a substantial influence.

The TIMESR relies on input files and uses time series analysis. It works by extracting the u , v and w components of the velocity, removing their mean values, and then subjecting them to a fast Fourier transform (FFT) to calculate spectral amplitudes and phase angles. To obtain the spectral amplitudes at the desired points, these data are interpolated using phase angles selected from a uniform distribution. These angles are correlated with those of a reference point obtained from the input time series.

Finally, the USRINP model generates uniform spectra for each component of the velocity field using a separate input file. These spectra are then scaled using the scaling factors provided in the user-defined spectra input file.

2.3.3.3 Wind profiles

This sections describes wind profiles supported by Turbsim.

The first one, the power law wind profile is expressed in Eq. 2.7, where $\bar{u}(z)$ is the mean wind

velocity at height z . $\bar{u}(z_{ref})$ is the reference velocity, z_{ref} is the reference height, and $PLExp$ is the input exponent used to calculate this profile.

$$\bar{u}(z) = \bar{u}(z_{ref}) \left(\frac{z}{z_{ref}} \right)^{PLExp} \quad (2.7)$$

The logarithmic profile, defined in Eq. 2.8, uses the surface roughness parameter $Z0$ and the stability parameter Richardson number Ψ_m (defined in Eq. 2.9) to compute the wind velocity.

$$\bar{u}(z) = \bar{u}(z_{ref}) \frac{\ln(z/Z0) - \Psi_m}{\ln(z_{ref}/Z0) - \Psi_m} \quad (2.8)$$

$$Rich = \frac{\frac{g}{\theta} \frac{\partial \theta}{\partial z}}{\left(\frac{\partial \bar{u}}{\partial z} \right)^2} \quad (2.9)$$

The IEC wind profile, used in Turbsim, combines the characteristics of both the power law and logarithmic profiles. It incorporates the power law profile to determine the wind velocity within the rotor disk, while employing the logarithmic profile for regions outside the disk. It is important to note that this profile might introduce a discontinuity at the bottom boundary of the rotor disk.

The API wind profile is expressed in Eq. 2.10, with $URef$ as the reference velocity and $RefHt$ as the reference height.

$$\bar{u}(z) = URef(1 + 0.0573\sqrt{1 + 0.15URef})\ln(z/RefHt) \quad (2.10)$$

Finally, the Low Level Jet (LLJ) wind profile is based on the LLLJP model and uses Chebyshev polynomials to calculate wind velocity, as expressed in Eq. 2.11. A plot of these wind profiles is shown in Fig. 2.10, which was generated using the TurbSim software.

$$\bar{u}(z) = \sum_{n=0}^{10} c_n \cdot T_n(z) \quad (2.11)$$

2.3.4 Non-IEC Meteorological Boundary Conditions

When utilizing a non-IEC wind profile model in Turbsim, certain additional parameters become necessary. These parameters encompass the latitude of the site, crucial for calculating the Coriolis term. Furthermore, the friction velocity over the rotor disk, the depth of the mixing layer

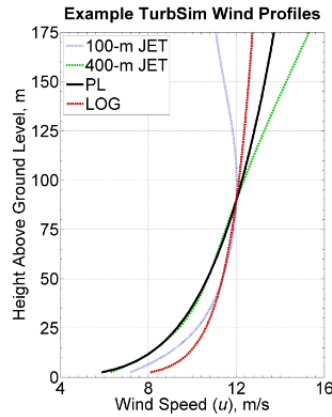


Figure 2.10: Example of wind profiles computed in TurbSim (Jonkman, 2009a)

(determined via the method proposed by Dutton et al. (1979), and the Reynolds stress components ($u'v'$, $u'w'$, $v'w'$) at the hub are also required. These parameters can be designated as "default," and for more precise values, more details are provided in Jonkman (2009a).

2.3.5 Spatial Coherence Parameters

TurbSim allows users to select from four types of spatial coherence models for each wind component. The first is the IEC model, which is based on the work of Thresher et al. (1981). The coherence functions for this model are defined by the expression:

$$Coh_{i,j} = \exp \left(-a_k \sqrt{\left(\frac{f, r}{u_{hub}} \right)^2 + (b_k, r)^2} \right) \quad (2.12)$$

Here, k subscript represents the wind component, f the frequency, r the distance between two grid points i and j , and u_{hub} represents the mean velocity at hub height. Users can define the parameters a_k and b_k or use default values (see Jonkman, 2009a for more details).

The General model extends the IEC model by including the term $\left(\frac{r}{z_m} \right)^{CohExp}$ from Solari's coherence definition (Solari, 1987), which considers the mean velocities of the points instead of the hub height velocity. The coherence function for this model is defined by:

$$Coh_{i,j} = \exp \left(-a_k \left(\frac{r}{z_m} \right)^{CohExp} \sqrt{\left(\frac{f, r}{u_{hub}} \right)^2 + (b_k, r)^2} \right) \quad (2.13)$$

Here, u_{hub} is the mean velocity of the two points, z_m is the average height, and $CohExp$ is

the coherence exponent. If $CohExp = 0$, the General model simplifies to the IEC model. The coherence exponent influences the rate at which the coherence function diminishes with distance. A smaller value of 'CohExp' leads to a slower decay, whereas a larger value accelerates the decay. Typically, a value of 0.5 is employed for $CohExp$ corresponding to the $-5/3$ power-law decay of the Kolmogorov turbulence spectrum.

The API model, based on Det Norske Veritas (2010) for wind simulations over water, is only applied to the u component of the wind and is defined by:

$$Coh_{i,j} = \exp\left(-\frac{1}{U_0} \sqrt{\sum_{k=1}^3 A_k^2}\right) \quad (2.14)$$

Here, U_0 is the reference wind speed, and A_k is a parameter that depends on the height of the two points and a set of parameters (see Jonkman, 2009a for more details).

Finally, users can select NONE as the coherence model, which satisfies the coherence condition with the expression:

$$Coh_{i,j} = \begin{cases} 1 & \text{if } i = j, \\ 0 & \text{if } i \neq j \end{cases} \quad (2.15)$$

2.3.6 Coherent Turbulence Scaling Parameters

The final section of the Turbsim input file pertains to situations where the Richardson number exceeds 0.05. It specifies the type of coherent events (summarized in Table 2.4) and the path where the corresponding files are stored.

Character Input Value	Description
DNS	Direct Numerical Simulation (DNS)
LES	Large Eddy Simulation (LES)
Random	Randomly chooses between LES and DNS

Table 2.4: List of TurbSim type of coherence events (Jonkman, 2009a)

This section also provides information about the properties and locations of the coherent structures. The disturbance scale parameter determines the size of the structure relative to the rotor disc, while the lateral and vertical location parameters determine the position of the structure in space. The minimum start time parameter specifies the earliest time step at which the structures can occur. An example of these coherent structures is illustrated in Figure 2.11.

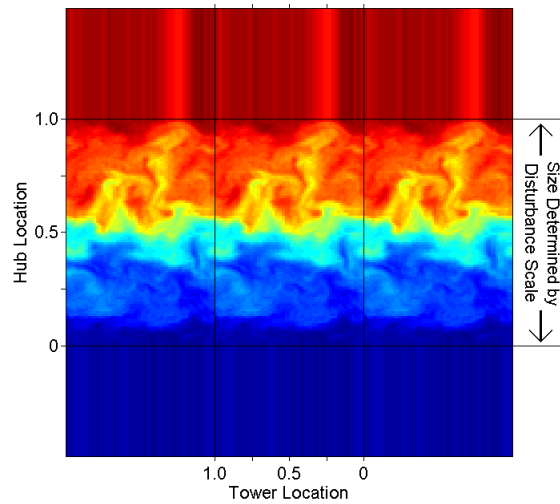


Figure 2.11: Illustration of coherent structures (Jonkman, 2009a)

2.3.7 Examples of use

In this study, we employ Turbsim for two primary objectives. Firstly, OpenFAST requires wind input data in a format compatible with the inflow module. For that reason, we utilize Turbsim to transform the simulated wind fields, whether scalar or vector fields, into a suitable format readable by OpenFAST. This involves providing Turbsim with the time series data for each point on the grid, enabling the adaptation of the wind fields to the required format.

Furthermore, as discussed before, Turbsim offers the capability to simulate turbulent wind fields, which we also explore in this study. Leveraging the available data from the anemometers located at known positions, we can utilize the time series recorded at these points to reconstruct the wind fields across the entire area encompassing the swept area of interest. In the following paragraphs we will investigate the properties of this second objective reconstructing an ensemble of 100 samples, using the data from the anemometer.

Fig. 2.12 provides an overview of the wind fields simulated using the Turbsim software. In the runtime options, the selection of "RanLux" for the second random seed and an anti-clockwise rotation is made. Since input time series are used, the ScaleIEC is not required in this case. Moving to the Turbine/Model Specifications section, a grid with a size of 27×27 points is chosen, covering a square area with a side length of 90 meters centered at a hub height of 78 meters. The AnalyseTime and UsableTime are set to 1024 seconds, with a time step of 4 seconds. The vertical and horizontal angles are computed using the wind components at the hub height. In the Meteorological Boundary Conditions section, the turbulence model "TIMESR" is selected, which is based on the anemometer time series. The wind profile used is the PowerLaw, with the reference height considered to be the hub height. The URef value represents the average velocity at this reference

2. Wind Simulation

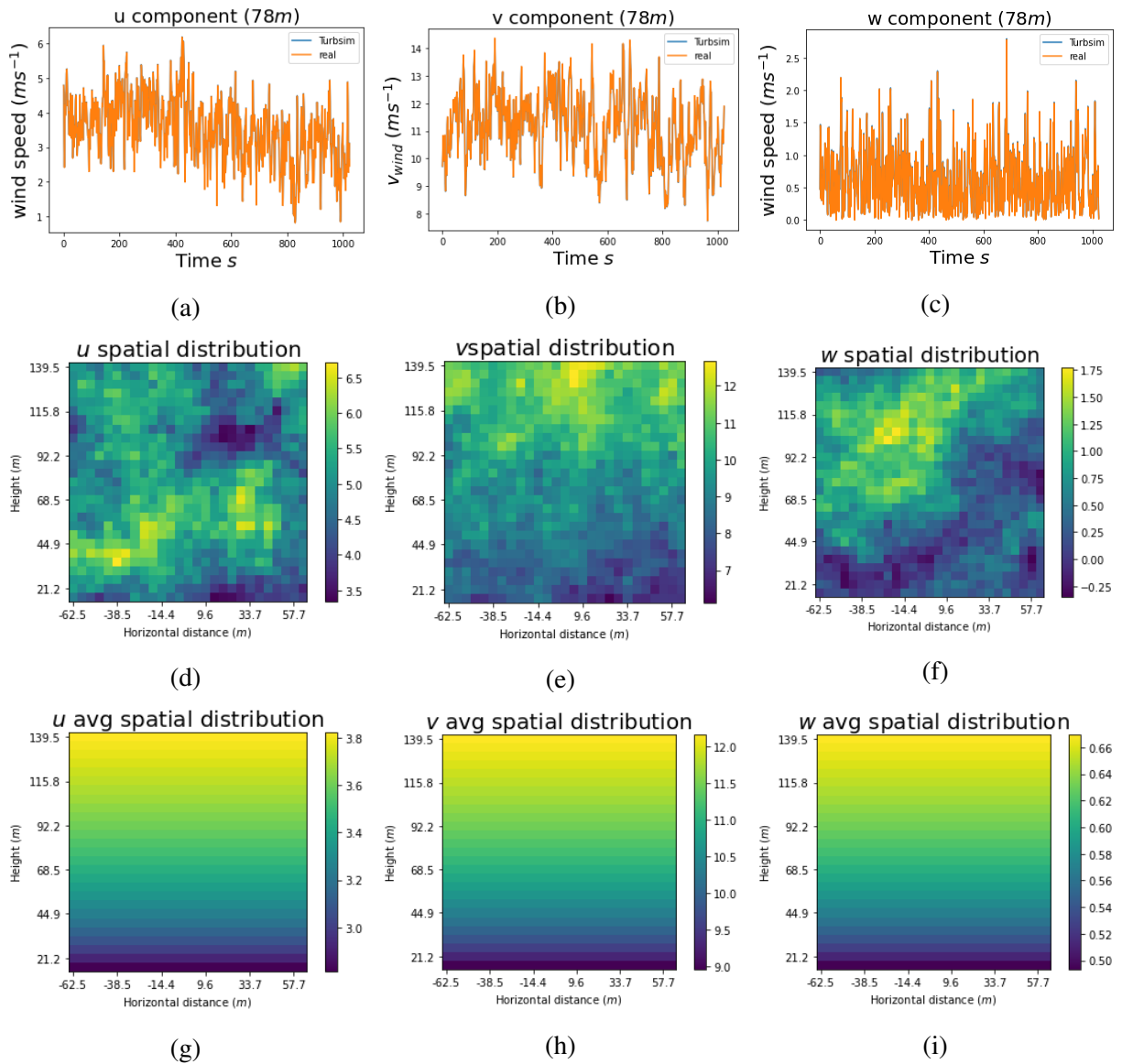


Figure 2.12: Example of Wind field simulated with Turbsim. First row is a comparison between the anemometer data and turbsim data at anemometer height (78m) ((a) u, (b) v, and (c) w), second row is an example of the spatial distribution of the wind components at time 10s ((d) u, (e) v, and (f) w), and the last row is the spatial distribution of the average wind speed in time ((g) u, (h) v, and (i) w).

height. For the remaining sections, the default values are selected for simplicity. We use a event recorded on 20/12/2020 during the RW_Turb measurement campaign (Section 2.2)

One noticeable observation is that the velocity input and the velocity obtained from the software are consistent for all three components, as depicted in Figs. 2.12a, 2.12b, and 2.12c at hub height. Examining the other figures, we can observe that all three components exhibit coherent structures in both space and time as shown in Figs. 2.12d, 2.12e, and 2.12f. The quantitative analysis of these structures is carried out after using the UM analysis tools presented in Section 2.6. Additionally, a too smooth wind shear is evident in all three components, with higher values observed at greater heights, as illustrated in Figs. 2.12g, 2.12h, and 2.12i.

It appears that upon conducting further analysis some limitations become evident in the realism of the simulated wind fields. The next paragraphs gives a initial illustration of the limitations which will be addressed in the next section (Section 2.6)

When we study a single point, as shown in Fig. 2.13, it becomes apparent that the scaling of the field is poor and exhibits a lot of spreading in the spectra. This outcome is typically expected when using a small number of samples, which is not the case here. It is likely to come from the fact the simulated points potentially replicate the behavior of the anemometer time series used as input.

We replicate this analysis for the time series of each grid point, in order to observe the spatial distribution of the UM parameters (Fig. 2.14). Although some spatial variability is initially observed in Fig. 2.14, particularly in the presence of a wind shear trend as seen in Figs. 2.14a and 2.14b, closer examination reveals that this variability is minimal when the magnitude of the variation is taken into account.

These observations suggest that there may be limitations in the ability of the Turbsim software to accurately capture the full spatial variability and scaling behavior of the wind fields. It is important to consider these limitations when interpreting the results and assessing the realism of the simulated wind fields for specific applications. Further analysis and evaluation may be necessary to improve the accuracy and reliability of the simulations.

2.4 Simplistic approach

2.4.1 Theoretical background

The first idea of non-Gaussian wind simulation involves the stochastic reconstruction of the wind field from a point measurement based on well-established scaling laws (Schertzer and Lovejoy, 1985a, Schertzer and Lovejoy, 1987a, Schertzer and Lovejoy, 1989, Lazarev et al., 1994 among others), following the methodology presented in Gires et al. (2022b). The wind fields are simulated,

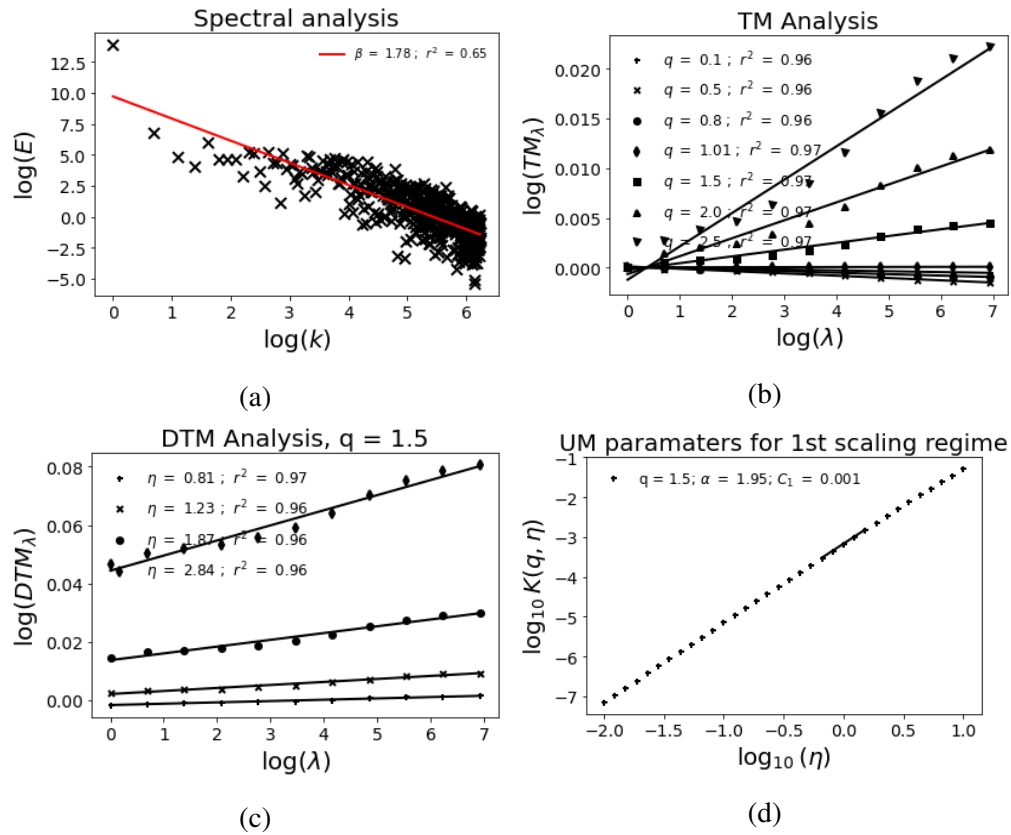


Figure 2.13: Analysis of one of the points of the Fig. 2.14 situated at $x=-24m$ and $z=123.31m$. (a) Spectral analysis (Eq. 1.21 in log-log), (b) TM (Eq. 1.6 in log-log), (c) and (d) DTM (Eqs. 1.70 and 1.72 in log-log respectively). It consists in an ensemble of 100 samples and 1024 time steps.

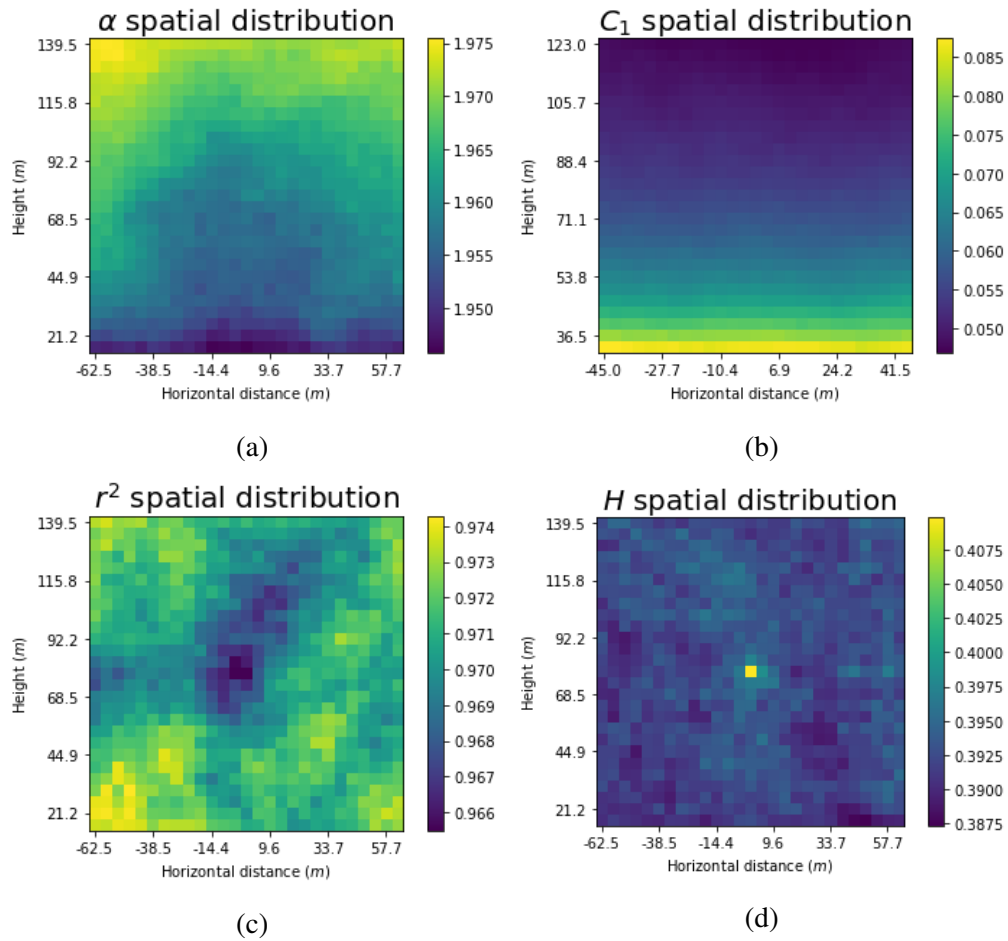


Figure 2.14: Spatial distribution of UM parameters retrieved on the analysis of the Turbsim wind fields. (a) α , (b) C_1 , (c) r^2 , and (d) H . The parameters are retrieved on an ensemble of 100 samples using the anemometers time series recorded on 20/12/2020. See the text for description of the specifications of the simulation

in a very simplistic approach (oversimplified, see section 2.4.3 for more details), at any location adding the product of a prefactor, a random UM fields (both ε and ϕ), and the distance increments raised to the respective scaling exponents to the data obtained from the available anemometer point. Under these assumptions, the initial 3D wind field model can be expressed as:

$$\begin{aligned} u(x+\Delta x, y+\Delta y, z+\Delta z, t) &= u(x, y, z, t) + c_{\varepsilon_x} \varepsilon_x(x+\Delta x, y+\Delta y, t)^{a_h} \Delta l^{H_h} + c_{\phi_x} \phi_x(z+\Delta z, t)^{a_v} \Delta z^{H_v} \\ v(x+\Delta x, y+\Delta y, z+\Delta z, t) &= v(x, y, z, t) + c_{\varepsilon_y} \varepsilon_y(x+\Delta x, y+\Delta y, t)^{a_h} \Delta l^{H_h} + c_{\phi_y} \phi_y(z+\Delta z, t)^{a_v} \Delta z^{H_v} \\ w(x+\Delta x, y+\Delta y, z+\Delta z, t) &= w(x, y, z, t) + c_{\varepsilon_z} \varepsilon_z(x+\Delta x, y+\Delta y, t)^{a_h} \Delta l^{H_h} + c_{\phi_z} \phi_z(z+\Delta z, t)^{a_v} \Delta z^{H_v} \end{aligned} \quad (2.16)$$

Where u , v , and w are the 3D wind components, $l = \sqrt{x^2 + y^2}$ is the traditional horizontal distance to the anemometer, ε is the kinetic energy flux with a scaling exponent $a_h = 1/3$ and ϕ is the buoyancy force flux density with scaling exponent $a_v = 1/5$. H_h and H_v are the anisotropic exponents obtained from the literature. In the horizontal case, $H_h = 1/3$ (Kolmogorov, 1941 and Obukhov, 1941) and in the vertical case, $H_v = 3/5$ (Bolgiano Jr, 1959 and Obukhov, 1959). More details can be found in section 1.3.1.1. For more details about the generator, please refer to the UM simulation section (section 1.3). Kinetic energy and buoyancy force fluxes are considered independent.

Initially, we started with the isotropic case adapting the expressions of Eq. 2.16 to:

$$\begin{aligned} u(x+\Delta x, y+\Delta y, z+\Delta z, t) &= u(x, y, z, t) + c_{\varepsilon_x} \varepsilon_x(x+\Delta x, y+\Delta y, z+\Delta z, t)^{a_h} \Delta l^{H_h} \\ v(x+\Delta x, y+\Delta y, z+\Delta z, t) &= v(x, y, z, t) + c_{\varepsilon_y} \varepsilon_y(x+\Delta x, y+\Delta y, z+\Delta z, t)^{a_h} \Delta l^{H_h} \\ w(x+\Delta x, y+\Delta y, z+\Delta z, t) &= w(x, y, z, t) + c_{\varepsilon_z} \varepsilon_z(x+\Delta x, y+\Delta y, z+\Delta z, t)^{a_h} \Delta l^{H_h} \end{aligned} \quad (2.17)$$

where l becomes $\sqrt{x^2 + y^2 + z^2}$

Finally as we are interested on the simulation of the wind fields in a grid over a 2D plane which cover the swept area of the wind turbine blades, we reduce the expressions to a 2D case in Eq. 2.18 using only axis x and z .

$$\begin{aligned} u(x+\Delta x, z+\Delta z, t) &= u(x, z, t) + c_{\varepsilon_x} \varepsilon_x(x+\Delta x, z+\Delta z, t)^{a_h} \Delta l^{H_h} \\ v(x+\Delta x, z+\Delta z, t) &= v(x, z, t) + c_{\varepsilon_y} \varepsilon_y(x+\Delta x, z+\Delta z, t)^{a_h} \Delta l^{H_h} \\ w(x+\Delta x, z+\Delta z, t) &= w(x, z, t) + c_{\varepsilon_z} \varepsilon_z(x+\Delta x, z+\Delta z, t)^{a_h} \Delta l^{H_h} \end{aligned} \quad (2.18)$$

where l becomes in this case to $\sqrt{x^2 + z^2}$

The kinetic energy flux, ε , is simulated as a UM field using discrete cascades. For that, first we analyse the data recorded by the two anemometers in the RW-Turb measurement campaign (section 2.2) located at a vertical distance of approximately 33 meters in order to obtain the UM parameters required as input for the simulation. Specifically, looking at Eq. 2.18 we decide to analyse the difference between the data from both anemometers since the terms c_ε and Δl^{H_h} act as a prefactors and they do not change the properties of the field. Fig. 2.15 shows an example of this analysis.

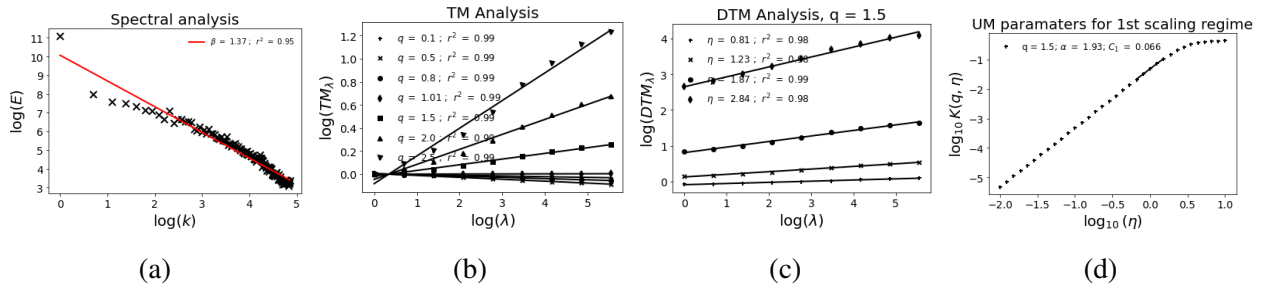


Figure 2.15: Illustration of analysis of the differences between the two anemometers. (a) Spectral analysis (Eq. 1.21 in log-log), (b) TM (Eq. 1.6 in log-log), (c) and (d) DTM (Eqs. 1.70 and 1.72 in log-log respectively). The studied data consists of an ensemble of 100 samples with 256 points covering the range of scales 4-1024s. Input data is a 17 min event recorded on 20/12/2020.

Once the inputs are known we can obtain a field with positive and negative values using a standard “complex trick” stated in Schertzer and Lovejoy (1995):

$$X = \text{Real} [\log X_1 + iX_2] \quad (2.19)$$

Where X_1 and X_2 are two fields simulated using the same properties.

Finally, we use the data of the two anemometers in order to obtain the prefactor c_ε empirically reformulating Eq. 2.18 as:

$$c_\varepsilon = \frac{|u(x + \Delta x, z + \Delta z, t) - u(x, z, t)|}{\varepsilon^{ah} \Delta l^{H_h}} \quad (2.20)$$

To select the c_ε value, we simulate a set of 100 samples of ε fields for different periods (17-minute intervals). Finally we calculate c_ε .

To select the value c_ε , we simulate an ensemble of 100 samples of ε fields for different periods (intervals of 17 minutes). Finally we calculate c_ε as the average of the results obtained with Eq. 2.20 using each of the fields and the data of the two anemometers. Fig. shows an illustration of the temporal evolution of the this parameter. For the following, we set $c_\varepsilon = 1.15$ which is the average of the whole time series.

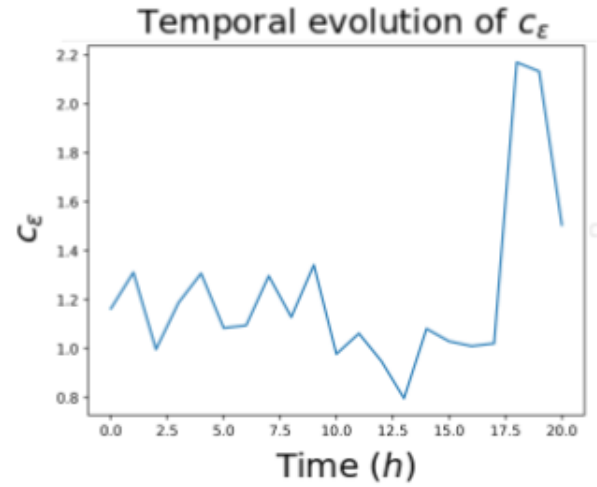


Figure 2.16: Temporal evolution of average c_ϵ computed using Eq. 2.20 and 100 samples for each time interval (17 minutes).

2.4.2 Example of simulations

This methodology enables the simulation of the wind field across all points in a grid. An example (using a 17 min event recorded on 20/12/2020, with UM parameters $\alpha = 1.93$, $C_1 = 0.066$ (Fig. 2.15) and $c_\epsilon = 1.15$ (as mentioned in previous section)) is illustrated in Fig. 2.17, which displays three consecutive time steps of the wind simulation. It can be observed that each point in the grid exhibits different values, but there are no extreme differences from one time step to the next. Moreover, this methodology allows for the generation of an ensemble of wind speed time series at all points in the grid. Fig. 2.18 provides an example of such an ensemble of 10 samples at three points located at increasing distances from the anemometer data (centered on the grid). The points are represented by blue, green, and red lines, corresponding to distances of 3 meters (blue), 24 meters (green), and 45 meters (red), respectively (as the field is isotropic the distance can be taken in any direction). From this figure, it is visible that as the distance from the anemometer data increases, the differences between the simulated field and the original data also increases, as it is expected.

To assess the performance of the model, we conducted an ensemble simulation consisting of 100 samples. For each sample involved, we compute wind time series in each point over a grid with 27×27 pixels, covering a square area of 90 meters on each side. The length of the simulated time series was set to 17 minutes, which is close to the typical 10 min average time used in wind power production industry (Burton et al., 2011, among others).

To validate the model's performance, we conducted two types of analysis. The first type involved a statistical analysis, calculating the 10th, 50th, and 90th percentiles of the wind velocity

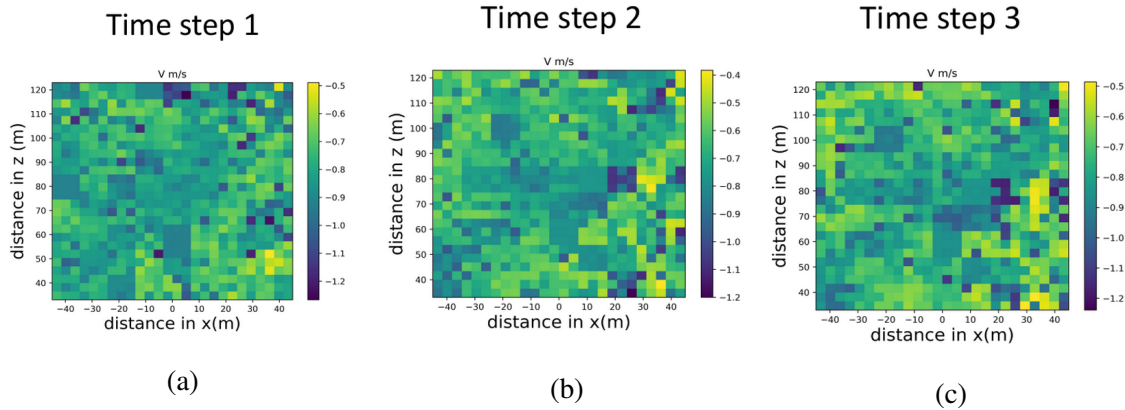


Figure 2.17: Spatial distribution of wind field on the 3 consecutive time steps simulated using Eq. 2.18 using a 17 min event recorded on 20/12/2020

and wind increments. Fig. 2.19a and 2.19b provide illustrations of these percentiles. Fig. 2.19 shows that as the distance from the anemometer increases, both the wind increments (Fig. 2.19b) and the wind velocity (Fig. 2.19a) increase. We compared the average difference between the data from the two anemometers located at different heights and found approximately $0.78 \text{ m}\cdot\text{s}^{-1}$ which is similar to the $0.8 \text{ m}\cdot\text{s}^{-1}$ found for the difference between the anemometer and simulation data (computed at the distance between the anemometers).

The second type of analysis conducted to validate the model is a UM analysis (section 1.4). For this analysis, we performed it on the ensemble time series at each pixel of the grid. This approach allows us to compute the spatial distribution of the UM parameters and compare them with the parameters obtained from the real data. Results are displayed in Fig. 2.20 for the same event that started on 20/12/2020. The UM parameters obtained from the anemometer data were $\alpha = 1.93$ and $C_1 = 0.009$. The simulated fields showed a maximum difference of 0.02 with respect to α and 0.07 with respect to C_1 . Despite these small differences, it is possible to see a radial trend in the distribution of the parameters.

2.4.3 Limitations

It is important to acknowledge that while this model serves as a foundation for creating a 3D wind field model with anisotropy (even if only the isotropic case is used in the previous sections), it is inherently limited by the numerous simplifications it employs. They are described in Gires et al., 2022b and are summarized here. Consequently, the model may not capture the full complexity of real-world wind fields.

In this simplistic simulation, we use a discrete scalar cascade, which introduces its own limitations, notably the non translation invariance issue (Gires et al., 2020). It also forces us to oversim-

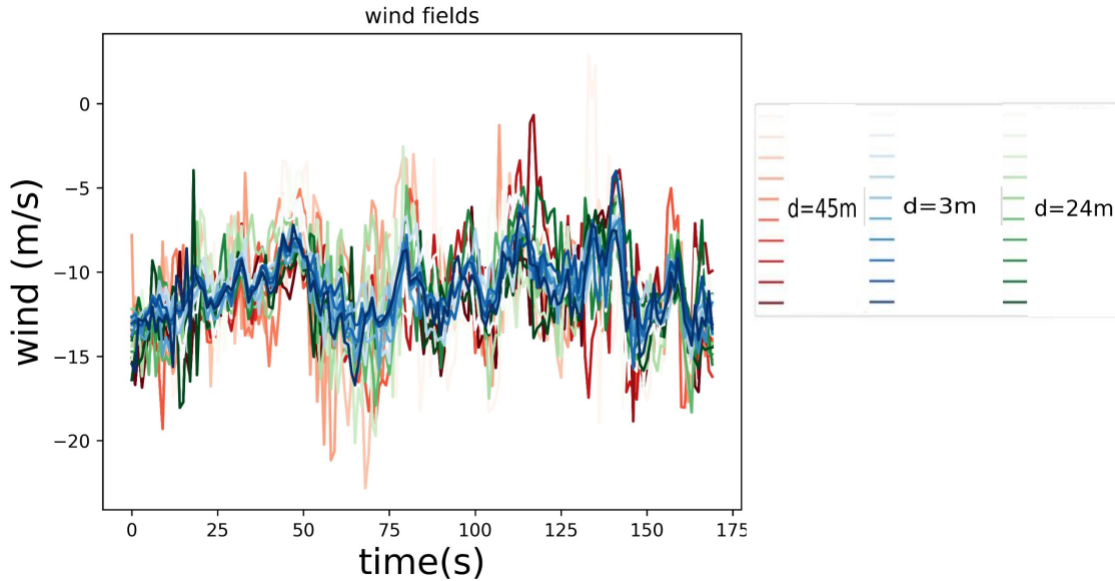


Figure 2.18: Ensemble of 10 wind time series at 3 different distances from available anemometer location. 3 meters (blue), 24 meters (green), and 45 meters (red) using a 17 min event recorded on 20/12/2020

plify the concept of general scaling invariance (GSI).

The flux density ε is defined only along three independent directions (ε_x , ε_y , and ε_z), which is a strong assumption because it should be done in all direction with correlated components. In addition, Eqs. 2.16 to 2.18 replace equalities in distribution with deterministic equalities, oversimplifying the dynamics of the system.

Assuming independence between ε and ϕ introduces a second isotropic scaling, which results in a linear crossover when changing scales. However, both density fluxes are considered at the simulation resolution, rather than at the pair resolution scale. This introduces a statistical bias in the simulation. Additionally, considering them at arbitrary locations ($x + \Delta x$, $y + \Delta y$, and $z + \Delta z$) introduces an asymmetry that negatively impacts the simulation.

Regarding time scales, all time steps are assumed to be independent, except for the empirical velocity measured by the 3D anemometer.

The inclusion of scalar anisotropic cascades may address some of these issues, but to overcome all limitations, an extension to vector fields (Schertzer and Tchiguirinskaia, 2015 and Schertzer and Tchiguirinskaia, 2020) will be necessary as it is discussed in Section 1.3.4.

2. Wind Simulation

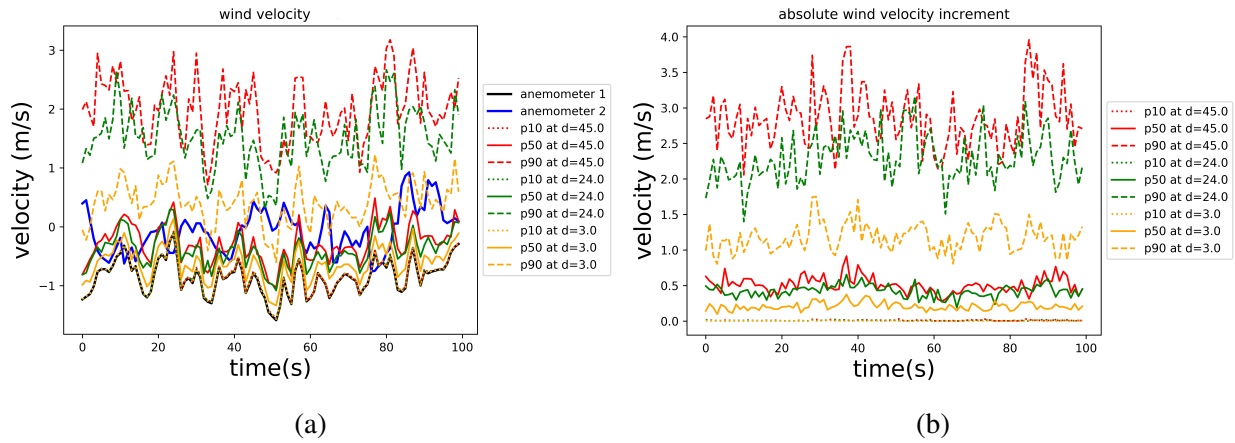


Figure 2.19: Percentiles 10, 50 and 90% of (a) simulated wind time series and of (b) Wind increments at different distances from anemometer data using a 17 min event recorded on 20/12/2020

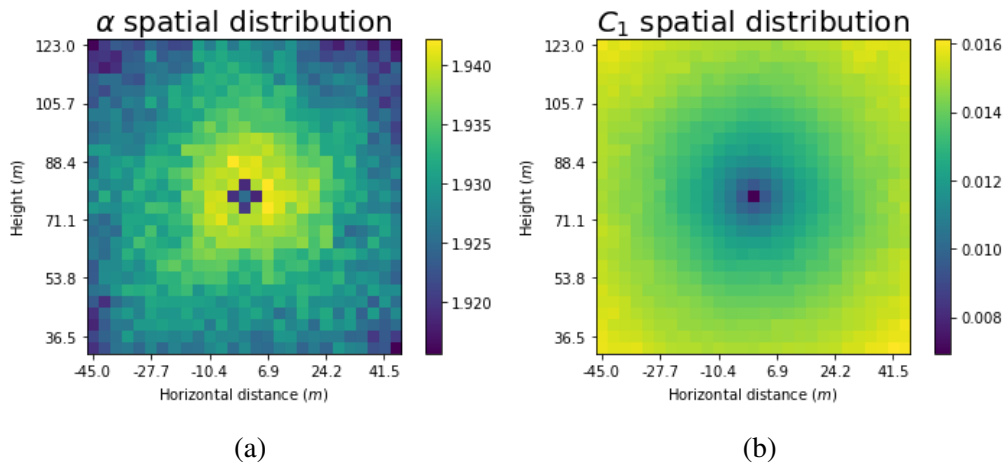


Figure 2.20: Spatial distribution of the UM parameters retrieved on the analysis of wind fields simulated with the help of the simplistic approach using a 17 min event recorded on 20/12/2020. (a) α and (b) C_1 .

2.5 The Fractionally Integrated Flux (FIF)

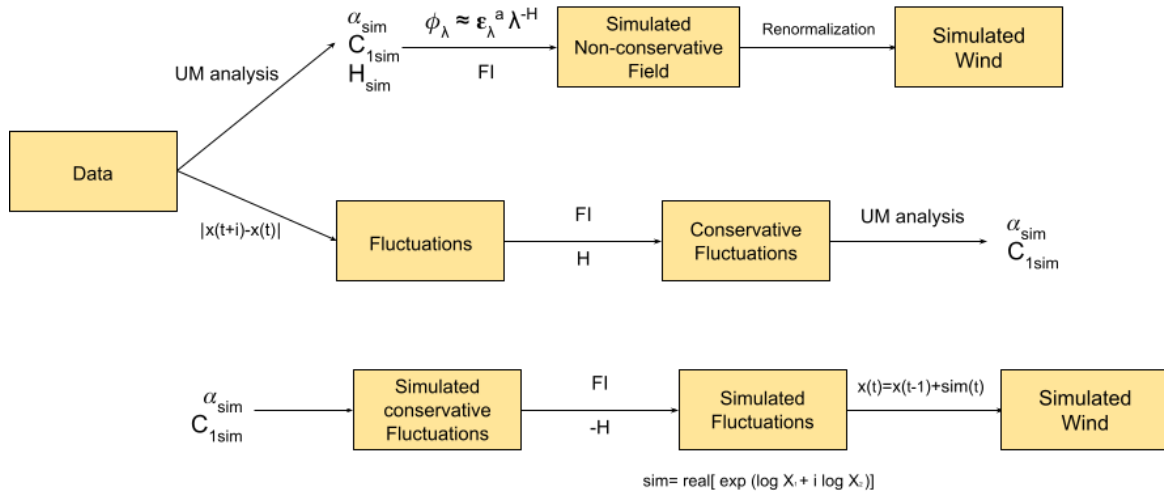


Figure 2.21: Scheme of the process followed to simulate wind fields using FIF approaches

For the simulation of the wind fields, we have developed two different approaches based on the same principles, in which the wind fields (or their fluctuations) are simulated as non-conservative fields (as discussed in the section 1.3.3.3 and Schertzer and Lovejoy, 1997). Both approaches start with the data from the RW-Turb measurement campaign as the initial point. Fig. 2.21 shows a descriptive scheme of both approaches which detailed in the following sections.

2.5.1 FIF on direct fields

The first approach is traditionally known as Fractionally Integrated Flux (FIF) (Schertzer and Lovejoy, 1997). First, it is needed to analyse the data (from the anemometer) in order to obtain the parameters required in the simulation as inputs (α , C_1 , and H , while a is set as $1/3$ as it is suggested in Kolmogorov, 1941). Once the field is simulated using those parameters, it is re-normalized to obtain a field with the desired mean. Fig. 2.22 shows an example of time series of fields simulated for target velocity equal to 9.5 m s^{-1} .

This methodology allows us to reproduce the properties that were retrieved in the analysis (Fig. 2.5). For the comparison we simulate an ensemble of 100 samples using 256 points in temporal dimension (to cover the range of scales 4 - 1024 seconds). Fig. 2.23 illustrates the comparison between the simulation and real data for each average velocity interval. For the correction of the fields we use the methodology reviewed in Section 1.4.3.3.

One notable observation is the good agreement between the simulated and real data for α and C_1 (Figs. 2.23a and 2.23b), both before and after the correction, specially after the correction, for

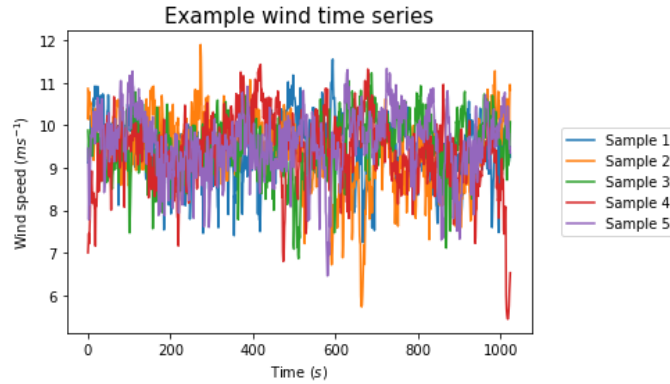


Figure 2.22: Example 5 realisations of five 17-minutes wind fields simulated using FIF approach for target average wind speed 9.5 ms^{-1} . The input parameters are retrieved from the analysis an ensemble of 100 samples of wind fields with 9.5 ms^{-1} average velocity.

all range of velocities. The r^2 (Fig. 2.23c) values also exhibit good agreement after the correction, while before the correction the simulated fields exhibit poor scaling (which is expected for the value of H inputted in the simulation). Finally the value of H (Fig. 2.23d) presents a better agreement before the correction (as it is imposed to be), since the simulated fields after the correction present $H \approx 0$ (consistent with theoretical results).

2.5.2 Reconstruction of Fluctuations (RoF)

The second approach is also based in the FIF approach, however, it differs from the first approach in terms of its objective. While the first approach aims to simulate directly wind fields, the focus of this second approach is to simulate their fluctuations and subsequently "reconstruct" the wind fields using these fluctuations. To initiate this approach, the wind field data obtained from the anemometer is used, and the fluctuations are computed. To ensure that we are working with a conservative field, a fractional integration is performed on the fluctuations data (Schertzer and Lovejoy, 1997, Fitton, 2013).

Once the fractional integration is performed, we follow the same methodology as the first approach. We use the parameters retrieved from the UM analysis of these conservative fluctuations, and $a = 1/3$, but in this case, the value of H is set to 0 since the field is conservative. The field is then fractionally differentiated (with the same order as the integration) to obtain the simulated fluctuations. In order to simulate a field with positive and negative values we use Eq. 2.19. See bottom part of Fig. 2.21 and Fig. 2.24 for an illustration of the process

After simulating the fluctuations, we can reconstruct the direct wind fields by applying the inverse process, i.e. the field at the time t is computed adding the simulated field to the field at time $t - 1$ and doing it for all the time steps. However, a crucial aspect is determining the initial

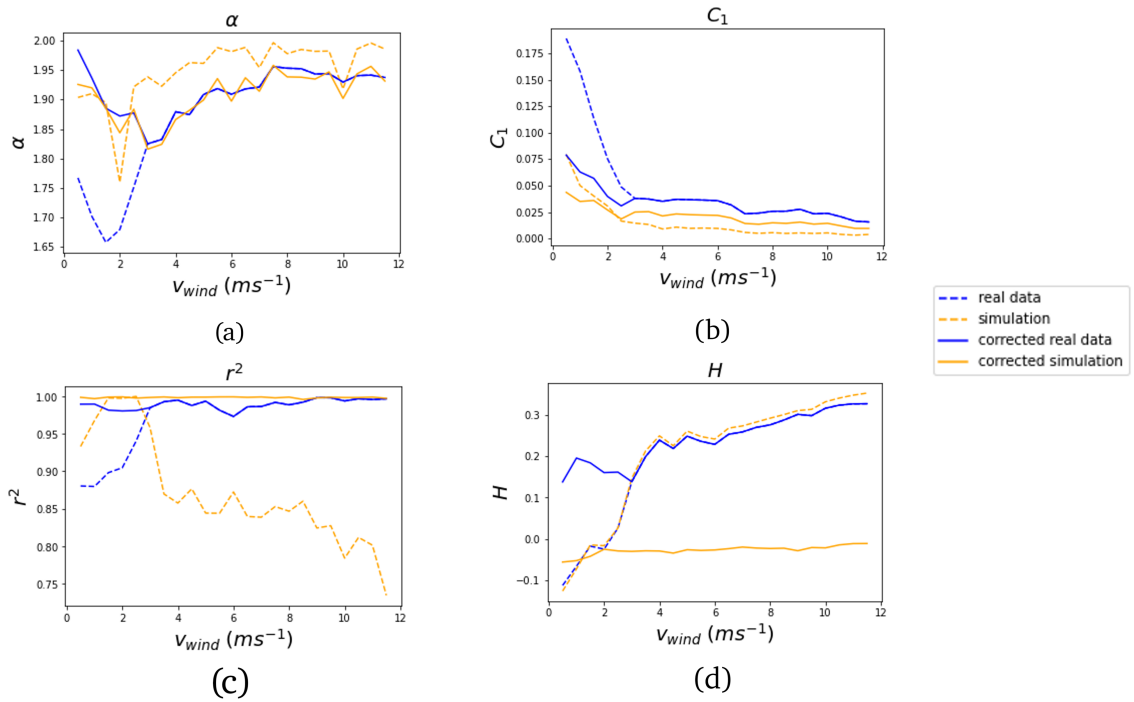


Figure 2.23: Evolution of the UM parameters with the wind speeds in the simulation using the FIF approach. Real fields are plotted in blue and simulated one are plotted in orange. Direct fields are plotted in dashed lines and corrected fields using methodology reviewed in 1.4.3.3 are plotted in solid lines. Ensembles of 100 samples for each wind class are used. a) shows the evolution of α , b) shows the evolution of C_1 , c) shows the evolution of r^2 , and d) shows the evolution of H .

state of the field. Given that the average of the field's fluctuations is zero by definition, we choose to initialize the field using the desired average wind speed that we aim to achieve in the simulation. Fig. 2.24 shows an example of each step of the process for simulating wind fields with 9.5 ms^{-1} average velocity.

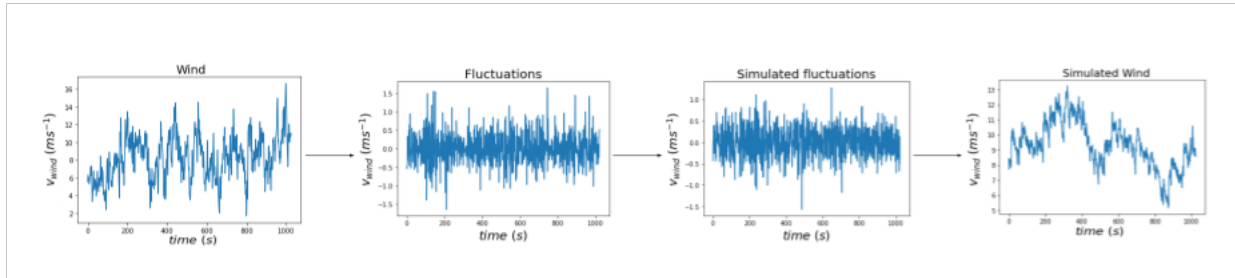


Figure 2.24: Example of each step of the process used for the simulation of the wind field using RoF approach. In this example a wind fields with 9.5 ms^{-1} average velocity is used.

Fig. 2.25 presents a comparison between the simulation and the real data, showing a good agreement between all the parameters with errors lower than 10% (C_1 error is bigger due to the small values of the parameter). This indicates that the second approach is also capable of reproducing the properties observed in the analysis of the fluctuations of the wind field. It is important to note that Fig. 2.25c exhibits poor scaling behavior. However, this is actually the expected outcome, considering that the field was fractionally integrated with a negative value of H (as described in Section 1.4.3.3) in an attempt to replicate the properties of fluctuations. The poor scaling behavior in this case is a good agreement between the simulated field and the real field.

For the comparison we use again a 100 samples ensemble of time series with 256 points in the temporal dimension (as in Section 2.5.1). This comparison is showed in Fig. 2.26 which once again demonstrates the good agreement between the simulation and the real data after applying the necessary corrections. This approach shows results slightly worse than with the previous approach. For parameter α (2.26a), the simulated field exhibits similar values than the real one after 3.5 ms^{-1} while for C_1 (2.26b) there is a good agreement in all range of velocities. The scaling behaviour (2.26c) is similar to the one found in the FIF approach. Finally the parameter H (2.26d) shows a higher values for the simulated field, after the correction, again the values tends to 0 (which is consistent with the simulations). Furthermore, initializing the process with the target average wind speed enables to retrieve the the desired results as Fig. 2.27 shows.

This methodology can be applied to various applications beyond wind field reconstruction. For instance, it can be used for stochastic nowcasting extending the existing time series based on known initial conditions. An example of this functionality is illustrated in Figure 2.28, in the panel Fig. 2.28a only one example is shown while in the Fig. 2.28b 5 different scenarios are plotted to illustrate the variability between samples. In this case, the simulated field utilizes the properties

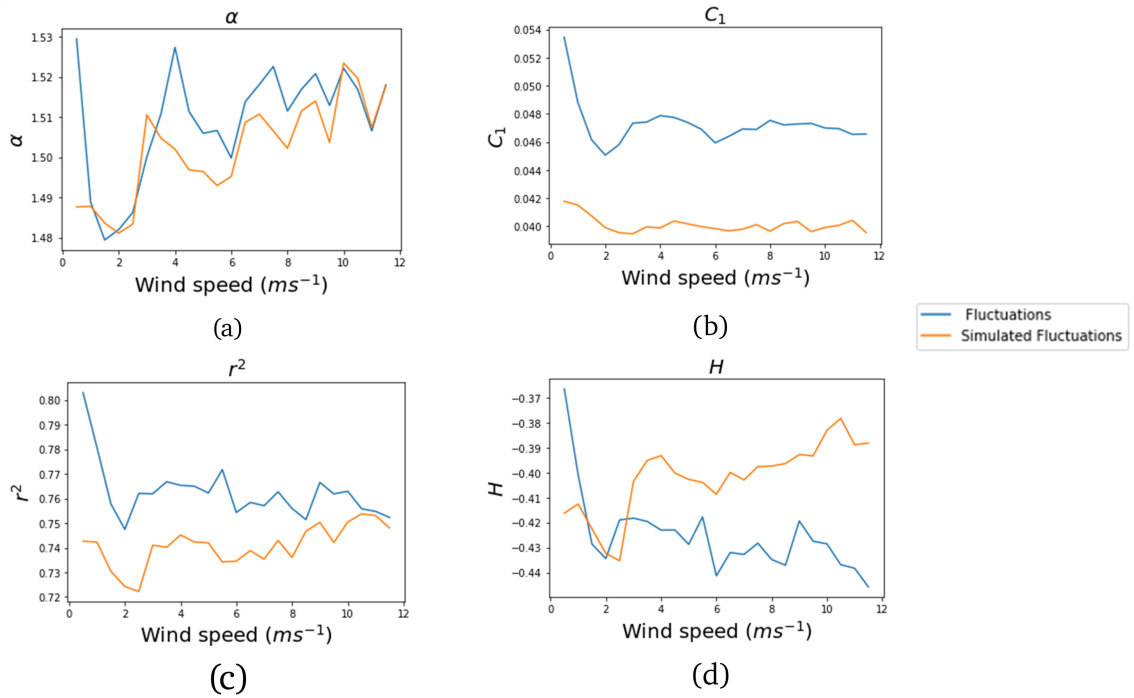


Figure 2.25: Evolution of the UM parameters with the wind speeds in the simulation of the fluctuations of the wind fields. Real fields are plotted in blue and simulated one are plotted in orange. Ensembles of 100 samples for each wind class are used. (a) shows the evolution of α , (b) shows the evolution of C_1 , (c) shows the evolution of r^2 , and (d) shows the evolution of H .

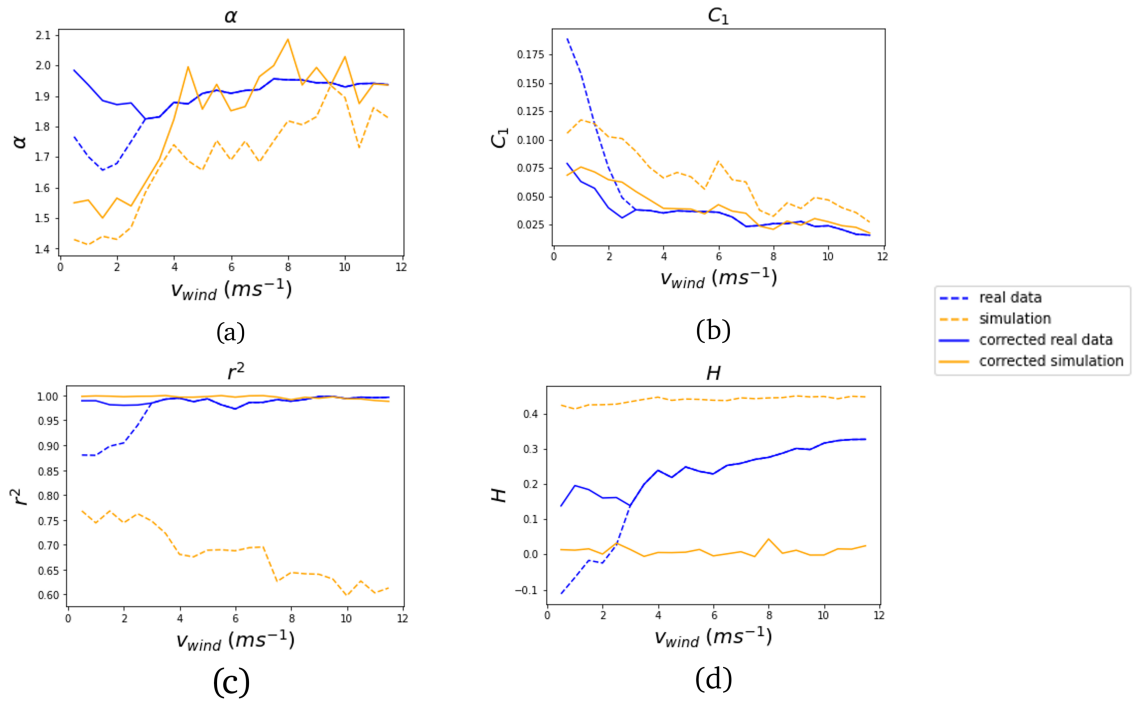


Figure 2.26: Evolution of the UM parameters with the wind velocities in the simulation using the RoF approach. Real fields are plotted in blue and simulated ones are plotted in orange. Direct fields are plotted in dashed lines and corrected fields using methodology reviewed in 1.4.3.3 are plotted in solid lines. Ensembles of 100 samples for each wind class are used. (a) shows the evolution of α , (b) shows the evolution of C_1 , (c) shows the evolution of r^2 , and (d) shows the evolution of H .

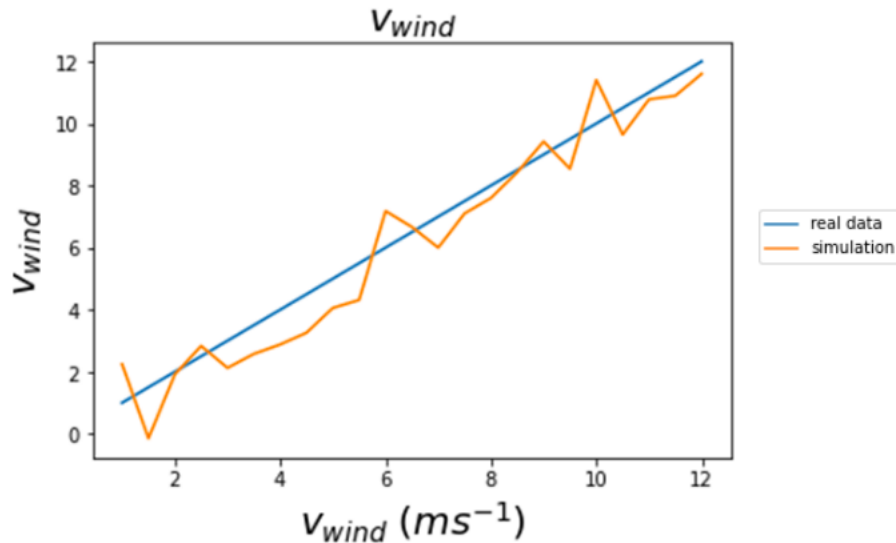


Figure 2.27: Comparison between the average velocity retrieved in the ensemble of the simulated wind fields and velocity used to initialize the simulation.

obtained from the initial field to generate the subsequent fields since the scaling properties are preserved. Fig. 2.28b shows that all the samples are close near the transition and after spread in a different possible scenarios which may confirm a limit in the predictability. However, this functionality is not explored in details since it is outside the scope of the PhD.

Both methodologies can be extended to the multidimensional case as soon as the simulated fluxes can be simulated not only in 1D (refer to the section 1.3 more details). Moreover, this process is not limited to the scalar case, we can extend also to the vector process with help of the Clifford Algebra adapting the equations to vectors as is mentioned in Section 1.3.4.

2.6 Comparison between the methods

In this final section, we compare the wind field simulations obtained with all the methods discussed in this chapter. It is therefore important to summarise how they are simulated in order to better understand the subsequent comparison. The first thing to note is that both the Turbsim software and the simplistic approach use a single event (located at the centre of the grid) to simulate the entire wind field on the grid, while both FIFs (which we will distinguish by calling them FIF and RoF, respectively) use the properties recovered in the analysis of a large number of events with the same mean velocity.

We conducted two types of analysis. First, given the unavailability of actual data for evaluating the outcomes produced by different models, we will make the assumption that the UM properties

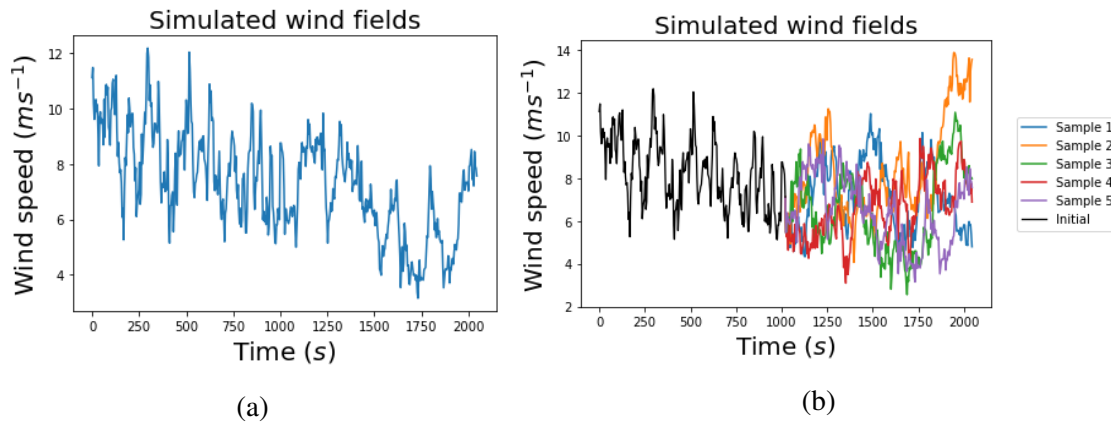


Figure 2.28: Example of extension (i.e. nowcasting) of wind fields. (a) shows the example of the extension of one field, starting point is 1024. (b) shows 5 different examples to show variability between samples

of each point on the grid should exhibit similarity in temporal dimension. Consequently, we will utilize the spatial distribution of these parameters as a basis for comparison, i.e. the parameters obtained with the analysis of time series of each pixel of the grid. These parameters are plotted in 2D maps (Figs. 2.30- 2.32).

The second method consists of analysis in the spatial dimension, i.e. analyzing 2D samples and considering each time step as a sample, where we expect to obtain parameters similar to those in the temporal dimension (taking into account spatio-temporal anisotropy). All analyses are performed using a set of 100 samples and corrected using the algorithm reviewed in Section 1.3.3.3. To be consistent Turbsim and simplistic approach use the same event recorded on 20/12/2020 (starting at approximately 19h 54min) and FIFs methods use fields simulated for the same average velocity as this event. The UM parameters obtained are $\alpha = 1.93$, $C_1 = 0.028$ and $H = 0.28$.

2.6.1 Temporal analysis of each pixel

The fields simulated for this section consist in an ensemble of 100 samples and $27 \times 27 \times 256$ where the 27 are the points in space dimensions and 256 are the points in time dimension.

The primary distinction between the models becomes evident in the quality of the scaling as indicated by the coefficient of determination of the TM graph. Turbsim (Fig. B.2.8i) shows the worst scaling with values of $r^2 \sim 0.97$, this is consistent with the behaviour showed in Fig. 2.13 related to the possibility that each point replicates the properties observed in the center of the grid. This poor scaling is observed also in the center of the grid for the Simplistic approach (Fig. B.2.8i) but with rather good scaling away from the center which is again expected due to the method of simulation. The remaining two methodologies exhibit consistent scaling throughout the entire grid,

finding the best scaling in the FIF since the second approach shows poor scaling at isolated points.

Focusing on the variable α , interesting results can be observed. Although the values are relatively similar in scale, discernible trends in their distribution can be identified, which are closely related to the simulation method employed.

In the case of the simplistic approach, a radial trend is noticeable, whereas Turbsim exhibits an increasing trend with height. The remaining two methods display a more random pattern. However, in Fig. 2.30b, certain structures become apparent, while in Fig. 2.30c, each point appears distinct from its neighboring points. In simplistic approach, FIF and Turbsim (Figs. 2.30a, 2.30b and 2.30d, respectively) the difference are minimal with values around 0.02 which less than 1%. In RoF, the differences are larger but still remain below 10%. All the cases show a good agreement with the expected values ($\alpha = 1.93$) for wind fields of 11.2 ms^{-1} .

Similar behavior can be observed in Fig. 2.31 for C_1 , where the trends described earlier remain visible. Notably, in the case of Turbsim, the parameter exhibits a decrease with increasing height. It is worth noting that the differences in this parameter are similar across all the methods. Again all the methods show a good agreement with the expected value ($C_1 = 0.028$) with an slight underestimation observed in the simplistic approach, and overestimation in the other methods. Yet, these are very small differences in absolute values.

With regards to the parameter H (retrieved in the analysis of the original field), the trends persist in the simplistic approach but are not apparent in Turbsim. Particularly in this scenario, the spatial differences are more pronounced in the simplistic approach, and in RoF approach. In terms of agreement with the expected values ($H = 0.28$) both FIFs approach show better agreement with closest results obtained with the help of the direct approach. Simplistic approach (2.29a) shows an underestimation of this parameters while Turbsim (2.32d) shows an overestimation which can be understood as over fluctuating fields in simplistic approach and under fluctuating field in Turbsim.

In summary, as an overall observation, Figs. 2.30-2.32 reveal a satisfactory spatial agreement among the models in terms of the differences observed. It is important to note that the panels related to Turbsim and the Simplistic approach (in Figs. 2.30-2.32) serve solely as an illustration of the tendencies observed in the methods. However, we have conducted these analyses over 10 different wind events, yielding consistent results. For a comprehensive collection of all these figures, please refer to Appendix B.

2.6.2 Spatial analysis

In the previous section, the number of points available for the analysis of the spatial dimension was not sufficient. To address this limitation, in this section, we will utilize fields with dimensions of $128 \times 128 \times 128$, where the temporal dimension (i.e. the successive time steps) is employed as

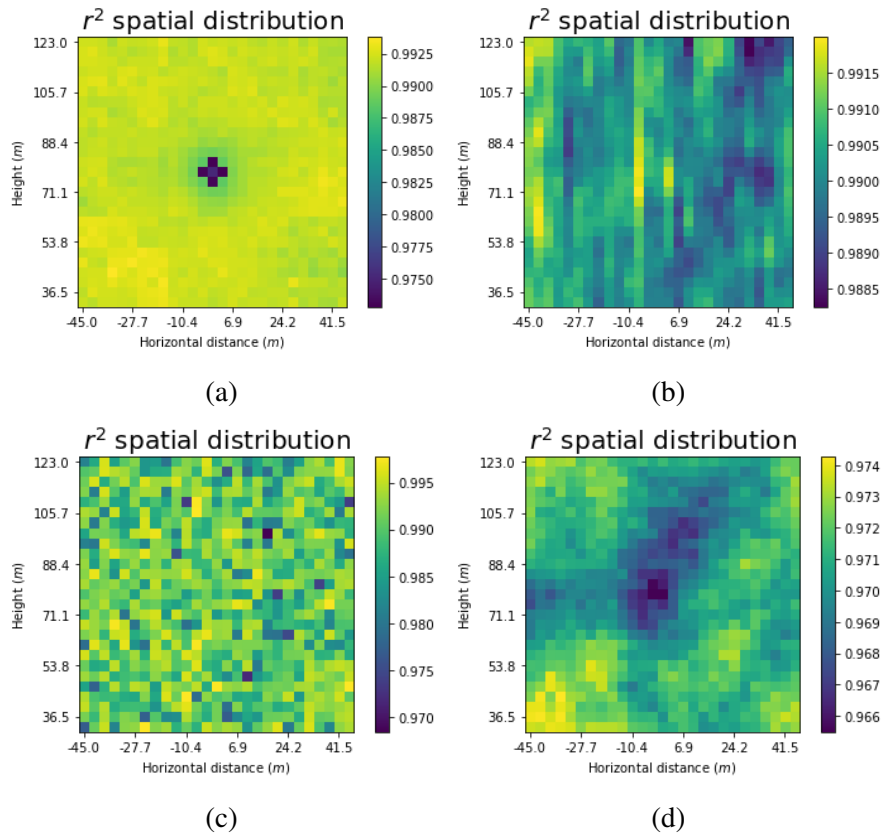


Figure 2.29: Spatial distribution of r^2 using different methods of wind simulation. (a) simplistic approach, (b) FIF approach, (c) RoF approach and, (d) Turbsim.

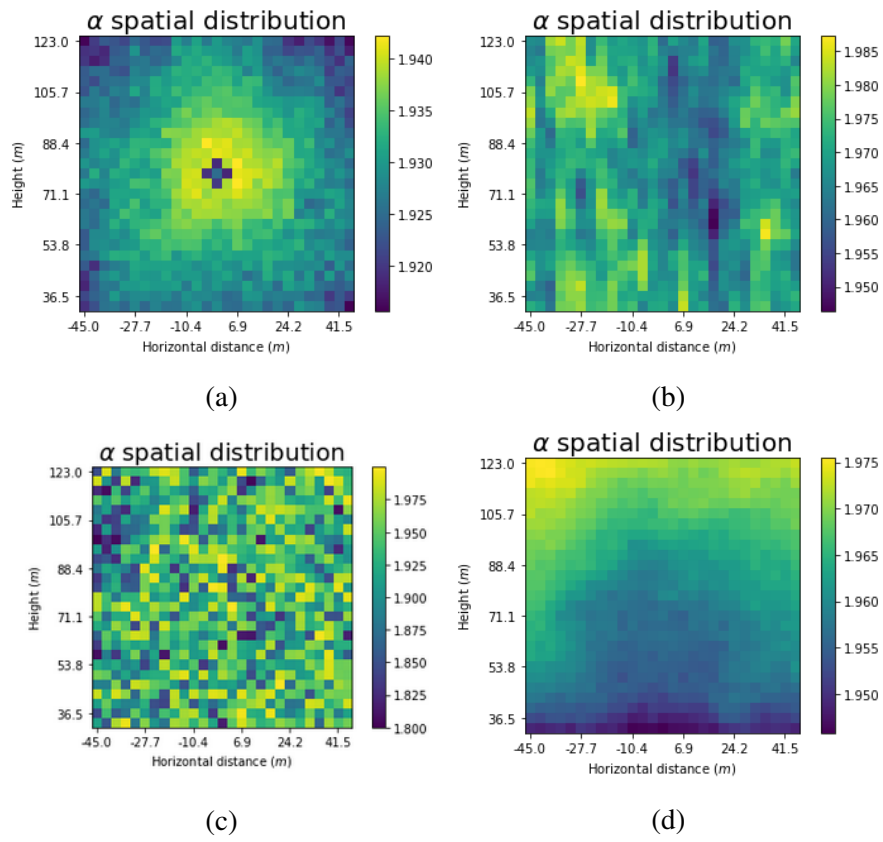


Figure 2.30: Spatial distribution of α using different methods of wind simulation. (a) simplistic approach, (b) FIF approach, (c) RoF approach and, (d) Turbsim.

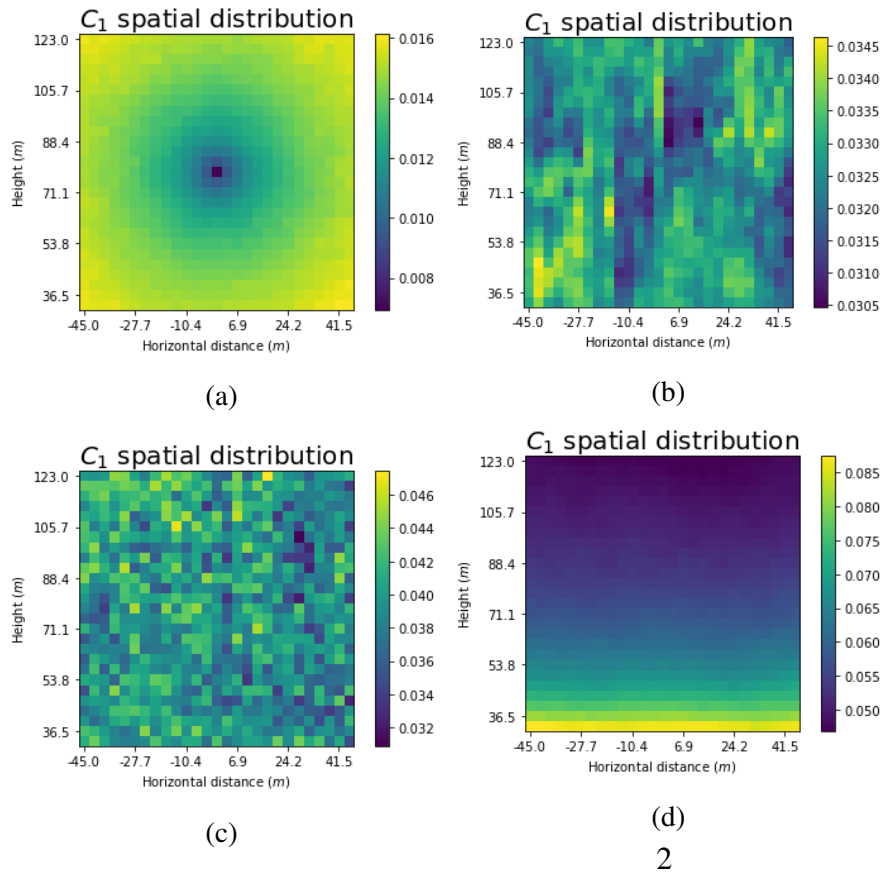


Figure 2.31: Spatial distribution of C_1 using different methods of wind simulation. (a) simplistic approach, (b) FIF approach, (c) RoF approach and, (d) Turbsim.

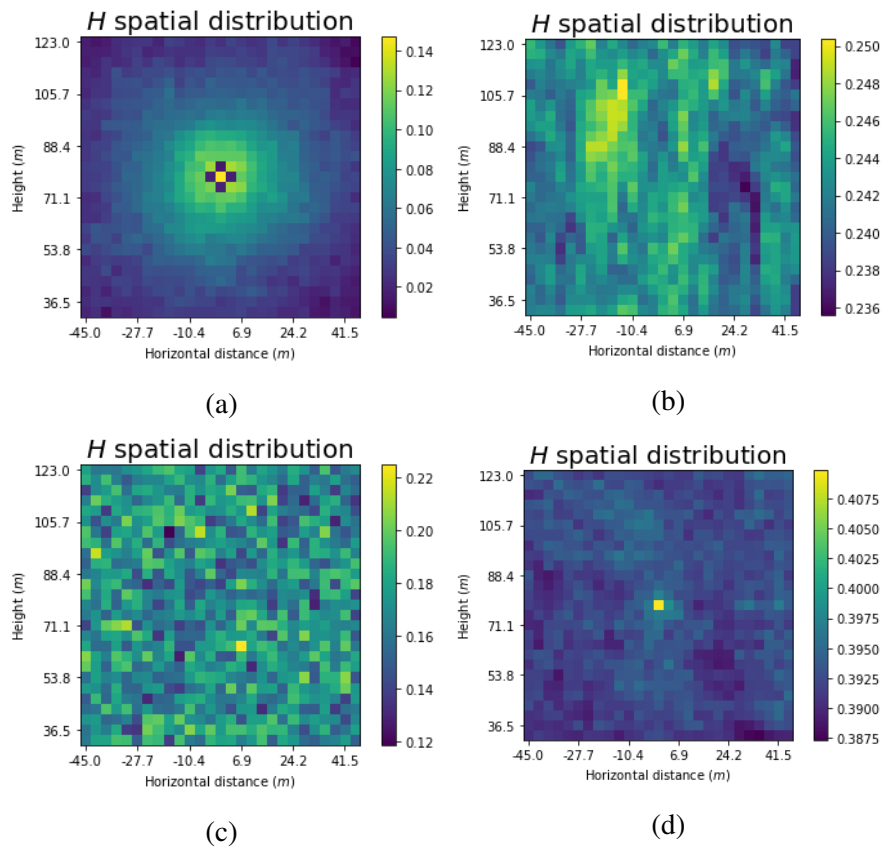


Figure 2.32: Spatial distribution of H using different methods of wind simulation. (a) simplistic approach, (b) FIF approach, (c) RoF approach and, (d) Turbsim.

samples. Figs. 2.33-2.36 show an illustration of this analysis and the summary results are collected in Table 2.5.

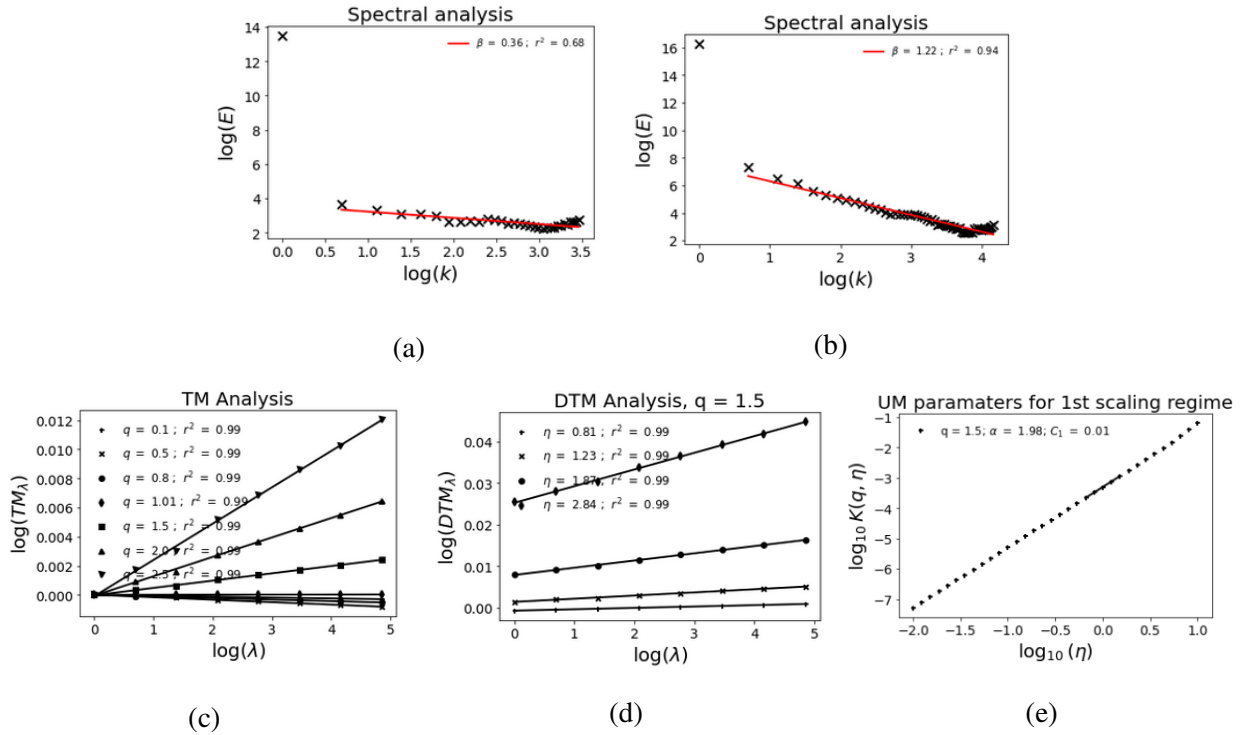


Figure 2.33: UM analysis in the spatial dimension of an ensemble of 100 samples simulated with Simplistic approach using the event of 20/12/2020 as input. (a) and (b) Spectral analysis, before and after the correction respectively (Eq. 1.21 in log-log), (c) TM (Eq. 1.6 in log-log), (d) and (e) DTM (Eqs. 1.70 and 1.72 in log-log respectively).

Upon examining Table 2.5, one can observe that all the methods demonstrate good scaling behaviour in the spatial dimension, with $r^2 = 0.99$ in all cases. This finding is further supported by panels *c*) and *d*) of Figs. 2.33-2.36.

Regarding the parameter α , the results obtained align with expectations for FIFs methods and simplistic approach. The FIF method exhibits a slight underestimation, while the fluctuations approach and the simplistic method show a slight overestimation. However, in the case of Turbsim, there is a significant bias from the expected value of $\alpha = 1.93$ which shows some limitations in the ability to capture expected spatial structure by this software.

For C_1 , we obtain a better agreement between the methods. For the expected value we have to take into account the anisotropy between space and time, in this case $C_{1_{space}} = C_{1_{time}} / (1 - H_t)$ (Schertzer and Lovejoy, 1987a) which yields to a $C_{1_{space}} = 0.04$. Although the value obtained by the Simplistic approach is not far from the value, there is a significant difference since the expected

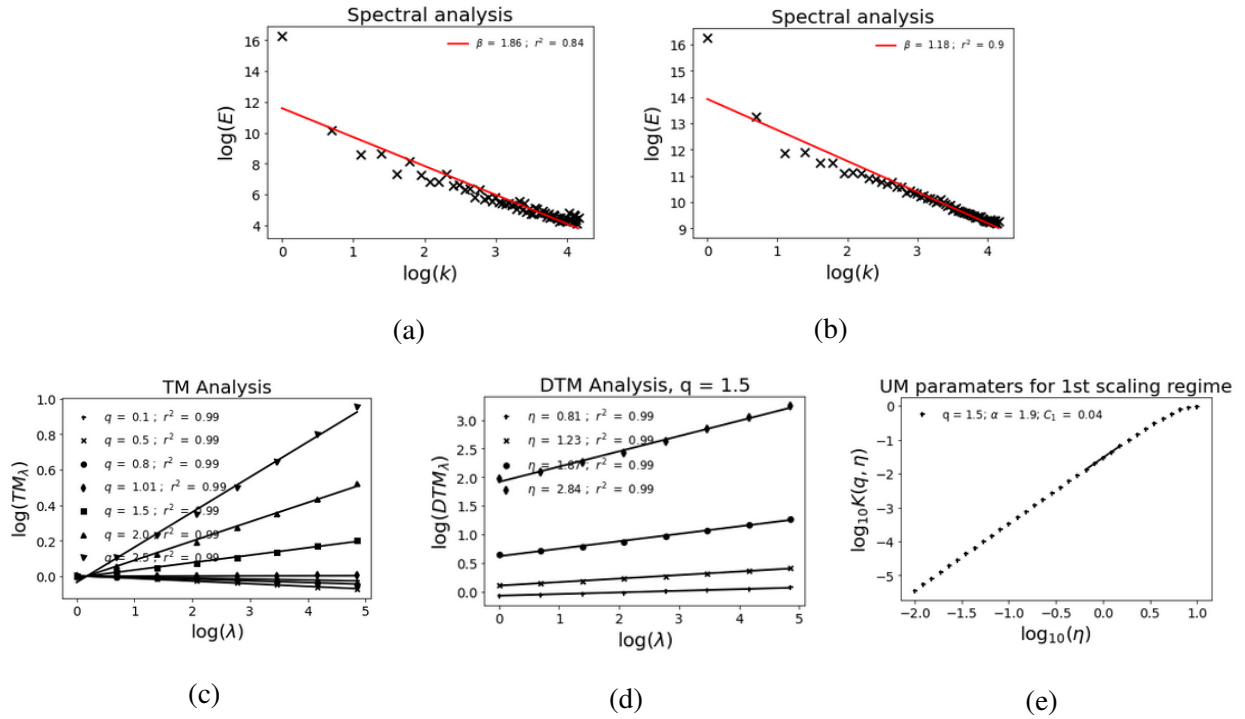


Figure 2.34: UM analysis in the spatial dimension of an ensemble of 100 samples simulated with FIF using the properties of fields with average velocity 11 ms^{-1} as input. (a) and (b) Spectral analysis, before and after the correction respectively (Eq. 1.21 in log-log), (c) TM (Eq. 1.6 in log-log), (d) and (e) DTM (Eqs. 1.70 and 1.72 in log-log respectively).

Method	α	C_1	r^2	H	$H_{original}$
Simplistic	1.98	0.01	0.99	0.11	-0.31
FIF	1.90	0.04	0.99	0.08	0.38
RoF	1.98	0.04	0.99	0.07	-0.41
Turbsim	1.44	0.04	0.99	0.39	0.65

Table 2.5: Summary of the UM parameters obtained in the analysis of the spatial dimension of the different methods

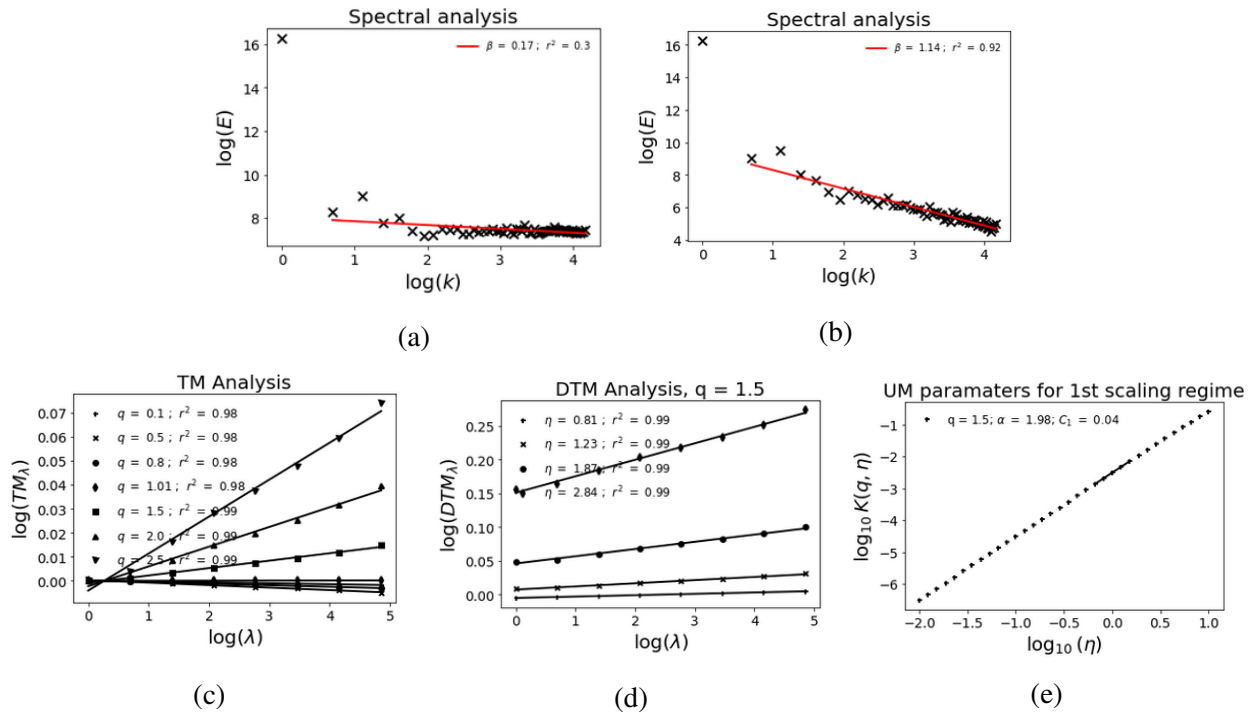


Figure 2.35: UM analysis in the spatial dimension of an ensemble of 100 samples simulated with RoF approach using the properties of fields with average velocity 11 ms^{-1} as input. (a) and (b) Spectral analysis, before and after the correction respectively (Eq. 1.21 in log-log), (c) TM (Eq. 1.6 in log-log), (d) and (e) DTM (Eqs. 1.70 and 1.72 in log-log respectively).

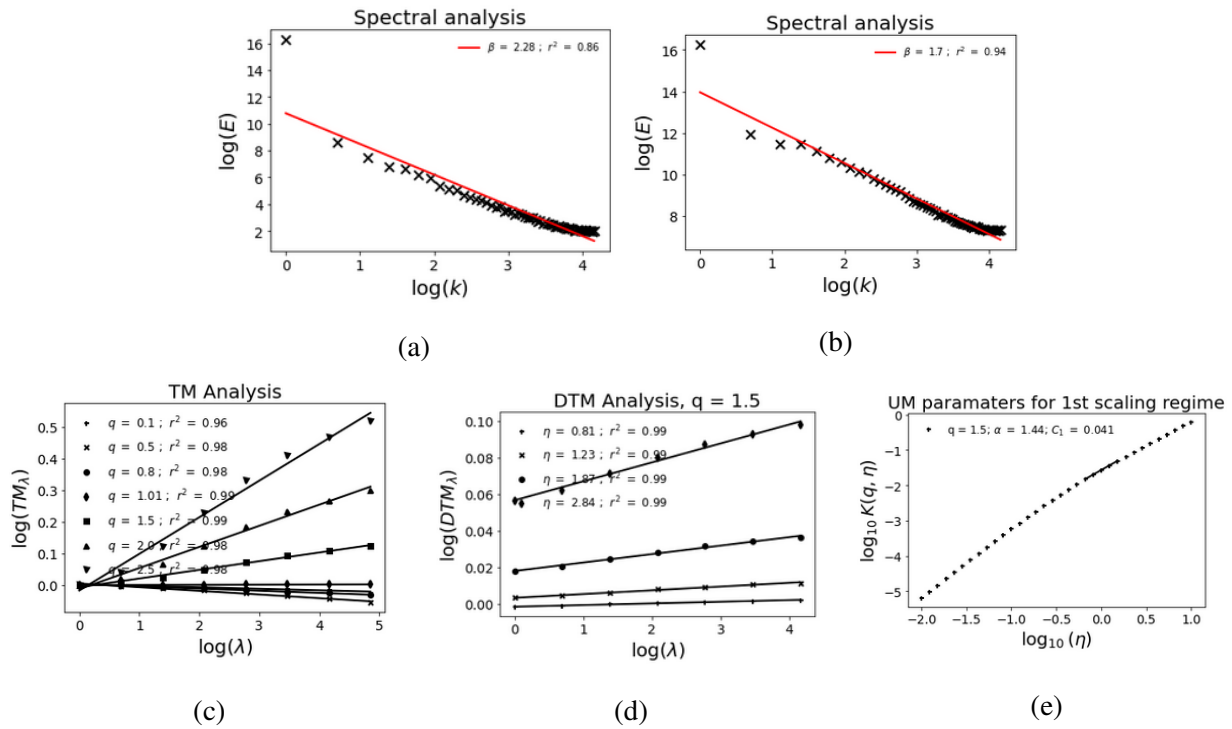


Figure 2.36: UM analysis in the spatial dimension of an ensemble of 100 samples simulated with Turbsim using the event of 20/12/2020 as input. (a) and (b) Spectral analysis, before and after the correction respectively (Eq. 1.21 in log-log), (c) TM (Eq. 1.6 in log-log), (d) and (e) DTM (Eqs. 1.70 and 1.72 in log-log respectively).

value for the spatial dimension was expected to be greater than the value obtained in the temporal, yet the obtained value is lower.

For the parameter H , we will consider the values before the correction. In this case, the FIF method is the only one that retrieves expected results. The Simplistic approach and the RoF approach yield negative values, which are not in line with expectations. Additionally, Turbsim provides higher values than expected.

Similar results are obtained for other events.

2.7 Summary

In this chapter we have analysed high-resolution 3D anemometer data, collected in the framework of the RW-Turb project measurement campaign, to retrieve the UM properties which were needed for the wind simulation. Ensemble analysis of samples with similar mean wind velocity was implemented. A good scaling is found over the range of scales 4-1024 s (~ 17 minutes) which was therefore used for simulations. A trend in the scaling quality (low quality scaling for wind below 4 m.s^{-1}) and UM parameters (increase of α and H , decrease of C_1 up to 4 m.s^{-1} before reaching a plateau) with the mean wind velocity is found, but it disappears after applying the data correction suggesting that only the degree of non-conservation H changes with increasing mean wind velocity. The results of these analysis were used for two purposes: first to serve as input to the simulations and second for checking the validity of the simulations by comparing same analysis results with them.

Using directly the wind fields and/or its retrieved UM properties, four distinct wind simulation methods have been tested. The first method uses the Turbsim software, developed by NREL, to reconstruct a wind grid over the turbine's swept area using the time series obtained from a high-resolution 3D anemometer. However, this method relies on Gaussian statistics that does not accurately capture the wind's actual variability across scales. The second method also relies on the use of a wind time series, but incorporates established scaling laws. More precisely, the wind field at any location is obtained by adding to the data, the product of a prefactor, a random UM field and distance increment raised to scaling exponents, allowing for the inclusion of non-Gaussian statistics. Despite showing promising results, this method involves several too drastic simplifications. The last two methods are based on the Fractionally Integrated Flux (FIF) principle but differ in their approach. The first method focuses on directly simulating wind fields. It uses the UM properties of the wind field (α , σ , and H) to simulate the wind field as a non-conservative field renormalized to obtain the desired mean. The second method begins by simulating wind's fluctuations. It uses the UM parameters obtained in the analysis of the fluctuations, after applying the appropriate required corrections, to simulate conservative fluctuations converted into synthetic fluctuations (using a fractional integration) from which the wind fields are reconstructed. Both

2. Wind Simulation

methods exhibit good agreement between the observed properties of real wind and the simulated fields, with the first method demonstrating slightly superior outcomes. The fields simulated with all methods were subjected to UM analysis of time series for each pixel over the swept area by the blade, as well as spatial analysis for each time step. When comparing the different methods, similar results are observed in the UM parameters maps which shows the temporal analysis of each pixel of the grid. However, noticeable differences emerge in spatial analysis. After correction, all non-Gaussian methods exhibit similar properties, but only the FIF simulation yields the expected results, while the Turbsim results deviate significantly. Consequently, it is concluded that the FIF direct simulation method yields the most realistic simulated wind fields.

Chapter 3

Modelling chains

3.1 Introduction

Wind modelling is an important tool for understanding and predicting the behaviour of wind farms as long as wind turbines extract the wind's kinetic energy, converting it into mechanical energy. Mechanical torque is widely used to measure the performance of wind turbines. A better understanding of the wind fields can improve different important aspects in the wind energy industry (Bilendo et al., 2023), such as the characteristic of wind turbines used in a wind farm (Sohoni et al., 2016) or the performance of the wind farm, e.g. through capacity factor estimation which measures the ratio between the maximum power produced by the farm and the average output (Song et al., 2019). Improving the wind modelling tools also improves the reliability of the power delivery reducing "overestimation" and "underestimation" of the power (Zeng and Qiao, 2012) caused by the extreme variability of the wind fields.

Many authors in recent years have reported overestimation in the wind power production between 10 and 20% due to the effect of the wind turbulence (Pope and Pope, 2000, Barthelmie et al., 2006, Kaiser et al., 2007, Stival et al., 2017 among other), this is not only reduced to the impact on a single turbine but also plays a significant role in the wind farms where wind gusts do not impact all the turbines at the same time (Ackermann, 2005). The intermittent nature of the wind fields causes that the convectional methods of power production performs in a sub-optimal regimes (Albadi and El-Saadany, 2010).

However, there is a lack of knowledge on the small scales wind modelling and how the wind interacts with the wind turbine (Van Kuik et al., 2016, Veers et al., 2019). Several authors have investigated this interaction by conducting combined analyses of power and wind using numerical simulations at various scales. Their work has revealed that certain wind characteristics, such as

intermittency, are transferred to wind power output and can even exert a dominant influence on turbine loads (Wächter et al., 2012 Milan et al., 2013, Milan et al., 2014, Calif and Schmitt, 2014). Torque can serve as a turbine controller, as it helps mitigate extreme load conditions and enables more stable operation with a faster response to aerodynamic changes, such as wind gusts, compared to other controlling types (Bossanyi, 2003, Zhang et al., 2018).

To investigate the impact of wind field variability on wind power production, we compared three modeling chains with increasing complexity for calculating the mechanical torque generated. The first two modeling chains rely solely on wind speed and the geometric properties of the wind turbine. The first one takes into account only temporal variability and computes torque using the velocity field at a single point, typically at hub height. This approach is widely used in the literature (Sørensen et al., 2002; Johnson, 2004; Fan et al., 2009; Manwell et al., 2010; Burton et al., 2011; Fu et al., 2018; Wu et al., 2019; Gumilar et al., 2020 to mention some examples). The second modeling chain is based on the angular momentum definition, allowing us to consider both spatial and temporal variability by computing torque at each point of the blade and then integrating (Dolan and Lehn, 2006; Burton et al., 2011; Chaudhary et al., 2014; Akbari et al., 2022). The final modeling chain employs the more realistic software OpenFAST (Jonkman et al., 2022), which integrates multiple modules, enabling non-linear aero-hydro-servo-elastic simulations in the time domain.

OpenFAST software is widely used in industry and research to simulate operational situations or to compare analytical results with experimental measurements. To this end, the authors modelled turbines with different geometries and characteristics in OpenFAST, which can be used as a reference (Rinker and Barter).

Numerous researchers have employed OpenFAST, or its antecedent version, FAST, in various configurations to establish the dependability of this software under practical initial conditions. For instance, investigations have been conducted on land-based reference wind turbines (Bortolotti et al., 2019), offshore wind turbines (Mendoza et al., 2022), and with data obtained from a small wind farm comprising five 1.5 MW turbines (Shaler et al., 2020). Other researchers, including Oguz et al., 2018 and Damiani et al., 2018, have evaluated OpenFAST using diverse metrics, such as the natural periods of pitch and surge, as well as Damage Equivalent Loads (DELs) and extreme loads, and have established a strong correlation between experimental outcomes and OpenFAST simulations.

Moreover, sometimes empirical data, which is needed to validate new approaches and tools, is not available, or is too costly to obtain. In these scenarios OpenFAST is widely used to provide "pseudo" wind turbine data under "real" operational conditions. Some examples of this type of use can be found in Golparvar et al., 2021, López-Queija et al., 2022, Moynihan et al., 2022, and Xiaohang et al., 2022 where this software provides the data required to validate new models and tools for different applications such as estimation of the forces, measurement of blade deflections

and performance of offshore wind turbines.

To describe the modelling chains used, we start with theoretical description of the the general concepts common to the three modelling chains. After that, we describe the particularities of each modelling chain, starting with the simplest one and increasing in complexity, followed by a validation. This section will be carried out through several tests to prove the validity of the modelling chains over different input parameters. Finally we present the results obtained using the wind fields simulated in the previous chapter.

3.2 Modelling chains

3.2.1 Theoretical background

During the extraction of a portion of its kinetic energy, the wind is slowed down when it passes through the wind turbine swept area (called the actuator disc from now). Due to the fact that the wind acts as an incompressible fluid, the effective area must be expanded. Downstream the wind turbine, the wind gradually slows down with the corresponding increase of the area until the equilibrium is reached and the static pressure becomes the environmental pressure again. The mass of air that does not pass through the actuator disc is not affected by this slowdown; hence, it creates a circular cross-section tube where the airflow is contained (scheme in Fig. 3.1a).

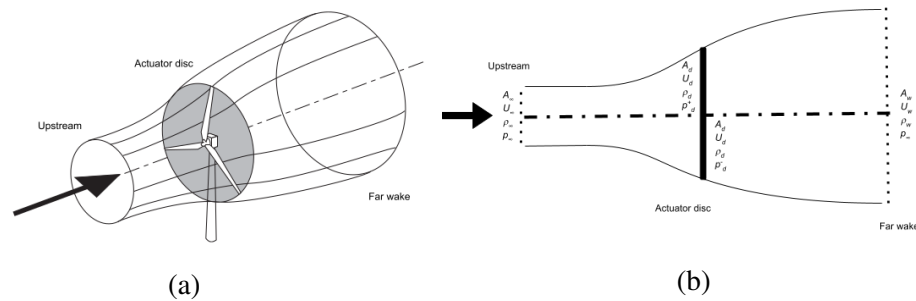


Figure 3.1: Scheme of the control volume used in the wind turbine, (a) Scheme of circular cross-section tube, and (b) Lateral section of the tube. Subscript ∞ represents the conditions upstream, subscript d the conditions at actuator disc, and subscript w the conditions at far wake. (Adapted from Burton et al., 2011)

3.2.1.1 Conservation of mass

Analyzing the aerodynamic behaviour of the general energy extraction process, we can distinguish three relevant zones, an expansion zone where the cross-section expands from the upstream conditions to the actuator disc, the disc itself, and a gradual expansion zone downstream the actu-

ator disc called wake zone (see scheme in Fig. 3.1b). Since the mass flow must be constant along the tube, we have:

$$\rho A_{\infty} U_{\infty} = \rho A_d U_d = \rho A_w U_w \quad (3.1)$$

Where ρ (kg/m^3), the air density, is considered constant over the volume (assumption of incompressible flow), A (m^2) represents the cross section area, and U (m/s) the velocity. Subscript ∞ represents the conditions upstream, subscript d the conditions at actuator disc, and subscript w the conditions at far wake.

It is generally considered that the actuator disc induces a change in the free stream velocity related to $-U_{\infty} a_b$ (Burton et al., 2011) where a_b is the axial flow induction factor (or inflow factor). Then the velocity at the actuator disc can be expressed as:

$$U_d = U_{\infty}(1 - a_b) \quad (3.2)$$

3.2.1.2 Momentum theory

In general, when a mass of air crosses a disc, it experiences a change in velocity that results in a rate of change of momentum equal to this velocity change multiplied by the mass flow rate (Burton et al., 2011). In this case, the rate of change of momentum undergone in the extraction process (Fig. 3.1) can be expressed as:

$$\text{rate of change of momentum} = (U_{\infty} - U_w)\rho A_d U_d \quad (3.3)$$

Given that the tube is enveloped by air at atmospheric pressure levels, all the change in momentum arises from the pressure difference between the upstream and downstream sides of the disc, which yields:

$$(p_d^+ - p_d^-)A_d = (U_{\infty} - U_w)\rho A_d U_{\infty}(1 - a) \quad (3.4)$$

Where p (Pa) is the pressure.

Bernoulli's equation states that the total energy of the an incompressible flow is constant under steady conditions along a streamline. It consists of three terms: kinetic energy, static pressure energy and gravitational energy, so for a unit volume of air we have:

$$\frac{1}{2}\rho U^2 + p + \rho gh = \text{constant} \quad (3.5)$$

This equation allows us to compute the difference of pressure ($p_d^+ - p_d^-$) using Bernoulli equation both upstream and downstream:

$$\frac{1}{2}\rho U_\infty^2 + p_\infty + \rho g h_\infty = \frac{1}{2}\rho U_d^2 + p_d^+ + \rho g h_d \quad (3.6)$$

For upstream conditions, and considering an horizontal wind ($h_\infty = h_d$), we have:

$$\frac{1}{2}\rho U_\infty^2 + p_\infty = \frac{1}{2}\rho U_d^2 + p_d^+ \quad (3.7)$$

With the same reasoning, downstream the wind turbine, we obtain:

$$\frac{1}{2}\rho U_d^2 + p_d^- = \frac{1}{2}\rho U_w^2 + p_\infty \quad (3.8)$$

Subtracting these equations:

$$(p_d^+ - p_d^-) = \frac{1}{2}\rho(U_\infty^2 - U_w^2) \quad (3.9)$$

And coming back to Eq. 3.4

$$\frac{1}{2}\rho(U_\infty^2 - U_w^2)A_d = (U_\infty - U_w)\rho A_d U_\infty(1 - a_b) \quad (3.10)$$

which yields:

$$U_w = U_\infty(1 - 2a_b) \quad (3.11)$$

3.2.1.3 Power coefficient

We can define the available power for a wind turbine as the maximum power that can be extracted from the not-disturbed (not affected by the presence of the turbine) wind flow. However, as shown in the previous section, the actuator disc induces a decrease in the wind speed, which is translated into a decrease in the power.

Using Eq. 3.4 and Eq. 3.2 we can define the aerodynamic force, F (N), as:

$$F = (p_d^+ - p_d^-)A_d = 2\rho A_d U_\infty^2 a_b(1 - a_b) \quad (3.12)$$

With this force, we can define the power extracted from the wind as:

$$Power\ extracted = FU_d = 2\rho A_d U_\infty^3 a_b (1 - a_b)^2 \quad (3.13)$$

Then, the power coefficient is defined as the ratio between this power and the available one:

$$C_P = \frac{Power\ extracted}{Power\ available} = \frac{2\rho A_d U_\infty^3 a_b (1 - a_b)^2}{\frac{1}{2}\rho A_d U_\infty^3} = 4a_b (1 - a_b)^2 \quad (3.14)$$

However, this coefficient is not fixed but it depends on the operation regimes and blade properties. To address it, in recent years some authors (Hwas and Katebi, 2012; Fu et al., 2018; Barambones et al., 2019; Sitharthan et al., 2020; among others) modelled C_p value using a empirical highly non-linear function dependant of the pitch angle of the blade (this angle is measured between the plane of the disc and aerofoil zero lift line), β_b ($^\circ$), and the Tip Speed Ratio, which links wind velocity with angular velocity through Eq. 3.16. For that, they use an empirical simplified expression (Anderson and Bose, 1983) which is shown in Eq. 3.15 :

$$\left\{ \begin{array}{l} C_p = 0.5176 \left(\frac{116}{TSR_i} - 4\beta - 5 \right) e^{\frac{21}{TSR_i}} + 0.0068 TSR \\ \frac{1}{TSR_i} = \frac{1}{TSR + 0.08\beta} - \frac{0.0035}{\beta^3 + 1} \end{array} \right. \quad (3.15)$$

TSR being defined as:

$$TSR = \frac{\Omega r}{U} \quad (3.16)$$

Where U is the wind speed, R_b (m) is the radius of the blade and, Ω (rad/s) is the angular velocity.

Fig. 3.2 reflects the evolution of the power coefficient with the TSR for different values of pitch angle.

Betz limit is a theoretical limit for this coefficient, in honour of the German aerodynamicist who calculated it in 1919. This limit is not caused by any design problem, but it comes from the fact that the area of the cross-section taken upwards is smaller (caused by the expansion of the flow) than the effective area at the actuator disc.

This maximum limit is found when:

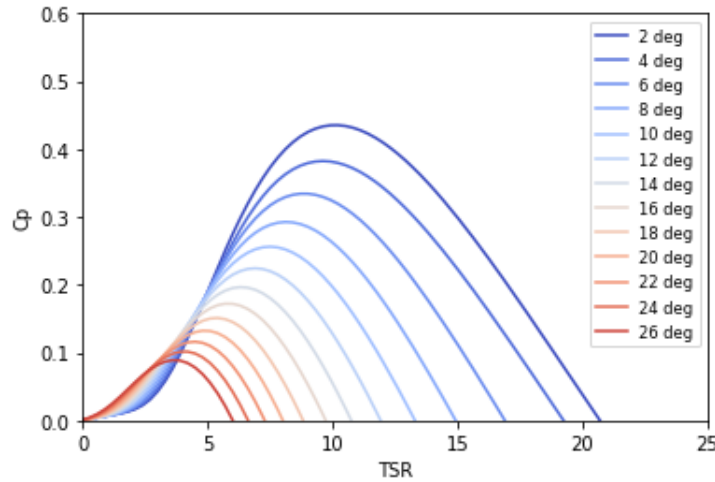


Figure 3.2: Wind turbine power coefficient vs. tip speed ratio at various pitch angles

$$\frac{dC_P}{da_b} = 4(1 - a_b)(1 - 3a_b) = 0 \quad (3.17)$$

this gives value of $a_b = 1/3$, and the limit can then be computed as:

$$C_{P_{max}} = \frac{16}{27} = 0.593 \quad (3.18)$$

3.2.1.4 Angular momentum theory

Considering that the control volume of Fig. 3.1 rotates with angular velocity of the blades Ω , it generates angular momentum. As a reaction to this, the flow behind the rotor rotates in the opposite direction. The appearance of this rotation implies a tangential component in addition to the axial velocity. All this process occurs across the thickness of the disc (Fig. 3.3). Therefore, if we consider ω as the angular velocity transmitted to the flow stream, the angular velocity of the air relative to the blade increases from Ω before the blade to $\Omega + \omega$ just after, while the axial component keeps constant (Manwell et al., 2010). With that we can reformulate Eq. 3.4 (see Glauert, 1935 for full derivation) as :

$$(p_d^+ - p_d^-) = (\Omega + \frac{1}{2}\omega)\rho\omega r_b^2 \quad (3.19)$$

It yields to adapt Eq. 3.12 as:

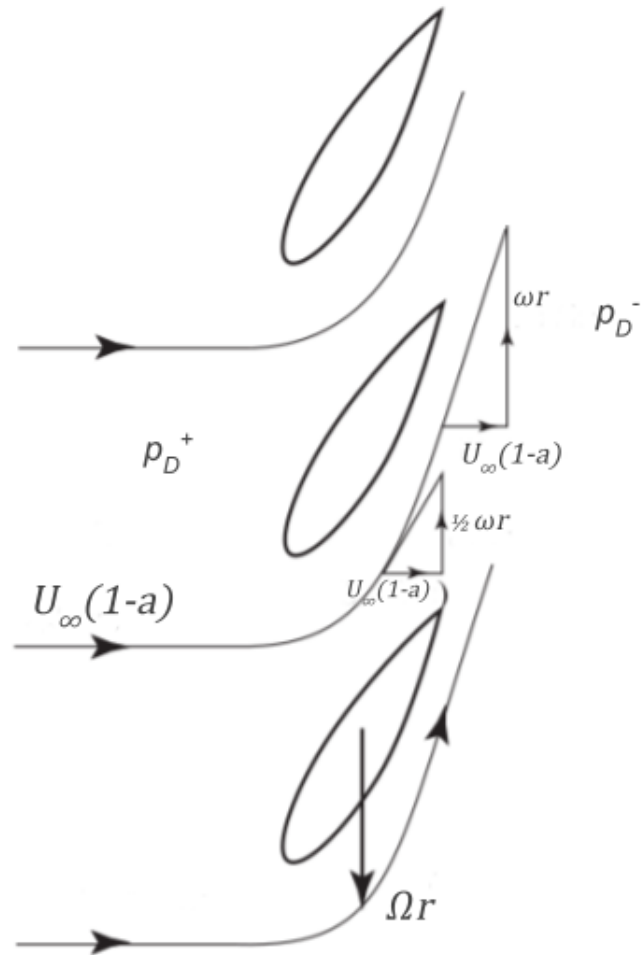


Figure 3.3: Illustration of how the tangential velocity grows across the blade thickness (Adapted from Burton et al., 2011).

$$F = (p_d^+ - p_d^-)A_d = (\Omega + \frac{1}{2}\omega)\rho\omega r_b^2 A_d \quad (3.20)$$

and it allows us to define the tangential induction factor a'_b as:

$$a'_b = \omega/2\Omega \quad (3.21)$$

This yields to transform Eq. 3.21 into:

$$F = (1 + a'_b)2a'_b\rho\Omega^2 r_b^2 A_d \quad (3.22)$$

This translates into the fact that before reaching the actuator disc, the induced tangential velocity is zero. However, immediately after passing through the actuator disc, the tangential velocity becomes $\omega r = 2\Omega r_b a'_b$ (Fig. 3.3).

However, the tangential velocity is different along all the radial positions of the actuator disc. This change in tangential velocity results in a rate of change of angular momentum, ∂Q , equal to the change in this tangential velocity multiplied by the mass flow rate and the radius on an incremental annular area (Manwell et al., 2010, Burton et al., 2011):

$$\text{rate of change of angular momentum} = \partial Q = 2\Omega r_b a'_b \times \rho U_d \partial A_d \times r_b \quad (3.23)$$

Where the ∂A_d is the area of an annular ring.

This rate of change of angular momentum can be understood as a change of torque such that:

$$\partial P = \partial Q \Omega \quad (3.24)$$

Developing this expression with the help of Eq. 3.13 and Eq. 3.23, we obtain:

$$2\rho\partial A_d U_\infty^3 a_b(1 - a_b)^2 = 2\Omega^2 a'_b \rho \partial A_d U_\infty (1 - a_b) r_b^2 \quad (3.25)$$

Hence,

$$U_\infty a(1 - a) = \Omega^2 r_b^2 a'_b \quad (3.26)$$

and,

$$a'_b = \frac{U_\infty a_b (1 - a_b)}{\Omega^2 r_b^2} = \frac{a_b (1 - a_b)}{TSR_r^2} \quad (3.27)$$

Where the $TSR_r = \frac{\Omega r}{v}$ is the local speed ratio at radius r_b , when $R_b = r_b$ local speed ratio becomes the TSR.

3.2.1.5 Vector behaviour

In the previous sections, we treated wind speed as a simple scalar value. However, it is important to note that wind speed is actually a vector with three components. Fig. 3.4 illustrates this vector decomposition.

When calculating the torque, only the horizontal components of the wind velocity play a role, as the vertical component is in the same plane as the swept area and its contribution to the torque is null. Therefore, we are primarily interested in the resultant of the horizontal components of the wind velocity.

Additionally, the orientation angle of the turbine plays a role in determining the effective wind velocity experienced by the turbine. If the turbine is fixed and cannot rotate, then the angle of the turbine relative to the wind direction varies. We can measure the mismatch between the horizontal resultant of the wind velocity and the turbine's orientation angle (measured from the North) with an angle called φ . This angle represents the deviation or misalignment between the turbine's orientation and the wind direction.

3.2.2 Traditional approach

3.2.2.1 Theoretical description

The first modelling chain (known as the traditional approach in the following sections), the simplest one, has been extensively reviewed and used in the literature (Sørensen et al., 2002, Johnson, 2004, Manwell et al., 2010, Burton et al., 2011, Fu et al., 2018 among others). It is based on the assumption that the power extracted from the wind, $P(W)$, is a product of the (average) torque, $Q(N/m)$, and angular velocity, Ω (derived from Eqs. 3.23 and 3.24).

$$P = Q\Omega \quad (3.28)$$

Coming back to Eqs 3.12-3.14 we can define the torque as:

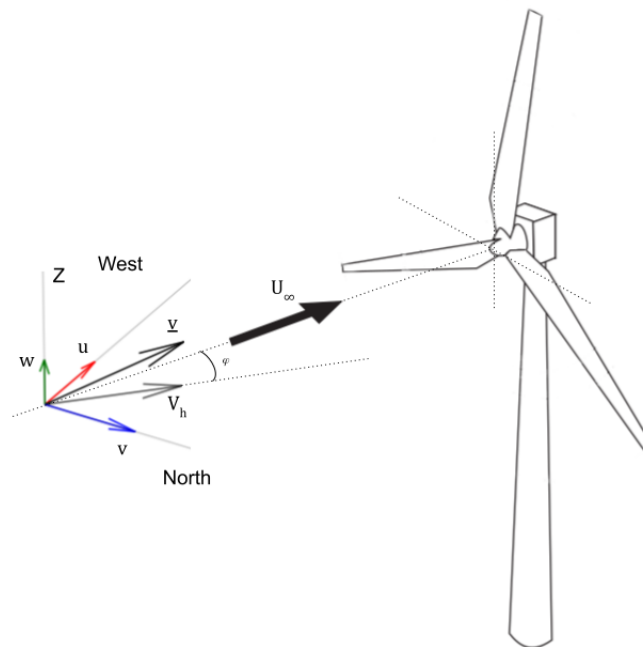


Figure 3.4: Scheme of the vector wind speed decomposition. \underline{v} represents the wind speed; u , v and w the wind components in west, north and vertical directions respectively; V_h the resultant in the horizontal plane; and U_∞ the velocity perpendicular to the swept plane of the turbine

$$Q = \frac{\frac{1}{2}\rho C_p A_d U_\infty^3}{\Omega} \quad (3.29)$$

U_∞ at hub height is typically used because that is where it is generally measured/known. However, if the wind field over the swept area is known, it is also possible to use the average wind speed.

This traditional approach does not enable to account for the spatial variability because only an average wind field is considered. So this method only takes into account the temporal variability of the field.

3.2.2.2 Tower shadow correction

The term "tower shadow" is employed to examine the impact of wind redirection caused by the presence of the tower structure. This effect is observable solely in the lower half-plane of rotation, specifically when the height is below the hub height. It reaches its maximum magnitude when any of the blades align directly in front of the mast. However, it is important to note that this alignment does not always result in a decrease in wind speed. This effect is further accentuated when the blades are positioned closer to the tower (indicated by x distance in Fig. 3.5) (Sørensen et al., 2002; Dolan and Lehn, 2006; Abo-Khalil et al., 2019). Certain studies, like the one conducted by Fu et al. (2018), have observed fluctuations in torque of approximately 8% attributable to the tower shadow effect (Fu et al., 2018).

With these assumptions wind field corrected with tower shadow effect obtained by Sørensen et al. (2002) using potential flow theory around the tower can be defined as:

$$v(y,x) = U_\infty + U_\infty m^2 \frac{y^2 - x^2}{(x^2 + y^2)^2} \quad (3.30)$$

where $v(y,x)$ (m/s) is the corrected wind horizontal field, m (m) is the radius of the tower mast, y (m) is the lateral distance of the blades, and x (m) is the distance from the blades to the mast, both y and x distances are defined in Fig.3.5.

Other expressions to model tower shadow effect have been reviewed (Sørensen et al., 2002), but we selected this because of its ability to model both deceleration near the mast and acceleration of the wind flow at each side of it.

3.2.2.3 Practical implementation

For the computation of the torque using the traditional approach, we use a wind field as input (see section 2.5 for more details) grid which covers the area swept by the wind turbine. Other inputs

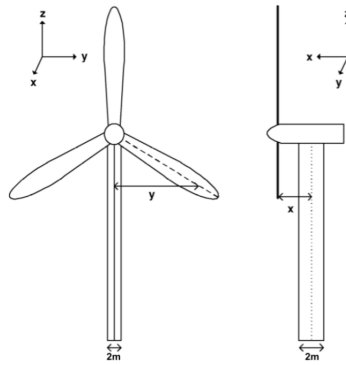


Figure 3.5: Geometry of the wind turbine used for the tower shadow correction (Adapted from Dolan and Lehn, 2006)

required for this model are the radius of the blade, the tip speed ratio and the air density. It is also possible to add the pitch angle to change the value of the power coefficient.

Tower shadow correction is implemented as an option of the model that can be used or not. It consists in a mask which multiplies the wind field grid before averaging to correct its values. It requires the geometrical properties of the wind turbine shown in Fig. 3.5.

We simulate the wind field in a point on the center of the pixel and considering it uniform over all the pixel. So each pixel of the grid contains a wind time series. An illustration of the grid is shown in the left part of Fig. 3.6.

As the wind velocity is known in several points over the swept area. To calculate the torque, we averaged the wind speed (considering it at hub-height (see Fig. 3.6) and used it in Eq. 3.29. The angular velocity is calculated from Eq. 3.16 with the assessed average wind speed. This process is repeated for the whole time series, which yields a torque time series of the same length as the original wind time series and at the same time step.

When the input wind field is a vector field we know the three components of the wind field over the pixels of the grid. Then, before averaging the field over the grid, we compute the perpendicular velocity in all the pixels as it is done in Fig. 3.4.

Illustration of the scripts developed for this method can be found in Appendix D.3.

3.2.3 Integral approach

The traditional approach helps to obtain a first approximation of the torque calculation. However, we are interested in the effect of not only the temporal but also the spatial variability of the wind. To be able to actually account for it, we have to increase the complexity of the modelling

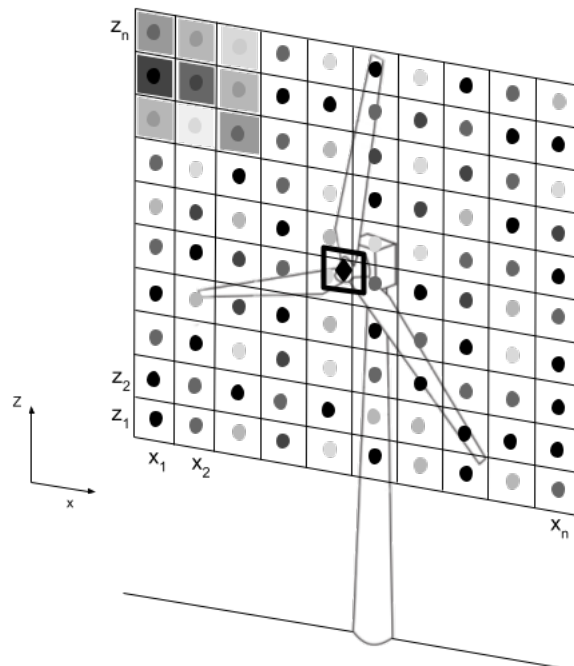


Figure 3.6: Scheme of traditional approach, points represent the wind speed simulated, squares the wind speed of the pixel (only in the upper-left corner for clarity). The diamond represents the average wind speed.

chain by considering more points along the blades instead of averaging and considering it at the center of the swept area.

3.2.3.1 Theoretical description

3.2.3.1.1 Blade element theory

Blade element theory states that it is possible to divide the blade into numerous elements where the aerodynamic forces can be calculated. It uses the 2D airfoil characteristics to compute the forces only on the cross-sectional plane of the element and neglecting the span-wise direction (Burton et al., 2011).

The tangential component of the velocity is defined by the composition of the induced tangential velocity, considered as $\Omega r_b a'_b$ in the chord of the blade, c_b , and tangential velocity of the blade, Ωr_b , due to the rotation. It varies along the radius of a blade; to compute the aerodynamic forces of each blade element, it is necessary to define the relative velocity W . Fig. 3.7a illustrates all the velocities over the blade where α is the angle of attack, i.e. the angle between the relative velocity and the chord line.

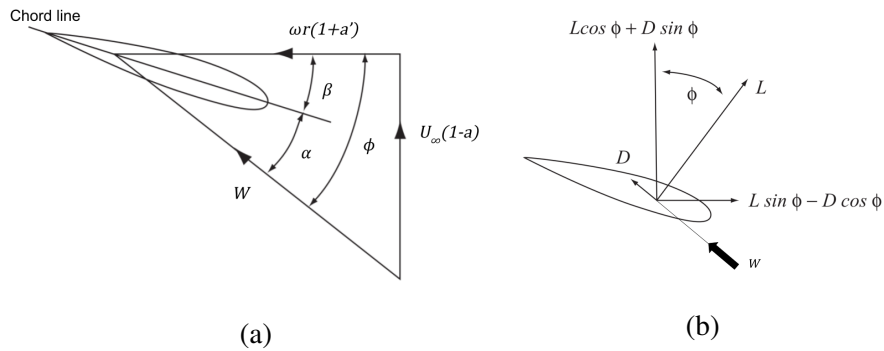


Figure 3.7: Illustration of velocities (a) and forces (b) presented in airfoil. (Adapted from Burton et al., 2011)

Using Fig. 3.7a, it is possible to define the relative velocity as:

$$W = \sqrt{[U_\infty(1 - a_b)]^2 + [\Omega r_b(1 + a'_b)]^2} \quad (3.31)$$

and,

$$\sin \phi_b = \frac{U_\infty(1 - a)}{W} \quad (3.32)$$

$$\cos\phi_b = \frac{\Omega r_b(1 + a'_b)}{W} \quad (3.33)$$

With the help of the relative velocity, we can define the aerodynamic forces. Lift, L (N), the force normal to the direction of the relative velocity and drag, D (N), the force parallel to the relative velocity (see Fig .3.7b for illustration):

$$\partial L = \frac{1}{2}\rho c_b C_L W^2 \partial r_b \quad (3.34)$$

$$\partial D = \frac{1}{2}\rho c_b C_D W^2 \partial r_b \quad (3.35)$$

Where C_L and C_D are the airfoil characteristic coefficients. Both are dependant of the angle of attack.

3.2.3.1.2 Torque computation

The second approach of computation is based on the theoretical definition of the angular moment as the product of the force and the distance at each point of the blade integrated along the radius. First, we can define the aerodynamic force T of the blade with the help of the lift and the drag (Eqs. 3.34 and 3.35) (Dolan and Lehn, 2006; Burton et al., 2011; Chaudhary et al., 2014; Akbari et al., 2022):

$$\partial T = \partial L \sin\phi_b - \partial D \cos\phi_b \quad (3.36)$$

so the torque becomes,

$$Q = \int_0^{R_b} r_b dT \quad (3.37)$$

In general Q depends of the length of the blade (R_b) and the pitch angle (β_b). However this angle can be different at each point of the blade. If we consider a fixed β_b along the blade, then Q depends only of R_b as long as the relative velocity (W) is known at each point of the blade.

To calculate the aerodynamic forces, the relative velocity of each element of the blade is used, which enables us to take into account the spatial variability of the wind field for each time step. Therefore this method allows us to account for the spatio-temporal variability of the wind field.

3.2.3.2 Practical implementation

In addition to the parameters required for the traditional approach, this method needs the number of blades, the number of elements of each blade, the aerodynamic coefficients C_D and C_L (usually given depending on the angle of attack), the pitch angle, the angle of attack and chord of the blade. Tower shadow correction can be applied using the same methodology as in the traditional approach.

In contrast to the previous method, here, the blades of the wind turbine are isolated rotating entities, so it is not only essential to model the wind fluctuations, but it is also necessary to model the rotation of the blades. As the blades are all fixed to the hub of the turbine, they have same angular velocity. To compute it, we use Eq. 3.16 using as the velocity the averaged wind speed over the swept area, which means a simplification considering the change of rotational speed instantaneous (neglecting any possible inertial effects) when a change in wind speed appears. This allows us to locate the blades in space at each time step.

Thanks to the blade element theory, we can discretize the blade as a finite number of elements, and to solve Eq. 3.34-3.37, the velocity at each element is required. As the wind field is not continuous, we linearly interpolate the velocity of the four nearest grid points of the blade element to compute it. Fig. 3.8 illustrates the process.

The torque is calculated by computing the discrete integral of the torque for each blade and adding the value of each blade.

It is possible to take into account the vector behaviour of the velocity field by considering the reference system over each blade point. This means considering the u and v components of the wind speed and the resulting wind speed with respect to the geographical angle of the turbine.

Scripts developed for this method can be found in Appendix D.3

3.2.4 OpenFAST

OpenFAST is an open-source software developed by the USA's National Renewable Energy Laboratory (NREL). It is based on FAST v8, which enables the simulation and analysis of a wide range of configurations, including different numbers of blades, types of blade profiles, control systems (pitch, stall), and structural properties (Jonkman et al., 2022).

OpenFAST utilizes advanced engineering tools by integrating multiple models, enabling the execution of nonlinear aero-hydro-servo-elastic simulations in the time domain. Fig. 3.9 provides an overview of the modules available in OpenFAST and their corresponding inputs and outputs. The aerodynamic models rely on wind-inflow data to calculate aerodynamic loads and rotor-wake effects. Hydrodynamics, on the other hand, is primarily utilized for addressing offshore configu-

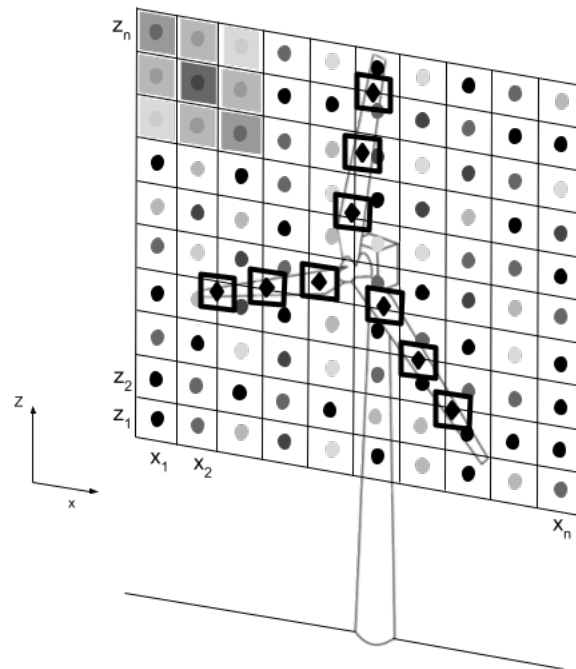


Figure 3.8: Scheme of Integral approach, points represent the wind speed simulated, squares the wind speed of the pixel (only in the left-up corner for clarity). The diamonds represent the wind speed over the blade points (interpolated using four nearest points)

rations, including diffraction, hydrostatics, radiation, and viscous loads. It also simulates incident waves and currents. The control and electrical system (servo) dynamics models analyze various control systems, such as nacelle-yaw and generator-torque control. These models simulate sensors, actuators, and controller logic devices, along with the operation of electrical system components. The structural (elastic) dynamics module leverages the results obtained from the previous modules to simulate the structural elasticity of the wind turbine's components (Jonkman et al., 2022).

OpenFAST incorporates FAST.Farm, a valuable extension that enables the simulation of wind farms across various scenarios, including land-based, fixed-bottom offshore, and floating offshore wind farms. This capability empowers users to make predictions regarding wind farm performance and assess fatigue loads for each individual turbine within the wind farm.

3.2.4.1 Overview of theoretical description

Full description of the operation can be found in Jonkman et al. (2022) and in Jonkman et al. (2015) (for aeroDyn module), we summarize here some of their properties.

AeroDyn is the time-domain aerodynamic module employed within OpenFAST to model wind turbine aerodynamics. It can also operate as a standalone code, enabling the simulation of aero-elastic behavior in horizontal axis wind turbines. When integrated into OpenFAST, it can be linearized as part of a fully linearized solution. This module extends its capabilities to simulate the hydrodynamic properties of marine hydrokinetic (MHK) turbines, including specific cavitation effects that are not applicable to wind turbines.

AeroDyn operates by receiving real-time structural information, encompassing velocities, positions, and orientation data for blades, the hub, and the tower from analysis nodes. It also takes in properties of the free stream fluid flow through the driver code. At each time step, AeroDyn calculates the aerodynamic loads acting on the structures and feeds this information back to OpenFAST. When used in standalone mode, AeroDyn assumes that the turbine geometry involves a one-, two-, or three-bladed rotor with a hub and an undeflected, straight, and vertically oriented tower. In this mode, aerodynamic and elastic inputs are not coupled.

AeroDyn is comprised of four sub-modules, which cover rotor wake/induction, blade airfoil aerodynamics, the impact of the tower on airflow, and tower drag.

3.2.4.1.1 Wake modelling

Aerodyn models the rotor wake using two different approaches. By default, It uses the Blade element momentum theory, but it is also possible to use the Generalized Dynamic Wake model.

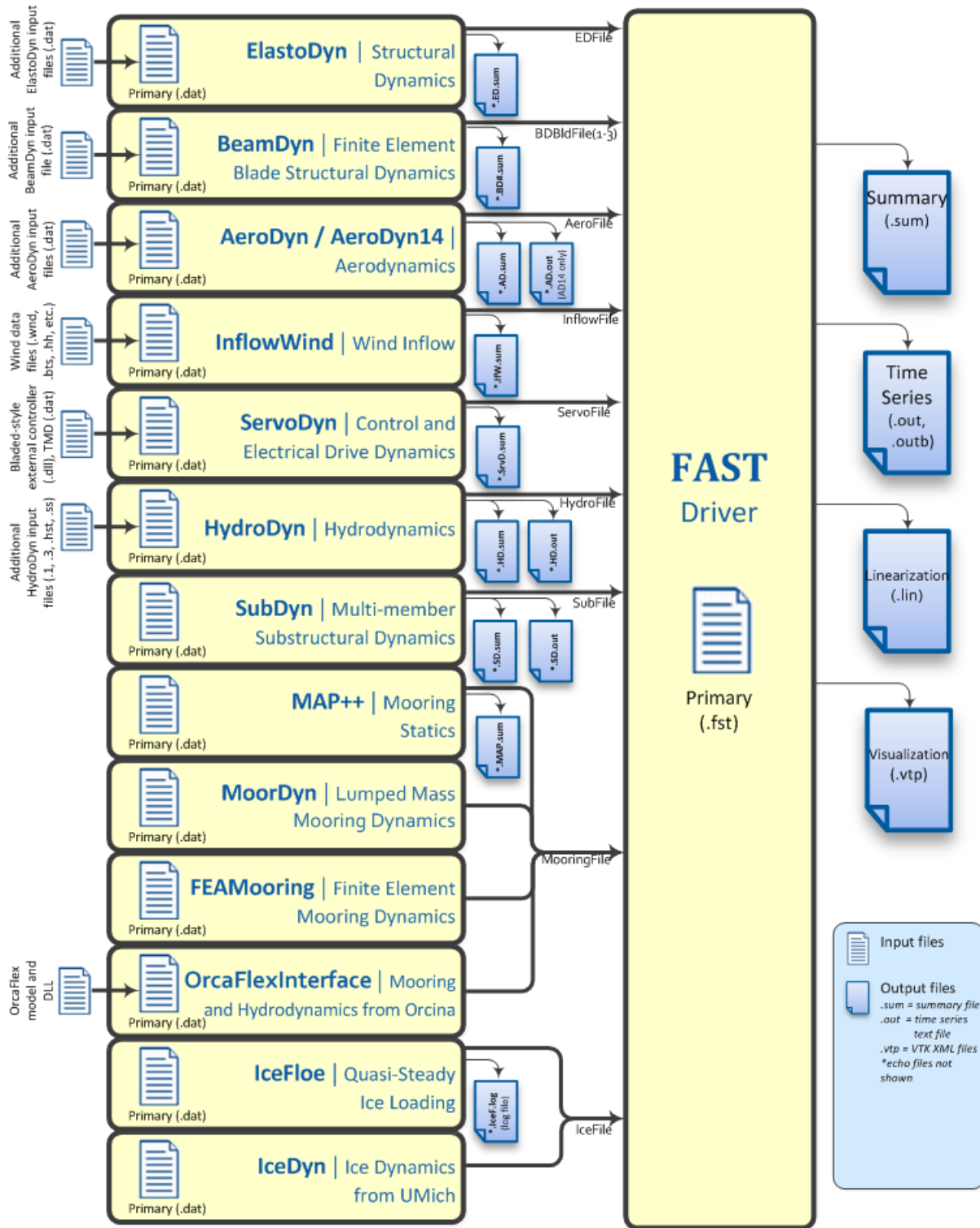


Figure 3.9: Scheme of the available modules on OpenFAST (from Jonkman et al., 2022)

Blade Element-Momentum theory

Blade Element-Momentum theory combines the Blade element and the Momentum theories (already reviewed in this chapter) with the basic assumption that the change of momentum in a blade element is only related to the force on this element (Burton et al., 2011). For this, it is also necessary to assume that there is no interaction between the flows through the contiguous annulus.

It translates into the velocities calculated using momentum theory affecting aerodynamics force calculated in blade element theory.

The axial component of the aerodynamic force can be written as (following Fig. 3.7b):

$$\partial L \cos(\phi_b) + \partial D \sin(\phi_b) = \frac{1}{2} \rho W^2 c_b N (C_L \cos \phi_b + C_D \sin \phi_b) \partial r_b \quad (3.38)$$

Where N is the number of blade elements. Coming back to Eq. 3.4 and adding the drop in pressure due to the effect of the radius, then, the axial component of aerodynamic force is equal to:

$$2\rho U_\infty^2 a_b (1 - a_b) \partial A_d + \frac{1}{2} \rho (2a'_b \Omega r)^2 \partial A_d \quad (3.39)$$

where $\partial A_d = 2\pi r_b \partial r_b$

Then equating the two expressions, we obtain:

$$\partial L \cos(\phi_b) + \partial D \sin(\phi_b) = 4\pi \rho [U_\infty^2 a_b (1 - a_b) + (a'_b \Omega r)] r_b \partial r \quad (3.40)$$

Similarly we can define the torque with the help of the Eq. 3.23 and Eq. 3.37 writing the expression as:

$$\partial Q = (\partial L \cos(\phi_b) - \partial D \sin(\phi_b)) r_b = \frac{1}{2} \rho W^2 c_b N (C_L \cos \phi_b - C_D \sin \phi_b) r_b \partial r_b = 4\pi \rho U_\infty (\Omega r) a'_b (1 - a_b) r^2 \partial r \quad (3.41)$$

Aerodyn solves Eq. 3.40-3.41 iteratively for induced velocities and forces in each blade element, i.e. solving the unknown induction parameters (a_b and a'_b). However, this method has some limitations. To face them, Aerodyn uses some corrections to compute the torque:

- The tip-Loss model is used to compensate for the effect of the vortex in wake-induced velocities; this effect is most significant near the tip, which is the zone with the most significant

influence on power production. Tip-Loss corrections are based on a Prandtl theory (see Glauert, 1935 for more details) adding a factor F to Eq. 3.40-3.41. Aerodyn counts with empirical correction (Xu and Sankar, 2002) based on Navier-Stokes equations (This solution is based on specific turbine design and may not work for all turbines).

- The hub-Loss model relies on the same principle as Tip-loss but alleviates the vortex effect in wake-induced velocities near the hub and could be coupled with the Tip-Loss factor to obtain the Total-Loss effect.
- Glauert correction (Glauert, 1926) is known as an empirical correction in thrust coefficient to compensate for the propagation of part of flow upstream when it enters in turbulent wake state (induction factor, a , is more significant than 0.5). This effect usually occurs when turbines operate with high tip speed ratios (TSR). Corrections developed in more recent studies (Buhl Jr, 2005) are used in Aerodyn.

Generalized Dynamic Wake

The other form to calculate the effect of rotor wake is the Generalized Dynamic Wake (GDW). It allows us to model other aspects taken as correction in BEM theory, like dynamic wake effect, translated as time-lags produced by the effect of shed vorticity from the blades in downstream induced velocity, tip-losses or skewed wake aerodynamics. GDW is based on a theory of Peters and He (1991) using a potential flow solution to the Laplace equation. This solution allows computing pressure distribution equations in the rotor plane. This pressure distribution represents an advantage to BEM theory.

As occurs in BEM theory, the GWD model also has limitations. When wind turbine behaviour approaches to turbulent wake state (at low velocities), induced velocities are no longer small compared with free stream flow velocity and leads to instability of the method. AeroDyn switches to the BEM method at velocities lower than 8 m/s to avoid this computational instability. GDW model also relies on BEM to solve wake rotation as it cannot solve it alone. Moreover, significant coning of the blades and aeroelastic are not well modelled because GDW assumes the rotor plane as a flat disk.

3.2.4.1.2 Blade aerodynamics

The computation of blade aerodynamics in AeroDyn relies on pseudo-2D properties of the local airfoil. This approach is considered pseudo-2D because it also allows for modifications related to 3D properties, such as aspect ratio and rotational augmentation. AeroDyn provides two available solutions to calculate these aerodynamics: static airfoil tables and dynamic stall models.

AeroDyn uses static airfoil solutions in the form of tables for lift, drag, and sometimes pitch moment coefficients as a function of Reynolds number (RE) and angle of attack. These tables allow us to compute all the coefficients for a given angle of attack using linear interpolation. Data from the wind tunnel is extrapolated to increase the range of angles available (i.e. completing the range $\pm 180^\circ$), assuming that the airfoil acts like a flat disk at high angles of attack. For this extrapolation, AeroDyn uses FoilCheck (NREL program developed by Laino and Hansen 2004) based on Viterna and Janetzke (1982) the equations:

$$C_{D_{max}} = 1.11 + 0.08AR \quad (3.42)$$

$$C_D = C_{D_{max}} \sin^2 \alpha_b + B_2 \cos \alpha_b \quad (3.43)$$

where,

$$B_2 = \frac{C_{D_s} - C_{D_{max}} \sin^2 \alpha_s}{\cos \alpha_s} \quad (3.44)$$

Being AR the aspect ratio of the blade, denoting stall (or matching point if stall is not available) with subscript s , and taking C_L as

$$C_L = \frac{C_{D_{max}}}{2} \sin 2\alpha + A_2 \frac{\cos^2 \alpha_b}{\sin \alpha_b} \quad (3.45)$$

where,

$$A_2 = (C_{D_s} - C_{D_{max}} \sin \alpha_s \cos \alpha_s) \frac{\sin \alpha_b}{\cos^2 \alpha_b} \quad (3.46)$$

Aerodyn enables having a set of airfoil data tables for each element of the blades taking into account the variation along the blade span; however, all the blades are treated with similar behaviour (Jonkman et al., 2015).

Tables accepted by Aerodyn use two inputs. One of them must be the angle of attack, but the other varies from RE to aileron or flap settings. When RE is used, the interpolation is done based on the RE of each element.

The dynamical stall model is a semi-empirical model that relies on the initial response of airfoil following theory developed by Leishman and Beddoes (1989). This response produces a normal

force coefficient (C_N), divided into circulatory (C_N^C) and non-circulatory (C_N^I) components, and moment force coefficient (C_M) as a function of change in angle of attack ($\Delta\alpha$). From C_N^C in the Beddoes-Leishman model, it is possible to derive the chordwise force component(C_C). Then aerodynamical coefficients (C_L and C_D) are computed with the help of C_N and C_C as:

$$C_L = C_N \cos \alpha_b + C_c \sin \alpha_b \quad (3.47)$$

$$C_D = C_N \sin \alpha_b - C_c \cos \alpha_b + C_{D0} \quad (3.48)$$

Where C_{D0} is the minimum drag coefficient.

3.2.4.1.3 Tower shadow correction

Aerodyn, and lately OpenFAST, models the effect of the tower on the wind turbine aerodynamics using a different method as we use for the other two approaches (Section 3.2.2.2). This method uses the potential flow solution dependent on the drag coefficient of the tower, C_d , for downwind influence and a tower dam model for upwind influence. The model is based on the work on Bak et al. (2001), and it allows to model both increased velocity around the sides and decrease close to the tower (schematic illustration in Fig. 3.10)

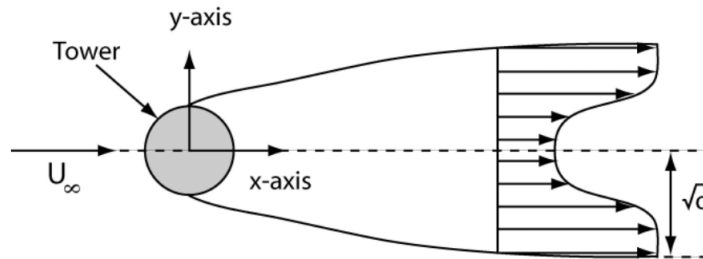


Figure 3.10: Effect of tower shadow modelled by AeroDyn (From Jonkman et al., 2015)

Influence of the tower mast upwind could be characterized with :

$$u = 1 - \frac{(x+0.1)^2 - y^2}{((x+0.1)^2 + y^2)^2} + \frac{C_d}{2\pi} \frac{x+0.1}{(x+0.1)^2 + y^2} \quad (3.49)$$

$$u = 2 \frac{(x+0.1)y}{((x+0.1)^2 + y^2)^2} + \frac{C_d}{2\pi} \frac{y}{(x+0.1)^2 + y^2} \quad (3.50)$$

Where u and v represent wind components horizontal x and y directions, x and y represent normalized distances in both directions.

For downwind influence modelling, equations may be written as:

$$u_{wake} = \frac{C_d}{\sqrt{d}} \cos\left(\frac{\pi}{2} \frac{y}{\sqrt{d}}\right)^2 \quad for |y| \leq \sqrt{d} \quad (3.51)$$

or

$$u_{wake} = 0 \quad for |y| > \sqrt{d} \quad (3.52)$$

being

$$d = \sqrt{x^2 + y^2} \quad (3.53)$$

Where d is the dimensionless radial distance to center tower.

Finally velocity components at local points with the tower effects are written as

$$U_{local} = (u - u_{wake})U_{\infty} \quad (3.54)$$

$$V_{local} = (v - v_{wake})v_{\infty} \quad (3.55)$$

3.2.4.2 Practical implementation

The inputs required for this model include the wind fields, as well as the necessary files for the OpenFAST software, as specified in the input section of the .fst file (as shown in Appendix A). These files are needed for various modules within OpenFAST, such as Aerodyn, ElastoDyn, BeamDyn, ServoDyn, or Inflow. The rest of the modules are kept unused.

Indeed, to input the wind field simulated in OpenFAST, an intermediate step is required to adapt the wind format to meet the specific requirements of OpenFAST. In this case, TurbSim is used to perform this adaptation and generate a file format that is readable by OpenFAST. For that reason, the drive code of TurbSim, (reviewed in Section 2.3) is also necessary for this process.

Once the formatting is finished, the wind field is now inputted in OpenFAST, which gives as output, among others, the torque time series. OpenFAST also requires an input file which gives the

information about the blade properties (required by BeamDyn and Aerodyn modules), the control system and electric behaviour of the turbine (required by ServoDyn module); and structural properties of the wind turbine (required by ElastoDyn module). For simplicity, we use the reference wind turbine of 1.7MW provided by the NREL (Quon and Abbas, 2021), inputting only the simulation length and the type of wake computation (BEM) for the Aerodyn module.

For this method, we create a Bash script which allows us to run the whole model using as input the wind field simulated and the length of the simulation. This script also allows us to do an ensemble of simulations, wherein the number of samples is also needed. It is composed of three parts, a python script which writes the input file of the TurbSim (.inp file), Turbsim simulation, which adapts the wind field to OpenFAST (.bts file), and OpenFAST simulation.

3.2.5 Summary

Table 3.1 shows a summary of the inputs required for each of the torque computation methods review in this chapter. It also summarize the variability they are able to take into account.

Method	Input	What take into account
Traditional	Wind field Atmospheric properties (ρ) Properties of the turbine (r_b , hub height, TSR, β_r)	Time variability
Integral	Wind field Atmospheric properties(ρ) Properties of the turbine (r_b , hub height, TSR, β_b , α_b , c_b) Aerodynamic coefficients (C_L , C_D)	Space-Time variability
OpenFAST	Wind field Driver codes of Turbsim Driver codes of all the modules used in OpenFAST	Space-Time variability

Table 3.1: Summary of the input required by the different methods of torque computation and the type of variability they take into account

3.3 Validation of modelling chains

3.3.1 Properties of the simulations

Prior to commencing the validation tests, we shall elucidate the atmospheric and geometric parameters that underpin the torque calculation. The air density (ρ) is set at $1.225 \text{ kg}, m^{-3}$, in accordance with standard atmospheric conditions. Leveraging data from the RW_Turb measurement campaign, specifically the Vestas V90 turbine model (A/S, 2010), we incorporate its blade radius (45m), blade chord (3.5m), and hub height (78m) for the simulation. Conforming to the suggested value in Yurdusev et al. (2006), we set the Tip-Speed Ratio (TSR) at 7. Furthermore, drawing insights from Sudhamshu et al. (2016), which posits the optimal pitch angle for the turbine lies within 5° and 20° for the speed range under consideration, we establish it at 12° .

In the context of the integral approach, We divided the blade into 27 equidistant points spanning from the hub to the tip. It is noteworthy that the airfoils of horizontal axis wind turbines (HAWT) are typically designed for operation at low angles of attack, attributed to the elevated lift coefficients and reduced drag coefficients (Manwell et al., 2010). Consequently, an angle of attack of 5° is selected, complemented by aerodynamic coefficients of $C_L = 1.1$ (lift coefficient) and $C_D = 0.022$ (drag coefficient).

In addition, since the Vestas V90 is a 2 MW wind turbine, the 1.7 MW reference wind turbine provided by NREL (Quon and Abbas, 2021), which has similar characteristics, is used for the OpenFAST simulations.

3.3.2 First tests with uniform fields

To validate the functioning of the three modelling chains, we first use as input a uniform wind field. For this purpose, we reconstructed a grid over the swept area with the time series of x-component(u) wind speed values recorded on 16/12/2020 during the RW-Turb measurement campaign (see section 2.2 for a complete description of the campaign). We selected this type of wind for these initial tests because the traditional approach is not able to account for any spatial variability.

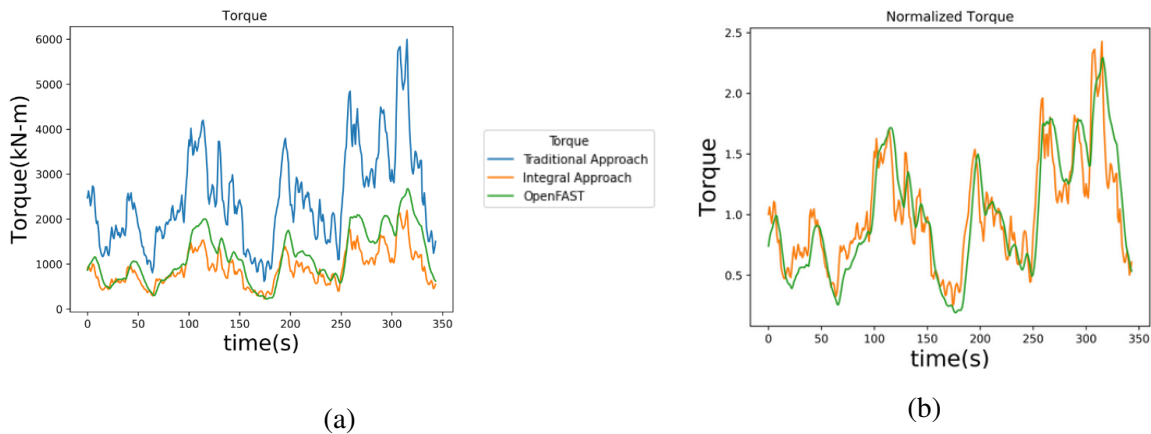


Figure 3.11: (a) Example of torque time series computed with different methods and (b) normalized time series (for an event that started on 16/12/2020 at 10h 14min 24s UTC). In 3.11b Traditional approach and Integral approach are overlapping

Fig 3.11a shows the torque time series calculated with the traditional approach in blue, with the integral approach in orange and OpenFAST in green for this event (which started on 16/12/2020 at 10h 14min 24s). We found greater values for the traditional approach and similar results for the integral approach and OpenFAST. However, although the values are different for each modelling chain, the trends of the time series are similar.

These differences appear because although we use the same wind input and similar wind turbine's geometrical properties, their modelling principles are not exactly the same and, consequently, the required parameters for each modelling chain are also different. For the traditional approach the module varies related to the pitch angle and the tip speed ratio used. For the integral approach the module further varies with aerodynamic coefficients. Finally, OpenFAST depends on a series of parameters (grouped in different drive code files) which models the wind turbine's design in several aspects (eg. aerodynamic properties, structural properties, electrical system ... etc.). The trends of simulated torque time series of these modelling chains are similar because we can group all these parameters as a prefactor to the wind speed, since they are kept constant over the simulation.

Fig. 3.11b shows normalized torque used to remove the effect of different prefactors on which we will not focus in this work, as we are focusing on the variability of the fields. A very good agreement between all the methods is obtained; we found the same values for traditional and integral approaches and no significant differences between traditional and OpenFAST. We found similar results over different time series analyzed with a perfect correlation between traditional-integral and an average correlation of 0.85 with OpenFAST. However in Fig. 3.11b two main difference are visible. First one is related to the fluctuations at small scales, where OpenFAST present less pronounced ones. This is fully addressed in section 3.4 through the parameter H . The other is a

time shift between the first two methods and OpenFAST, which is discussed below.

We repeated this methodology for the validation of the modelling chains using vector wind field. For that, we used the horizontal components (u , oriented to the West, and v , oriented to the North Fig. 3.4) for the same day and recorded under the same conditions as the scalar case. Fig. 3.12 shows the normalized torque obtained with the three modelling chains for different angles of the turbine. Both figures show similar behaviour as in the scalar case but with a small decrease in the torque obtained when the angle of the turbine is fixed at 50° . It is also translated to the level of correlation with OpenFAST (~ 0.82 and 0.77 from left to right).

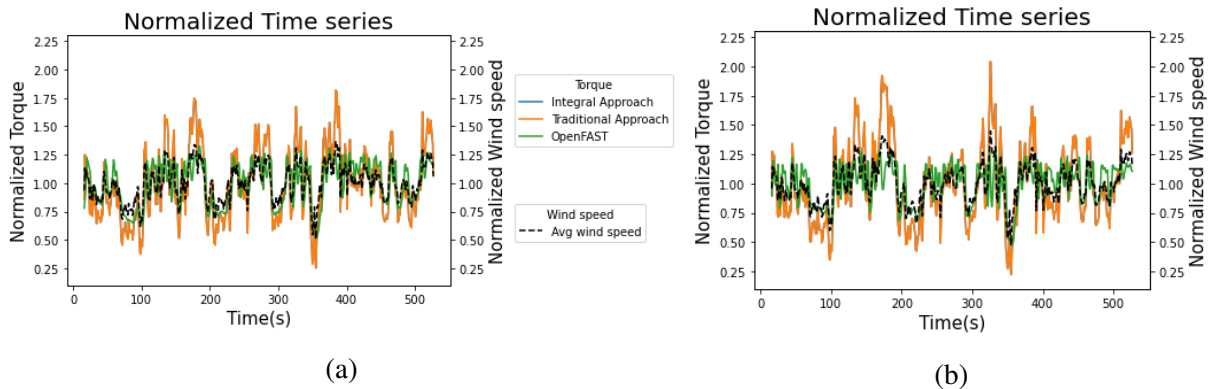


Figure 3.12: Example of normalized torque time series (for an event that started on 16/12/2020 at 10h 14min 24s UTC) computed with different methods for (a) a turbine angle of 50° and (b) a turbine of angle 30° . Traditional and Integral approaches obtain the same value and overlap.

In 3.12 and specially in Fig. 3.11 is possible to see a tiny shift on the torque obtained in OpenFAST. To measure this effect, we introduce some lag in the torque result to shift the time series trying to find a better correlation between the various simulated torque series. Table 3.2 summarizes the correlation between OpenFAST and the traditional approach under different lags. It appears that a 2 s shift on OpenFAST maximises the correlation in both scenarios, suggesting that this is the real time shift between the first two modelling chains and OpenFAST. This time shift is likely to be caused by the inertial forces accounted by the realistic model. It means that the change in tangential velocities are not directly translated into a change in angular velocity as it is done for the first two modelling chains. Accounting for the time shift yields to increase the correlation from 0.85 to 0.89 between OpenFAST and the other two methods.

Lag (s)		0	1	2	3	4	5	6	7	8
Correlation	T50	0.82	0.88	0.90	0.87	0.84	0.80	0.76	0.72	0.62
	T30	0.77	0.84	0.87	0.86	0.83	0.79	0.74	0.70	0.67

Table 3.2: Correlation between OpenFAST and traditional approach with different Lags. T30 and T50 represent the angle of the turbine (for an event that started on 16/12/2020 at 10h 14min 24s UTC).

3.3.3 Test of input parameters

To ensure the correct functioning of the modelling chains these tests are not enough. Due to the fact that integral approach script is developed from scratch sensitivity tests to the input parameters are needed to confirm that the modelling chain is working as expected. First, we check how the wind speed inputted affects the torque computation. For this test we use a 1024s uniform vector field multiplied by a prefactor. Fig. 3.13 illustrate this test obtaining the expected results, i.e. the torque increase with the increasing velocity but in a non-linear way, approximately proportional to v^2 (Manwell et al., 2010) as it is shown in Fig. 3.13b where the regression of the torque over v_{wind}^2 is a straight line.

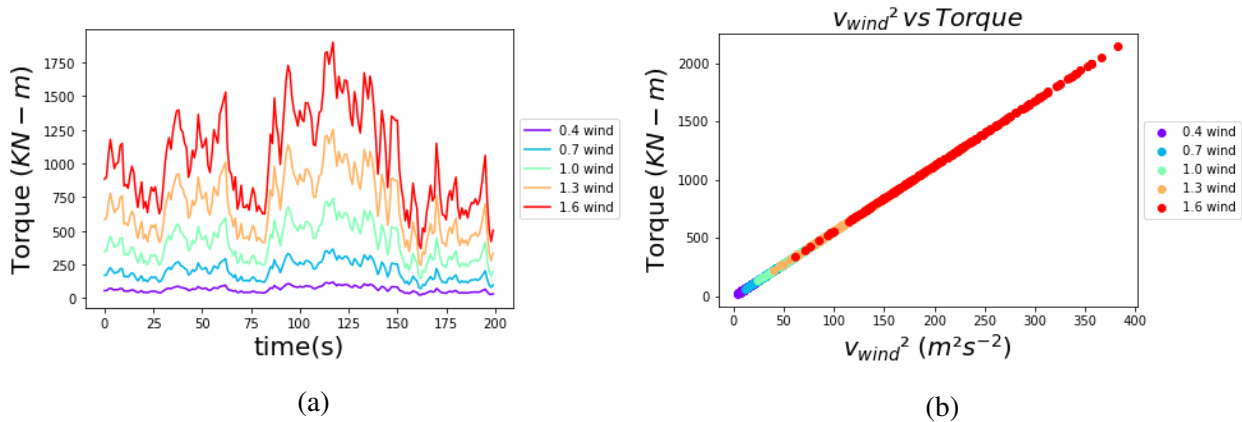


Figure 3.13: (a) Example of torque time series computed with a uniform vector field (for an event that started on 16/12/2020 at 10h 14min 24s UTC) with increasing wind speed. (b) Plot of the computed torque vs. v^2

Other important test is how the angle of the turbine affects the computation of the torque. For that, we prepare two different tests illustrated in Fig. 3.14:

- First, we fix the angle of the wind forcing the two components to be the same (angle= 45°) and computing the torque changing the angle of the turbine. In Fig. 3.14a we can see that when

angle of the turbine moves away from the angle of the wind, a decrease on the torque appear. We can note that the decrease is symmetric with the distance to the angle. It is illustrated in the figure by pairs (shifted 2.5° to avoid overlapping) e.g. red and purple or orange and blue.

- The second one, uses different components of the wind of the same event as in section 3.3.2 (16/12/2020), i.e. the angle of the wind change each time step, and we compute the torque also changing the angle of the turbine. Fig. 3.14b shows that when the angle of the turbine is 0° the torque is proportional to the square of the North component of the wind, analogously with 90° and West component. All the angles in between show the transition from one to the other component.

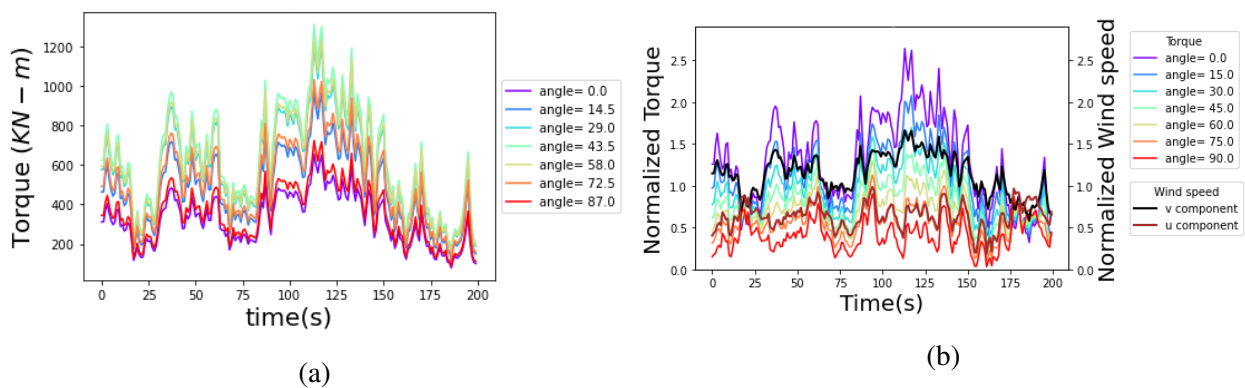


Figure 3.14: Example of torque time series computed with a uniform vector field (for an event that started on 16/12/2020 at 10h 14min 24s UTC): (a) fixing the angle of the wind and changing the angle of the turbine; and (b) with wind angle changing each time step and changing the angle of the turbine

3.3.4 Test with non-uniform fields

In the final test, non-uniform wind fields are used, which are simulated using the FIF method described in section 2.5.1. These wind fields exhibit spatial variability. Fig. 3.15 illustrates an example of the normalized torque simulated using UM parameters $\alpha = 1.5$ and $C_1 = 0.1$, with a target wind velocity of 11 m/s .

In the figure, a decrease in correlation between the traditional approach and both the integral approach and OpenFAST can be observed (from 1 and 0.89 to 0.95 and 0.8 respectively). However, there is good agreement between the trends exhibited by the three methods and the average wind speed inputted (averaged over the grid).

This test provides a qualitative understanding of the impact of spatial variability on the different methods. As seen in Fig. 3.15, the integral approach exhibits the strongest fluctuations. However,

a more detailed quantitative analysis will be carried out in section 3.4 to further evaluate the effects of wind spatial variability.

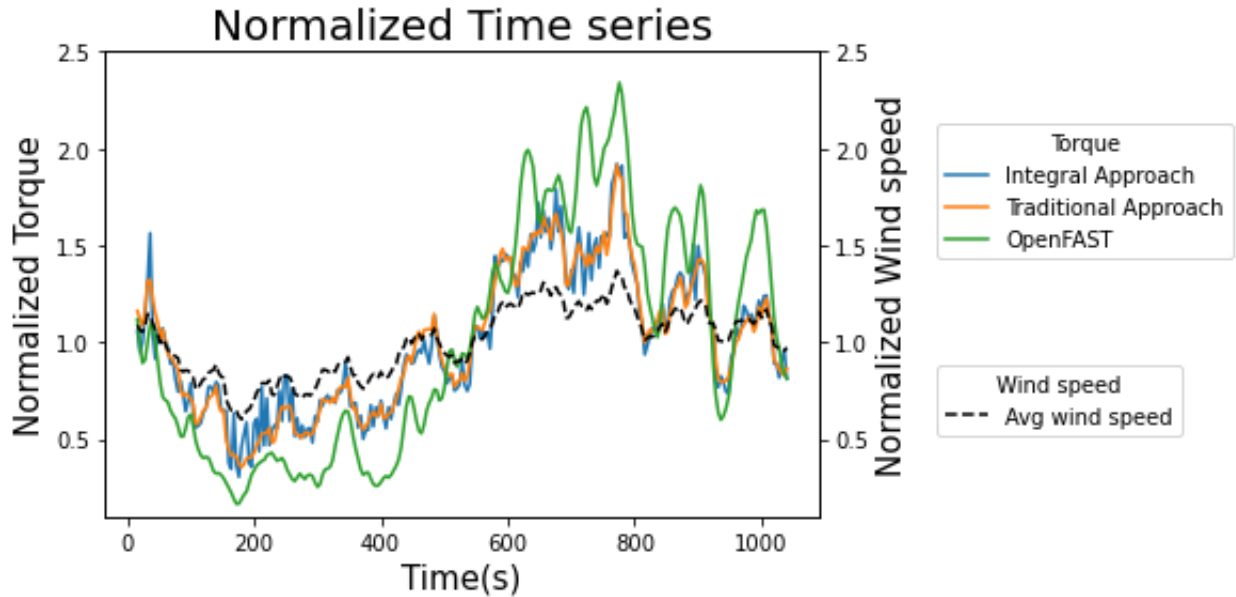


Figure 3.15: Example of normalized torque time series computed with different methods using as input wind fields simulated using the FIF approach and input parameters $\alpha = 1.5$ and $C_1 = 0.1$, and target velocity of 11 ms^{-1} .

3.4 Results & discussion

In this section, we will explore how the different methods of torque computation respond to the variability observed in the wind fields. To conduct this investigation, we will use vector wind fields simulated using the FIF approach (as described in Section 2.5). These wind fields will be generated with different sets of parameters, specifically varying α and C_1 , while keeping H and a equal to $1/3$, as these values are commonly observed in the literature (Schmitt et al., 1994, Lazarev et al., 1994). This approach will allow us to analyze the behavior of the torque computation methods under different levels of wind field variability.

The input wind fields encompass a square grid with a side length of 90 meters and consist of 27 points in each spatial direction. The temporal dimension of the wind fields spans 1024 seconds. However, for the analysis, we will focus on a specific time range from 4 seconds to 17 minutes (since $17 \text{ min} \sim 1024\text{s}$), which is selected based on the wind properties (as discussed in Section 2.2).

Due to the computational demands of the OpenFAST software, we will divide this section into

two parts. In the first part, we will utilize ensembles of 10 wind field samples and employ the three methods of computation for analysis. In the second part, we will increase the ensemble size to 100 wind field samples and only use the Traditional and Integral approach.

To gain a comprehensive understanding of the behavior of the torque computation methods, we will analyze not only the torque time series but also examine the horizontal wind at a specific point in the grid. Additionally, we will analyze the average wind field across the spatial dimensions to facilitate a comparison of the results. By considering these additional analyses, we can evaluate how the different methods respond to the wind field variability and assess their overall performance.

3.4.1 Results using 10 samples

This section consists in analysis with 4 set of parameters, one with the traditional values $\alpha = 1.55$ and $C_1 = 0.05$, one with greater values of α as $\alpha = 1.8$ and $C_1 = 0.05$, one with lower values of α as $\alpha = 1.1$ and $C_1 = 0.05$ and finally one with greater values of C_1 as $\alpha = 1.5$ and $C_1 = 0.3$.

To avoid redundancy, one example of the analysis will be presented in the main body of the thesis, specifically in Figs. 3.17 to 3.21. The analysis consist in implementing three different techniques (see Section 1.4 for a description of the different analysis techniques) for the punctual velocity, the average velocity, the Traditional approach, the Integral approach, and OpenFAST. In panels (a), a spectral analysis is visible, from which a good scaling is appreciated for this range of scales. The slope of this figures the parameter H is computed using Eq. 1.75. In panels (b), a TM analysis is displayed. We used a correction based on the methodology presented in 1.4.3.3 to maximize the quality of the scaling. One example is showed in Fig. 3.16 where the coefficient of linear regression increases from $r^2 = 0.9$ before the correction (Fig. 3.16a) to $r^2 = 0.99$ after (Fig. 3.16b).

Finally panels (c) and (d) display DTM analysis from which the UM parameters are computed. The figures of the remaining analysis exhibit similar patterns in general and are included in Appendix C.

Tables 3.3 to 3.6 present the retrieved parameters from the analysis of the five fields. It is notable that the scaling is generally good for all the methods across the different parameter sets (once the correction presented in Section 1.4.3.3 is implemented). The quality of the scaling is illustrate in panels (b) and (c) of Figs. 3.17 to 3.21. In cases where the scaling decreases to $r^2 \sim 0.97$ for the punctual velocity, this may be attributed to the reduced number of samples. Indeed, this issue is resolved in the case of 100 samples, as discussed in Section 3.4.2. It is worth mentioning that the integral approach consistently yields the best scaling obtaining $r^2 > 0.99$ across all the parameter sets. These tables show an improvement of the quality of scaling from the original field to the corrected one.

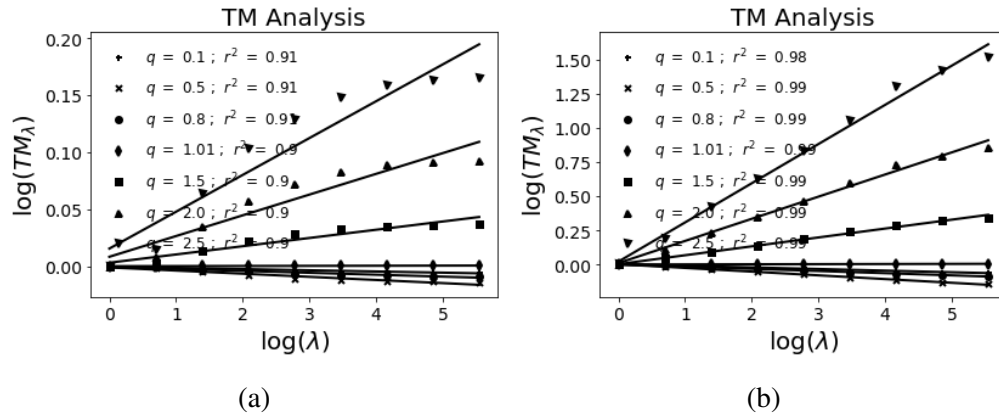


Figure 3.16: Illustration of the correction in torque data TM graphs of (a) before the correction and (b) after. The field used is the torque computed using Traditional Approach and input parameters $\alpha = 1.55$, $C_1 = 0.05$, and $a = H = 1/3$.

Looking at the values of α , a notable observation is the difference of approximately 0.1 between the punctual velocity and the average velocity. Similar trends are observed between the traditional approach and the integral approach. In Tables 3.3 and 3.5, the values obtained by the integral approach align more closely with the punctual velocity, while the traditional approach aligns better with the average velocity. In Table 3.4, the integral approach yields values that are closer to the velocity results. As the simulations involve higher values of C_1 , a bias becomes evident between the results of the velocity fields and the torque computation methods. It is possible to see a decrease of the slope in the curves Fig. 3.22 due to a plateau in the upper right part of them which results in a smaller value of the parameter α . Furthermore, OpenFAST consistently exhibits lower values of α , with an average decrease of around 0.4 compared to the average velocity (except in Table 3.5). This can be explained in the same way as the plateau of figure 3.21d is larger than in its counterparts Figs. 3.19d and 3.20d.

Regarding C_1 , we can observe two different parameters. The first one is the retrieved parameter from the field, denoted as C_1 . The second one is the expected value assuming a relationship between velocity and torque to the power of 2 (Manwell et al., 2010, Fitton et al., 2014), using the expression $C_{1\tau} = C_1 \cdot 2^\alpha$ (Lavallée et al., 1993).

In the case of C_1 , we can see similar values between the traditional and integral approaches, while OpenFAST exhibits much higher values. When comparing to the theoretical results, there is good agreement between theoretical and empirical results in the integral approach and the traditional approach (although slightly worse), while OpenFAST obtains higher values than expected. In order to explain this discordance a deeper analysis of the software operation is needed. However, a possible explanation could be that, due to inertial forces, some fluctuations are neglected and changes in trend (i.e. from increasing speed to decreasing speed or vice versa) are delayed

causing peaks of higher intensity (in both directions) increasing the value of C_1 . This behaviour can be seen in Fig. 3.15 where the green line (OpenFAST simulation) experiences less fluctuations but with more amplitude.

The last parameter to consider is H , for which we use the parameter retrieved before the correction. In the traditional approach, higher values of H are obtained compared to the punctual velocity, which is also reported in Fitton et al. (2014). The values obtained by this method are similar to the average velocity, which is expected due to the torque is computed using the average velocity. On the other hand, in the integral approach, the values are closer to the punctual velocity. Lastly, OpenFAST retrieves the highest value of H .

This behavior is expected as the integral approach captures the strongest fluctuations by considering the spatio-temporal variability of the wind fields, while the traditional approach only considers the temporal variability. The high value of H obtained from the average wind fields may be attributed to the averaging effect. OpenFAST takes more aspects of wind turbine operation into account, including inertial forces, which means that the properties of the wind field are not directly transferred to the torque computation neglecting the fluctuations at small scales (as it is shown in Fig. 3.15) and increasing the value of H .

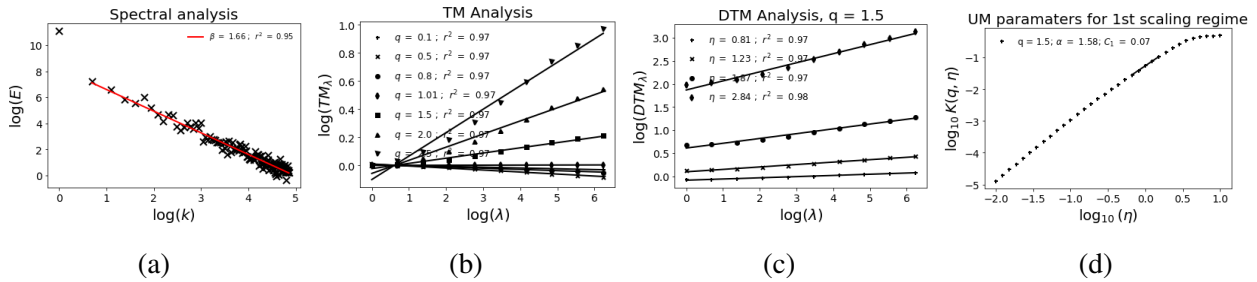


Figure 3.17: Analysis of the horizontal wind field of the center of the grid: (a) Spectral analysis (Eq. 1.21 in log-log), (b) TM (Eq. 1.6 in log-log), (c) and (d) DTM (Eqs. 1.70 and 1.72 in log-log respectively). The analysis is made on an ensemble of 10 samples and input parameters $\alpha = 1.55$, $C_1 = 0.05$, and $a = H = 1/3$.

3.4.2 Results using 100 samples

To further validate the initial results and obtain more robust findings, we increase the number of wind field samples, which will lead to more reliable and statistically significant results. Similarly to the previous section, to avoid redundancy, one example of the analysis is presented in the main body of the thesis, specifically in Figs 3.23 to 3.26. In this case the OpenFAST is not available due to the computational cost of the simulation. The remaining analyses and figures are included in Appendix C.

3. Modelling Chains

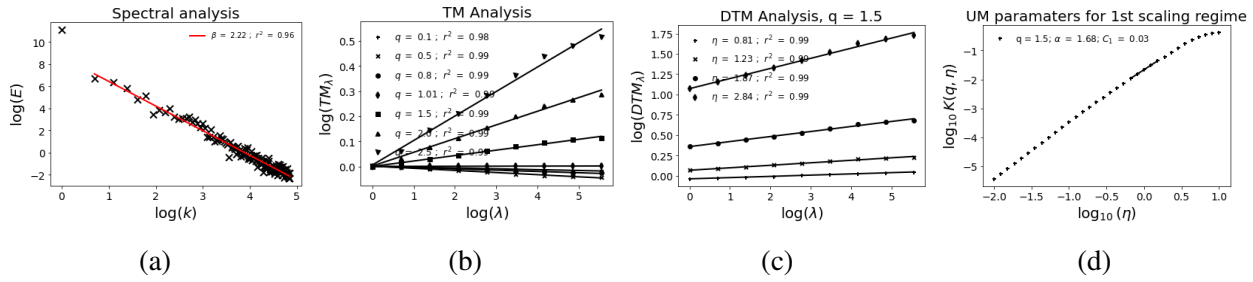


Figure 3.18: Analysis of the horizontal wind field averaged over the grid: (a) Spectral analysis (Eq. 1.21 in log-log), (b) TM (Eq. 1.6 in log-log), (c) and (d) DTM (Eqs. 1.70 and 1.72 in log-log respectively). The analysis is made on an ensemble of 10 samples and input parameters $\alpha = 1.8$, $C_1 = 0.05$, and $a = H = 1/3$.

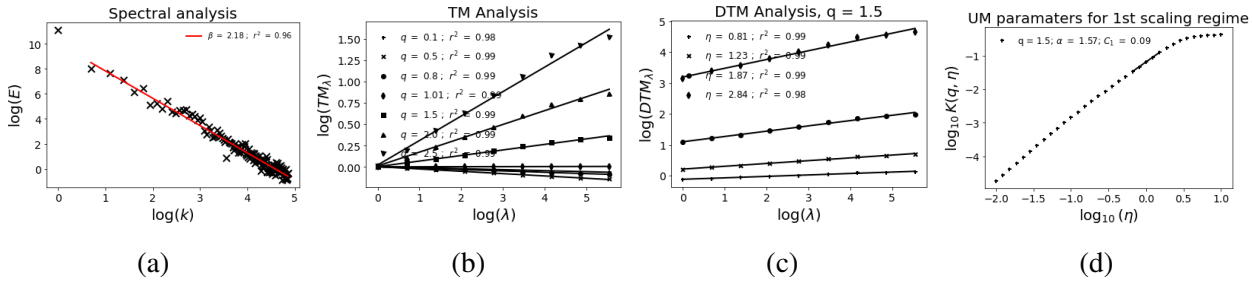


Figure 3.19: Analysis of the torque time series computed using Traditional Approach: (a) Spectral analysis (Eq. 1.21 in log-log), (b) TM (Eq. 1.6 in log-log), (c) and (d) DTM (Eqs. 1.70 and 1.72 in log-log respectively). The analysis is made on an ensemble of 10 samples and input parameters $\alpha = 1.1$, $C_1 = 0.1$, and $a = H = 1/3$.

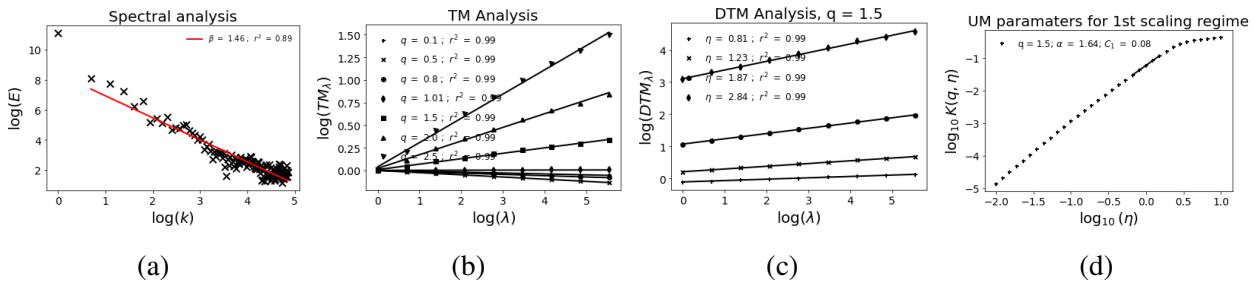


Figure 3.20: Analysis of the torque time series computed using Integral Approach: (a) Spectral analysis (Eq. 1.21 in log-log), (b) TM (Eq. 1.6 in log-log), (c) and (d) DTM (Eqs. 1.70 and 1.72 in log-log respectively). The analysis is made on an ensemble of 10 samples and input parameters $\alpha = 1.5$, $C_1 = 0.3$, and $a = H = 1/3$.

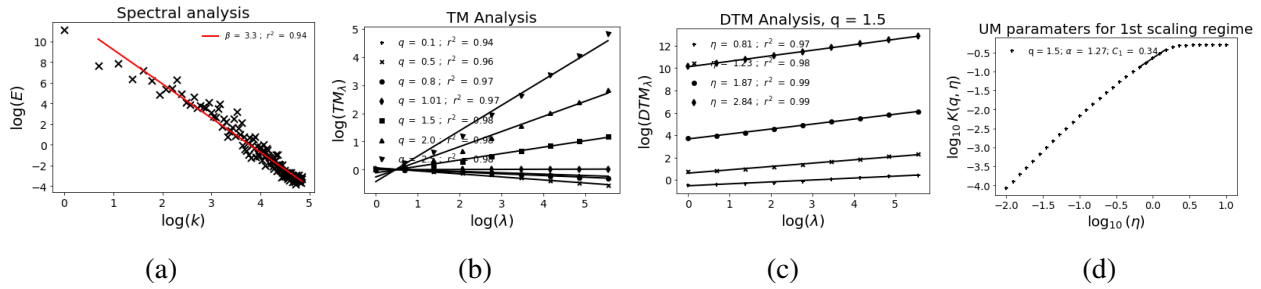


Figure 3.21: Analysis of the torque time series computed using OpenFAST: (a) Spectral analysis (Eq. 1.21 in log-log), (b) TM (Eq. 1.6 in log-log), (c) and (d) DTM (Eqs. 1.70 and 1.72 in log-log respectively). The analysis is made on an ensemble of 10 samples and input parameters $\alpha = 1.55$, $C_1 = 0.05$, and $a = H = 1/3$.

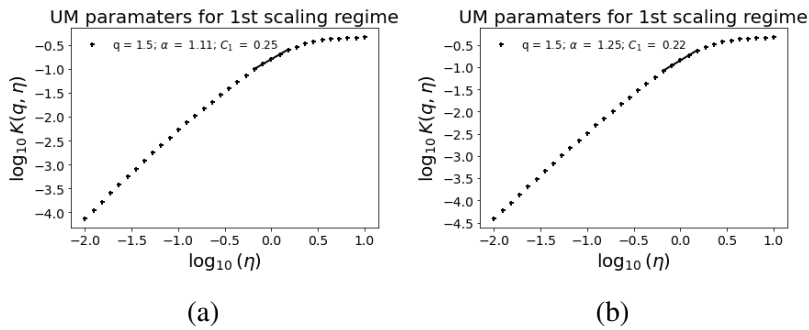


Figure 3.22: Effect of C_1 on the computation of UM parameters. The analysis is made on an ensemble of 10 samples and input parameters $\alpha = 1.5$, $C_1 = 0.3$, and $a = H = 1/3$ for the traditional and integral approaches.

Field	α	C_1	C_{1Th}	r^2	$r^2_{original}$	H
V_{point}	1.58	0.07	-	0.98	0.97	0.33
V_{avg}	1.68	0.03	-	0.99	0.89	0.66
Traditional	1.64	0.09	0.09	0.99	0.89	0.64
Integral	1.57	0.09	0.09	0.99	0.91	0.23
OpenFAST	1.28	0.34	0.07	0.98	0.88	1.04

Table 3.3: Summary of the parameters retrieved in the analysis of the time series simulated with input parameters $\alpha = 1.55$, $C_1 = 0.05$, and $a = H = 1/3$ and 10 samples. The parameter $r^2_{original}$ is computed before the correction.

Field	α	C_1	C_{1Th}	r^2	$r_{original}^2$	H
V_{point}	1.77	0.06	-	0.97	0.97	0.33
V_{avg}	1.83	0.03	-	0.98	0.91	0.63
Traditional	1.56	0.15	0.09	0.98	0.92	0.62
Integral	1.79	0.08	0.10	0.99	0.93	0.33
OpenFAST	1.44	0.35	0.08	0.99	0.91	1.14

Table 3.4: Summary of the parameters retrieved in the analysis of the time series simulated with input parameters $\alpha = 1.8$, $C_1 = 0.05$, and $a = H = 1/3$ and 10 samples. The parameter $r_{original}^2$ is computed before the correction.

Field	α	C_1	C_{1Th}	r^2	$r_{original}^2$	H
V_{point}	1.21	0.10	-	0.97	0.97	0.33
V_{avg}	1.39	0.05	-	0.98	0.90	0.66
Traditional	1.32	0.15	0.12	0.98	0.91	0.64
Integral	1.22	0.12	0.12	0.99	0.93	0.23
OpenFAST	1.20	0.25	0.11	0.99	0.83	1.04

Table 3.5: Summary of the parameters retrieved in the analysis of the time series simulated with input parameters $\alpha = 1.1$, $C_1 = 0.1$, and $a = H = 1/3$ and 10 samples. The parameter $r_{original}^2$ is computed before the correction.

Field	α	C_1	C_{1Th}	r^2	$r_{original}^2$	H
V_{point}	1.46	0.24	-	0.98	0.94	0.32
V_{avg}	1.54	0.1	-	0.99	0.89	0.61
Traditional	1.12	0.26	0.21	0.99	0.90	0.60
Integral	1.26	0.22	0.23	0.99	0.93	0.31
OpenFAST	1.02	0.28	0.20	0.97	0.90	1.11

Table 3.6: Summary of the parameters retrieved in the analysis of the time series simulated with input parameters $\alpha = 1.5$, $C_1 = 0.3$, and $a = H = 1/3$ and 10 samples. The parameter $r_{original}^2$ is computed before the correction.

3. Modelling Chains

The trends observed in the previous section (Section 3.4.1) are further confirmed in Tables 3.7 to 3.10, with minor differences. All the methods demonstrate good scaling across the different parameter sets. In α The differences between the punctual velocity and the average velocity are smaller compared to the previous section (Section 3.4.1). However, the differences between the Traditional and Integral approaches keep in the same order, with values around 0.15.

In the case of C_1 and H , the analysis in this section confirms the results obtained in the 10-sample analysis. There is a good agreement between the theoretical results and the retrieved results for C_1 .

Similarly, the trends observed for H in the 10-sample analysis are also confirmed in this section. The traditional approach yields higher values of H compared to the punctual velocity, while the integral approach tends to align more closely with the punctual velocity. These findings highlight the influence of spatio-temporal variability on the retrieved values of H .

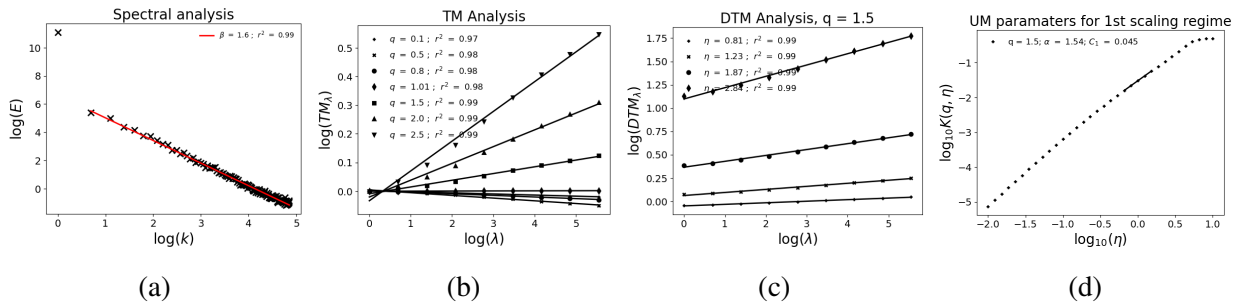


Figure 3.23: Analysis of the horizontal wind field of the center of the grid: (a) Spectral analysis (Eq. 1.21 in log-log), (b) TM (Eq. 1.6 in log-log), (c) and (d) DTM (Eqs. 1.70 and 1.72 in log-log respectively). The analysis is made on an ensemble of 10 samples and input parameters $\alpha = 1.55$, $C_1 = 0.05$, and $a = H = 1/3$.

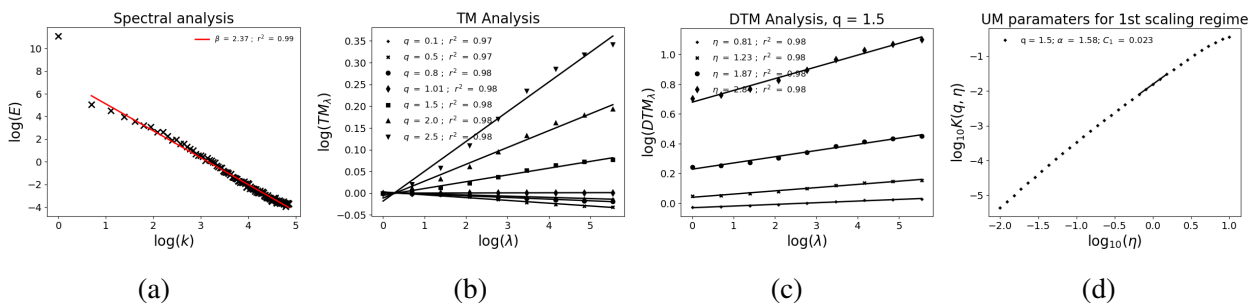


Figure 3.24: Analysis of the horizontal wind field averaged over the grid: (a) Spectral analysis (Eq. 1.21 in log-log), (b) TM (Eq. 1.6 in log-log), (c) and (d) DTM (Eqs. 1.70 and 1.72 in log-log respectively). The analysis is made on an ensemble of 100 samples and input parameters $\alpha = 1.5$, $C_1 = 0.05$, and $a = H = 1/3$.

3. Modelling Chains

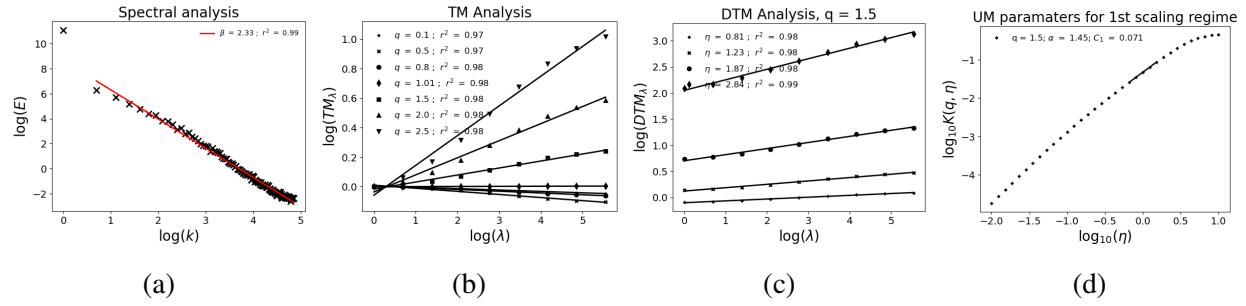


Figure 3.25: Analysis of the torque time series computed using Traditional Approach: (a) Spectral analysis (Eq. 1.21 in log-log), (b) TM (Eq. 1.6 in log-log), (c) and (d) DTM (Eqs. 1.70 and 1.72 in log-log respectively). The analysis is made on an ensemble of 100 samples and input parameters $\alpha = 1.5$, $C_1 = 0.05$, and $a = H = 1/3$.

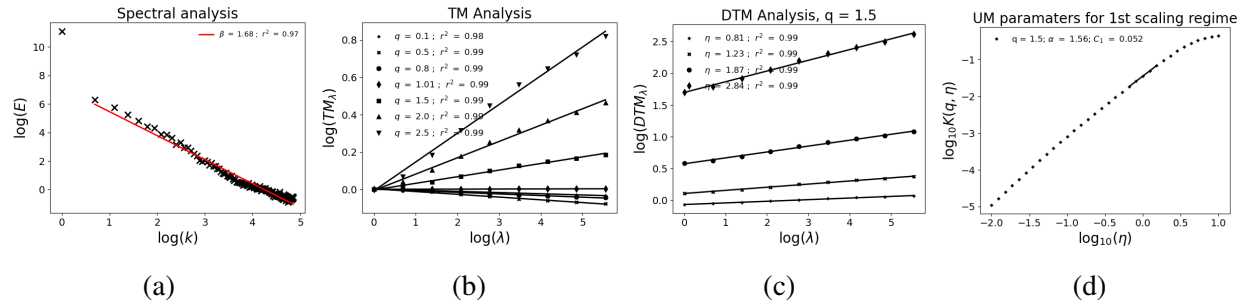


Figure 3.26: Analysis of the torque time series computed using Integral Approach: (a) Spectral analysis (Eq. 1.21 in log-log), (b) TM (Eq. 1.6 in log-log), (c) and (d) DTM (Eqs. 1.70 and 1.72 in log-log respectively). The analysis is made on an ensemble of 100 samples and input parameters $\alpha = 1.5$, $C_1 = 0.05$, and $a = H = 1/3$.

Field	α	C_1	C_{1Th}	r^2	$r_{original}^2$	H
V_{point}	1.54	0.05	-	0.99	0.97	0.30
V_{avg}	1.59	0.02	-	0.98	0.92	0.69
Traditional	1.46	0.07	0.06	0.99	0.92	0.67
Integral	1.56	0.05	0.06	0.99	0.94	0.34

Table 3.7: Summary of the parameters retrieved in the analysis of the time series simulated with input parameters $\alpha = 1.5$, $C_1 = 0.05$, and $a = H = 1/3$ and 100 samples. The parameter $r_{original}^2$ is computed before the correction.

Field	α	C_1	C_{1Th}	r^2	$r^2_{original}$	H
V_{point}	1.82	0.04	-	0.99	0.97	0.30
V_{avg}	1.84	0.02	-	0.98	0.92	0.67
Traditional	1.65	0.09	0.06	0.98	0.93	0.66
Integral	1.80	0.06	0.07	0.99	0.94	0.33

Table 3.8: Summary of the parameters retrieved in the analysis of the time series simulated with input parameters $\alpha = 1.8$, $C_1 = 0.05$, and $a = H = 1/3$ and 100 samples. The parameter $r^2_{original}$ is computed before the correction.

Field	α	C_1	C_{1Th}	r^2	$r^2_{original}$	H
V_{point}	1.14	0.10	-	0.99	0.97	0.33
V_{avg}	1.33	0.05	-	0.98	0.94	0.69
Traditional	1.17	0.13	0.11	0.99	0.94	0.68
Integral	1.32	0.12	0.12	0.99	0.96	0.28

Table 3.9: Summary of the parameters retrieved in the analysis of the time series simulated with input parameters $\alpha = 1.1$, $C_1 = 0.1$, and $a = H = 1/3$ and 100 samples. The parameter $r^2_{original}$ is computed before the correction.

Field	α	C_1	C_{1Th}	r^2	$r^2_{original}$	H
V_{point}	1.51	0.29	-	0.99	0.97	0.31
V_{avg}	1.4	0.24	-	0.99	0.91	0.67
Traditional	0.83	0.47	0.42	0.99	0.93	0.60
Integral	1.15	0.36	0.53	0.99	0.95	0.23

Table 3.10: Summary of the parameters retrieved in the analysis of the time series simulated with input parameters $\alpha = 1.5$, $C_1 = 0.3$, and $a = H = 1/3$ and 100 samples. The parameter $r^2_{original}$ is computed before the correction.

3.5 Summary

In this last chapter, after reviewing their theoretical foundations, we have implemented or developed three distinct methods for calculating simulated torque series using wind fields generated with the tools presented in the previous chapter. The first one, which is widely used in the literature, computes the torque using the average wind speed enabling to take into account only the temporal variability of the wind. The second one relies in the concept of the angular momentum computing the torque in each point of the blade and integrating the contribution of each portion along it. This allows to take into account both spatial and temporal variability. The third one employs the widely used in research and industry software OpenFAST, which integrates multiple modules enabling non-linear aero-hydro-servo-elastic simulations in the time domain. To compare these methods, we used normalized time series to remove the effects of different prefactors on which we were not focusing in this work, since we are interested in better understanding the the variability the studied fields, here the torque.

When comparing the results, we observed a high agreement between the time series calculated with the help of the different methods and the mean velocity on the grid. However, the use of Universal Multifractal (UM) analysis allowed us to identify and quantify few differences among the methods. The integral method exhibited stronger fluctuations due to its consideration of both temporal and spatial variability, resulting in a lower parameter H . In contrast, the traditional method displayed fluctuations similar to those observed in the wind field. Both methods conformed to the expected theoretical results, confirming a power-law relationship between wind and torque. Traditional approach shows lower value of α compared to the Integral one which is consistent with a decrease in extremes due to averaging.

On the other hand, OpenFAST consistently demonstrated the lowest level of small scale fluctuations which is visible on the fields and quantified through the parameter H which exhibits greater values. This behavior can be attributed to the occurrence of inertia forces and the coupling between the software modules, which dampens changes in wind speed and their transfer to torque, contrasting with the instantaneous responses observed in the other two methods. This behaviour might also bias the computation of C_1 yielding greater values than the theoretical expectations.

It is important to note that the analysis using OpenFAST was limited to 10 samples (in each of the different study scenarios) due to the computational cost of the software. Increasing the number of samples could provide a more comprehensive understanding of its behavior. Additionally, we have only used basic OpenFAST's capabilities in this work, and further investigations could open up a wide range of possibilities for studying small-scale wind power production.

Conclusions and perspectives

This PhD primarily aimed at simulating vector wind fields in space-time to quantify the impact of small scale wind fluctuations on wind power production.

In a first step, a comprehensive review of the Universal Multifractal (UM) framework has been conducted, starting by reminding the need for this framework and its theoretical foundations. A review of the tools available for analysis such as spectral analysis, Trace and Double Trace Moment techniques has also been carried out. Python scripts to simulate UM fields with continuous cascades relying on existing methods in the literature have been developed. Scalar fields in 1, 2 and 3 dimension as well as their extension to non-conservative cases were simulated. Then, existing theory combining stable Levy stochastic processes and Clifford algebra has been applied to enable simulations of vector fields with two or three components. UM analysis techniques were implemented on ensembles of simulated fields and sensitivity analysis to input parameters performed. As expected, all the techniques showed a good scaling with good agreement between the input and the output UM parameters. Additionally, the effect of the degree of non-conservation in these analysis techniques has been analyzed, finding a decrease in the quality of the scaling when H differs from 0. To overcome this difficulty, relying on previous findings, we developed an algorithm to optimize the correction, i.e. the level of fractional integration implemented prior to use of TM and DTM analysis, of the analyzed fields based on the quality of the scaling used. These tools provide the basis for characterising wind fields as well as for realistic stochastic simulations mimicking the observed properties.

In a second step, a toolbox for four different methods for wind simulation has been developed, relying on existing theoretical framework, and compared. Wind fields are simulated in space-time over wind turbine swept area and for duration between 4 s and 17 min. The latter corresponds to range of scale over which a unique scaling regime was identified using time series acquired from a high-resolution 3D anemometer deployed on an operational wind farm in the framework of the RW-Turb project. The first method utilizes Turbsim, developed by NREL, to reconstruct a wind grid over the turbine's swept area using a time series acquired from a high-resolution 3D anemometer, but it relies on Gaussian statistics, which do not enable to realistically reproduce extreme wind variability across scales. To account for non-Gaussian statistics, alternative methods were explored.

The first one is based on the reconstruction of wind grids from punctual measurements based on established scaling laws. The last two methods are based on the Fractionally Integrated Flux (FIF) principle but differ in their approach. The first method focuses on directly simulating wind fields using the properties retrieved from the analysis of the field, while the second method concentrates on simulating fluctuations. It uses the parameters obtained in the analysis of the corrected fluctuations to simulate synthetic fluctuations from which the physical wind fields are reconstructed. In the comparison of the different methods, it is observed that they all exhibit similar results in the analysis of the time series of all the pixels over the grid. However, the most prominent differences appear in the spatial analysis. After correction, all non-Gaussian methods show similar scaling features, but only the direct FIF simulation yields the expected results, while the results obtained by Turbsim are far from the expected ones. Therefore, it is concluded that the FIF simulation enables the most realistic method for wind field simulation.

Utilizing vector fields provides a significant advantage, as it allows for more accurate computations of effective velocities over the turbine blades. This is because it takes into account the direction of the wind, whereas scalar fields only provide information about the wind's magnitude. Using these simulated vector wind fields as input, three different methods with increasing complexity were employed to simulate wind turbine torque time series. First one computes the torque using the average wind speed enabling to take into account only the temporal variability of the wind. The second one relies on the concept of the angular momentum computing the torque in each point of the blade and then integrating over the whole radius. This allows to take into account both spatial and temporal variability of the wind. The third one, employs the realistic and widely used in the industry and academia software OpenFAST. To compare these methods, we have used normalised time series to avoid effects of different prefactors which are not of interest in this work, since we are focusing on the variability of the torque. The comparison of the results showed a high agreement between the torque time series calculated by the different methods with perfect correlation between Traditional and Integral and 0.89 between Traditional and OpenFAST for uniform fields. This correlation decreases to 0.95 and 0.8 respectively when non-uniform fields are used. However, the UM analysis revealed some differences, which highlights the interest of employing such tools to characterize and analyze torque time series, particularly because of their high fluctuations across scales which are not accounted for with traditional approaches. The integral method exhibited stronger fluctuations due to its consideration of both temporal and spatial variability, resulting in a lower H parameter. The traditional method displayed fluctuations similar to those observed in the wind, and both methods confirmed the expected power-law relationship between wind and torque. The value of α was lower in the traditional method, which is consistent with a decrease in extremes due to averaging. On the other hand, OpenFAST consistently demonstrated the lowest fluctuations, likely due to the incorporation of inertia forces and coupling between software modules, which dampened changes in wind speed and their transfer to torque.

Regarding future perspectives, numerous opportunities arise based on the findings presented in

this work. Firstly, this thesis has laid the foundations for simulations of more realistic geophysical fields extremely variable over wide range of space-time scales such as rainfall or wind, expanding beyond the limitations scalar fields and two spatial dimensions. The implemented methods, which relied on existing theoretical framework, allow for the extension to three spatial dimensions or even higher dimensions, and also to vector processes. While these extensions require further theoretical developments in vector analysis tools, they hold promising applications in various fields which are discussed below.

Expanding the spatial coverage by obtaining data from additional points would allow for results comparison also in space which is currently missing, and adaptation of the methods to the new properties identified through the analysis of such data. This would require deployment of networks of 3D sonic anemometer (Fitton et al., 2011, Fitton et al., 2014) or use of scanning lidars (Wang et al., 2015 or Shimada et al., 2020). The former offer great temporal resolution but limited spatial one while it is contrary for the latter. Within such framework, multifractal interpolation tools would be very useful. Furthermore, while this study has primarily focused on time scales ranging from 4 seconds to 17 minutes, extending the investigations to other time scales will enable to address wind variability issues not only at that scales but also over longer time intervals or smaller scales. This would allow broader issues to be addressed. For example, simulation of larger scales can be used for climate purposes, allowing the simulation of extreme weather events or the impact of climate change in different scenarios or the integration of wind energy into the energy system. Smaller scales studies could be useful to better understand differences between wind measurements obtained at different scales. A challenge associated with working on larger range of space-time scales will be to introduce scale breaks in simulation, which remains a challenge with continuous cascades.

High resolution wind simulations offer numerous opportunities for a wide range of applications, in addition to the effect on torque calculation analysed in this work. For example, it is possible to use them in the wind turbine interactions in a wind farm with the wake effect. Indeed, investigations are here limited to single turbine and this could be extended. However its use is not restricted to the wind energy industry, other examples can be found in city planning, e.g. adaptation (cooling) of cities in climate change scenarios (Grylls and van Reeuwijk, 2021;Meili et al., 2021), the impact of extreme events on trees (Bai et al., 2013;Angelou et al., 2022), construction sites with cranes, or raindrop trajectories in complex turbulent wind field for better accounting wind drift effect with weather radar measurements (Gires et al., 2022b). Another possible application is the comparison of turbulence measurements with instruments of various spatial and temporal resolution (e.g. sonic anemometers and lidars) or also the stochastic downscaling of climate or numerical weather models to obtain fields at the higher desired resolution. Such effort has been often been done with rain and seldom with wind (Deidda, 2000 , Biauou et al., 2003, Gires et al., 2014, Gires et al., 2020).

The modeling chains developed in this thesis are based on simplifications of wind turbine design, considering only a few aspects of its geometry. Increasing the level of complexity and incorporating a detailed design of the blades, such as the change of angle of attack and the pitch angle with distance to the rotor, could lead to a better understanding of the loads on the blades during extreme wind events such as wind gusts. This enhanced understanding could potentially extend the lifetime of the turbine, as these events are often underestimated using traditional tools. Additionally, another possibility is to extend the modeling chains by incorporating interactions between different turbines in a wind farm, which would enable the study of wake effects. Furthermore, it is important to note that these modelling chains are currently adapted to onshore wind turbines. Adapting and extending their functionality to cover offshore wind turbines presents a promising avenue for future research since offshore environments introduce unique challenges that are not encountered on land, such as the oscillations caused by waves for floating ones (induced motion on the turbines) which results in misalignment between the turbine and the wind, coupling structure turbine or hydrodynamic loads (Henderson and Witcher, 2010, Perveen et al., 2014). The importance of offshore wind energy has grown exponentially in recent years, making it a critical area for exploration and development.

Finally, the possibility of using the FIFO approach for stochastic nowcasting needs to be explored in more detail, as it can open up many possibilities in this area. Only initial study are mentioned in this work as it was outside of its initial scope. This approach enables to use the properties of a given event to simulate an ensemble of realistic future scenarios in which the scaling properties are preserved, obtaining a stochastic nowcasting. UM tools are used in the literature for the nowcasting in other geophysical fields such as rainfall (Macor et al., 2007, Paz et al., 2018, Gires et al., 2023), and their use should be extended to wind.

In summary, this thesis has established a robust framework for the continuation of realistic geophysical field simulation, enhancing versatility and applicability in various research fields. To this end, several simulation tools have been developed based mainly on the existing theory of continuous cascades and vector processes. This thesis also lays the foundation for future research and improvements in wind field simulation, with the aim of achieving more accurate and realistic results through the analysis of wind data from a high resolution campaign and the development of four wind simulation methods that use the properties obtained in the analysis. These simulated wind fields are used as input for three methods for calculating torque that have proven their effectiveness and agreement with theory, shedding light on how spatio-temporal wind variability influences wind energy production. The various approaches used in this study pave the way for further research in this field, relying on Universal Multifractal framework which enables to properly tackle the extreme variability observed over wide range of space-time scales.

Bibliography

- Iec 61400-1 “wind turbine generator systems-part 1: Safety requirements.” 2nd edition. Technical report, International Electrotechnical Commission, Geneva, Switzerland, 1999.
- A. G. Abo-Khalil, S. Alyami, K. Sayed, and A. Alhejji. Dynamic modeling of wind turbines based on estimated wind speed under turbulent conditions. *Energies*, 12(10):1907, 2019.
- T. Ackermann. Wind power in power systems. 2005.
- V. Akbari, M. Naghashzadegan, R. Kouhikamali, F. Afsharpanah, and W. Yaïci. Multi-objective optimization of a small horizontal-axis wind turbine blade for generating the maximum startup torque at low wind speeds. *Machines*, 10(9):785, 2022.
- M. Albadi and E. El-Saadany. Wind power in ontario: An economical valuation. In *2007 IEEE Canada Electrical Power Conference*, pages 496–501. IEEE, 2007.
- M. H. Albadi and E. El-Saadany. Overview of wind power intermittency impacts on power systems. *Electric power systems research*, 80(6):627–632, 2010.
- P. Anderson and A. Bose. Stability simulation of wind turbine systems. *IEEE transactions on power apparatus and systems*, (12):3791–3795, 1983.
- N. Angelou, J. Mann, and E. Dellwik. Wind lidars reveal turbulence transport mechanism in the wake of a tree. *Atmospheric Chemistry and Physics*, 22(4):2255–2268, 2022.
- S. Angriman, P. Cobelli, P. Mininni, M. Obligado, and P. C. Di Leoni. Generation of turbulent states using physics-informed neural networks. *arXiv preprint arXiv:2209.04285*, 2022.
- M. Anvari, G. Lohmann, M. Wächter, P. Milan, E. Lorenz, D. Heinemann, M. R. R. Tabar, and J. Peinke. Short term fluctuations of wind and solar power systems. *New Journal of Physics*, 18(6):063027, 2016.
- V. W. S. A/S. General specification v90-1.8/2.0 mw 50 hz vcs. 2010.
- P. Bach. Costs of wind power integration into electricity grids: integration of wind power into

- electricity grids economic and reliability impacts. In *IEA Workshop on Wind Integration, Paris*, www.iea.org/textbase/work/2004/nea/bach.pdf, 2004.
- K. Bai, C. Meneveau, and J. Katz. Experimental study of spectral energy fluxes in turbulence generated by a fractal, tree-like object. *Physics of Fluids*, 25(11), 2013.
- X. Bai, K. Clark, G. A. Jordan, N. W. Miller, and R. J. Piwko. Intermittency analysis project: Appendix b impact of intermittent generation on operation of california power grid. *GE Energy Consulting, Report CEC-500-2007-081-APB*, 2007.
- C. Bak, H. A. Madsen, and J. Johansen. Influence from blade-tower interaction on fatigue loads and dynamics (poster). In *2001 European Wind Energy Conference and Exhibition (EWEC'01)*, pages 394–397. WIP-Renewable Energies, 2001.
- O. Barambones, J. A. Cortajarena, I. Calvo, J. M. G. de Durana, P. Alkorta, and A. Karami-Mollae. Variable speed wind turbine control scheme using a robust wind torque estimation. *Renewable energy*, 133:354–366, 2019.
- R. J. Barthelmie, G. Larsen, S. Frandsen, L. Folkerts, K. Rados, S. Pryor, B. Lange, and G. Schepers. Comparison of wake model simulations with offshore wind turbine wake profiles measured by sodar. *Journal of atmospheric and oceanic technology*, 23(7):888–901, 2006.
- A. Bashirzadeh Tabrizi, B. Wu, J. Whale, and M. Shahabi Lotfabadi. Using turbsim stochastic simulator to improve accuracy of computational modelling of wind in the built environment. *Wind Engineering*, 43(2):147–161, 2019.
- S. Basu, E. Foufoula-Georgiou, and F. Porté-Agel. Synthetic turbulence, fractal interpolation, and large-eddy simulation. *Physical Review E*, 70(2):026310, 2004.
- R. Benzi, G. Paladin, G. Parisi, and A. Vulpiani. On the multifractal nature of fully developed turbulence and chaotic systems. *Journal of Physics A: Mathematical and General*, 17(18):3521, 1984.
- A. Biauou. *De la méso-échelle à la micro-échelle: désagrégation spatio-temporelle multifractale des précipitations*. PhD thesis, Paris, ENMP, 2004.
- A. Biauou, P. Hubert, D. Schertzer, I. Tchiguirinskaia, and H. Bendjoudi. Fractals, multifractals et prévision des précipitations. *Sud Sciences et Technologies*, 10:10–15, 2003.
- W. Bierbooms and P.-W. Cheng. Stochastic gust model for design calculations of wind turbines. *Journal of Wind Engineering and Industrial Aerodynamics*, 90(11):1237–1251, 2002.
- F. Bilendo, A. Meyer, H. Badihi, N. Lu, P. Cambron, and B. Jiang. Applications and modeling

- techniques of wind turbine power curve for wind farms—a review. *Energies*, 16(1):180, 2023.
- R. Bolgiano Jr. Turbulent spectra in a stably stratified atmosphere. *Journal of Geophysical Research*, 64(12):2226–2229, 1959.
- P. Bortolotti, H. C. Tarres, K. L. Dykes, K. Merz, L. Sethuraman, D. Verelst, and F. Zahle. Iea wind tcp task 37: Systems engineering in wind energy-wp2. 1 reference wind turbines. Technical report, National Renewable Energy Lab.(NREL), Golden, CO (United States), 2019.
- E. Bossanyi. Wind turbine control for load reduction. *Wind Energy: An International Journal for Progress and Applications in Wind Power Conversion Technology*, 6(3):229–244, 2003.
- R. N. Bracewell and R. N. Bracewell. *The Fourier transform and its applications*, volume 31999. McGraw-Hill New York, 1986.
- A. J. Brand, J. Peinke, and J. Mann. Turbulence and wind turbines. In *Journal of Physics: Conference Series*, volume 318, page 072005. IOP Publishing, 2011.
- A. S. Brouwer, M. Van Den Broek, A. Seebregts, and A. Faaij. Impacts of large-scale intermittent renewable energy sources on electricity systems, and how these can be modeled. *Renewable and Sustainable Energy Reviews*, 33:443–466, 2014.
- M. L. Buhl Jr. New empirical relationship between thrust coefficient and induction factor for the turbulent windmill state. Technical report, National Renewable Energy Lab.(NREL), Golden, CO (United States), 2005.
- T. Burton, N. Jenkins, D. Sharpe, and E. Bossanyi. *Wind energy handbook*. John Wiley & Sons, 2011.
- L. Buzdugan and S. Stefan. A comparative study of sodar, lidar wind measurements and aircraft derived wind observations. *Rom. J. Phys*, 65(5-6):1–15, 2020.
- R. Calif and F. G. Schmitt. Multiscaling and joint multiscaling description of the atmospheric wind speed and the aggregate power output from a wind farm. *Nonlinear Processes in Geophysics*, 21(2):379–392, 2014.
- R. Calif, F. G. Schmitt, and Y. Huang. Multifractal description of wind power fluctuations using arbitrary order hilbert spectral analysis. *Physica A: Statistical Mechanics and Its Applications*, 392(18):4106–4120, 2013.
- D. Carvalho, A. Rocha, M. Gómez-Gesteira, and C. Santos. A sensitivity study of the wrf model in wind simulation for an area of high wind energy. *Environmental Modelling & Software*, 33: 23–34, 2012.

- G. W. Cauley, D. N. Cook, H. A. Hawkins, and C. I. Protection. North american electric) reliability corporation). 2011.
- J. M. Chambers, C. L. Mallows, and B. Stuck. A method for simulating stable random variables. *Journal of the american statistical association*, 71(354):340–344, 1976.
- U. Chaudhary, P. Mondal, P. Tripathy, S. K. Nayak, and U. K. Saha. Modeling and optimal design of small hawt blades for analyzing the starting torque behavior. In *2014 Eighteenth National Power Systems Conference (NPSC)*, pages 1–6. IEEE, 2014.
- A. Y. C. Cheng. *Economic modeling of intermittency in wind power generation*. PhD thesis, Massachusetts Institute of Technology, 2005.
- H. Choi, P. Moin, and J. Kim. Active turbulence control for drag reduction in wall-bounded flows. *Journal of Fluid Mechanics*, 262:75–110, 1994.
- C. Clifford. Preliminary sketch of biquaternions. *Proceedings of the London Mathematical Society*, 1(1):381–395, 1871.
- W. K. Clifford. *Mathematical papers*, volume 210. American Mathematical Soc., 2007.
- G. W. E. Council. Gwec global wind report 2019. *Global Wind Energy Council: Bonn, Germany*, 2019.
- G. W. E. Council. Gwec global wind report 2021. *Global Wind Energy Council: Bonn, Germany*, 2021.
- L. Dale, D. Milborrow, R. Slark, and G. Strbac. Total cost estimates for large-scale wind scenarios in uk. *Energy Policy*, 32(17):1949–1956, 2004.
- R. Damiani, S. Dana, J. Annoni, P. Fleming, J. Roadman, J. van Dam, and K. Dykes. Assessment of wind turbine component loads under yaw-offset conditions. *Wind Energy Science*, 3(1):173–189, 2018.
- M. De Lima and J. De Lima. Investigating the multifractality of point precipitation in the madeira archipelago. *Nonlinear Processes in Geophysics*, 16(2):299–311, 2009.
- M. De Lima and J. Grasman. Multifractal analysis of 15-min and daily rainfall from a semi-arid region in portugal. *Journal of hydrology*, 220(1-2):1–11, 1999.
- M. I. de Lima. *Multifractals and the temporal structure of rainfall*. De Lima, 1998.
- L. de Montera, L. Barthès, C. Mallet, and P. Golé. Rain universal multifractal parameters revisited with dual-beam spectropluviometer measurements. *J Hydrometeorol*, 10:493, 2009.

- R. Deidda. Rainfall downscaling in a space-time multifractal framework. *Water Resources Research*, 36(7):1779–1794, 2000.
- E. Denny and M. O’Malley. Wind generation, power system operation, and emissions reduction. *IEEE Transactions on power systems*, 21(1):341–347, 2006.
- A. Det Norske Veritas. Recommended practice dnv-rp-c205: environmental conditions and environmental loads. 8.7. 1 *Slamming Loads on a Rigid Body*, 2010.
- D. S. Dolan and P. W. Lehn. Simulation model of wind turbine 3p torque oscillations due to wind shear and tower shadow. *IEEE Transactions on energy conversion*, 21(3):717–724, 2006.
- J. A. Dutton, H. A. Panofsky, D. Larko, H. N. Shirer, G. Stone, and M. Vilaro. Statistics of wind fluctuations over complex terrain. Technical report, Pennsylvania State Univ., University Park (USA). Dept. of Meteorology, 1979.
- Electricite de France. L’éolien en chiffres — edf.fr. <https://www.edf.fr/groupe-edf/espaces-dedies/l-energie-de-a-a-z/tout-sur-l-energie/produire-de-l-electricite/l-eolien-en-chiffres>, 2021. [Accessed 17-Jul-2023].
- G. Energy and A. Truewind. Ontario wind integration study. *GE Energy for Ontario Power Authority, Tech. Rep*, 2006.
- S. Evans, D. Bradney, and P. Clausen. Development and experimental verification of a 5 kw small wind turbine aeroelastic model. *Journal of Wind Engineering and Industrial Aerodynamics*, 181: 104–111, 2018.
- EWEA. Wind energy’s frequently asked questions (faq), 2012. URL <https://www.ewea.org/wind-energy-basics/faq/>.
- A. Fabbri, T. G. Roman, J. R. Abbad, and V. M. Quezada. Assessment of the cost associated with wind generation prediction errors in a liberalized electricity market. *IEEE Transactions on Power Systems*, 20(3):1440–1446, 2005.
- L. Fan, Z. Miao, and X. Wang. Sensorless maximum power point tracking in multi-type wind energy conversion systems. In *Proceedings of the 48th IEEE Conference on Decision and Control (CDC) held jointly with 2009 28th Chinese Control Conference*, pages 6823–6828. IEEE, 2009.
- G. Fitton. *Multifractal analysis and simulation of wind energy fluctuations*. PhD thesis, Citeseer, 2013.
- G. Fitton, I. Tchiguirinskaia, D. Schertzer, and S. Lovejoy. The anisotropic multifractal model and wind turbine wakes. In *7th PhD Seminar on Wind Energy in Europe*, page 115, 2011.

- G. Fitton, I. Tchiguirinskaia, D. Schertzer, and S. Lovejoy. Torque fluctuations in the framework of a multifractal 23/9-dimensional turbulence model. In *Journal of Physics: Conference Series*, volume 555, page 012038. IOP Publishing, 2014.
- France Energie Eolienne. Éolien en mer - France Energie Eolienne — fee.asso.fr. <https://fee.asso.fr/eolien-en-mer/>, 2022. [Accessed 17-Jul-2023].
- U. Frisch, P.-L. Sulem, and M. Nelkin. A simple dynamical model of intermittent fully developed turbulence. *Journal of Fluid Mechanics*, 87(4):719–736, 1978.
- L. Fu, Y.-d. Wei, S. Fang, G. Tian, and X.-j. Zhou. A wind energy generation replication method with wind shear and tower shadow effects. *Advances in mechanical engineering*, 10(3):1687814018759216, 2018.
- K. Fukami, K. Fukagata, and K. Taira. Super-resolution reconstruction of turbulent flows with machine learning. *Journal of Fluid Mechanics*, 870:106–120, 2019a.
- K. Fukami, Y. Nabae, K. Kawai, and K. Fukagata. Synthetic turbulent inflow generator using machine learning. *Physical Review Fluids*, 4(6):064603, 2019b.
- M. Gamahara and Y. Hattori. Searching for turbulence models by artificial neural network. *Physical Review Fluids*, 2(5):054604, 2017.
- A. P. García-Marín, F. Jiménez-Hornero, and J. Ayuso-Muñoz. Multifractal analysis as a tool for validating a rainfall model. *Hydrological Processes: An International Journal*, 22(14):2672–2688, 2008.
- S. O. George, H. B. George, and S. V. Nguyen. Risk quantification associated with wind energy intermittency in california. *IEEE Transactions on Power Systems*, 26(4):1937–1944, 2011.
- A. Gires. *Analyses et simulations multifractales pour une meilleure gestion des eaux pluviales en milieu urbain et péri-urbain*. PhD thesis, Université Paris-Est, 2012.
- A. Gires, I. Tchiguirinskaia, D. Schertzer, A. Schellart, A. Berne, and S. Lovejoy. Influence of small scale rainfall variability on standard comparison tools between radar and rain gauge data. *Atmospheric research*, 138:125–138, 2014.
- A. Gires, I. Tchiguirinskaia, D. Schertzer, and A. Berne. 2dvd data revisited: Multifractal insights into cuts of the spatiotemporal rainfall process. *Journal of Hydrometeorology*, 16(2):548–562, 2015.
- A. Gires, I. Tchiguirinskaia, and D. Schertzer. Two months of disdrometer data in the paris area. *Earth System Science Data*, 10(2):941–950, 2018.

- A. Gires, I. Tchiguirinskaia, and D. Schertzer. Blunt extension of discrete universal multifractal cascades: development and application to downscaling. *Hydrological Sciences Journal*, 65(7): 1204–1220, 2020.
- A. Gires, I. Tchiguirinskaia, and D. Schertzer. Infilling missing data of binary geophysical fields using scale invariant properties through an application to imperviousness in urban areas. *Hydrological Sciences Journal*, pages 1–14, 2021.
- A. Gires, J. Jose, I. Tchiguirinskaia, and D. Schertzer. Three months of combined high resolution rainfall and wind data collected on a wind farm. *Earth System Science Data Discussions*, pages 1–19, 2022a.
- A. Gires, I. Tchiguirinskaia, and D. Schertzer. 3d trajectories and velocities of rainfall drops in a multifractal turbulent wind field. *Atmospheric Measurement Techniques*, 15(19):5861–5875, 2022b.
- A. Gires, I. Tchiguirinskaia, and D. Schertzer. Generating a missing half of multifractal fields with a blunt extension of discrete cascades. *Hydrological Sciences Journal*, 68(2):261–275, 2023.
- H. Glauert. *The analysis of experimental results in the windmill brake and vortex ring states of an airscrew*. HM Stationery Office, 1926.
- H. Glauert. Airplane propellers. In *Aerodynamic theory*, pages 169–360. Springer, 1935.
- B. Golparvar, P. Papadopoulos, A. A. Ezzat, and R.-Q. Wang. A surrogate-model-based approach for estimating the first and second-order moments of offshore wind power. *Applied Energy*, 299: 117286, 2021.
- J. C. Gonzalez-Hidalgo, J.-A. Lopez-Bustins, P. Štěpánek, J. Martin-Vide, and M. de Luis. Monthly precipitation trends on the mediterranean fringe of the iberian peninsula during the second-half of the twentieth century (1951–2000). *International Journal of Climatology: A Journal of the Royal Meteorological Society*, 29(10):1415–1429, 2009.
- J. Gottschall and J. Peinke. How to improve the estimation of power curves for wind turbines. *Environmental Research Letters*, 3(1):015005, 2008.
- R. Gross, P. Heptonstall, D. Anderson, T. Green, M. Leach, and J. Skea. The costs and impacts of intermittency: An assessment of the evidence on the costs and impacts of intermittent generation on the british electricity network, 2006.
- T. Grylls and M. van Reeuwijk. Tree model with drag, transpiration, shading and deposition: Identification of cooling regimes and large-eddy simulation. *Agricultural and Forest Meteorology*, 298:108288, 2021.

- L. Gumilar, M. A. Habibi, D. Prihanto, H. Wicaksono, J. R. Larasati, and A. Gunawan. Analysis curve of maximum power and torque turbine generated by vertical axis wind turbine based on number of blades. In *AIP Conference Proceedings*, volume 2217. AIP Publishing, 2020.
- X. Guo, W. Li, and F. Iorio. Convolutional neural networks for steady flow approximation. In *Proceedings of the 22nd ACM SIGKDD international conference on knowledge discovery and data mining*, pages 481–490, 2016.
- V. K. Gupta and E. C. Waymire. A statistical analysis of mesoscale rainfall as a random cascade. *Journal of Applied Meteorology and Climatology*, 32(2):251–267, 1993.
- F. Gutiérrez-Martín, R. Da Silva-Álvarez, and P. Montoro-Pintado. Effects of wind intermittency on reduction of co2 emissions: The case of the spanish power system. *Energy*, 61:108–117, 2013.
- E. Hedevang, K. Biß, J. Cleve, and M. Greiner. Intermittent fingerprints in wind-turbine interactions. In *Progress in Turbulence and Wind Energy IV: Proceedings of the iTi Conference in Turbulence 2010*, pages 243–246. Springer, 2012.
- A. R. Henderson and D. Witcher. Floating offshore wind energy—a review of the current status and an assessment of the prospects. *Wind Engineering*, 34(1):1–16, 2010.
- J. Højstrup. Velocity spectra in the unstable planetary boundary layer. *Journal of Atmospheric Sciences*, 39(10):2239–2248, 1982.
- H. Holmes. Waudit guidance report. *WP6 Deliverable D24*, page 1–30, 2011.
- P. Hubert, J. P. Carbonnel, and A. Chaouche. Segmentation des séries hydrométéorologiques—application à des séries de précipitations et de débits de l’afrique de l’ouest. *Journal of hydrology*, 110(3-4):349–367, 1989.
- P. Hubert, Y. Tessier, S. Lovejoy, D. Schertzer, F. Schmitt, P. Ladoy, J. Carbonnel, S. Violette, and I. Desurosne. Multifractals and extreme rainfall events. *Geophysical Research Letters*, 20(10): 931–934, 1993.
- A. Hwas and R. Katebi. Wind turbine control using pi pitch angle controller. *ifac proceedings volumes*, 45(3):241–246, 2012.
- IEA. Net zero by 2050 a roadmap for the global energy sector 222. 2021.
- IEC. Iec 61400-2 “wind turbines - part2: Design requirements of small wind turbines”, edition 2015. Technical report, International Electrotechnical Commission, Geneva, Switzerland, 2015.
- IEC. Iec 61400-3 “wind turbines - part 3-1: Design requirements for fixed offshore wind turbines”.

- Technical report, International Electrotechnical Commission, Geneva, Switzerland, 2019.
- H. Jafarnejadsani, J. Pieper, and J. Ehlers. Adaptive control of a variable-speed variable-pitch wind turbine using radial-basis function neural network. *IEEE transactions on control systems technology*, 21(6):2264–2272, 2013.
- P. A. Jiménez, J. Dudhia, J. F. González-Rouco, J. Montávez, E. García-Bustamante, J. Navarro, J. Vilà-Guerau de Arellano, and A. Muñoz-Roldán. An evaluation of wrf’s ability to reproduce the surface wind over complex terrain based on typical circulation patterns. *Journal of Geophysical Research: Atmospheres*, 118(14):7651–7669, 2013.
- K. E. Johnson. *Adaptive torque control of variable speed wind turbines*. University of Colorado at Boulder, 2004.
- B. Jonkman, R. M. Mudafort, A. Platt, E. Branlard, M. Sprague, jjonkman, HaymanConsulting, G. Vijayakumar, M. Buhl, H. Ross, P. Bortolotti, M. Masciola, S. Ananthan, M. J. Schmidt, J. Rood, rdamiani, nrmendoza, sinolonghai, M. Hall, ashesh2512, kshaler, K. Bendl, pschuenemann, psakievich, ewquon, mattphillips, N. KUSUNO, alvarogonzalezsalcedo, T. Martinez, and rcorniglian. Openfast/openfast: Openfast v3.1.0, Mar. 2022. URL <https://doi.org/10.5281/zenodo.6324288>.
- B. J. Jonkman. Turbsim user’s guide: Version 1.50. Technical report, National Renewable Energy Lab.(NREL), Golden, CO (United States), 2009a.
- J. M. Jonkman. *Dynamics modeling and loads analysis of an offshore floating wind turbine*. University of Colorado at Boulder, 2007.
- J. M. Jonkman. Dynamics of offshore floating wind turbines—model development and verification. *Wind Energy: An International Journal for Progress and Applications in Wind Power Conversion Technology*, 12(5):459–492, 2009b.
- J. M. Jonkman and D. Matha. Dynamics of offshore floating wind turbines—analysis of three concepts. *Wind Energy*, 14(4):557–569, 2011.
- J. M. Jonkman, G. Hayman, B. Jonkman, R. Damiani, and R. Murray. Aerodyn v15 user’s guide and theory manual. *NREL Draft Report*, page 46, 2015.
- J. Jose. *Independent and joint multifractal characterization of atmospheric variability in real and controlled environments*. PhD thesis, Ecole des Ponts, 2023.
- Journal de l’éolien. La puissance éolienne en France - Journal de l’éolien - Tout sur l’éolien — journal-eolien.org. <http://www.journal-eolien.org/tout-sur-l-eolien/la-puissance-eolienne-en-france/>, 2021. [Accessed 17-Jul-2023].

- S.-H. Ju. Increasing the fatigue life of offshore wind turbine jacket structures using yaw stiffness and damping. *Renewable and Sustainable Energy Reviews*, 162:112458, 2022.
- A. Juneja, D. Lathrop, K. Sreenivasan, and G. Stolovitzky. Synthetic turbulence. *Physical Review E*, 49(6):5179, 1994.
- H. Kadum, S. Rockel, M. Hölling, J. Peinke, and R. B. Cal. Wind turbine wake intermittency dependence on turbulence intensity and pitch motion. *Journal of Renewable and Sustainable Energy*, 11(5), 2019.
- K. Kaiser, W. Langreder, H. Hohlen, and J. Højstrup. Turbulence correction for power curves. In *Wind Energy: Proceedings of the Euromech Colloquium*, pages 159–162. Springer, 2007.
- S. Kanev and T. van Engelen. Wind turbine extreme gust control. *Wind Energy: An International Journal for Progress and Applications in Wind Power Conversion Technology*, 13(1):18–35, 2010.
- N. Kelley, M. Hand, S. Larwood, and E. McKenna. The nrel large-scale turbine inflow and response experiment: preliminary results. In *Wind Energy Symposium*, volume 7476, pages 412–426, 2002.
- N. Kelley, M. Shirazi, D. Jager, S. Wilde, J. Adams, M. Buhl, P. Sullivan, and E. Patton. Lamar low-level jet project interim report. *National Renewable Energy Laboratory Technical Report*, 2004.
- N. D. Kelley. Full vector (3-d) inflow simulation in natural and wind farm environments using an expanded version of the snlwind (veers) turbulence code. Technical report, National Renewable Energy Lab., Golden, CO (United States), 1992.
- N. Kelly and A. D. Wright. A comparison of predicted and observed turbulent wind fields present in natural and internal wind park environments. Technical report, National Renewable Energy Lab., Golden, CO (United States), 1991.
- K. S. Khan and M. Tariq. Wind resource assessment using sodar and meteorological mast—a case study of pakistan. *Renewable and Sustainable Energy Reviews*, 81:2443–2449, 2018.
- K. E. Kinani, S. Meunier, L. Vido, and S. Le Ballois. Interdisciplinary analysis of wind energy—a focus on france. *Sustainable Energy Technologies and Assessments*, 55:102944, 2023.
- A. N. Kolmogorov. The local structure of turbulence in incompressible viscous fluid for very large reynolds numbers. *Cr Acad. Sci. URSS*, 30:301–305, 1941.
- A. N. Kolmogorov. A refinement of previous hypotheses concerning the local structure of turbu-

- lence in a viscous incompressible fluid at high reynolds number. *Journal of Fluid Mechanics*, 13 (1):82–85, 1962.
- J. N. Kutz. Deep learning in fluid dynamics. *Journal of Fluid Mechanics*, 814:1–4, 2017.
- D. Labat, A. Mangin, and R. Ababou. Rainfall–runoff relations for karstic springs: multifractal analyses. *Journal of Hydrology*, 256(3-4):176–195, 2002.
- M. A. Lackner and M. A. Rotea. Passive structural control of offshore wind turbines. *Wind energy*, 14(3):373–388, 2011a.
- M. A. Lackner and M. A. Rotea. Structural control of floating wind turbines. *Mechatronics*, 21(4): 704–719, 2011b.
- P. Ladoy, S. Lovejoy, and D. Schertzer. Extreme variability of climatological data: scaling and intermittency. In *Non-linear variability in geophysics*, pages 241–250. Springer, 1991.
- P. Ladoy, F. Schmitt, D. Schertzer, and S. Lovejoy. Variabilité temporelle multifractale des observations pluviométriques à nîmes. *CR Acad. Sci. Paris*, 317(II):775–782, 1993.
- D. Laino and A. C. Hansen. Current efforts toward improved aerodynamic modeling using the aerodyn subroutines. In *42nd AIAA Aerospace Sciences Meeting and Exhibit*, page 826, 2004.
- D. Lavallée, D. Schertzer, and S. Lovejoy. On the determination of the codimension function. In *Non-linear variability in geophysics*, pages 99–109. Springer, 1991.
- D. Lavallée, S. Lovejoy, D. Schertzer, and P. Ladoy. Nonlinear variability and landscape topography: analysis and simulation. *Fractals in geography*, pages 158–192, 1993.
- A. Lazarev, D. Schertzer, S. Lovejoy, and Y. Chigirinskaya. Unified multifractal atmospheric dynamics tested in the tropics: part ii, vertical scaling and generalized scale invariance. *Nonlinear processes in Geophysics*, 1(2/3):115–123, 1994.
- C. Lee, J. Kim, D. Babcock, and R. Goodman. Application of neural networks to turbulence control for drag reduction. *Physics of Fluids*, 9(6):1740–1747, 1997.
- S. T. Lee and Z. A. Yamayee. Load-following and spinning-reserve penalties for intermittent generation. *IEEE Transactions on Power Apparatus and Systems*, (3):1203–1211, 1981.
- J. G. Leishman and T. Beddoes. A semi-empirical model for dynamic stall. *Journal of the American Helicopter society*, 34(3):3–17, 1989.
- O. Liik, R. Oidram, and M. Keel. Estimation of real emissions reduction caused by wind generators. In *International Energy Workshop*, pages 24–26, 2003.

- J. Ling, A. Kurzwski, and J. Templeton. Reynolds averaged turbulence modelling using deep neural networks with embedded invariance. *Journal of Fluid Mechanics*, 807:155–166, 2016.
- J. López and F. Frances. Influence of the north atlantic oscillation and the western mediterranean oscillation in the maximum flow events in spain. In *International Workshop on Advances in Statistical Hydrology, Taormina, Italy*, pages 23–25, 2010.
- J. López-Queija, E. Robles, J. I. Llorente, I. Touzon, and J. López-Mendia. A simplified modeling approach of floating offshore wind turbines for dynamic simulations. *Energies*, 15(6):2228, 2022.
- P. Lounesto. Clifford algebras and spinors. In *Clifford Algebras and Their Applications in Mathematical Physics*, pages 25–37. Springer, 2001.
- S. Lovejoy and D. Schertzer. Our multifractal atmosphere: A unique laboratory for non-linear dynamics. *Physics in Canada*, 46(4):62–71, 1990.
- S. Lovejoy and D. Schertzer. On the simulation of continuous in scale universal multifractals, part i: Spatially continuous processes. *Computers & Geosciences*, 36(11):1393–1403, 2010a.
- S. Lovejoy and D. Schertzer. On the simulation of continuous in scale universal multifractals, part ii: Space–time processes and finite size corrections. *Computers & geosciences*, 36(11):1404–1413, 2010b.
- W. D. Lubitz. Impact of ambient turbulence on performance of a small wind turbine. *Renewable Energy*, 61:69–73, 2014.
- J. L. Lumley. The spectrum of nearly inertial turbulence in a stably stratified fluid. *Journal of the Atmospheric Sciences*, 21(1):99–102, 1964.
- T. S. Lund, X. Wu, and K. D. Squires. Generation of turbulent inflow data for spatially-developing boundary layer simulations. *Journal of computational physics*, 140(2):233–258, 1998.
- M. Lüscher. A portable high-quality random number generator for lattice field theory simulations. *Computer physics communications*, 79(1):100–110, 1994.
- J. Macor, D. Schertzer, and S. Lovejoy. Multifractal methods applied to rain forecast using radar data. *La Houille Blanche-Revue internationale de l’eau*, (4):92–98, 2007.
- J. L. Macor. *Développement de techniques de prévision de pluie basées sur les propriétés multi-échelles des données radar et satellites*. PhD thesis, Ecole des Ponts ParisTech, 2007.
- T. Maeda, Y. Kamada, N. Mori, et al. Investigation of wake effects on a horizontal axis wind turbine in field experiments (part i: Horizontal axis direction). *Energy*, 134:482–492, 2017.

- B. B. Mandelbrot. Intermittent turbulence in self-similar cascades: divergence of high moments and dimension of the carrier. *Journal of fluid Mechanics*, 62(2):331–358, 1974.
- B. B. Mandelbrot. Fractals. *Form, chance and dimension*, 1977.
- B. B. Mandelbrot. The fractal geometry of nature wh freeman and company. *New York*, page 468, 1983.
- B. B. Mandelbrot. Self-affine fractal sets, i: the basic fractal dimensions. In *Fractals in physics*, pages 3–15. Elsevier, 1986.
- J. F. Manwell, J. G. McGowan, and A. L. Rogers. *Wind energy explained: theory, design and application*. John Wiley & Sons, 2010.
- D. Marsan. *Multifractals espace-temps, dynamique et prédictibilité; application aux précipitations*. PhD thesis, Paris 6, 1998.
- I. Marusic, B. J. McKeon, P. A. Monkewitz, H. M. Nagib, A. J. Smits, and K. R. Sreenivasan. Wall-bounded turbulent flows at high reynolds numbers: Recent advances and key issues. *Physics of fluids*, 22(6), 2010.
- M. B. McElroy, X. Lu, C. P. Nielsen, and Y. Wang. Potential for wind-generated electricity in china. *science*, 325(5946):1378–1380, 2009.
- O. D. Medina, F. G. Schmitt, and R. Calif. Multiscale analysis of wind velocity, power output and rotation of a windmill. *Energy Procedia*, 76:193–199, 2015.
- N. Meili, G. Manoli, P. Burlando, J. Carmeliet, W. T. Chow, A. M. Coutts, M. Roth, E. Velasco, E. R. Vivoni, and S. Fatichi. Tree effects on urban microclimate: Diurnal, seasonal, and climatic temperature differences explained by separating radiation, evapotranspiration, and roughness effects. *Urban Forestry & Urban Greening*, 58:126970, 2021.
- N. Mendoza, A. Robertson, A. Wright, J. Jonkman, L. Wang, R. Bergua, T. Ngo, T. Das, M. Odeh, K. Mohsin, et al. Verification and validation of model-scale turbine performance and control strategies for the iea wind 15 mw reference wind turbine. *Energies*, 15(20):7649, 2022.
- C. Meneveau. Big wind power: seven questions for turbulence research. *Journal of Turbulence*, 20(1):2–20, 2019.
- P. Milan, M. Wächter, and J. Peinke. Turbulent character of wind energy. *Physical review letters*, 110(13):138701, 2013.
- P. Milan, M. Wächter, and J. Peinke. Stochastic modeling and performance monitoring of wind farm power production. *Journal of Renewable and Sustainable Energy*, 6(3), 2014.

- M. Milano and P. Koumoutsakos. Neural network modeling for near wall turbulent flow. *Journal of Computational Physics*, 182(1):1–26, 2002.
- B. Moynihan, B. Moaveni, S. Liberatore, and E. Hines. Estimation of blade forces in wind turbines using blade root strain measurements with openfast verification. *Renewable Energy*, 184:662–676, 2022.
- T. Mücke, D. Kleinhans, and J. Peinke. Atmospheric turbulence and its influence on the alternating loads on wind turbines. *Wind Energy*, 14(2):301–316, 2011.
- I. Neunaber. *Stochastic investigation of the evolution of small-scale turbulence in the wake of a wind turbine exposed to different inflow conditions*. PhD thesis, Universität Oldenburg, 2019.
- G. Notton, M.-L. Nivet, C. Voyant, C. Paoli, C. Darras, F. Motte, and A. Fouilloy. Intermittent and stochastic character of renewable energy sources: Consequences, cost of intermittence and benefit of forecasting. *Renewable and sustainable energy reviews*, 87:96–105, 2018.
- E. Novikov and R. Stiuart. The intermittency of turbulence and the spectrum of energy dissipation fluctuations(turbulence intermittency model to calculate spectrum of energy dissipation fluctuations). *1964.*, 1964.
- A. M. Oboukhov. Some specific features of atmospheric tubulence. *Journal of Fluid Mechanics*, 13(1):77–81, 1962.
- A. Obukhov. On the distribution of energy in the spectrum of turbulent flow. *Bull. Acad. Sci. USSR, Géog. Géophys.*, 5:453–466, 1941.
- A. Obukhov. On influence of buoyancy forces on the structure of temperature field in a turbulent flow. In *Dokl Acad Nauk SSSR*, volume 125, page 1246, 1959.
- E. Oguz, D. Clelland, A. H. Day, A. Incecik, J. A. López, G. Sánchez, and G. G. Almeria. Experimental and numerical analysis of a tlp floating offshore wind turbine. *Ocean Engineering*, 147:591–605, 2018.
- S. Okubo. Pseudo-quartenion and pseudo-octonion algebras. *Hadronic J.:(United States)*, 1(4), 1978.
- H. Olesen, S. E. Larsen, and J. Højstrup. Modelling velocity spectra in the lower part of the planetary boundary layer. *Boundary-Layer Meteorology*, 29(3):285–312, 1984.
- A. O. Onol and S. Yesilyurt. Effects of wind gusts on a vertical axis wind turbine with high solidity. *Journal of Wind Engineering and Industrial Aerodynamics*, 162:1–11, 2017.
- OTT Hydromet GmbH. Operating instructions Present Weather Sensor OTT Parsivel 2. (70):52,

2014. URL <https://www.ott.com/download/operating-instructions-present-weather-sensor-ott-parsivel2-without-screen-heating/>.
- T. M. Over and V. K. Gupta. Statistical analysis of mesoscale rainfall: Dependence of a random cascade generator on large-scale forcing. *Journal of Applied Meteorology and Climatology*, 33(12):1526–1542, 1994.
- G. Parisi, U. Frisch, et al. A multifractal model of intermittency. *Turbulence and predictability in geophysical fluid dynamics and climate dynamics*, pages 84–88, 1985.
- I. Paz, B. Willinger, A. Gires, A. Ichiba, L. Monier, C. Zobrist, B. Tisserand, I. Tchiguirinskaia, and D. Schertzer. Multifractal comparison of reflectivity and polarimetric rainfall data from c-and x-band radars and respective hydrological responses of a complex catchment model. *Water*, 10(3):269, 2018.
- R. Perveen, N. Kishor, and S. R. Mohanty. Off-shore wind farm development: Present status and challenges. *Renewable and Sustainable Energy Reviews*, 29:780–792, 2014.
- D. A. Peters and C. J. He. Correlation of measured induced velocities with a finite-state wake model. *Journal of the American Helicopter Society*, 36(3):59–70, 1991.
- S. B. Pope and S. B. Pope. *Turbulent flows*. Cambridge university press, 2000.
- E. Quon and N. J. Abbas. Openfast turbine models, 2021. URL <https://github.com/NREL/openfast-turbine-models/tree/master>.
- V. Rao, A. Bedford, M. Mokhtar, and J. M. Howe. Power profiling and inherent lag prediction of a wind power generating system for its integration to an energy storage system. In *2013 IEEE International Conference on Systems, Man, and Cybernetics*, pages 133–138. IEEE, 2013.
- G. Ren, J. Liu, J. Wan, Y. Guo, and D. Yu. Overview of wind power intermittency: Impacts, measurements, and mitigation solutions. *Applied Energy*, 204:47–65, 2017.
- Y. Ren, V. Venugopal, and W. Shi. Dynamic analysis of a multi-column tlp floating offshore wind turbine with tendon failure scenarios. *Ocean Engineering*, 245:110472, 2022.
- P. Renaud. *CLIFFORD ALGEBRAS LECTURE NOTES ON APPLICATIONS IN PHYSICS*. Nov. 2020. URL <https://hal.science/hal-03015551>.
- J. Rinker and G. Barter. Wisdem ref turbines: Deprecated: Reference turbines from windpact and other nrel work. URL https://github.com/WISDEM/Ref_Turbines.
- V. A. Riziotis and S. G. Voutsinas. Fatigue loads on wind turbines of different control strategies operating in complex terrain. *Journal of Wind Engineering and Industrial Aerodynamics*, 85(3):

- 211–240, 2000.
- A. N. Robertson, F. Wendt, J. M. Jonkman, W. Popko, H. Dagher, S. Gueydon, J. Qvist, F. Vittori, J. Azcona, E. Uzunoglu, et al. Oc5 project phase ii: validation of global loads of the deepcwind floating semisubmersible wind turbine. *Energy Procedia*, 137:38–57, 2017.
- J. S. Rodrigo. State-of-the-art of wind resource assessment. *Deliverable D7, CENER*, 2010.
- C. Rosales and C. Meneveau. A minimal multiscale lagrangian map approach to synthesize non-gaussian turbulent vector fields. *Physics of Fluids*, 18(7):075104, 2006.
- C. Rosales and C. Meneveau. Anomalous scaling and intermittency in three-dimensional synthetic turbulence. *Physical Review E*, 78(1):016313, 2008.
- J.-F. Royer, A. Biau, F. Chauvin, D. Schertzer, and S. Lovejoy. Multifractal analysis of the evolution of simulated precipitation over france in a climate scenario. *Comptes Rendus Geoscience*, 340(7):431–440, 2008.
- A. D. Sahin and Z. Sen. First-order markov chain approach to wind speed modelling. *Journal of Wind Engineering and Industrial Aerodynamics*, 89(3-4):263–269, 2001.
- C. Salles, J.-D. Creutin, and D. Sempere-Torres. The optical spectropluviometer revisited. *Journal of Atmospheric and Oceanic Technology*, 15(5):1215–1222, 1998.
- D. Schertzer and S. Lovejoy. The dimension and intermittency of atmospheric dynamics. In *Turbulent Shear Flows 4*, pages 7–33. Springer, 1985a.
- D. Schertzer and S. Lovejoy. Generalised scale invariance in turbulent phenomena. *PhysicoChemical Hydrodynamics*, 6(5-6):623–635, 1985b.
- D. Schertzer and S. Lovejoy. Physical modeling and analysis of rain and clouds by anisotropic scaling multiplicative processes. *Journal of Geophysical Research: Atmospheres*, 92(D8):9693–9714, 1987a.
- D. Schertzer and S. Lovejoy. Singularités anisotropes, divergences des moments en turbulence: Invariance échelle généralisée et processus multiplicatifs. *Ann. Sci. Math. Que.*, 11(1):139–181, 1987b.
- D. Schertzer and S. Lovejoy. Nonlinear variability in geophysics: Multifractal simulations and analysis. In *Fractals' Physical Origin and Properties*, pages 49–79. Springer, 1989.
- D. Schertzer and S. Lovejoy. Nonlinear variability in geophysics. *Scaling and Multifractal processes*, 1991.

- D. Schertzer and S. Lovejoy. From scalar cascades to lie cascades: Joint multifractal analysis of rain and cloud processes. *Space/time variability and interdependence for various hydrological processes*, edited by: Feddes, RA, Cambridge University Press, pages 153–173, 1995.
- D. Schertzer and S. Lovejoy. Universal multifractals do exist!: Comments on “a statistical analysis of mesoscale rainfall as a random cascade”. *Journal of Applied Meteorology*, 36(9):1296–1303, 1997.
- D. Schertzer and S. Lovejoy. Multifractals, generalized scale invariance and complexity in geophysics. *International Journal of Bifurcation and Chaos*, 21(12):3417–3456, 2011.
- D. Schertzer and I. Tchiguirinskaia. Multifractal vector fields and stochastic clifford algebra. *Chaos: An Interdisciplinary Journal of Nonlinear Science*, 25(12):123127, 2015.
- D. Schertzer and I. Tchiguirinskaia. Pandora box of multifractals: Barely open? *Advances in nonlinear geosciences*, pages 543–563, 2018.
- D. Schertzer and I. Tchiguirinskaia. A century of turbulent cascades and the emergence of multifractal operators. *Earth and Space Science*, 7(3):e2019EA000608, 2020.
- D. Schertzer, S. Lovejoy, and P. Hubert. An introduction to stochastic multifractal fields. In *ISFMA Symposium on Environmental Science and Engineering with related Mathematical Problems*, volume 4, pages 106–179. Higher Education Press Beijing, 2002.
- D. Schertzer, I. Tchiguirinskaia, S. Lovejoy, and A. Tuck. Quasi-geostrophic turbulence and generalized scale invariance, a theoretical reply. *Atmospheric Chemistry and Physics*, 12(1):327–336, 2012.
- F. Schmitt, D. Schertzer, S. Lovejoy, and Y. Brunet. Estimation of universal multifractal indices for atmospheric turbulent velocity fields. In *Fractals in natural sciences*, pages 274–281. World Scientific, 1994.
- F. Schmitt, S. Vannitsem, and A. Barbosa. Modeling of rainfall time series using two-state renewal processes and multifractals. *Journal of Geophysical Research: Atmospheres*, 103(D18):23181–23193, 1998.
- J. Schottler, N. Reinke, A. Hölling, J. Whale, J. Peinke, and M. Hölling. On the impact of non-gaussian wind statistics on wind turbines—an experimental approach. *Wind Energy Science*, 2(1): 1–13, 2017.
- K. Shaler, M. Debnath, and J. Jonkman. Validation of fast. farm against full-scale turbine scada data for a small wind farm. In *Journal of Physics: Conference Series*, volume 1618, page 062061. IOP Publishing, 2020.

- A. Shamshad, M. Bawadi, W. W. Hussin, T. A. Majid, and S. Sanusi. First and second order markov chain models for synthetic generation of wind speed time series. *Energy*, 30(5):693–708, 2005.
- S. Shimada, J. P. Goit, T. Ohsawa, T. Kogaki, and S. Nakamura. Coastal wind measurements using a single scanning lidar. *Remote Sensing*, 12(8):1347, 2020.
- M. Shinozuka and C.-M. Jan. Digital simulation of random processes and its applications. *Journal of sound and vibration*, 25(1):111–128, 1972.
- G. Shur. *Experimental investigations of the energy spectrum of atmospheric turbulence*. Aeronautical Research Council, 1964.
- Y. Si, H. R. Karimi, and H. Gao. Modelling and optimization of a passive structural control design for a spar-type floating wind turbine. *Engineering structures*, 69:168–182, 2014.
- R. Sitharthan, M. Karthikeyan, D. S. Sundar, and S. Rajasekaran. Adaptive hybrid intelligent mppt controller to approximate effectual wind speed and optimal rotor speed of variable speed wind turbine. *ISA transactions*, 96:479–489, 2020.
- W. C. Skamarock, J. B. Klemp, J. Dudhia, D. O. Gill, D. M. Barker, M. G. Duda, X.-Y. Huang, W. Wang, J. G. Powers, et al. A description of the advanced research wrf version 3. *NCAR technical note*, 475:113, 2008.
- V. Sohoni, S. Gupta, and R. Nema. A critical review on wind turbine power curve modelling techniques and their applications in wind based energy systems. *Journal of Energy*, 2016, 2016.
- G. Solari. Turbulence modeling for gust loading. *Journal of Structural Engineering*, 113(7):1550–1569, 1987.
- D. Song, Y. Yang, S. Zheng, W. Tang, J. Yang, M. Su, X. Yang, and Y. H. Joo. Capacity factor estimation of variable-speed wind turbines considering the coupled influence of the qn-curve and the air density. *Energy*, 183:1049–1060, 2019.
- P. Sørensen, A. D. Hansen, and P. A. C. Rosas. Wind models for simulation of power fluctuations from wind farms. *Journal of wind engineering and industrial aerodynamics*, 90(12-15):1381–1402, 2002.
- P. R. Spalart. Direct simulation of a turbulent boundary layer up to $r\theta = 1410$. *Journal of fluid mechanics*, 187:61–98, 1988.
- L. J. L. Stival, A. K. Guetter, and F. O. de Andrade. The impact of wind shear and turbulence intensity on wind turbine power performance. *Espaço Energia*, 27:11–20, 2017.
- A. Sudhamshu, M. C. Pandey, N. Sunil, N. Satish, V. Mugundhan, and R. K. Velamati. Numerical

- study of effect of pitch angle on performance characteristics of a hawt. *Engineering Science and Technology, an International Journal*, 19(1):632–641, 2016.
- C. Svensson, J. Olsson, and R. Berndtsson. Multifractal properties of daily rainfall in two different climates. *Water Resources Research*, 32(8):2463–2472, 1996.
- D. J. Swider and C. Weber. The costs of wind’s intermittency in germany: application of a stochastic electricity market model. *European Transactions on Electrical Power*, 17(2):151–172, 2007.
- Y. Tessier, S. Lovejoy, and D. Schertzer. Universal multifractals: Theory and observations for rain and clouds. *Journal of Applied Meteorology and Climatology*, 32(2):223–250, 1993.
- Y. Tessier, S. Lovejoy, P. Hubert, D. Schertzer, and S. Pecknold. Multifractal analysis and modeling of rainfall and river flows and scaling, causal transfer functions. *Journal of Geophysical Research: Atmospheres*, 101(D21):26427–26440, 1996.
- ThiesCLIMA. Ultrasonic Anemometer 3D Instruction for Use. 2013a.
- ThiesCLIMA. Clima sensor US, Instructions for use. 2013b.
- J. Thomson, B. Polagye, V. Durgesh, and M. C. Richmond. Measurements of turbulence at two tidal energy sites in puget sound, wa. *IEEE Journal of Oceanic Engineering*, 37(3):363–374, 2012.
- R. Thresher, W. Holley, C. Smith, N. Jafarey, and S. Lin. Modeling the response of wind turbines to atmospheric turbulence. Technical report, Oregon State Univ., Corvallis (USA). Dept. of Mechanical Engineering, 1981.
- J. Valencia, A. S. Requejo, J. Gascó, and A. Tarquis. A universal multifractal description applied to precipitation patterns of the ebro river basin, spain. *Climate Research*, 44(1):17–25, 2010.
- W. van der Deijl, M. Obligado, C. Sicot, and S. Barre. Experimental study of mean and turbulent velocity fields in the wake of a twin-rotor vertical axis wind turbine. In *Journal of Physics: Conference Series*, volume 2265, page 022073. IOP Publishing, 2022.
- G. Van Kuik, J. Peinke, R. Nijssen, D. Lekou, J. Mann, J. N. Sørensen, C. Ferreira, J.-W. van Wingerden, D. Schlipf, P. Gebraad, et al. Long-term research challenges in wind energy—a research agenda by the european academy of wind energy. *Wind energy science*, 1(1):1–39, 2016.
- P. Veers, K. Dykes, E. Lantz, S. Barth, C. L. Bottasso, O. Carlson, A. Clifton, J. Green, P. Green, H. Holttinen, et al. Grand challenges in the science of wind energy. *Science*, 366(6464):eaau2027, 2019.

- P. S. Veers. Three-dimensional wind simulation. Technical report, Sandia National Labs., Albuquerque, NM (USA), 1988.
- L. Vermeer, J. N. Sørensen, and A. Crespo. Wind turbine wake aerodynamics. *Progress in aerospace sciences*, 39(6-7):467–510, 2003.
- V. Vestas Wind Systems A/S. V90-2.0 mw™ iec iia/iec s turbines, 2023. URL <https://www.vestas.com/en/products/2-mw-platform/V90-2-0-MW>.
- L. A. Viterna and D. C. Janetzke. Theoretical and experimental power from large horizontal-axis wind turbines. Technical report, National Aeronautics and Space Administration, Cleveland, OH (USA). Lewis . . . , 1982.
- M. Wächter, H. Heißelmann, M. Hölling, A. Morales, P. Milan, T. Mücke, J. Peinke, N. Reinke, and P. Rinn. The turbulent nature of the atmospheric boundary layer and its impact on the wind energy conversion process. *Journal of Turbulence*, (13):N26, 2012.
- T. Wallbank. Windsim validation study. *CFD validation in complex terrain*, 2008.
- Y.-h. Wan and B. K. Parsons. Factors relevant to utility integration of intermittent renewable technologies. Technical report, National Renewable Energy Lab.(NREL), Golden, CO (United States), 1993.
- H. Wang, R. Barthelmie, A. Clifton, and S. Pryor. Wind measurements from arc scans with doppler wind lidar. *Journal of Atmospheric and Oceanic Technology*, 32(11):2024–2040, 2015.
- W. Wangdee. Reliability impact of intermittent renewable energy source integration into power system. In *2014 International Electrical Engineering Congress (iEECON)*, pages 1–4. IEEE, 2014.
- X. Wu. Inflow turbulence generation methods. *Annual Review of Fluid Mechanics*, 49:23–49, 2017.
- Z. Wu, G. Bangga, and Y. Cao. Effects of lateral wind gusts on vertical axis wind turbines. *Energy*, 167:1212–1223, 2019.
- Q. Xiaohang, G. Zhiteng, W. Tongguang, W. Long, and K. Shitang. Nonlinear aeroelastic response analysis of 100-meter-scale flexible wind turbine blades. , 40(3):1–11, 2022.
- G. Xu and L. N. Sankar. Application of a viscous flow methodology to the nrel phase vi rotor. In *Wind Energy Symposium*, volume 7476, pages 83–93, 2002.
- W. Xu, P. Liu, L. Cheng, Y. Zhou, Q. Xia, Y. Gong, and Y. Liu. Multi-step wind speed prediction by combining a wrf simulation and an error correction strategy. *Renewable Energy*, 163:772–782,

2021.

- A. Yaglom. The influence of fluctuations in energy dissipation on the shape of turbulence characteristics in the inertial interval. In *Sov. Phys. Dokl.*, volume 11, pages 26–29, 1966.
- Y. Yang, K. Wu, H. Long, J. Gao, X. Yan, T. Kato, and Y. Suzuoki. Integrated electricity and heating demand-side management for wind power integration in china. *Energy*, 78:235–246, 2014.
- B. Yuan, M. Zhou, and J. Zong. An overview on peak regulation of wind power integrated power systems. In *2011 4th International Conference on Electric Utility Deregulation and Restructuring and Power Technologies (DRPT)*, pages 145–150. IEEE, 2011.
- M. Yurdusev, R. Ata, and N. Çetin. Assessment of optimum tip speed ratio in wind turbines using artificial neural networks. *Energy*, 31(12):2153–2161, 2006.
- J. Zeng and W. Qiao. Short-term wind power prediction using a wavelet support vector machine. *IEEE transactions on sustainable energy*, 3(2):255–264, 2012.
- H. Zhang, R. Ortiz de Luna, M. Pilas, and J. Wenske. A study of mechanical torque measurement on the wind turbine drive train—ways and feasibilities. *Wind Energy*, 21(12):1406–1422, 2018.
- K. Zhou, N. Cherukuru, X. Sun, and R. Calhoun. Wind gust detection and impact prediction for wind turbines. *Remote Sensing*, 10(4):514, 2018.

Appendix A

Drive codes

In the chapter, the drive codes used to run Turbsim / OpenFAST are inserted.

A.1 Turbsim input File

Example of Turbsim primary input file

```
-----TurbSim v2.00.* Input File-----  
  
for user-defined time series input  
  
-----Runtime Options-----  
  
False          Echo          - Echo input data to <RootName>.ech (flag)  
  
43456          RandSeed1      - First random seed (-2147483648 to  
                2147483647)  
  
"RanLux "      RandSeed2      - Second random seed (-2147483648 to  
                2147483647) for intrinsic pRNG, or an  
                alternative pRNG: "RanLux" or "  
                RNSNLW"  
  
False          WrBHHTP        - Output hub-height turbulence parameters in  
                binary form? (Generates RootName.  
                bin)  
  
True           WrFHHTP        - Output hub-height turbulence parameters in  
                formatted form? (Generates RootName
```

		.dat)
False	WrADHH	- Output hub-height time-series data in AeroDyn form? (Generates RootName.hh)
True	WrADFF	- Output full-field time-series data in TurbSim/AeroDyn form? (Generates RootName.bts)
True	WrBLFF	- Output full-field time-series data in BLADED/AeroDyn form? (Generates RootName.wnd)
False	WrADTWR	- Output tower time-series data? (Generates RootName.twr)
False	WrFMTEFF	- Output full-field time-series data in formatted (readable) form? (Generates RootName.u, RootName.v, RootName.w)
False	WrACT	- Output coherent turbulence time steps in AeroDyn form? (Generates RootName.cts)
False	Clockwise	- Clockwise rotation looking downwind? (used only for full-field binary files - not necessary for AeroDyn)
0	ScaleIEC	- Scale IEC turbulence models to exact target standard deviation? [0=no additional scaling; 1=use hub scale uniformly; 2=use individual scales]
-----Turbine/Model Specifications-----		
27	NumGrid_Z	- Vertical grid-point matrix dimension
27	NumGrid_Y	- Horizontal grid-point matrix dimension
4	TimeStep	- Time step [seconds]
1040	AnalysisTime	- Length of analysis time series [seconds]
"ALL"	UsableTime	- Usable length of output time series [seconds] (program will add GridWidth/

```

MeanHHWS seconds unless UsableTime is
"ALL")

90      HubHt      - Hub height [m] (should be > 0.5*GridHeight
)

175     GridHeight - Grid height [m]

175     GridWidth  - Grid width [m] (should be >= 2*(
RotorRadius+ShaftLength))

0       VFlowAng   - Vertical mean flow (uptilt) angle [degrees
]

30.0794 HFlowAng    - Horizontal mean flow (skew) angle [degrees
]

-----Meteorological Boundary Conditions-----

"TIMESR" TurbModel - Turbulence model ("IECKAI","IECVKM",
GP_LLJ","NWTcup","SMOOTH","WF_UPW",
WF_07D","WF_14D","TIDAL","API",
USRINP","TIMESR", or "NONE")
"/home/angel/Turbsim/input/run/wind.TimeSer" UserFile - Name of
the file that contains inputs for
user-defined spectra or time series
inputs (used only for "USRINP" and "
TIMESR" models)

1 IECstandard - Number of IEC 61400-x standard (x=1,2, or 3
with optional 61400-1 edition number
(i.e. "1-Ed2") )

"A"      IECturbc - IEC turbulence characteristic ("A", "B", "
C" or the turbulence intensity in
percent) ("KHTEST" option with NWTcup
model, not used for other models)

"NTM"    IEC_WindType - IEC turbulence type ("NTM"=normal, "xETM"=
extreme turbulence, "xEWM1"=extreme 1
-year wind, "xEWM50"=extreme 50-year
wind, where x=wind turbine class 1, 2
, or 3)

"default" ETMc - IEC Extreme Turbulence Model "c" parameter
[m/s]

```

```

"default"      WindProfileType - Velocity profile type ("LOG";"PL"=power
                    law;"JET";"H2L"=Log law for TIDAL
                    model;"API";"USR";"TS";"IEC"=PL on
                    rotor disk, LOG elsewhere; or "
                    default")

"unused"      ProfileFile   - Name of the file that contains input
                    profiles for WindProfileType="USR"
                    and/or TurbModel="USRVKM" [-]

          90    RefHt         - Height of the reference velocity (URef) [m
                    ]

          7.9609  URef        - Mean velocity at the reference height [ms
                    -1]

          350    ZJetMax     - Jet height [m] (used only for JET velocity
                    profile, valid 70-490 m)

"default"      PLExp        - Power law exponent [-] (or "default")

"default"      ZO           - Surface roughness length [m] (or "default"
                    )

-----Non-IEC Meteorological Boundary Conditions-----

"default"      Latitude     - Site latitude [degrees] (or "default")
          0.05    RICH_NO    - Gradient Richardson number [-]
"default"      UStar       - Friction or shear velocity [m/s] (or "
                    default")

"default"      ZI          - Mixing layer depth [m] (or "default")
"default"      PC_UW       - Hub mean u'w' Reynolds stress [m^2/s^2] (
                    or "default" or "none")
"default"      PC_UV       - Hub mean u'v' Reynolds stress [m^2/s^2] (
                    or "default" or "none")
"default"      PC_VW       - Hub mean v'w' Reynolds stress [m^2/s^2] (
                    or "default" or "none")

-----Spatial Coherence Parameters-----

"default"      SCMod1      - u-component coherence model ("GENERAL",
                    IEC,"API","NONE", or "default")

"default"      SCMod2      - v-component coherence model ("GENERAL",
                    IEC,"NONE", or "default")

```

```

"default"      SMod3          - w-component coherence model ("GENERAL", "
                        IEC", "NONE", or "default")

"5.310901, 0.000341"  InCDec1      - u-component coherence
                        parameters for general or IEC models
                        [-, m^-1] (e.g. "10.0 0.3e-3" in
                        quotes) (or "default")

"2.638217, 0.001692"  InCDec2      - v-component coherence
                        parameters for general or IEC models
                        [-, m^-1] (e.g. "10.0 0.3e-3" in
                        quotes) (or "default")

"1.633211, 0.005484"  InCDec3      - w-component coherence
                        parameters for general or IEC models
                        [-, m^-1] (e.g. "10.0 0.3e-3" in
                        quotes) (or "default")

0      CohExp          - Coherence exponent for general model [-]
                        (or "default")

-----Coherent Turbulence Scaling Parameters-----

"/home/angel/CertTurbSim\EventData"  CTEventPath  - Name of the path
                        where event data files are located

"les"      CTEventFile  - Type of event files ("LES", "DNS", or "
                        RANDOM")

true      Randomize    - Randomize the disturbance scale and
                        locations? (true/false)

1      DistScl        - Disturbance scale [-] (ratio of event
                        dataset height to rotor
                        disk). (Ignored when
                        Randomize = true.)

0.5      CTLy         - Fractional location of tower centerline
                        from right [-] (looking
                        downwind) to left side of the
                        dataset. (Ignored when
                        Randomize = true.)

0.5      CTLz         - Fractional location of hub height from the
                        bottom of the dataset. [-] (
                        Ignored when Randomize = true
                        .)

```

```
10  CTStartTime      - Minimum start time for coherent structures
                          in RootName.cts [seconds]
```

```
=====
! NOTE: Do not add or remove any lines in this file!
=====
```

A.2 OpenFAST Drive Code

OpenFAST primary input file

```

----- OpenFAST EXAMPLE INPUT FILE -----
FAST Certification Test #26: NREL 5.0 MW Baseline Wind Turbine (Onshore)
----- SIMULATION CONTROL -----
True          Echo          - Echo input data to <RootName>.ech (flag)
"FATAL"       AbortLevel    - Error level when simulation should abort (
                        string) {"WARNING", "SEVERE", "FATAL"
                        }
1040          TMax          - Total run time (s)
0.05          DT            - Recommended module time step (s)
2             InterpOrder  - Interpolation order for input/output time
                        history (-) {1=linear, 2=
                        quadratic}
0             NumCrctn     - Number of correction iterations (-) {0=
                        explicit calculation, i.e.,
                        no corrections}
99999         DT_UJac       - Time between calls to get Jacobians (s)
1E+06         UJacScfFact   - Scaling factor used in Jacobians (-)
----- FEATURE SWITCHES AND FLAGS -----
2             CompElast     - Compute structural dynamics (switch) {1=
                        ElastoDyn; 2=ElastoDyn +
                        BeamDyn for blades}
1             CompInflow    - Compute inflow wind velocities (switch) {0
                        =still air; 1=InflowWind; 2
                        =external from OpenFOAM}
2             CompAero      - Compute aerodynamic loads (switch) {0=None
                        ; 1=AeroDyn v14; 2=AeroDyn
                        v15}
1             CompServo     - Compute control and electrical-drive
                        dynamics (switch) {0=None;
                        1=ServoDyn}
0             CompHydro     - Compute hydrodynamic loads (switch) {0=
                        None; 1=HydroDyn}
0             CompSub       - Compute sub-structural dynamics (switch) {
                        0=None; 1=SubDyn; 2=
                        External Platform MCKF}
0             CompMooring   - Compute mooring system (switch) {0=None; 1
                        =MAP++; 2=FEAMooring; 3=
                        MoorDyn; 4=OrcaFlex}
0             CompIce       - Compute ice loads (switch) {0=None; 1=
                        IceFloe; 2=IceDyn}
----- INPUT FILES -----
"NRELOffshrBslne5MW_Onshore_ElastoDyn_BDoutputs.dat"  EDFFile  -

```



```

Name of file containing ElastoDyn
input parameters (quoted string)
"../5MW_Baseline/NRELOffshrBsline5MW_BeamDyn.dat"   BDBldFile(1)   -
Name of file containing BeamDyn input
parameters for blade 1 (quoted
string)
"../5MW_Baseline/NRELOffshrBsline5MW_BeamDyn.dat"   BDBldFile(2)   -
Name of file containing BeamDyn input
parameters for blade 2 (quoted
string)
"../5MW_Baseline/NRELOffshrBsline5MW_BeamDyn.dat"   BDBldFile(3)   -
Name of file containing BeamDyn input
parameters for blade 3 (quoted
string)
"../5MW_Baseline/NRELOffshrBsline5MW_InflowWind_12mps.dat"   InflowFile
- Name of file containing inflow
wind input parameters (quoted string
)
"NRELOffshrBsline5MW_Onshore_AeroDyn15.dat"   AeroFile   - Name of
file containing aerodynamic input
parameters (quoted string)
"NRELOffshrBsline5MW_Onshore_ServoDyn.dat"   ServoFile   - Name of
file containing control and
electrical-drive input parameters (
quoted string)
"unused"   HydroFile   - Name of file containing hydrodynamic input
parameters (quoted string)
"unused"   SubFile   - Name of file containing sub-structural
input parameters (quoted string)
"unused"   MooringFile   - Name of file containing mooring system
input parameters (quoted string)
"unused"   IceFile   - Name of file containing ice input
parameters (quoted string)
----- OUTPUT -----
True   SumPrint   - Print summary data to "<RootName>.sum" (
flag)
1   SttsTime   - Amount of time between screen status
messages (s)
99999   ChkptTime   - Amount of time between creating checkpoint
files for potential restart (s
)
"default"   DT_Out   - Time step for tabular output (s) (or "
default")
0   TStart   - Time to begin tabular output (s)
0   OutFileFmt   - Format for tabular (time-marching) output
file (switch) {0:
uncompressed binary [<

```

```

RootName>.outb], 1: text
file [<RootName>.out], 2:
binary file [<RootName>.
outb], 3: both 1 and 2}
True      TabDelim      - Use tab delimiters in text tabular output
file? (flag) {uses spaces if false}
"ES10.3E2" OutFmt      - Format used for text tabular output,
excluding the time channel.
Resulting field should be 10
characters. (quoted string)
----- LINEARIZATION -----
False     Linearize    - Linearization analysis (flag)
False     CalcSteady   - Calculate a steady-state periodic
operating point before linearization?
[unused if Linearize=False] (flag)
3         TrimCase    - Controller parameter to be trimmed {1:yaw;
2:torque; 3:pitch} [used
only if CalcSteady=True] (-
)
0.001    TrimTol      - Tolerance for the rotational speed
convergence [used only if
CalcSteady=True] (-)
0.01     TrimGain    - Proportional gain for the rotational speed
error (>0) [used only if
CalcSteady=True] (rad/(rad/s)
for yaw or pitch; Nm/(rad/s)
for torque)
0        Twr_Kdmp     - Damping factor for the tower [used only if
CalcSteady=True] (N/(m/s))
0        Bld_Kdmp     - Damping factor for the blades [used only
if CalcSteady=True] (N/(m/s
))
2        NLinTimes   - Number of times to linearize (-) [>=1] [
unused if Linearize=False]
30,      60          LinTimes      - List of times at which to
linearize (s) [1 to
NLinTimes] [used only when
Linearize=True and
CalcSteady=False]
1        LinInputs    - Inputs included in linearization (switch)
{0=none; 1=standard; 2=all
module inputs (debug)} [
unused if Linearize=False]
1        LinOutputs   - Outputs included in linearization (switch)
{0=none; 1=from OutList(s)
; 2=all module outputs (
debug)} [unused if

```

False	LinOutJac	<p style="text-align: right;">Linearize=False]</p> <p>- Include full Jacobians in linearization output (for debug) (flag) [unused if Linearize=False; used only if LinInputs=LinOutputs=2]</p>
False	LinOutMod	- Write module-level linearization output files in addition to output for full system? (flag) [unused if Linearize=False]
----- VISUALIZATION -----		
0	WrVTK	- VTK visualization data output: (switch) {0 =none; 1=initialization data only; 2=animation; 3=mode shapes}
2	VTK_type	- Type of VTK visualization data: (switch) {1=surfaces; 2=basic meshes (lines/points); 3=all meshes (debug)} [unused if WrVTK=0]
True	VTK_fields	- Write mesh fields to VTK data files? (flag) {true/false} [unused if WrVTK=0]
15	VTK_fps	- Frame rate for VTK output (frames per second){will use closest integer multiple of DT} [used only if WrVTK=2 or WrVTK=3]

A.3 AeroDyn Drive Code

Examples of AeroDyn input files

```

----- AERODYN v15 for OpenFAST INPUT FILE -----
NREL 5.0 MW offshore baseline aerodynamic input properties.
===== General Options =====
False      Echo      - Echo the input to "<rootname>.AD.ech"?
                    (flag)
"default"   DTAero      - Time interval for aerodynamic
                    calculations {or "default"} (s)
1          WakeMod  - Type of wake/induction model (switch) {
                    0=none, 1=BEMT, 2=DBEMT, 3=
                    OLAF} [WakeMod cannot be 2
                    or 3 when linearizing]
2          AFAeroMod - Type of blade airfoil aerodynamics
                    model (switch) {1=steady
                    model, 2=Beddoes-Leishman
                    unsteady model} [AFAeroMod
                    must be 1 when linearizing]
1          TwrPotent - Type tower influence on wind based on
                    potential flow around the
                    tower (switch) {0=none, 1=
                    baseline potential flow, 2=
                    potential flow with Bak
                    correction}
0          TwrShadow - Calculate tower influence on wind based
                    on downstream tower shadow
                    (switch) {0=none, 1=Powles
                    model, 2=Eames model}
True       TwrAero   - Calculate tower aerodynamic loads? (
                    flag)
False     FrozenWake - Assume frozen wake during linearization
                    ? (flag) [used only when WakeMod=1
                    and when linearizing]
False     CavitCheck - Perform cavitation check? (flag) [
                    AFAeroMod must be 1 when CavitCheck=
                    true]
False     CompAA    - Flag to compute AeroAcoustics
                    calculation [used only when WakeMod =
                    1 or 2]
"unused"  AA_InputFile - AeroAcoustics input file [used only
                    when CompAA=true]
===== Environmental Conditions =====
1.225     AirDens   - Air density (kg/m^3)
1.464E-05 KinVisc   - Kinematic air viscosity (m^2/s)
335       SpdSound  - Speed of sound (m/s)

```

```

103500  Patm          - Atmospheric pressure (Pa) [used only
                        when CavitCheck=True]
1700    Pvap          - Vapour pressure of fluid (Pa) [used
                        only when CavitCheck=True]
0.5     FluidDepth   - Water depth above mid-hub height (m) [
                        used only when CavitCheck=
                        True]
===== Blade-Element/Momentum Theory Options =====
[unused when WakeMod=0 or 3]
2       SkewMod      - Type of skewed-wake correction model (
                        switch) {1=uncoupled, 2=
                        Pitt/Peters, 3=coupled} [
                        unused when WakeMod=0 or 3]
"default" SkewModFactor - Constant used in Pitt/Peters skewed
                        wake model {or "default" is 15/32*pi}
                        (-) [used only when SkewMod=2;
                        unused when WakeMod=0 or 3]
True     TipLoss     - Use the Prandtl tip-loss model? (flag)
                        [unused when WakeMod=0 or 3]
True     HubLoss     - Use the Prandtl hub-loss model? (flag)
                        [unused when WakeMod=0 or 3]
True     TanInd      - Include tangential induction in BEMT
                        calculations? (flag) [unused when
                        WakeMod=0 or 3]
False    AIDrag      - Include the drag term in the axial-
                        induction calculation? (flag) [unused
                        when WakeMod=0 or 3]
False    TIDrag      - Include the drag term in the tangential
                        -induction calculation? (flag) [
                        unused when WakeMod=0,3 or TanInd=
                        FALSE]
"default" IndToler   - Convergence tolerance for BEMT
                        nonlinear solve residual equation {or
                        "default"} (-) [unused when WakeMod=
                        0 or 3]
100     MaxIter      - Maximum number of iteration steps (-) [
                        unused when WakeMod=0]
===== Dynamic Blade-Element/Momentum Theory Options =====
[used only when WakeMod=2]
2       DBEMT_Mod    - Type of dynamic BEMT (DBEMT) model {1=
                        constant tau1, 2=time-
                        dependent tau1} (-) [used
                        only when WakeMod=2]
4       tau1_const   - Time constant for DBEMT (s) [used only
                        when WakeMod=2 and
                        DBEMT_Mod=1]
== OLAF -- (Free Vortex Wake) Theory Options =====

```

```

[used only when WakeMod=3]
"unused"      OLAFInputFileName  - Input file for OLAF [used only when
                               WakeMod=3]
=== Beddoes-Leishman Unsteady Airfoil Aerodynamics Options ===
[used only when AFAeroMod=2]
    3    UAMod                    - Unsteady Aero Model Switch (switch) {1=
                                   Baseline model (Original),
                                   2=Gonzalez's variant (
                                   changes in Cn,Cc,Cm), 3=
                                   Minnema/Pierce variant (
                                   changes in Cc and Cm)} [
                                   used only when AFAeroMod=2]
True       FLookup                - Flag to indicate whether a lookup for f
                                   ' will be calculated (TRUE) or
                                   whether best-fit exponential
                                   equations will be used (FALSE); if
                                   FALSE S1-S4 must be provided in
                                   airfoil input files (flag) [used only
                                   when AFAeroMod=2]
===== Airfoil Information =====
    1    AFTabMod                 - Interpolation method for multiple
                                   airfoil tables {1=1D
                                   interpolation on AoA (first
                                   table only); 2=2D
                                   interpolation on AoA and Re
                                   ; 3=2D interpolation on AoA
                                   and UserProp} (-)
    1    InCol_Alfa               - The column in the airfoil tables that
                                   contains the angle of
                                   attack (-)
    2    InCol_Cl                 - The column in the airfoil tables that
                                   contains the lift
                                   coefficient (-)
    3    InCol_Cd                 - The column in the airfoil tables that
                                   contains the drag
                                   coefficient (-)
    4    InCol_Cm                 - The column in the airfoil tables that
                                   contains the pitching-
                                   moment coefficient; use
                                   zero if there is no Cm
                                   column (-)
    0    InCol_Cpmin              - The column in the airfoil tables that
                                   contains the Cpmin
                                   coefficient; use zero if
                                   there is no Cpmin column (-
                                   )
    8    NumAFfiles               - Number of airfoil files used (-)

```

```

"../5MW_Baseline/Airfoils/Cylinder1.dat"   AFNames           - Airfoil
                                         file names (NumAFfiles lines) (quoted
                                         strings)
"../5MW_Baseline/Airfoils/Cylinder2.dat"
"../5MW_Baseline/Airfoils/DU40_A17.dat"
"../5MW_Baseline/Airfoils/DU35_A17.dat"
"../5MW_Baseline/Airfoils/DU30_A17.dat"
"../5MW_Baseline/Airfoils/DU25_A17.dat"
"../5MW_Baseline/Airfoils/DU21_A17.dat"
"../5MW_Baseline/Airfoils/NACA64_A17.dat"
===== Rotor/Blade Properties =====
True           UseBlCm           - Include aerodynamic pitching moment in
                                         calculations? (flag)
"../5MW_Baseline/NRELOffshrBsline5MW_AeroDyn_blade.dat"   ADBlFile(1)
                                         - Name of file containing
                                         distributed aerodynamic properties
                                         for Blade #1 (-)
"../5MW_Baseline/NRELOffshrBsline5MW_AeroDyn_blade.dat"   ADBlFile(2)
                                         - Name of file containing
                                         distributed aerodynamic properties
                                         for Blade #2 (-) [unused if NumBl < 2
                                         ]
"../5MW_Baseline/NRELOffshrBsline5MW_AeroDyn_blade.dat"   ADBlFile(3)
                                         - Name of file containing
                                         distributed aerodynamic properties
                                         for Blade #3 (-) [unused if NumBl < 3
                                         ]
===== Tower Influence and Aerodynamics =====
[used only when TwrPotent/=0, TwrShadow/=0, or TwrAero=True]
      12   NumTwrNds           - Number of tower nodes used in the
                                         analysis (-) [used only
                                         when TwrPotent/=0, TwrShadow
                                         /=0, or TwrAero=True]

TwrElev      TwrDiam      TwrCd      TwrTI (used only with
              (m)          (-)          TwrShadow=2)
(m)          (m)          (-)          (-)
0.0000000E+00  6.0000000E+00  1.0000000E+00  1.0000000E-01
8.5261000E+00  5.7870000E+00  1.0000000E+00  1.0000000E-01
1.7053000E+01  5.5740000E+00  1.0000000E+00  1.0000000E-01
2.5579000E+01  5.3610000E+00  1.0000000E+00  1.0000000E-01
3.4105000E+01  5.1480000E+00  1.0000000E+00  1.0000000E-01
4.2633000E+01  4.9350000E+00  1.0000000E+00  1.0000000E-01
5.1158000E+01  4.7220000E+00  1.0000000E+00  1.0000000E-01
5.9685000E+01  4.5090000E+00  1.0000000E+00  1.0000000E-01
6.8211000E+01  4.2960000E+00  1.0000000E+00  1.0000000E-01
7.6738000E+01  4.0830000E+00  1.0000000E+00  1.0000000E-01
8.5268000E+01  3.8700000E+00  1.0000000E+00  1.0000000E-01

```

```

8.7600000E+01  3.8700000E+00  1.0000000E+00  1.0000000E-01
===== Outputs =====
True          SumPrint          - Generate a summary file listing input
              options and interpolated properties
              to "<rootname>.AD.sum"? (flag)
0  NBlOuts    - Number of blade node outputs [0 - 9] (
              -)
1,           9,           19  BlOutNd      - Blade nodes
              whose values will be output
              (-)
0  NTwOuts    - Number of tower node outputs [0 - 9]
              (-)
1,           2,           6   TwOutNd      - Tower nodes
              whose values will be output
              (-)
              OutList      - The next line(s) contains a list of
                              output parameters. See
                              OutListParameters.xlsx
                              for a listing of
                              available output
                              channels, (-)

END of input file (the word "END" must appear in the first 3 columns of
                    this last OutList line)
-----

```


Appendix B

Simulations with Turbsim and Simplistic Approach

In this chapter, the same curves, which are presented and discussed in details in section 2.6.1 for a wind event occurring on 20/12/2020, are displayed, but for other events.

Days of study: (a) 15/12/2020, (b) 14/01/2021, (c) 20/01/2021, (d) 25/01/2021, (e) 01/02/2021, (f) 10/02/2021, (g) 20/02/2021, (h) 04/03/2021, (i) 10/05/2021. These days have been selected to cover wind events with different average velocity.

B.1 Turbsim

B.2 Simplistic Approach

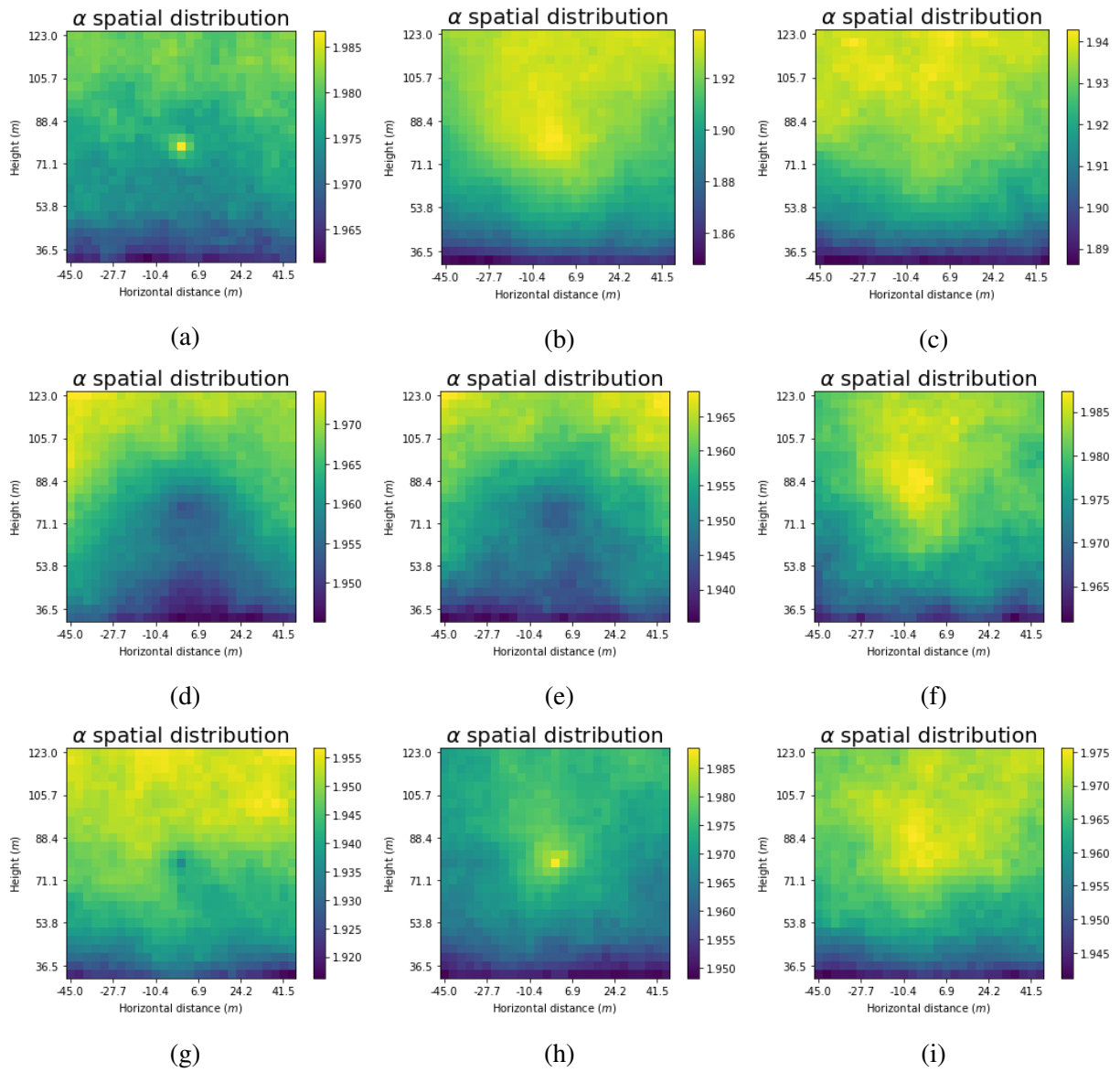


Figure B.1.1: Spatial distribution of α for different input days simulated with Turbsim. Days are listed chronologically as mention in the text at the beginning of the section.

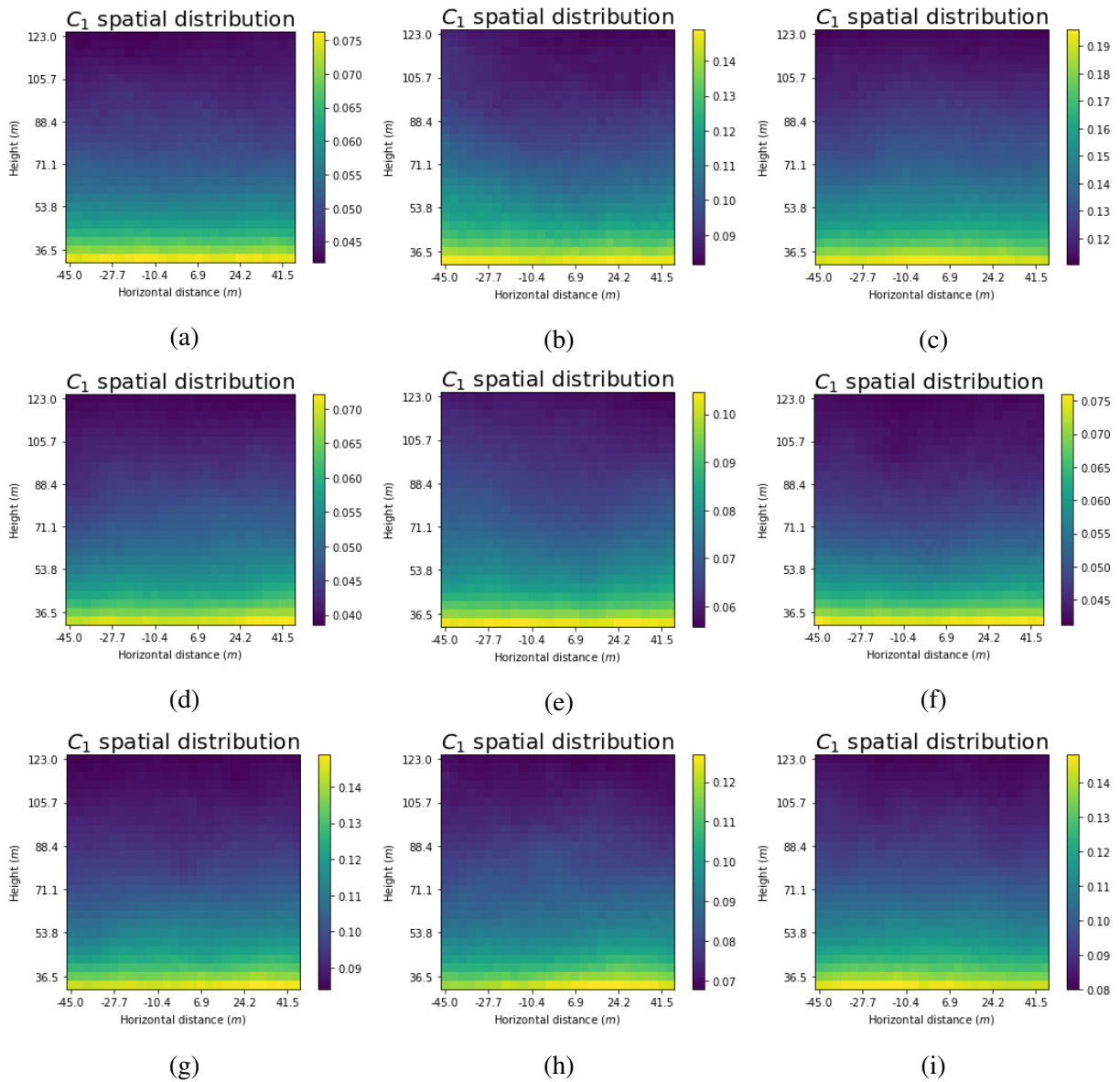


Figure B.1.2: Spatial distribution of C_1 for different input days simulated with Turbsim. Days are listed chronologically as mention in the text at the beginning of the section.

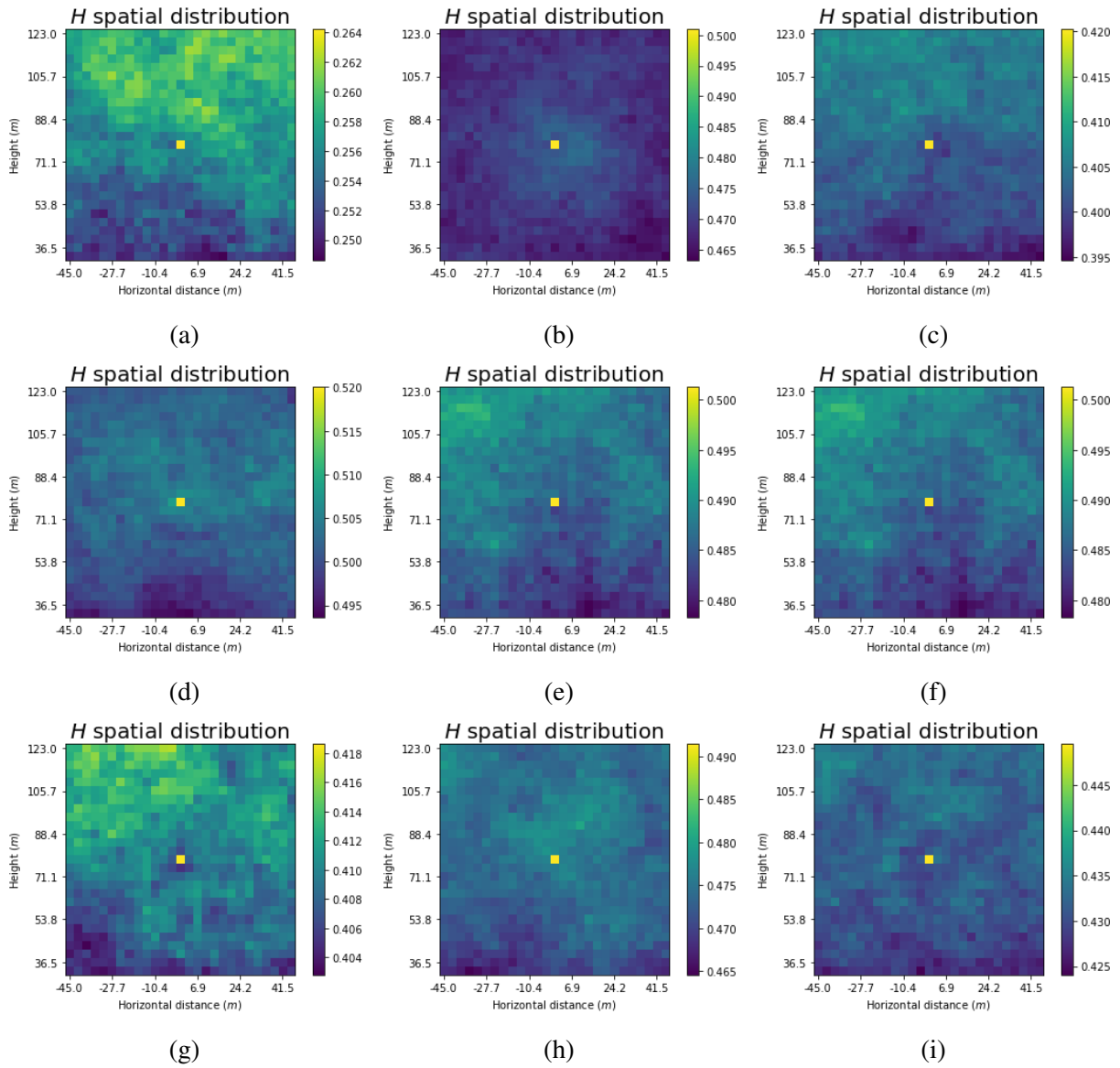


Figure B.1.3: Spatial distribution of H for different input days simulated with Turbsim. Days are listed chronologically as mention in the text at the beginning of the section.

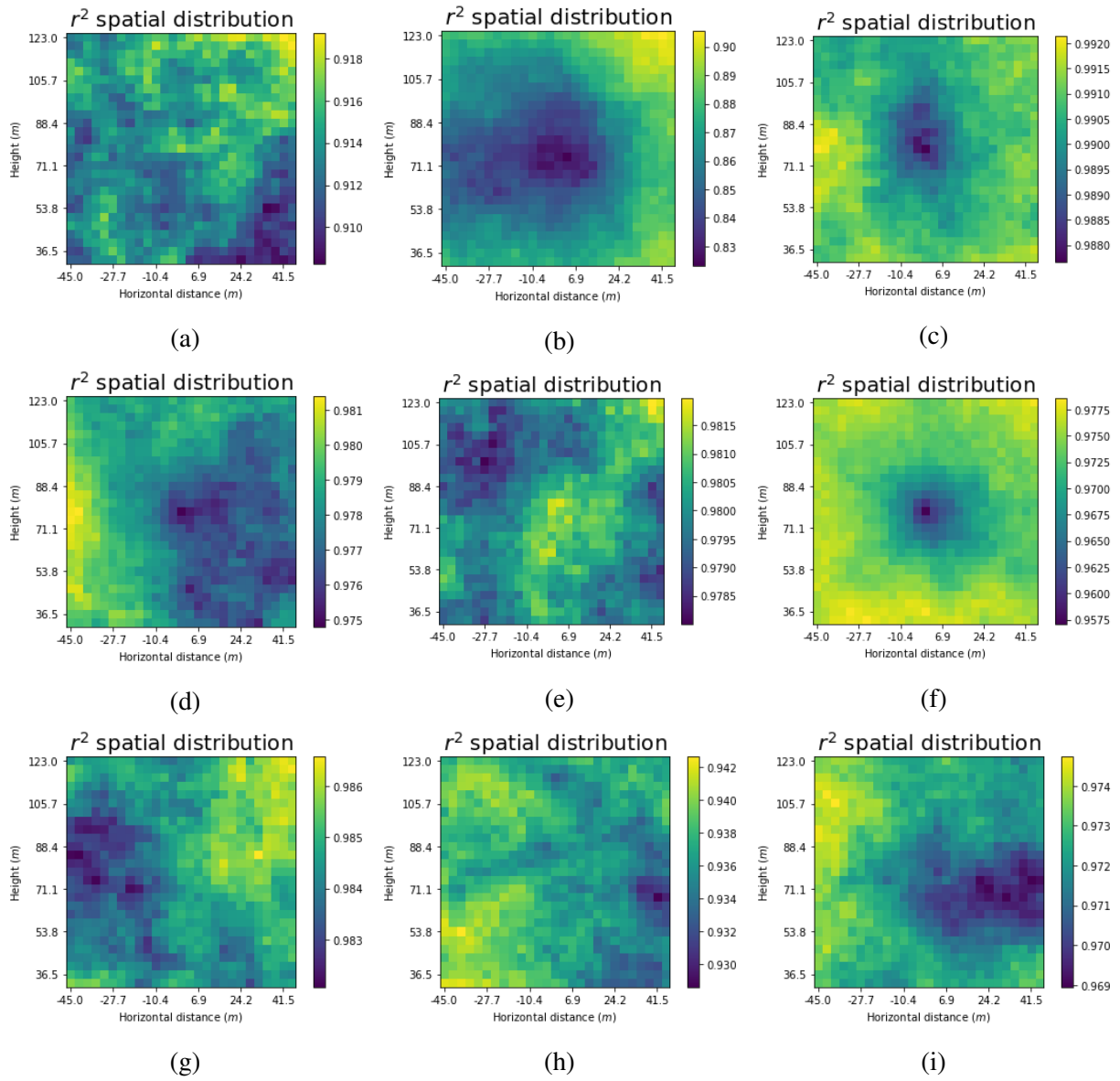


Figure B.1.4: Spatial distribution of r^2 for different input days simulated with Turbsim. Days are listed chronologically as mention in the text at the beginning of the section

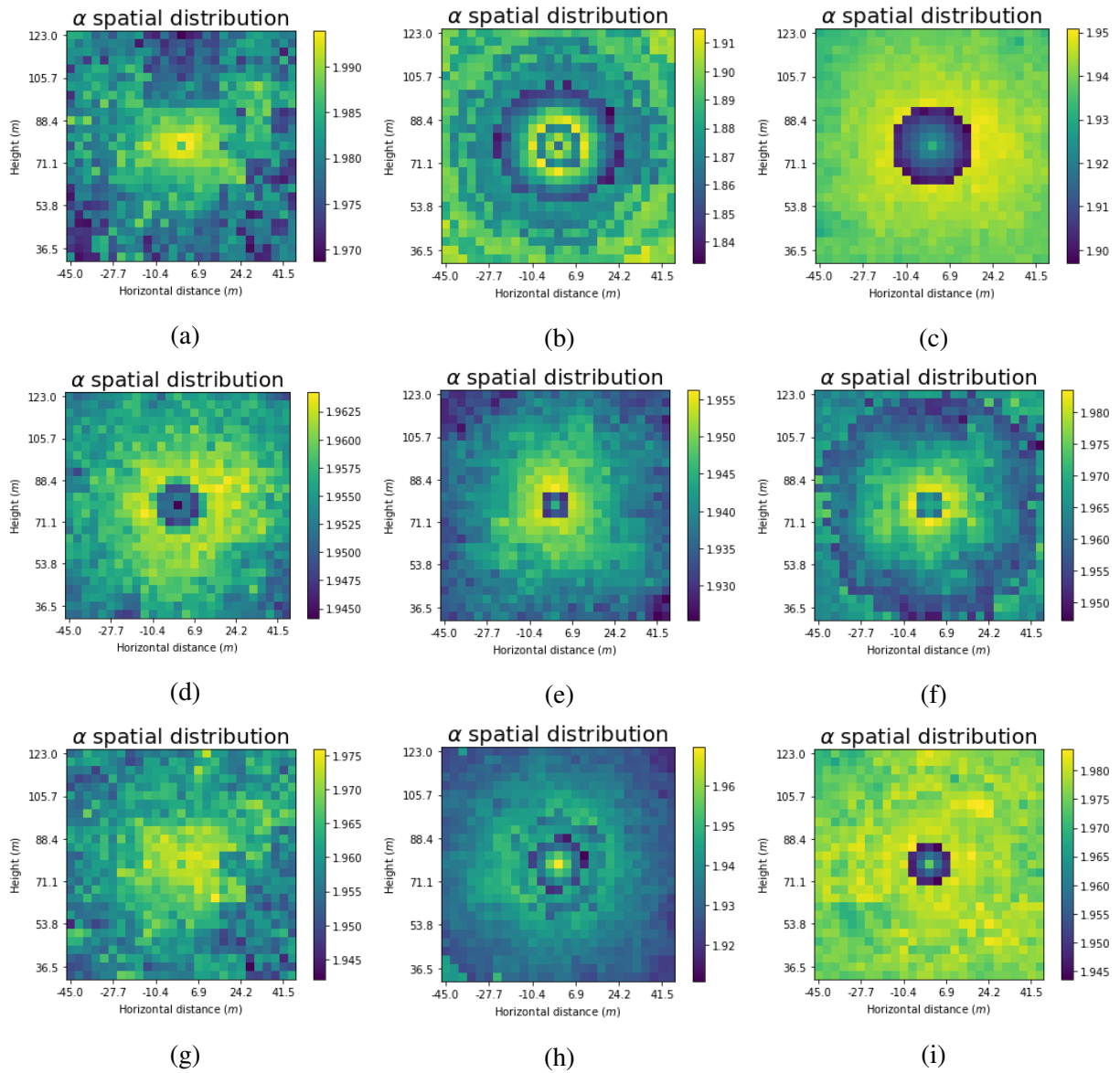


Figure B.2.5: Spatial distribution of α for different input days simulated with Simplistic approach. Days are listed chronologically as mention in the text at the beginning of the section

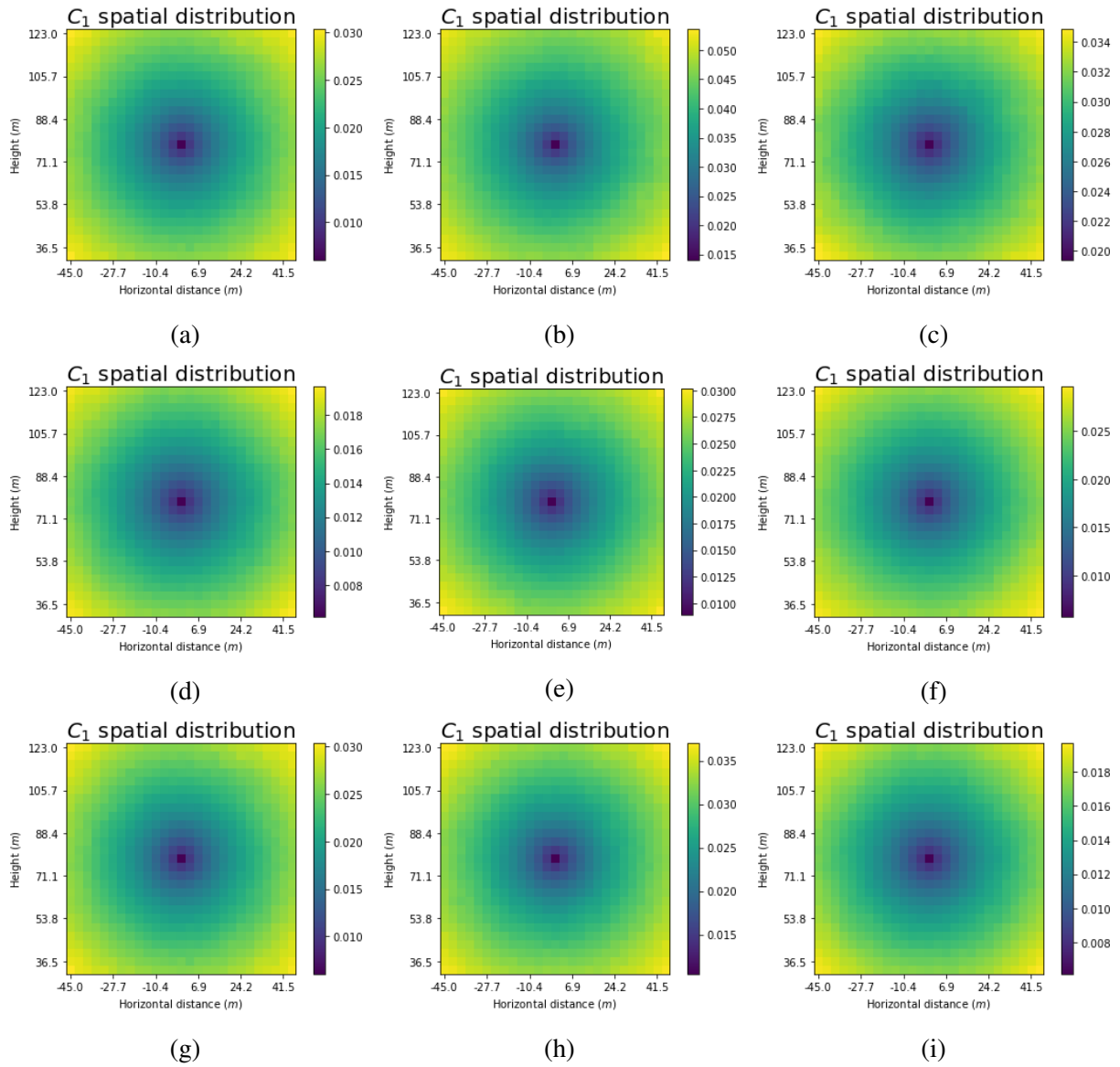


Figure B.2.6: Spatial distribution of C_1 for different input days simulated with Simplistic approach. Days are listed chronologically as mention in the text at the beginning of the section.

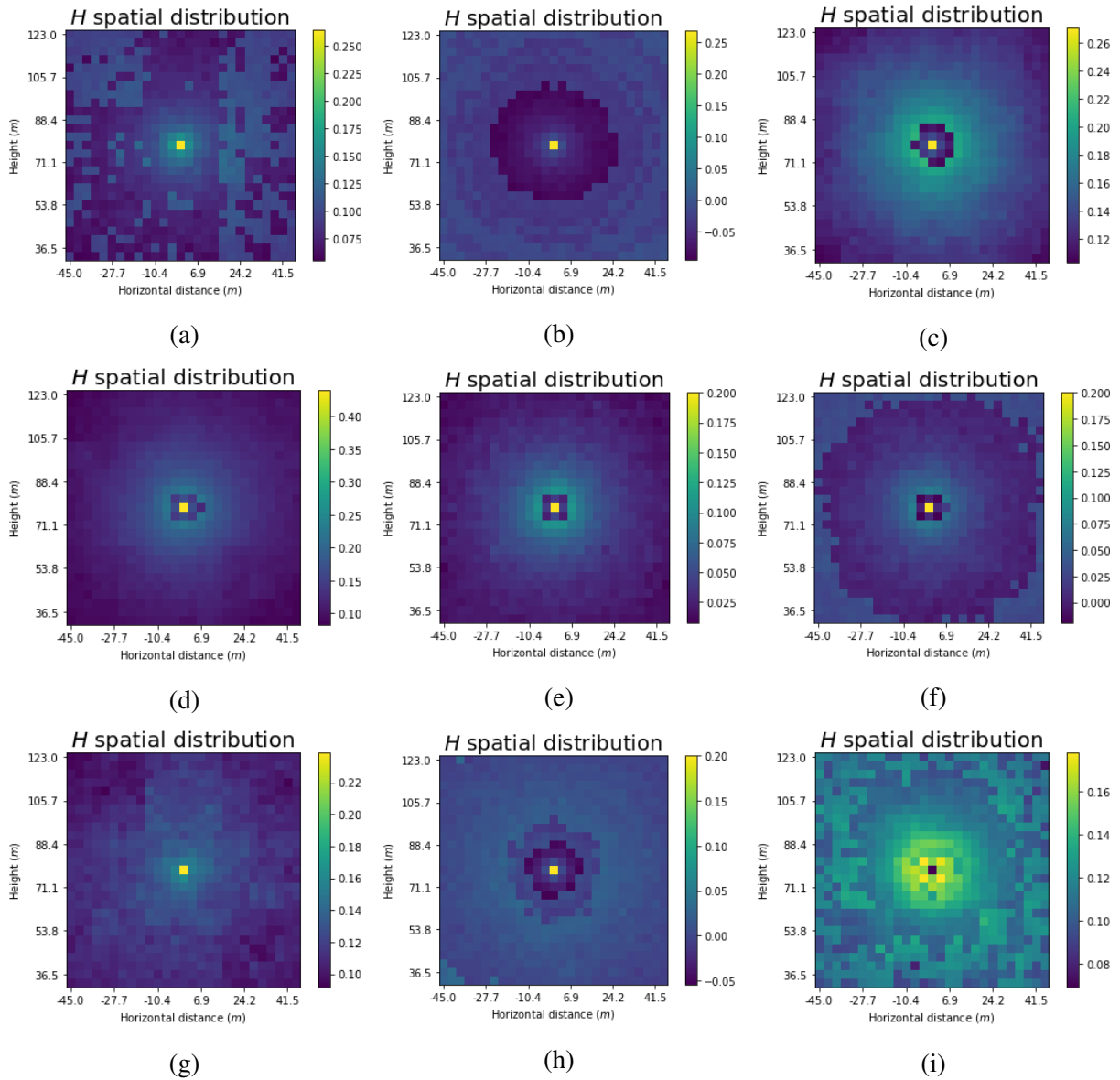


Figure B.2.7: Spatial distribution of H for different input days simulated with Simplistic approach. Days are listed chronologically as mention in the text at the beginning of the section.

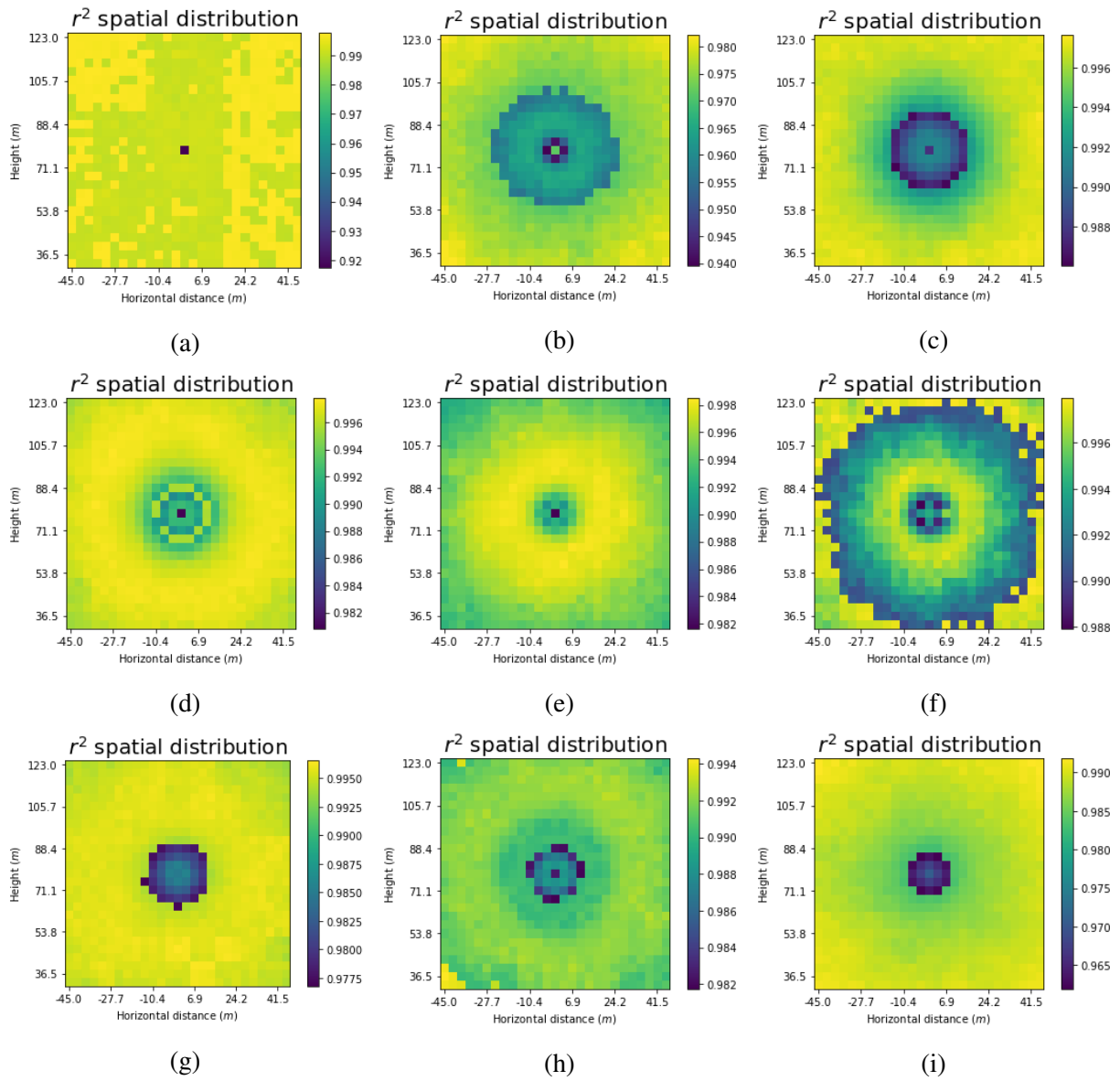


Figure B.2.8: Spatial distribution of r^2 for different input days simulated with Simplistic approach. Days are listed chronologically as mention in the text at the beginning of the section.

Appendix C

UM analysis Torque

In this chapter, all the figures corresponding to the multifractal analysis of the simulated wind and torque time series for various UM parameters input are showed. They are discussed in details in section 3.4.1 for the "10 samples" case and in section 3.4.2 for the "100 samples" case.

C.1 10 samples

C.2 100 samples

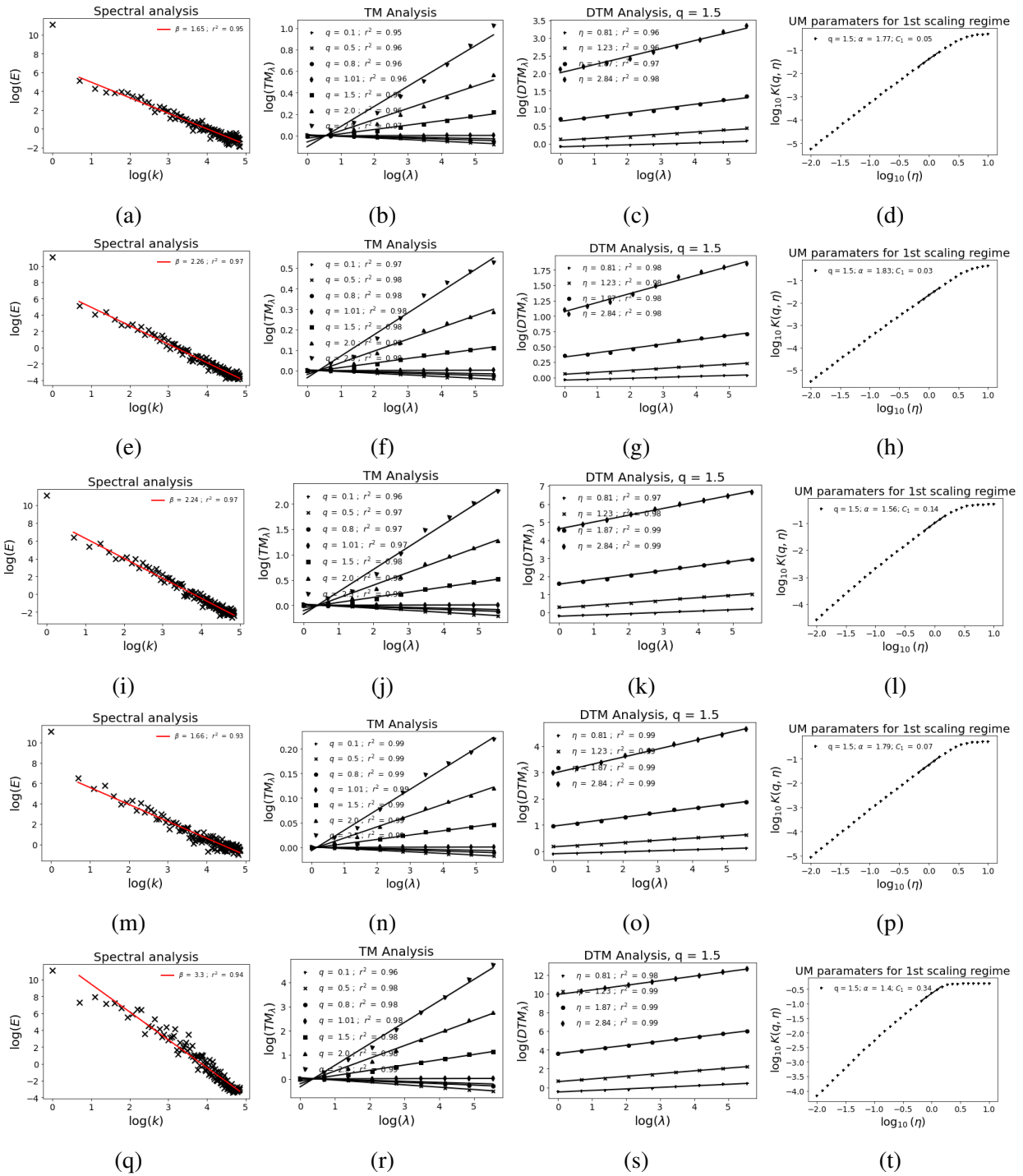


Figure C.1.1: Analysis of the horizontal wind field of the center of the grid. The analysis is made in an ensemble of 10 samples and input parameters $\alpha = 1.8$, $C_1 = 0.05$, and $a = H = 1/3$. 1st row is the analysis of the punctual velocity, 2nd avg velocity, 3rd Traditional torque, 4th Integral and, 5th OpenFAST

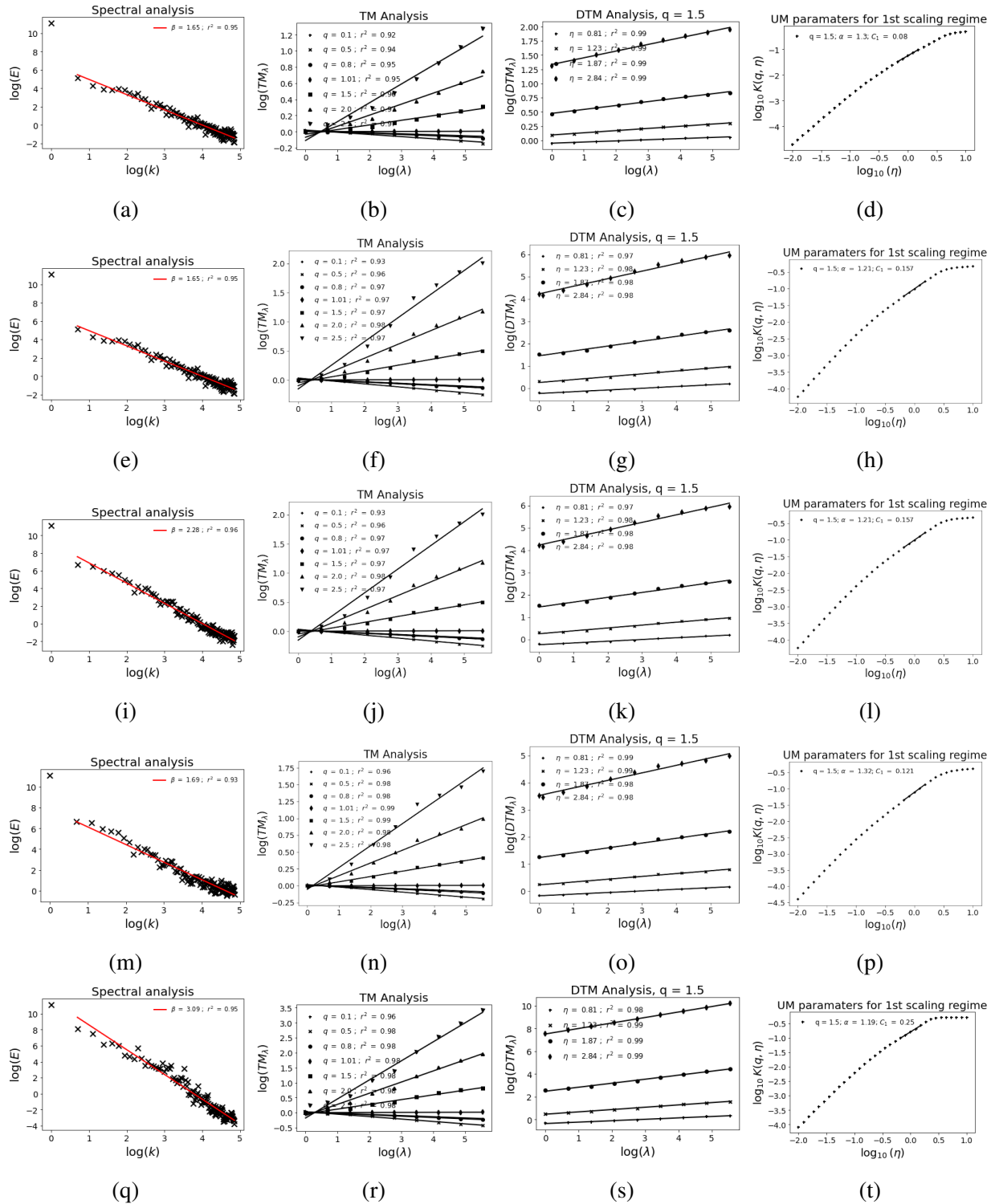


Figure C.1.2: Analysis of the horizontal wind field of the center of the grid. The analysis is made in an ensemble of 10 samples and input parameters $\alpha = 1.1$, $C_1 = 0.1$, and $a = H = 1/3$. 1st row is the analysis of the punctual velocity, 2nd avg velocity, 3rd Traditional torque, 4th Integral and, 5th OpenFAST.

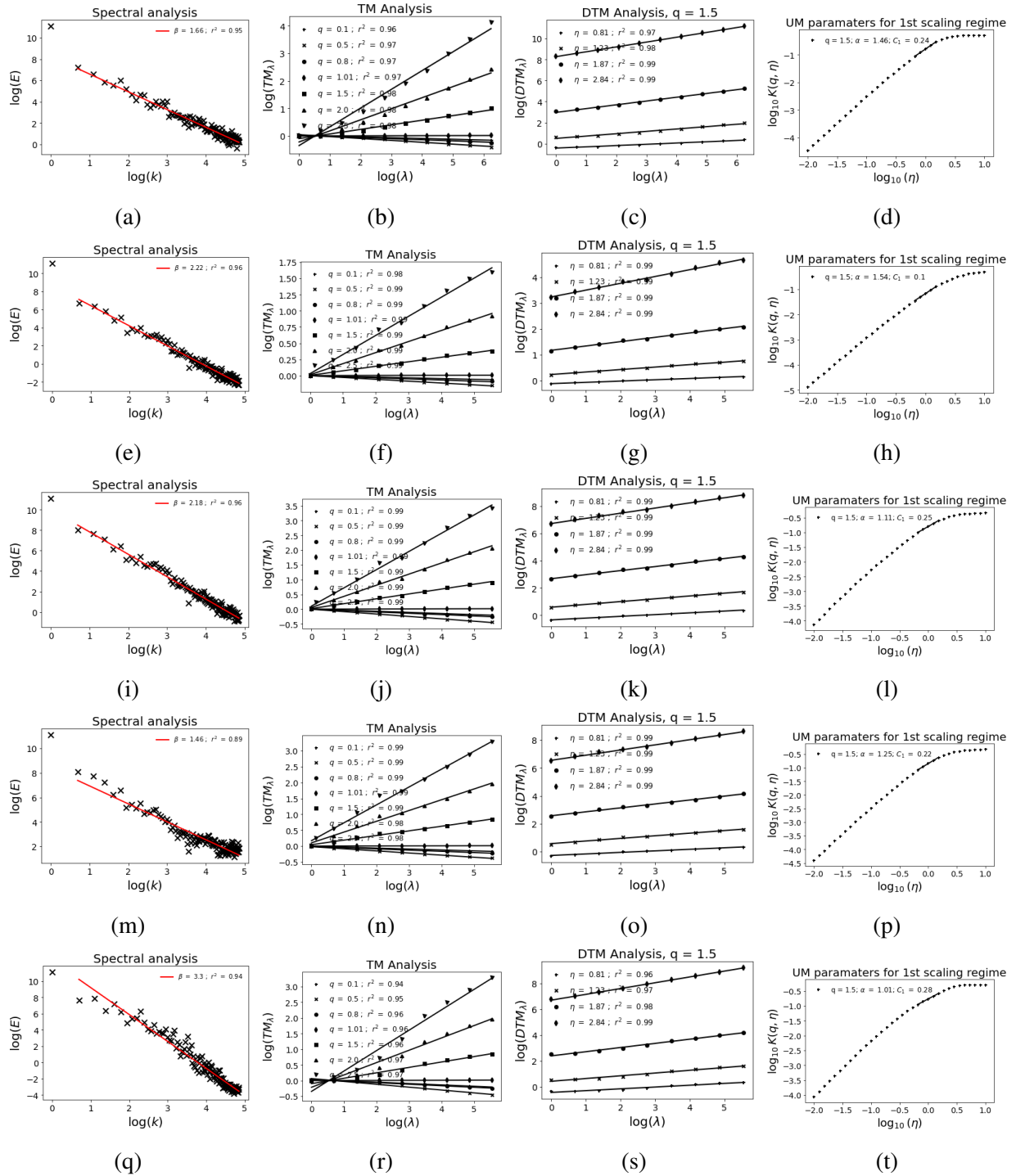


Figure C.1.3: Analysis of the horizontal wind field of the center of the grid. The analysis is made in an ensemble of 10 samples and input parameters $\alpha = 1.5$, $C_1 = 0.3$, and $a = H = 1/3$. 1st row is the analysis of the punctual velocity, 2nd avg velocity, 3rd Traditional torque, 4th Integral and, 5th OpenFAST.

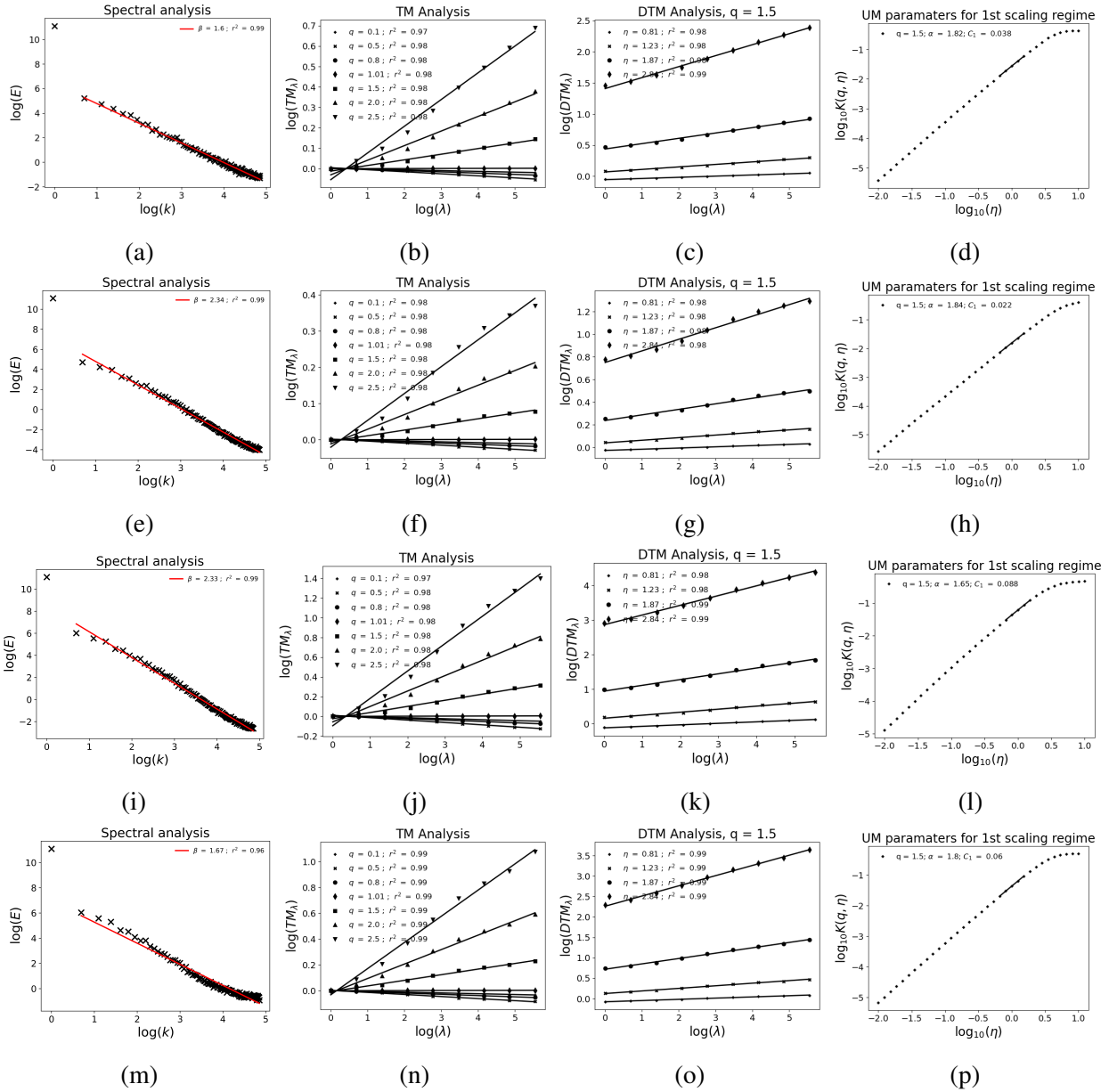


Figure C.2.4: Analysis of the horizontal wind field of the center of the grid. The analysis is made in an ensemble of 100 samples and input parameters $\alpha = 1.8$, $C_1 = 0.05$, and $a = H = 1/3$. 1st row is the analysis of the punctual velocity, 2nd avg velocity, 3rd Traditional torque and, 4th Integral

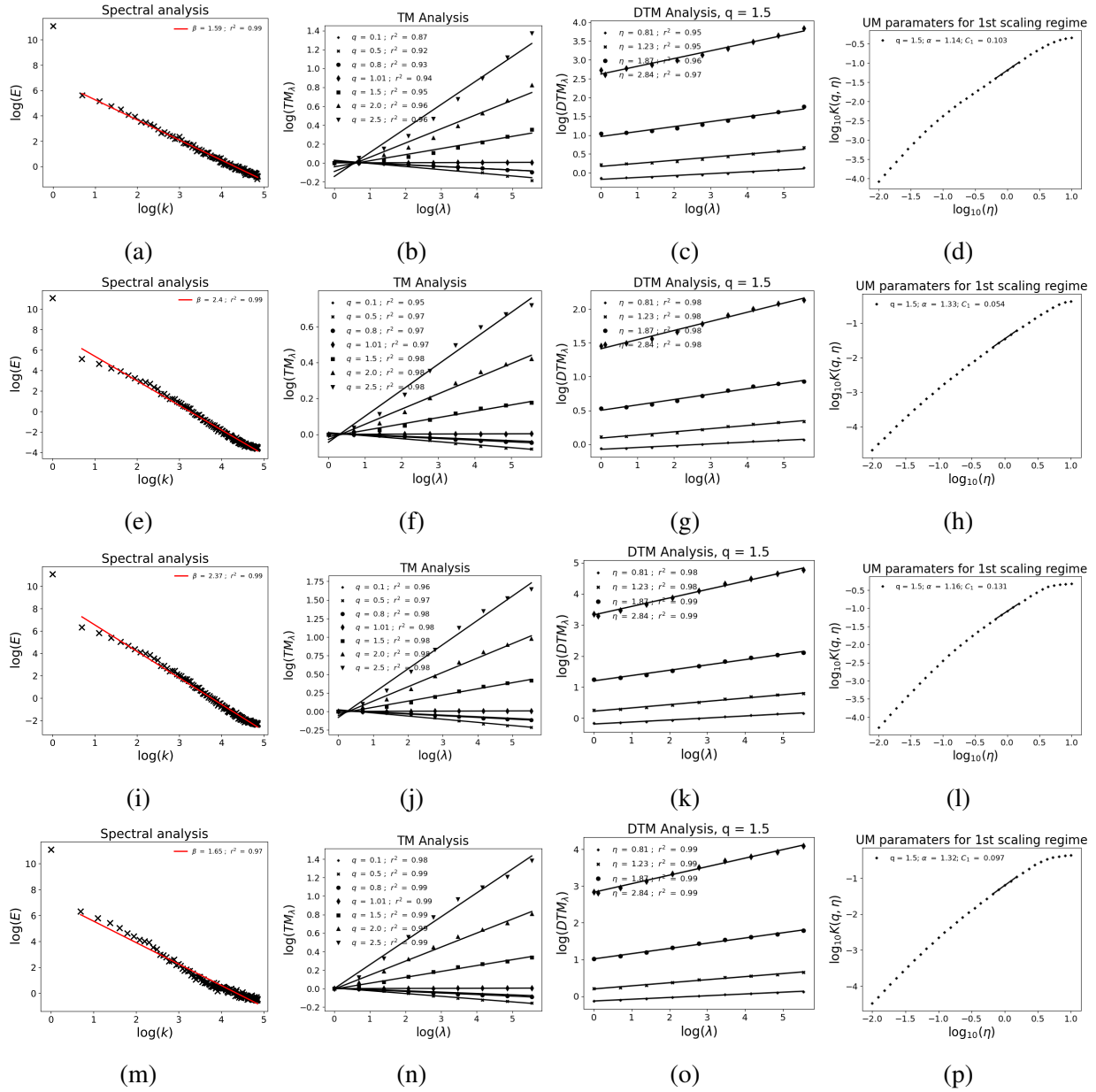


Figure C.2.5: Analysis of the horizontal wind field of the center of the grid. The analysis is made in an ensemble of 100 samples and input parameters $\alpha = 1.1$, $C_1 = 0.1$, and $a = H = 1/3$. 1st row is the analysis of the punctual velocity, 2nd avg velocity, 3rd Traditional torque and, 4th Integral

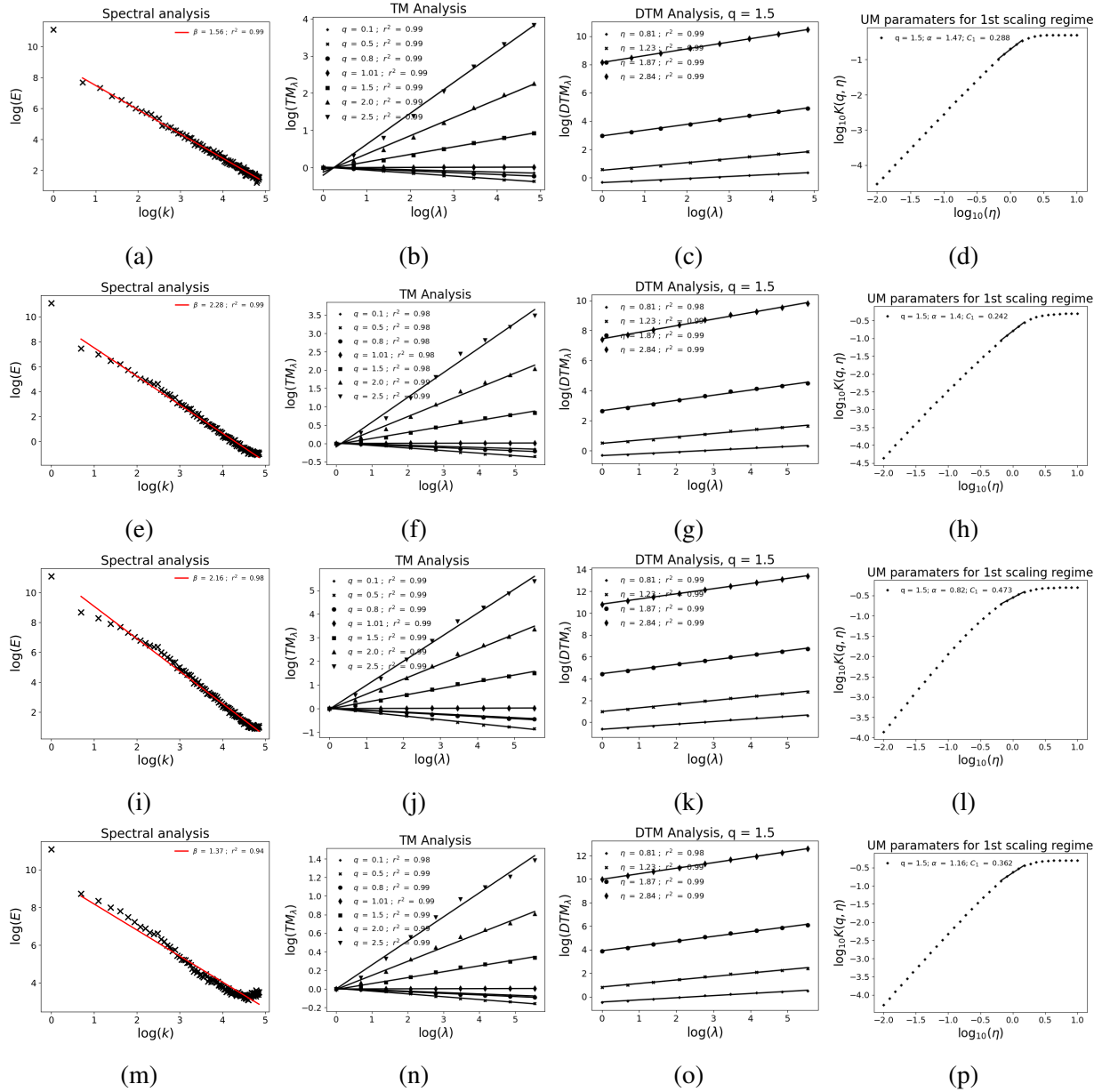


Figure C.2.6: Analysis of the horizontal wind field of the center of the grid. The analysis is made in an ensemble of 100 samples and input parameters $\alpha = 1.5$, $C_1 = 0.3$, and $a = H = 1/3$. 1st row is the analysis of the punctual velocity, 2nd avg velocity, 3rd Traditional torque and, 4th Integral

Appendix D

Scripts

Due to the length of the scripts in this Appendix we review only the main function used, with the required input and the outputs. The scripts are collected in a dedicated project of gitlab (https://gitlab.enpc.fr/auguste.gires/RW_Turb_Toolbox.git)

D.1 UM scripts

continuous_cascade(lamx,lamy,lamz,lamt,Hx,Hy,Ht,alpha,c1,dim,cau,H,a)

Creates a UM field using continuous cascades (full description in Section 1.3.3)

Inputs:

- lamx, lamy, lamz, lamt are the number of points in each dimension (x,y,z,t)
- Hx and Hy are anisotropic exponents for the spatial dimensions x and z respectively
- Ht is anisotropic exponent space-time
- alpha is the multifractality index
- c1 is the mean intermittency codimension
- dim is the dimension of the simulated field
- cau=1 is an index to include zero padding in the convolution
- H is the degree of non conservation
- a is the dimensional exponent

Outputs

- Conservative field of size (lamx,lamy,lamz,lamt)
- Non-Conservative field of size (lamx,lamy,lamz,lamt). If $H = 0$ then the Non-Conservative field is a field of zeros

vector(lamx,lamy,lamz,lamt,H_z,H_y,H_t,alpha,c1,dim,cau,H,a,nc)

Creates a UM vector field (full description in Section 1.3.4)

Inputs:

- lamx, lamy, lamz, lamt are the number of points in each dimension (x,y,z,t)
- H_z and H_y are anisotropic exponents for the spatial dimensions x and z respectively
- H_t is anisotropic exponent space-time
- alpha is the multifractality index
- c1 is the mean intermittency codimension
- dim is the dimension of the simulated field
- cau=1 is an index to include zero padding in the convolution
- H is the degree of non conservation
- a is the dimensional exponent
- nc number of components

Output

- Vector field of size (lamx,lamy,lamz,lamt,nc). If $H \neq 0$ the vector then is a non-conservative field of degree of non conservation H and dimensional exponent a

frac_intmd(data,f0,po)

Perform the fractional integration (full description in Section 1.4.3.3)

Inputs:

- data is variable to be convoluted (of length 2^n)
- f0 is the highest frequency measurement

- po is the exponent of the k -vector (the order of the Fractional integration)

Output

- Convolved field, i.e. the field after FI

find_H(data)

Find the value of H which maximize the regression coefficient performing a fractional integration of order H (full description in Section 1.4.3.3)

Inputs:

- data to be optimized
- Multifractal toolbox is required to run this function

Output

- The optimum value H to use in the fractional integration

D.2 Wind simulation scripts

simplistic_3D(av,ah,Hv,Hh,alpha,C1,dim,samples,size,grid,Height,cmeant)

Creates a 3D wind field using simplistic approach to simulate the field (full description of the mathematical process it is found in Section 2.4)

Inputs:

- av and ah scaling exponent in vertical and horizontal
- Hv and Hh are anisotropic exponents for the vertical and horizontal
- α is the multifractality index of the analysis of the difference between two heights
- $c1$ is the mean intermittency codimension of the analysis of the difference between two heights
- dim is the dimension of the desired field
- $samples$ is the number of samples
- $size$ is the number of steps of the discrete cascades
- $Grid$ gives distances in vertical (heights) and horizontal (distances to the center)

- Height is the height of the center of the grid
- cmeant is the prefactor computed from the anemometers

Output

- Simulated 3D field (x,z,t)

Reconstruct_field(inp,field,prefactor,npr)

Creates a wind field using FIF approach to simulate the fluctuations and then reconstruct the field (full description of the mathematical process it is found in Section 2.5.2)

Inputs:

- inp gives the inputs of the simulation (alpha_FI, C1_FI, H_fluct, mean)
- alpha_FI is the multifractality index of the analysis of the corrected fluctuations
- C1_FI is the mean intermittency codimension of the analysis of the corrected fluctuations heights
- H_fluc is the degree of non-conservation retrieved in the analysis of the fluctuations
- field gives the information about the size of the target field i.e. number of points in each direction
- Prefactor is the avg value of the absolute fluctuations analysed
- npr is the number of cores used for the parallel process

Output

- reconstructed field

D.3 Torque computation scripts

Torque computation scripts

torque(r,rho,TSR,beta,angle,TS,c,angleb,data,cl,cd,angle_turbine,at,x)

Creates a torque time series (full description of the mathematical process it is found in Section 3.2)

Inputs:

- r is the radius of the blade
- ρ is the air density
- TSR tip speed ratio of the blade
- β is the pitch angle of the blade
- α is the angle of attack
- TS is an index to use the tower shadow correction if TS=1 is applied
- c is the length of the chord of the blade
- angleb is the angle between the blades
- data is the input wind field
- c_l and c_d are the aerodynamic coefficients for lift and drag
- angle_turbine is the angle of the turbine to the north
- a_t is the distance between the hub and the tower mast
- x is the diameter of the tower mast

Output

- Torque time series computed using traditional approach
- Torque time series computed using integral approach

Appendix E

Publications

Conference presentations:

- García Gago, Á., Schertzer, D., & Gires, A. (2021, April). Interactions between rainfall and wind turbulence in a Universal Multifractal framework. In EGU General Assembly Conference Abstracts (pp. EGU21-10799)., <https://doi.org/10.5194/egusphere-egu21-10799>. Oral presentation.
- García Gago, Á., Gires, A., Veers, P., Schertzer, D., & Tchiguirinskaia, I. (2022, May). Transfer of small scales space-time fluctuations of wind fields to wind turbines torque computation. In EGU General Assembly Conference Abstracts (pp. EGU22-10583), <https://doi.org/10.5194/egusphere-egu22-10583>. Oral presentation.
- García Gago, Á. (2022, 29 June), Transfer of small scales space-time variability of wind fields to wind turbine torque computation, oral communication in Journee scientifique EDSIE, Champs-sur-Marne.
- García Gago, Á. , Gires, A., Veers, P., Schertzer, D., & Tchiguirinskaia, I. (2022, December). Transfer of Small Scales Space-Time Variability of Wind Fields to Wind Turbine Torque Computation using Simulations of 3D Vector Fields. In AGU Fall Meeting 2022, Bibcode: 2022AGUFMNG25B0397G. Poster presentation.
- García Gago, Á., Gires, A., Veers, P., Tchiguirinskaia, I., & Schertzer, D. (2023, May). Small Scales Space-Time Variability of Wind Fields: Simulations with Vector Fields and Transfer to Turbine Torque Computation. In EGU General Assembly Conference Abstracts (pp. EGU-11767), <https://doi.org/10.5194/egusphere-egu23-11767>. Oral presentation.

- García Gago, Á. (2023, 29 June), Characterizing and Simulating Small-Scale Wind Variability for Wind Turbine Torque Calculations, poster communication in Journee scientifique EDSIE, Créteil.
- Gires, A., Jose, J., García Gago, Á., Tchiguirinskaia, I., & Schertzer, D. (2023, December). Small scales space-time variability of rainfall and wind fields and its impact on wind power production. In AGU Fall Meeting 2023

Seminars given:

- García Gago, Á. (2021, 08 May), El tiempo para dummies - Collège d'Espagne Cité internationale universitaire de Paris, as colaboration in the Fête de la science, Paris.
- García Gago, Á.,(2023, 23 March), Variabilidad espacio-temporal del viento a pequeña escala: Simulaciones y transferencia al cálculo del torque en aerogeneradores, framed in “ciclo de seminarios del Máster de Meteorología y Geofísica”, Universidad complutense, Madrid.

Journal papers (from previous works):

- Díaz-Fernández, J., Quitián-Hernández, L., Bolgiani, P. , Santos-Muñoz, D., García Gago, Á., Fernández-González, S. , Valero, A. Merino F., García-Ortega E., Sánchez, J. L., et al. Mountain waves analysis in the vicinity of the madrid-barajas airport using the wrf model. *Advances in Meteorology*, 2020:1–17, 2020. <https://doi.org/10.1155/2020/8871546>

Other activities:

- PhD representative of the HM&Co laboratory in the École des ponts. April 2021-September 2023
- Deputy Early Career Scientist (ECS) representative of the Nonlinear Processes in Geosciences (NP) Division of the EGU. April 2023- April 2025
- Organiser of NP Division campfire November 2023
 - 4 sessions (14, 16, 21 and 23 of November)
 - 13 speakers
- Co-convenor of the session Non linear dynamic analysis and simulations of complex systems across scales for EGU2024